SURFACE CHEMISTRY CHARACTERIZATION OF HYDRODESULFURIZATION AND METHANOL SYNTHESIS MODEL NANOCATALYSTS

A Dissertation
Submitted to the Graduate Faculty
of the
North Dakota State University
of Agriculture and Applied Science

By

Mallikharjuna Rao Komarneni

In Partial Fulfillment
for the Degree of
DOCTOR OF PHILOSOPHY

Major Department:
Department of Chemistry and Biochemistry

June 2012

Fargo, North Dakota

North Dakota State University

North Dakota State University

Graduate School

Title

Surface Chemistry Characterization of Hydrodesulfurization and Methanol Synthesis Model Nanocatalysts

By

Mallikharjuna Rao Komarneni

The Supervisory Committee certifies that this ***disquisition*** complies with North Dakota State University's regulations and meets the accepted standards for the degree of

DOCTOR OF PHILOSOPHY

SUPERVISORY COMMITTEE:

Dr. Uwe Burghaus
Chair

Dr. John F. Hershberger

Dr. Guodong Liu

Dr. Alan. R. Denton

Approved:

06.06.2012
Date

Dr. Gregory R. Cook
Department Chair

ABSTRACT

Surface science investigations of model catalysts have contributed significantly to heterogeneous catalysis over the past several decades. The unique properties of nanomaterials are being exploited in catalysis for the development of highly active and selective catalysts. Surface science investigations of model catalysts such as inorganic fullerene-like (IF) nanoparticles (NP), inorganic nanotubes (INT), and the oxide-supported nanoclusters are included in this dissertation. Thermal desorption spectroscopy and molecular beam scattering were respectively utilized to study the adsorption kinetics and dynamics of gas phase molecules on catalyst surfaces. In addition, ambient pressure kinetics experiments were performed to characterize the catalytic activity of hydrodesulfurization (HDS) nanocatalysts. The nanocatalysts were characterized with a variety of techniques, including Auger electron spectroscopy, x-ray photoelectron spectroscopy, electron microscopy, and x-ray diffraction. The adsorption kinetics studies of thiophene on novel HDS catalysts provided the first evidence for the presence of different adsorption sites on INT-WS_2. Additionally, the adsorption sites on IF- MoS_2 NP and silica-supported Mo clusters (Mo/silica) were characterized. Furthermore, the C-S bond activation energy of thiophene on Mo/silica was determined. These studies finally led to the fabrication of Ni/Co coated INT-WS_2, which showed good catalytic activity towards HDS of thiophene. The studies of methanol synthesis catalysts include the adsorption kinetics and dynamics studies of CO and CO_2 on Cu/silica and silica-supported EBL-fabricated Cu/CuO_x nanoclusters. The adsorption dynamics of CO on Cu/silica are modeled within the frame work of the capture zone model (CZM), and the active sites of the silica-supported Au/Cu catalysts are successfully mapped. Studies on EBL model catalysts identify the rims of the CuO_x nanoclusters as catalytically active sites. This observation has implications for new methanol catalyst design.

ACKNOWLEDGMENTS

I heartily thank my adviser, Uwe Burghaus for his consistent support and professional guidance throughout my graduate studies. His mindful mentorship, research expertise, and moral support enabled me to grow as a researcher as well as a person and to attain the degree of my dream. Any research credentials as an experimentalist that I could possibly claim at this point are due to his authentic training, supervision, and evaluation.

I thank my committee members John F. Hershberger, Guodong Liu, and Alan R. Denton for their valuable guidance, insightful comments, and constructive criticism during my committee meetings and research proposals preparation. Their time and support were invaluable in helping me to succeed in graduate school.

I would like to gratefully acknowledge the financial support provided by NSF and DOE. These grants enabled me to embark on multiple novel research projects contained in this dissertation.

I would like to thank all our collaborators, especially Reshef Tenne of the Weizmann Institute of Science for the synthesis of novel hydrodesulfurization catalysts and Stefano Cabrini of The Molecular Foundry at Lawrence Berkeley National Laboratory for the fabrication of model array nanocatalysts.

I would like to thank Kenton Rodgers for allowing me to use an ultrasonic probe from his lab for my research work on carbon nanotubes. I also wish to thank Pinzing Zhao for lending me a magnetic hotplate/stirrer together with an oil bath from his lab for two months while conducting ambient pressure catalytic experiments on HDS nanocatalysts.

I must wholeheartedly thank my uncle, Professor Sridhar Komarneni from Pennsylvania State University, for his guidance and encouragement during my time in graduate school.

I gratefully thank my past colleagues John Goering and Evgueni Kadossov for giving me basic training in surface chemistry experimental techniques and surface analysis techniques. My thanks also to Andrew Sand, Junjun Shan, and Ashish Chakradhar for working with me on several joint projects covered by this dissertation. I greatly appreciate their knowledge, research insights, and cooperation in successfully carrying out these projects.

I am indebted to my parents Komarneni Seshaiah, Seetamma and my sisters Lalitha Vani and Nagarani for their love, unwavering support, and blessings throughout my life. I gratefully thank my in-laws, Kolasani Chinavenkata Rao and Sivakumari, for their unconditional support and encouragement.

Finally, I thank my wife, Sirisha, for being the main person to reinforce my motivation to pursue graduate studies in the USA. She helped me in every possible way to accomplish my dream of getting a doctorate degree in Chemistry. I also thank my wonderful children, Sravan Balaji and Nitya, who motivated me to do better in graduate school.

DEDICATION

This dissertation is dedicated to my parents Komarneni Seshaiah and Seetamma for their endless love and support throughout my life and education; and to my wife, Sirisha, for her love, patience, constant support and encouragement.

TABLE OF CONTENTS

LIST OF TABLES

LIST OF FIGURES

LIST OF ABBREVIATIONS

AES ..... Auger Electron Spectroscopy

BET ..... Brunauer-Emmett-Teller

CMA ..... Cylindrical Mirror Analyzer

CNTs ..... Carbon Nanotubes

CoMoCAT ..... Cobalt-Molybdenum Catalyst

CVD ..... Chemical Vapor Deposition

CZM ..... Capture Zone Model

DFT ..... Density Functional Theory

EBL ..... Electron Beam Lithography

EDX or EDS ..... Energy-Dispersive X-ray Spectroscopy

EELS ..... Electron Energy Loss Spectroscopy

EFTEM ..... Energy-Filtered Transmission Electron Microscopy

ESCA ..... Electron Spectroscopy for Chemical Analysis

FESEM ..... Field Emission Scanning Electron Microscopy

FTIR ..... Fourier Transform Infrared Spectroscopy

GC ..... Gas Chromatography

GLC ..... Gas-Liquid Chromatography

GSC ..... Gas-Solid Chromatography

HAADF ..... High Annular Dark Field Analyzer

HDS ..... Hydrodesulfurization

HiPco ..... High Pressure CO

HOPG ..... Highly Oriented Pyrolytic Graphite

HREELS ..... High Resolution Electron Energy Loss Spectroscopy

HRTEM..... High Resolution Transmission Electron Microscopy

HV..... High Voltage

IF ..... Inorganic Fullerene

INT..... Inorganic Nanotube

IR..... Infrared Spectroscopy

KE ..... Kinetic Energy

LASER..... Light Amplification by Stimulated Emission of Radiation

LEED ..... Low Energy Electron Diffraction

m-CNTs..... Metallic Carbon Nanotubes

ML..... Monolayer

NP ..... Nanoparticle

NT ..... Nanotube

PID ..... Proportional Integral Derivative

PVD..... Physical Vapor Deposition

RGA ..... Residual Gas Analyzer

SAR..... Structure-Activity Relationship

s-CNTs ..... Semiconducting Carbon Nanotubes

SDS ..... Sodium Dodecyl Sulfate

SEM ..... Scanning Electron Microscopy

STEM..... Scanning Transmission Electron Microscopy

STM ..... Scanning Tunneling Microscopy

TDS ..... Thermal Desorption Spectroscopy

TMS ..... Transition Metal Sulfide

TOF ..... Time-of-Flight Spectroscopy

TOF ..... Turnover Frequency

UHV ..... Ultra-high Vacuum

XPS ..... X-ray Photoelectron Spectroscopy

XRD ..... X-ray Diffraction

LIST OF SYMBOLS

ΔG ..... The change in Gibbs free energy

Δt ..... Time duration

A ..... Adsorbate

A_s ..... Number of atoms on the surface of a catalyst

d ..... Diameter

E ..... Energy

E_{app} ..... Apparent bond activation energy

E_b ..... Binding energy

E_d ..... Energy of desorption

E_{des} ..... Activation energy for desorption

E_f ..... Fermi level

E_i ..... Impact energy

$E_r(k)$ ..... Relaxation energy

eV ..... Electron volt

E_{vac} ..... Vacuum level

F ..... Flux

F_R ..... Flow rate

h ..... Planck's constant

k ..... Desorption rate or Reaction rate coefficient

k_d ..... Desorption rate coefficient

keV ..... Kilo electron volt

L ..... Langmuir

M ..... Metal

M/ ..... Metal coated

m/e ..... Mass to charge ratio

M@ ..... Metal doped

N ..... Number of molecules

n ..... Order of the reaction

N(E) ..... Number of electrons with energy E

p ..... Pressure

P_0 ..... Initial pressure

P_b ..... Base pressure

P_{sat} ..... Saturation pressure

P^{sat} ..... Vapor pressure

r ..... Reaction rate

R ..... Universal gas constant

S(Θ) ..... Coverage dependent adsorption probability

S_0 ..... Initial adsorption probability

T or T_s ..... Surface temperature

T_0 ..... Initial surface temperature

t_0 ..... Initial time

T_{max} ..... Peak temperature

Ŧ ..... Deposition time

V ..... Valence band

x ..... Stoichiometry

Z ..... Atomic number

α ..... Fraction of a compound converted

β ..... Heating rate

ε_{corr} ..... Correlation energy

ε_k ..... Orbital energy

ε_{rel} ..... Relativistic energy

Θ ..... Coverage

Θ_A ..... Coverage of adsorbate

Θ_{sat} ..... Saturation coverage

λ ..... Molecular mean free path length

ξ ..... Probability for molecular adsorption

ρ ..... Density of particles

υ ..... Frequency

υ_d ..... Pre-exponential factor

ϕ ..... Work function of the surface

ϕ_e ..... Energy of charge neutralization electron

ϕ_{sp} ..... Spectrometer work function

χ ..... Exposure

χ_M ..... Deposition time of metal M

CHAPTER 1. INTRODUCTION

The motivation for the research covered in this dissertation arises from "Nanocatalysis for green chemistry." The concept of "green chemistry" was introduced in the early 1990s in the scientific community. Green chemistry was considered as a new approach of chemistry in opposition to the "pollute first, clean up later" strategy followed by industries. According to the US Environmental Protection Agency (EPA), the objective of "green chemistry" is to design environmentally benign products and processes for pollution prevention. Green chemistry has 12 basic principles,[1] including catalysis, renewable feed stocks, waste prevention, and energy efficiency. Catalysis, being an important concept of green chemistry, allows us to develop efficient catalysts to meet the objective of green chemistry. If smaller (10^{-9} m, nano) amounts of active metals could be utilized in catalysts, then significant cost reduction could be achieved. The research concerning the use of nanomaterials for catalysis (nanocatalysis) has grown dramatically over the past decade.[2-3]

1.1. Nanocatalysis for Green Chemistry

The prefix "nano" is derived from the Greek word for "dwarf." When the size of a solid decreases to nanoscale dimensions, it develops unique electronic and chemical properties that are not observed in the "bulk" form of the material. In recent years, the advancements in nanoscience and nanotechnology has brought a revolution in the field of catalysis.[4] Sustainable catalytic processes are known to have great impact on human society and its development, e.g., the Haber-Bosch process that produces ammonia from N_2 and H_2 using an iron ore-based catalyst played a vital role in meeting the food supply demand and the production of chemicals. The iron catalyst used in the Haber-Bosch process contains nanometer-sized particles.[5-6] In 1989, Haruta et al. discovered the high catalytic activity of α-Fe_2O_3-supported Au nanoparticles (< 5 nm) for CO

oxidation[7]. This led to a great research activity in the field of catalysis concerning the particle size effects on catalytic activities.[8-10]

Most of the heterogeneous catalytic reactions take place at the active sites of the bulk catalyst.[11] The catalytic activity of supported metal nanoclusters has been extensively investigated.[4] It is well known that the surface area to volume ratio plays a vital role in the reactivity of solid catalysts. Therefore smaller active metal particles are expected to be catalytically more reactive due to their high surface area. However, surface area alone does not ensure high reactivity, e.g., the catalytic activity of Pt nanoparticles is correlated with the number of surface atoms on corners and edges.[12] While designing a nanocatalyst, several parameters, such as the variation in the number of low-and high-coordinated sites with respect to particle size, quantum confinement effects, and the metal support interactions have to be considered.[4]

The properties of nanomaterials can be tuned by altering their size, shape, and chemical composition.[13-15] Studying the effects of size, shape, and chemical composition of metal clusters on the catalytic activity is the current area of research.[16] Nanocatalysts often exhibit comparable catalytic activities and selectivities to that of homogeneous catalysts, and, therefore they are considered as quasi-homogeneous systems.[17] Nanoscience combined with catalysis allows for the atomic level manipulation of the active metal particles in catalysts that lead to catalyst optimization.[4]

1.2. Heterogeneous Catalysis and Model Catalysts

Heterogeneous catalysis (solid/gas) has wide spread applications ranging from hydrocarbon refining to fuel-cell technologies.[18] Typical heterogeneous metal catalysts contain dispersed active metal particles on a highly porous, high-surface-area oxide (e.g., Al_2O3, CeO_2, SiO_2, TiO_2). The catalytic activity and selectivity of a heterogeneous catalyst is governed by

several factors such as the type and nature of the metal particle, atomic and electronic structure of metal particle, particle size, support effects, particle-support interactions, type and nature of catalyst promoter, type of treatment, and the reaction conditions.

Surface science techniques combined with surface-sensitive spectroscopic techniques led to the molecular-level understanding of surfaces, surface-adsorbate, adsorbate-adsorbate interactions, adsorption/desorption of gases, and chemical reactions on model catalysts.[19-23] The model catalysts provide a suitable replicate for real-world catalysts, i.e., they mimic the active surface(s) present on industrial catalysts. The typical model catalysts used in surface science consist of metal single crystals, metal thin films, multimetallic thin films, oxide-supported metal catalysts, and metal-supported oxide catalysts. Several studies have shown a clear correlation between the catalytic behavior of model and industrial catalysts.[19, 22] However, two barriers, the so-called pressure and material gaps, are encountered in relating the UHV investigations on model catalysts to industrial catalysts.

Surface science studies on model catalysts are conducted at UHV conditions; whereas, the industrial catalysts are operated at high pressures (> 1atm). This large difference in operating conditions is the so-called 'pressure gap.'[19] Recently, some systems which enable the kinetics reaction measurements to be done at high pressures on clean surfaces have been designed.[24-25]

As discussed earlier, industrial catalysts typically have dispersed active metal particles on a highly porous, high-surface-area oxide. On the other hand, metal single crystals do not allow one to investigate the support effects, particle size effects, structure effects, etc. This is the the so-called 'material gap.'[19, 22] Over the past two decades, several techniques have been developed to fabricate/create well-characterized model catalyst (metal clusters on ultra-thin metal oxide surfaces) samples under UHV conditions. These well-characterized model catalysts enabled the

investigations concerning the cluster-support interactions and particle size effects.[21-23, 26-27] Ultrathin metal oxide films are conductive, enabling the use of scanning tunneling microscopy (STM) to gain molecular-level understanding of surface reactions.

Several prior studies addressed the significance of metal single crystals as model catalysts. When the catalytic reactions are carried out on metal single crystals at realistic conditions, the related surface chemistry and kinetics can be used to model the behavior of real industrial catalysts, e.g., a kinetic model for methanol synthesis was based on the Cu(100) single crystal studies.[28]

In the case of metal catalysts, the relative concentration of adsorption sites, such as terraces, steps, kinks, and defects are changed by the method of formation and particle sizes.[19-20] These factors can modify the coordination of surface atoms which can impact adsorbate binding energies and eventually the catalytic activities. Thus, structure-sensitive reactions are expected. However, some reactions exhibit kinetics that is independent of metal particle size and surface orientations (surface-insensitive reactions), e.g., CO methanation,[29] CO oxidation on Rh, Pd, and Pt,[19-20] ethylene hydrogenation, etc.[19] In these cases, the single crystal kinetics were very similar to those obtained for industrial catalysts.[30] The reason for structure insensitivity may be mostly due to the poisoning/screening of surface sites that are responsible for structure-sensitive activity by the reactants/intermediates. Metal catalyst particles are typically modified by impurity species. Studies investigating the role of these impurities in either promoting or poisoning the catalytic reactions are of practical interest in catalysis.[31] Poison/promotion effects of impurities and electronic effects[32] can be investigated using metal single crystal model catalysts.

Some reactions exhibit kinetics that heavily depend on metal particle size and surface orientations (surface-sensitive reactions), e.g., alkane hydrogenolysis,[33] CO oxidation by NO on

Pd surfaces,[34] ammonia synthesis on Fe, etc.[19-20] In the case of structure-sensitive reactions, the coordination numbers, atomic spacing, and electronic properties play vital roles in the rate-limiting kinetics.

Single crystal surfaces do not completely mimic the real-world catalysts. Studies on single crystal surfaces cannot address particle size effects, support effects or particle-support interactions. However, this material gap can be bridged using the planar oxide-supported metal cluster model catalysts. The planar oxide catalysts are prepared either by cleaving the bulk oxide single crystals or growing thin films on refractory metal substrates. The thin (metal) oxide films have been extensively used to study particle-support interactions.

In the case of oxide-supported metal cluster model catalysts, the metal particle size influences the electronic structure, support interactions, chemical and catalytic activities, and thermal behavior. Fabrication procedures for several model oxide films, including SiO_2,[35] Al_2O_3,[36] MgO,[37] and TiO_2[38] are available in the literature. Several metal cluster deposition methods are available for the fabrication of oxide-supported metal cluster model catalysts, including physical vapor deposition,[39-41] high frequency laser vaporization,[42] mass-selective cluster deposition,[43-44] nanolithography,[45-47] and electron beam lithography (EBL).[48] Although the last two techniques are time-consuming, the samples fabricated by these methods can be used to study particle size and shape effects, sintering, lateral mass transport, etc.

The development of structure-activity relationships at an atomic level is very important for heterogeneous catalysis. Unlike the high-surface-area industrial catalysts, the planar model catalysts can be used to study structure-activity relationships. For example, Au particles (with particle diameter below 10 nm) dispersed on TiO_2 exhibited very high catalytic activity for reactions such as CO oxidation and propylene epoxidation.[49-50] The effect of cluster size on

reaction rates is clearly observed for Au/TiO_2 catalysts.[41, 50-54] Au clusters with ~ 3 nm size exhibited the maximum reaction rate for CO oxidation.[54] The unique catalytic activity of Au bilayer structure for CO oxidation has recently been reported for Au/TiO_2 catalysts. The (1 x 3) bilayer structure was 45 times more highly active than high-surface-area Au/TiO_2 catalysts.[55-56] Although both the catalysts contained the TiO_2 support, the TiO_2 support alone did not increase the catalytic activity. Thus, the surface-science models are not only capable of mimicking the catalytic properties of real-world catalysts but also set targets for catalyst optimization.

Surface science investigations of novel nanocatalysts such as inorganic fullerene-like (IF) nanoparticles (NP), inorganic nanotubes (INT), oxide-supported nanoclusters, and carbon nanotubes (CNTs) are included in this dissertation.

1.3. Hydrodesulfurization Model Catalysts

Hydrodesulfurization (HDS) is an industrial process used for the removal of sulfur from natural gas and refined petroleum products. Organo-sulfur compounds present in the fuel include thiophene, dibenzothiophene, and related compounds. The current need for the development of novel HDS catalysts stems from the stringent fuel sulfur regulations and increasing environmental concerns. The catalytic activity of several novel nanocatalysts (model catalysts) towards HDS of thiophene is investigated herein.

Hydrodesulfurization model catalysts investigated in this dissertation include: pristine[57] and Re doped IF-MoS_2 NP, pristine[58] and metal (M) coated INT-WS_2 (M = Co, Ni, Au),[59-60] and physical vapor deposited (PVD) silica-supported Mo clusters.[61] Adsorption kinetics of thiophene on these hydrodesulfurization model catalysts was investigated using thermal desorption spectroscopy (TDS). In addition, the adsorption dynamics of thiophene on silica-supported Mo clusters was investigated. Furthermore, the ambient pressure kinetics experiments were

performed to screen the catalytic activity of pristine and Re doped IF-MoS_2 NP, pristine and metal (M) coated INT-WS_2 (M = Co, Ni, Au), commercial catalysts NiMo, CoMo from Haldor Topsoe, and nano MoS_2 from Impex Corp. The green aspects of hydrodesulfurization model studies in this research include: catalysis, pollution prevention, and energy efficiency.

1.4. Methanol Synthesis Model Catalysts

Methanol is industrially synthesized from synthesis gas over $Cu/ZnO/Al_2O_3$ catalysts at temperatures of 493-573 K and pressures 50-100 bar.[62] Synthesis gas (90% H_2, 5% CO, and 5% CO_2) is manufactured by steam reforming of natural gas. Metallic copper is the active phase of the catalyst since the catalytic activity correlates linearly with the area of copper.[63-64] This was later confirmed by in situ x-ray photoelectron spectroscopy[65] and surface x-ray diffraction studies.[66] Some prior studies reported that CO_2 is the necessary component in synthesis gas for the production of methanol.[67] However, it was later proved by ^{14}C labeling experiments that methanol is mainly synthesized from CO_2 in the synthesis gas.[68] This was further supported by the measurements on working catalysts.[69] These results suggested the following reactions are involved in methanol synthesis:

$$CO + H_2O \rightleftharpoons CO_2 + H_2 \qquad (1)$$

$$CO_2 + 3H_2 \rightleftharpoons CH_3OH + H_2O \qquad (2)$$

Methanol synthesis from H_2/CO_2 feedstock over Cu single crystals,[70] Cu/SiO_2 and $Cu/ZnO/SiO_2$[71] were also reported. Furthermore, the UHV experimental data obtained on Cu(100) single crystal was also used to propose kinetic models for methanol synthesis.[28] Surprisingly, the calculated methanol synthesis rates were in very good agreement with those obtained on a real catalyst. Thus, the kinetic models based on model catalyst studies at UHV conditions are useful to analyze the reaction mechanisms of industrial catalysts.

Methanol synthesis model catalysts investigated in this dissertation include: PVD silica-supported Cu clusters,[39, 72] electron beam lithography (EBL)-fabricated silica-supported Cu and CuO_x clusters.[48, 73] Adsorption dynamics of CO on PVD silica-supported Cu clusters was investigated using molecular beam scattering. In addition, the adsorption kinetics and dynamics of CO and CO_2 on EBL-fabricated Cu and CuO_x clusters was investigated. The green aspects of methanol synthesis model studies in our research include: catalysis, renewable feedstocks, and energy efficiency.

CHAPTER 2. EXPERIMENTAL TECHNIQUES

A variety of experimental techniques were used for studying the model catalysts. Thermal desorption spectroscopy (TDS) was used to study the adsorption kinetics of gas phase molecules on model catalyst surfaces. Molecular beam scattering was used to study the gas-to-surface energy transfer (adsorption dynamics) processes. An atmospheric pressure flow reactor coupled to a gas chromatograph (GC) was used to perform ambient pressure kinetics experiments on powder catalysts. Auger electron spectroscopy (AES) and x-ray photoelectron spectroscopy (XPS) were used to characterize the chemical cleanliness/state of the nanocatalysts. In addition, with great effort and collaboration, researchers were able to characterize the nanocatalyst materials using a variety of experimental techniques, including scanning electron microscopy (SEM), high-resolution transmission electron microscopy (HRTEM), x-ray diffraction (XRD), energy dispersive spectroscopy (EDS), and electron energy loss spectroscopy (EELS). A description of each technique available in the research laboratory is presented hereafter.

2.1. Ultra-high Vacuum

A vacuum environment is a prerequisite for a majority of surface science and surface analysis techniques. At a pressure of $1x10^{-6}$ Torr, a surface can be covered with a monolayer of adsorbed gases in about one second. Thus, it is necessary to keep the surface free from adsorbed gases during the course of a surface science/surface analysis experiment. This needs an ultra-high vacuum (UHV) environment. Vacuum pressures in the range of $< 10^{-9}$ Torr are required to create ultra-high vacuum conditions. There are several reasons for a UHV environment, the most important being the requirement for long mean free path for particles, such as ions, electrons, and molecules used in surface analysis/surface science and the need to keep a surface free from

adsorbed gases during the course of a surface science/surface analysis experiment. In addition, the UHV is also required to maintain high voltages in a surface analysis system without breakdown or glow discharges. The creation of an ultra-high vacuum and the description of UHV chambers are presented in the next section.

2.2. Kinetic Measurements: Thermal Desorption Spectroscopy

Thermal desorption spectroscopy (TDS) is an important kinetic technique to determine the kinetic parameters of desorption processes, such as heat of adsorption of a gas on a surface. This simplest method of surface analysis is utilized in almost all projects covered in this dissertation. TDS can be used to measure the heat of adsorption, which is a measure of the strength of interaction between an adsorbate and a surface. TDS can determine many other useful values, such as the degree of coverage of the surface, desorption order, and, to some extent, the nature of the adsorbed species. A brief TDS experimental procedure is described below.

The sample is mounted in an ultra-high vacuum (UHV) chamber. The sample is either maintained at room temperature or sub-ambient temperature (~ 90 K). A leak valve is opened to dose a particular gas into the UHV chamber, i.e., the clean surface is first exposed to the desired gas molecules until some coverage is reached. The gas molecules are desorbed with a linear increase in surface temperature over time. It is ensured that the surface is heated above the molecular desorption temperature of the adsorbate. The desorbed gas molecules are detected by a mass spectrometer to determine the desorption rates, as well as other parameters described above. TDS measurements are carried out by varying the surface coverage of the adsorbate. The gas exposures are given in Langmuir (1 L = 1 s gas exposure at $1x10^{-6}$ mbar). Surface temperature strongly influences the desorption behavior and this phenomenon can be described by the Polanyi-Wigner equation, derived below.

Consider an adsorbate A which is adsorbed on a surface. It desorbs into the gaseous state on heating the surface. k_d is the desorption rate coeficient.

$$A_{ads} \xrightarrow{k_d} A_{gas} \qquad (3)$$

The desorption rate (k) is expressed by a rate law of n^{th} order and is given by the negative rate of change of the coverage of adsorbate molecules. Θ_A is the coverage of adsorbate molecules in monolayers.

$$k = k_d[A_{ads}]^n \qquad (4)$$

$$k = -\frac{d\Theta_A}{dt} = k_d \Theta_A{}^n \qquad (5)$$

An Arrhenius equation, describing the desorption rate coefficient k_d, is given below, where υ_d is the frequency factor or the pre-exponential factor, E_{des} is the activation energy for desorption, R is the Universal gas constant, and T_S is the surface temperature.

$$k_d = \upsilon_d \, e^{-\frac{E_{des}}{RT_s}} \qquad (6)$$

By combining equations 5 and 6, the desorption rate law, which is usually referred to as the Polanyi-Wigner equation, can be obtained.

$$-\frac{d\Theta_A}{dt} = \upsilon_d \, e^{-\frac{E_{des}}{RT_s}} \Theta_A{}^n \qquad (7)$$

The surface temperature T is increased linearly in a TDS experiment according to the equation given below, where T_0 is the initial temperature, β is the heating rate, and t is the time.

$$T = T_0 + \beta t \qquad (8)$$

Heating rate β is the derivative of temperature with respect to time.

$$\Rightarrow \frac{dT}{dt} = \beta \Rightarrow dt = \frac{1}{\beta} dT \qquad (9)$$

By substituting the value of dt in equation 5, one arrives at

$$k = -\frac{d\Theta_A}{dt} = -\frac{d\Theta_A}{\frac{1}{\beta}dT} = -\beta\frac{d\Theta_A}{dT} \qquad (10)$$

By substituting this term in the Polanyi-Wigner equation, one arrives at

$$-\beta\frac{d\Theta_A}{dT} = \upsilon_d e^{-\frac{E_{des}}{RT_s}}\Theta_A{}^n \Rightarrow -\frac{d\Theta_A}{dT} = \frac{\upsilon}{\beta}e^{-\frac{E_{des}}{RT_s}}\Theta_A{}^n \qquad (11)$$

The pressure burst of desorbing gas in a TDS experiment is directly proportional to the derivative of adsorbate coverage with respect to temperature. The activation energy for desorption is calculated by determining the peak in pressure which corresponds to the maximum desorption rate or peak temperature (T_{max}). Peak in pressure is determined by taking the second derivative of adsorbate coverage with respect to temperature and make it equal to zero.

$$p \propto \frac{d\Theta_A}{dT} \Rightarrow \frac{d}{dT}\left(\frac{d\Theta_A}{dT}\right) = \left(\frac{d^2\Theta_A}{dT^2}\right) = 0 \qquad (12)$$

$$\frac{d}{dT}\left(-\frac{\upsilon}{\beta}e^{-\frac{E_{des}}{RT_s}}\Theta_A{}^n\right) = \left(\frac{d^2\Theta_A}{dT^2}\right) = 0 \qquad (13)$$

One can use the product rule for differentiation to the left side of equation 13 to get the following equation:

$$\Rightarrow \frac{\upsilon}{\beta}\left(n\Theta^{n-1}\frac{d\Theta_A}{dT}e^{-\frac{E_{des}}{RT_{max}}} + \frac{\Theta^n E_{des}}{RT^2{}_{max}}e^{-\frac{E_{des}}{RT_{max}}}\right) = 0 \qquad (14)$$

By rearranging the terms in equation 14, one arrives at the following equation:

$$\Rightarrow n\Theta^{n-1}\frac{d\Theta_A}{dT} = -\frac{\Theta^n E_{des}}{RT^2{}_{max}} \qquad (15)$$

After substituting the value of $\frac{d\Theta_A}{dT}$ from equation 11 in the above equation and rearranging the terms, the following equation is created, which is usually referred to as the Redhead equation.

$$\frac{\upsilon}{\beta}n\Theta^{n-1}e^{-\frac{E_{des}}{RT_{max}}} = \frac{E_{des}}{RT^2{}_{max}} \qquad (16)$$

Redhead assumed that activation parameters are independent of surface coverage and estimated the desorption activation energy, E_{des}, for the first order desorption using the Redhead equation as follows:

$$E_{des} = RT_{max}[\ln(\frac{\upsilon T_{max}}{\beta}) - 3.64] \qquad (17)$$

The Redhead method is often used to determine the activation energy from a single desorption spectrum by choosing the pre-exponential factor value as 10^{13} s^{-1}. Details of the desorption spectra, such as the shapes, number, and position of the peaks, help to understand the chemistry of the adsorbate-surface system. Redhead analysis methods are used to determine the order of desorption of the desorbing species as described below.

2.2.1. Desorption of zero order

TDS curves corresponding to different surface coverages have a common leading edge which looks exponential. T_{max} increases with an increase in surface coverage, and the peak intensity drops immediately after reaching the maximum.

2.2.2. Desorption of fractional order

TDS curves corresponding to different surface coverages do not have a common leading edge. T_{max} increases with an increase in surface coverage, and the peak intensity does not drop immediately after reaching the maximum.

2.2.3. Desorption of first order

TDS curves corresponding to different surface coverages are asymmetrical about the maximum. The peak width at half maximum and T_{max} are independent of the surface coverage.

2.2.4. Desorption of second order

TDS curves corresponding to different surface coverages are symmetrical about T_{max} and are bell shaped. T_{max} decreases with an increase in surface coverage. Multiple peaks

corresponding to different biding sites on the surface are often observed in the second order desorption process.

The desorption spectra can be analyzed as a function of heating rate and coverage to determine the pre-exponential factor. The activation energy for desorption can be determined by using the Redhead equation. Two conditions have to be met to use the Polanyi-Wigner equation to perform accurate spectral interpretation. The first condition is that the mass spectrometer signal is proportional to the rate of desorption. This condition is met if the pumping speed is high enough to prevent the re-adsorption of desorbed particles on the sample. The second condition is that the desorption process consists of at least one rate limiting elementary step. The activation parameters such as the pre-exponential factor, desorption order, and the activation energy generated by Polanyi-Wigner equation will only be applicable to such a rate limiting step. Activation parameters are dependent on the surface coverage and the sample temperature. However, the Polanyi-Wigner equation cannot be used for the analysis of complex desorption spectra due to the dynamic nature of the desorption process. Monte-Carlo simulations are considered as the alternatives to the interpretation by means of the Polanyi-Wigner equation.

An example of TDS spectra of benzene on metallic carbon nanotubes (m-CNTs) is shown in Figure 1. Four distinct peaks A, B, C, and D are observed in this TDS spectra. They indicate the presence of kinetically different adsorption sites. The peaks A, B, C refer to benzene adsorption on internal, external, and groove sites of m-CNTs respectively. The low temperature edges of the TDS curves line up to form a peak D, an adsorption (and system) unspecific condensation peak of benzene. The Redhead equation can be used to calculate the binding energies of benzene on these sites, e.g., benzene has a binding energy of 70 kJ/mol on the internal sites (peak corresponding to 270 K) of m-CNTS.

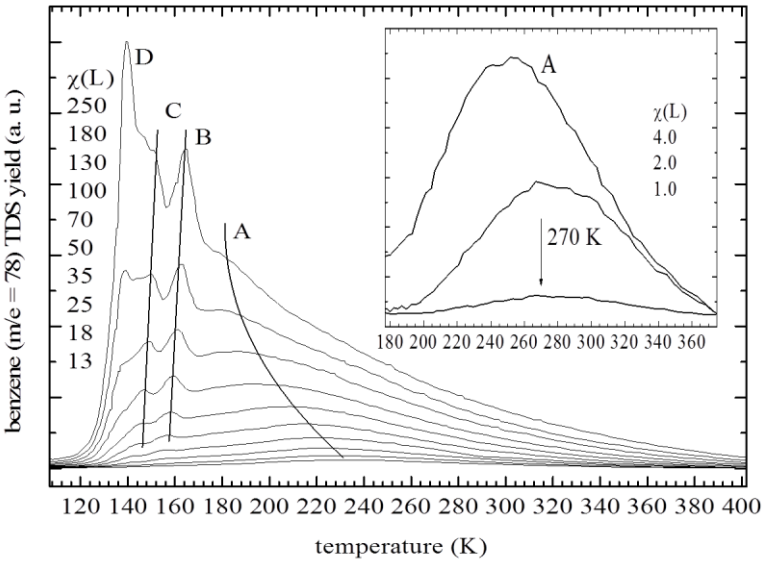

Figure 1. Benzene TDS on m-CNTs.[74] The different curves represent TDS data at different initial surface coverages, χ. The TDS peaks A, B, and C correspond to the adsorption of benzene on internal, external, and groove sites of CNTs respectively. D is the condensation peak of benzene. The inset shows the TDS data for small exposures.

Adsorption kinetics experiments were conducted in an ultra-high vacuum (UHV) chamber (scattering chamber for the molecular beam system). A photograph of the scattering chamber at NDSU is shown in Figure 2A. TDS experiments related to some projects were conducted in another TDS chamber shown in Figure 2B. The scattering chamber is pumped by two turbo molecular pumps (Varian), backed by a fore-line pump (Trivac), an ion pump (Gamma Vacuum Titan Ion Pump) with battery backup, and a titanium sublimation pump (Varian). It is estimated by the mass spectrometer that the Ti sublimation pump would reduce hydrogen background to $5x10^{-11}$ mbar.

An xyz manipulator (McAllister) with a differentially pumped rotary platform is also installed on the scattering chamber. A sample holder is mounted on the manipulator and can be rotated 360^{o} with a stepper motor. The rotary platform is pumped by a turbo molecular pump

(Leybold, NT 360) backed by a fore-line pump (Leybold). The vacuum system can be baked at 150 ^{o}C using heating belts and surface heaters to achieve a base pressure of $3x10^{-10}$ mbar. The system is also equipped with UHV gate valves (VAT) to protect the vacuum in the event of power failure.

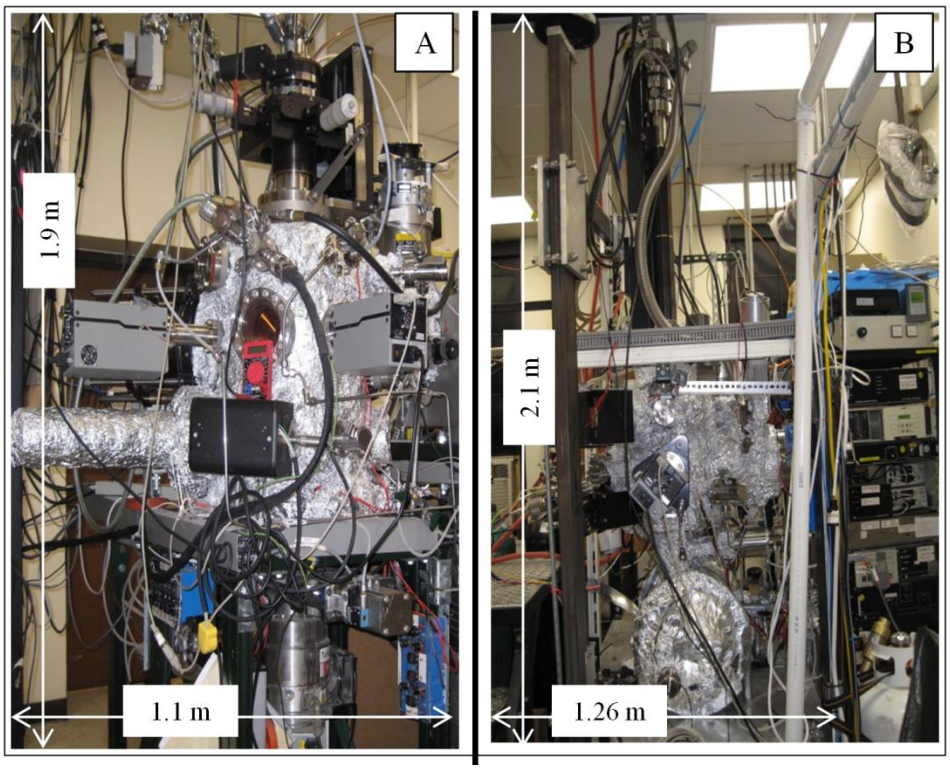

Figure 2. Photographs of ultra-high vacuum chambers. (A) photograph of the scattering chamber and (B) photograph of the second TDS chamber used for kinetics experiments. Scales are shown to show the actual dimensions of the UHV chambers.

A schematic of the scattering chamber is shown in Figure 3. The scattering chamber is equipped with two mass spectrometers (SRS RGA 100): one of which is a time-of -flight (TOF) mass spectrometer aligned collinearly with the molecular beam for beam characterization, and the other is aligned perpendicular to the molecular beam for molecular beam and TDS experiments. In addition, the scattering chamber is equipped with a dual Mg/Al anode x-ray source for x-ray photoelectron spectroscopy and a double pass cylindrical mirror analyzer

(CMA) with coaxial electron gun for Auger electron spectroscopy (AES) measurements (all from Perkin-Elmer including an upgrade from RBD). Furthermore, the scattering chamber is equipped with an electron beam evaporator (McAllister), a home-built metal doser, an atomic hydrogen source (Tectra GmbH), and a sputter gun (SPECS, IGE 11).

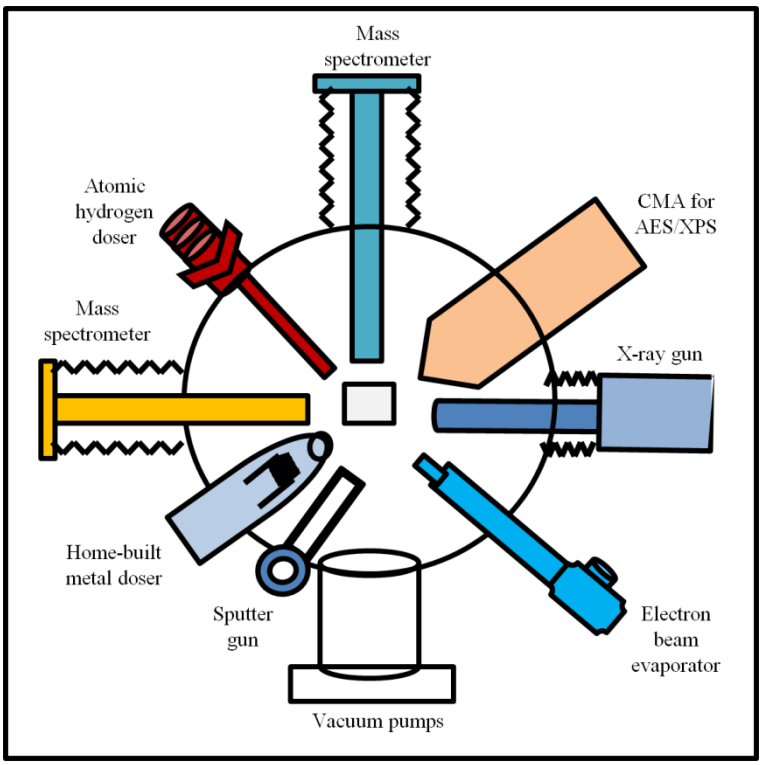

Figure 3. Schematic of the scattering chamber and its major components.

The sample holder consists of a stainless steel tube, one side of which is welded to a through-hole conflat flange to form a dewar tube, and the other is connected to a 4-pin molybdenum conductor CF 16 flange. The through-hole conflat flange is also equipped with two electrical feedthroughs for sample heating and simultaneous temperature measurement. A photograph of the body of the sample holder is shown in Figure 4A. Typically, the sample (1x1 cm) is mounted on a tantalum plate which is spot-welded to two front pins of molybdenum, as shown in Figure 4B. A chromel-alumel thermocouple is spot-welded on the back of tantalum

plate for in situ measurement of sample temperature (T_s). A tungsten (W) filament (0.25 mm, Goodfellow) is mounted behind the tantalum plate by clamping it to the two back pins of molybdenum with tantalum pieces as shown in Figure 4C. The air-side of the stainless steel tube acts as a dewar and can be filled with liquid nitrogen for cooling the sample to low temperatures (~ 95 K). Sample temperature can be further lowered (~ 87 K) by blowing He gas into the dewar. An electron bombardment heating method is used for sample heating while performing TDS experiments on less conducting samples.

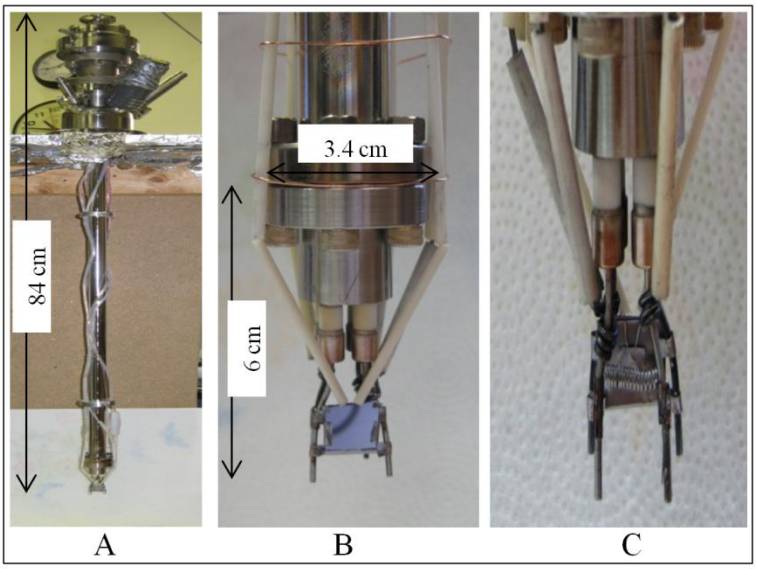

Figure 4. Photographs showing (A) the sample holder, (B) mounted sample, and (C) rearview of the mounted sample. Scales are shown to show the actual dimensions of sample and sample holder.

A tungsten filament is resistively heated by means of a computer controlled power supply (HP 6433 B). The thermal electrons emitted from the filament are accelerated on to the sample by means of another computer controlled high voltage (HV) power supply (Gassman PS/G59). A homemade data acquisition program driven proportional-integral-derivative (PID) controller is used to control the total heating power and attain a linear heating ramp (T_s vs. time) over a wide range of temperatures. PID uses the real time clock of the computer as its primary source of time.

The second TDS chamber, shown in Figure 2B, is equipped with two mass spectrometers (SRS RGA 100 and SRS RGA 300), a low energy electron diffraction (LEED) optics combined with an Auger electron spectroscopy system (SPECS, ErLEED 3000D), a home-built metal doser, an atomic hydrogen source (a capillary doser with a hot W filament at the end), and a sputter gun (SPECS, IGE 11). The system is pumped by three turbo molecular pumps (two Leybold, NT 360 and one Varian) backed by a fore-line pump (Leybold) and an ion pump (Varian) with battery backup. Sample mounting and experimental procedures are the same as described above for the scattering chamber.

2.3. Molecular Beam Scattering

Adsorption of the gas phase species is the first step in heterogeneous catalysis. Gas-surface energy transfer processes occur under non-equilibrium conditions and have a profound effect on adsorption/desorption or reaction pathways. Molecular beam scattering is an effective technique to study such gas-to-surface energy transfer processes (adsorption dynamics) because it can simulate such non-equilibrium conditions. The photograph and schematic in Figure 5 show the triply differentially pumped supersonic molecular beam scattering system at NDSU. A close-up photograph of the molecular beam system is shown in Figure 6A.

The first and second chambers of the molecular beam system are respectively connected to Varian diffusion pumps (a VHS-10 with a pumping speed of 6600 l/s and a VHS-6 with 3000 l/s) backed by a D25B/WSU500 rotary/booster pump combination (Leybold). The third chamber is pumped by a turbo molecular pump (Leybold, NT 360) backed by a foreline pump (Leybold). The second and third chambers are separated by a screw valve. The nozzle is mounted on a xyz-tilt-manipulator (McAllister) and is housed in the first chamber. The nozzle consists of a steel tube onto which Pt/Ir μm nozzle plate is press fitted. The nozzle heating element (up to 800 K) is

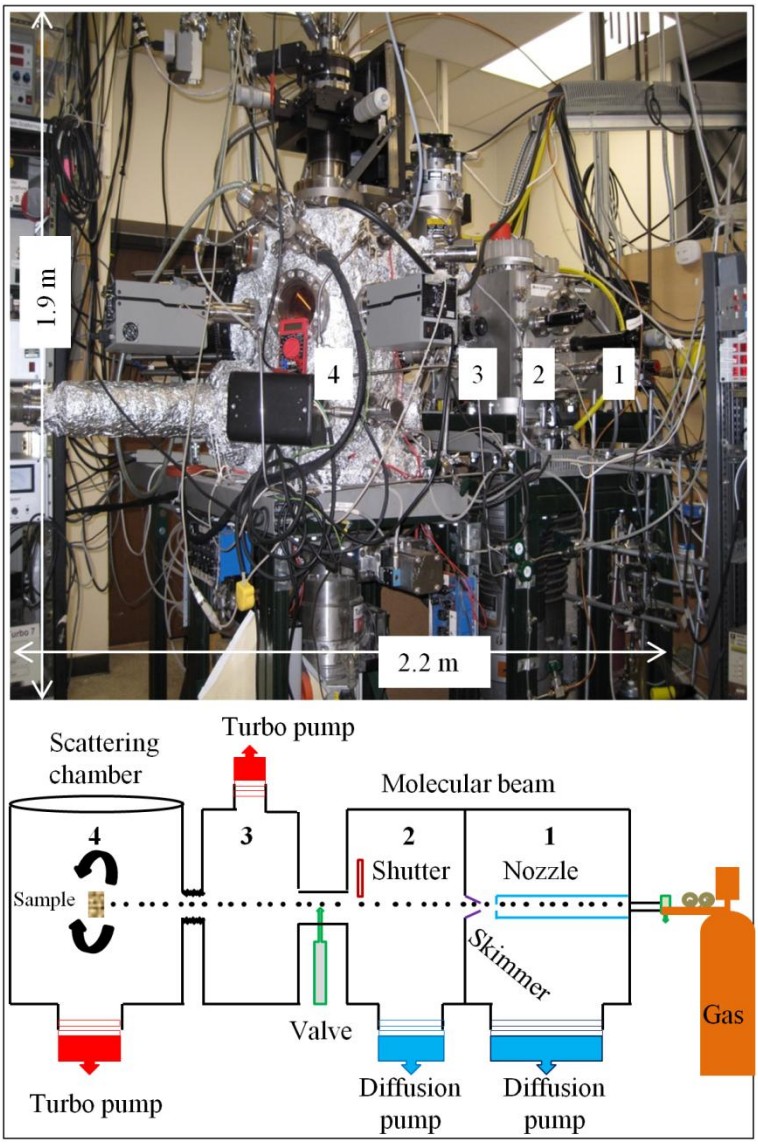

Figure 5. Photograph and schematic of the molecular beam scattering chamber. The molecular beam system with first (1), second (2), and third (3) chambers is connected to 4, the scattering chamber. First chamber houses the beam nozzle and a skimmer. In addition to a shutter, the second chamber houses a beam chopper and a light sensor for time of flight (TOF) experiments. Scattering chamber houses the sample and mass spectrometers. Scales are shown to show the actual dimensions of molecular beam scattering chamber.

made of small ceramic beads strung on a nichrome wire. A conical skimmer (facing the nozzle) is mounted on the wall of the first chamber, as shown in Figure 6B. A linear drive (Huntington)

combined with a tilter is used to adjust the second aperture of the beam chamber. A beam shutter driven by a miniature servo motor (Pololu) is mounted in the second chamber. The second chamber also houses a beam chopper and a light sensor for the time of flight (TOF) analysis of the supersonic molecular beam. The supersonic molecular beam system is attached to a scattering chamber. A description of the scattering chamber is already given in the previous section on TDS. Molecular beam scattering experiments are controlled by a homemade computer program in the "C" language.

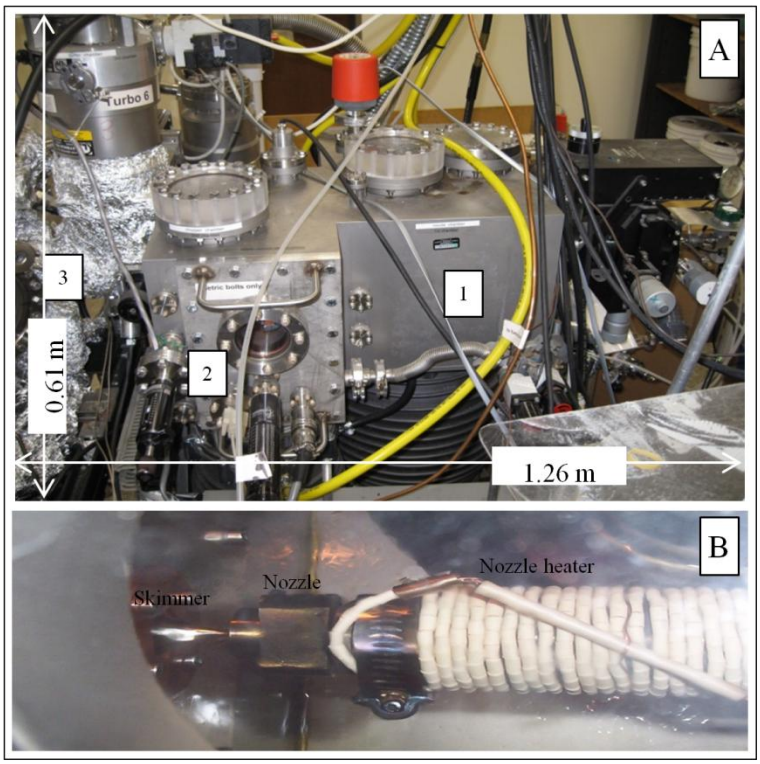

Figure 6. Close-up photographs of (A) the molecular beam system, (B) beam nozzle, skimmer, and the nozzle heater. Scales are shown to show the actual dimensions of the molecular beam system. Refer to Figure 5 for chamber labeling.

In a typical experiment, a molecular beam is formed by expanding a gas at high pressure (few bars) through a small nozzle diameter (few μm), as shown in Figure 5. The expanded gas is funneled through the small and collinear orifices located in three stages of differential pumping

to drop the pressure to 10^{-10} mbar. The gas undergoes adiabatic expansion, which results in a decrease in internal energy. The temperature of the gas decreases due to adiabatic cooling, and it corresponds to the speed of the gas molecules perpendicular to the beam direction. The internal energy is transformed into translational energy in the beam direction. A supersonic molecular beam has narrow speed distribution. The molecules undergo a large number of collisions before they exit the nozzle resulting in a decrease of the collisional mean free path leading to the narrow speed distribution. The central core of the supersonic molecular beam is screened by the conical skimmer, narrowing the angular distribution.

The so-called Knudsen number (Kn) is used to classify the type of beam formed. It is the ratio of the molecular mean free path length (λ) to the effusion hole/nozzle diameter (d). High pressure gas (small λ) and a μm nozzle (small d) combination produces a supersonic molecular beam. An effusive beam will be produced when the molecular mean free path length is comparable to the effusion hole size. The efficiency of the gas cooling during an adiabatic expansion can be characterized using the Mach number (M). The Mach number is the ratio of the average velocity of the expanding gas (u) to the local speed of sound of the expanding gas (a). The higher Mach number means narrow speed/energy distribution of the gas molecules and low beam temperature. Typical beam temperatures of ~ milli K can be achieved in supersonic molecular beam formation. The kinetic energy of the molecular beam can be changed by either changing the nozzle temperature or using a seeded gas, i.e., a gas mixture consisting of low concentrated heavy seed gas in a light carrier gas.

The method of King and Wells is used to measure initial adsorption probability, S_0, which is the adsorption probability at zero coverage. The method is illustrated in Figure 7. The vacuum chamber has a base pressure (P_b) when the beam is off. Assuming the absence of a

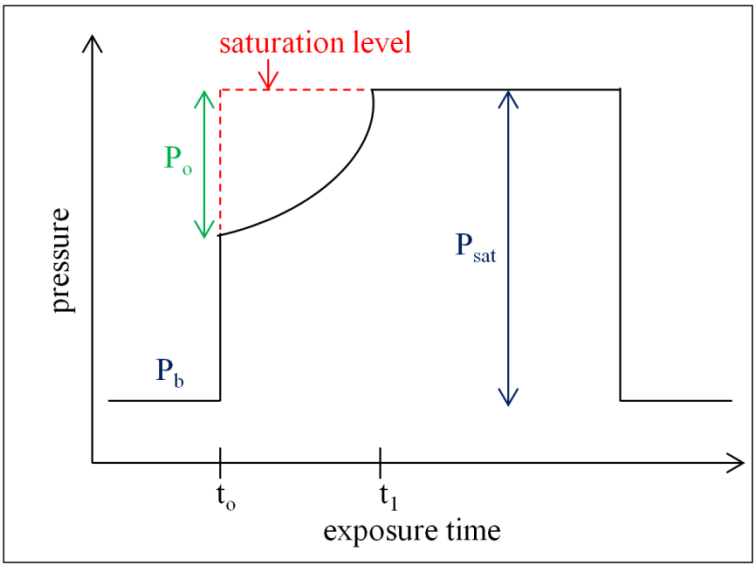

Figure 7. Schematic illustration of the principle of King and Wells up-take experiment. P_b is the base pressure in the vacuum chamber. The molecular beam entering the vacuum chamber saturates the sample's surface with in time t_1-t_0. The initial adsorption probability (S_0) is equal to the ratio of the initial pressure rise (P_0) to the saturation pressure (P_{sat}).

sample in the vacuum chamber, the entering molecular beam will increase the pressure in the vacuum chamber to a saturation level (P_{sat}). When a clean sample's surface is exposed to the beam at time t_0, the sample acts like a small vacuum pump and adsorbs some gas molecules at time t_0. The molecules fill up all the available adsorption sites and saturate the surface at time t_1. The sample temperature is maintained just enough to adsorb a monolayer of molecules but not to condense them. The initial pressure rise in the vacuum chamber at time t_0 is due to the back scattered gas molecules. The probability of adsorption of molecules can be quantified by measuring the adsorbed/backscattered ratio. The initial adsorption probability (S_0) is equal to the ratio of the initial pressure rise (P_0) to the saturation pressure (P_{sat}). Mechanistic details about gas-surface energy transfer processes can be obtained from S_0 measurements. The area above the pressure transient between t_0 and t_1 and below the saturation level quantifies the amount of

molecules adsorbed. Coverage (Θ) dependent adsorption probability S(Θ) can be obtained by integrating the pressure transient between t_0 and t_1.

The King and Wells type uptake curves for CO on SiO_2 (Silica) and 63 nm Cu clusters supported on silica are shown in Figure 8. The pressure transient for CO on silica indicates no adsorption of CO. However, the pressure transient of CO on Cu clusters approaches the saturation level much slower when compared to bare silica. This indicates the adsorption of CO on Cu clusters. The area above the pressure transient and below the saturation coverage can be integrated to calculate the number of molecules of CO adsorbed, provided the beam flux is known. The shape of coverage dependent adsorption probability curves reveal many important details about the process of adsorption.

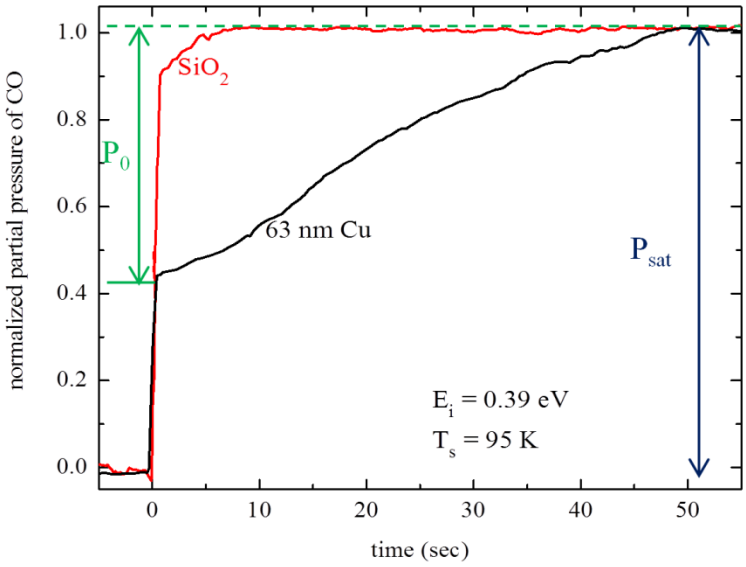

Figure 8. Sample King and Wells experiment showing the adsorption transients of CO on clean silica and 63 nm Cu clusters supported on silica.[48] T_s is the sample temperature and E_i is the impact energy of CO. The initial adsorption probability (S_0) is equal to the ratio of the initial pressure rise (P_0) to the saturation pressure (P_{sat}).

The Langmuirian model is the first among the basic models proposed to describe the adsorption and related processes. In the Langmuir model, the initial adsorption probability

decreases linearly with surface coverage. This model assumes that the gas molecules will only adsorb on vacant adsorption sites and not on the molecules adsorbed on the surface and is depicted in Figure 9A. In some systems, the initial adsorption probability remains almost constant and drops quickly to zero in approaching the saturation coverage, as shown in Figure 9B. Such phenomenon is explained by the Kisliuk model. Gas molecules can become either intrinsic or extrinsic precursors after impinging upon a surface. An intrinsic precursor state is formed on a vacant active site; whereas, the extrinsic precursor state is formed on an occupied chemisorption site. According to the Kisliuk model, the molecules get trapped temporarily in a mobile precursor state before they become chemisorbed. In some systems, the initial adsorption probability increases with an increase in surface coverage and drops rapidly to zero when the adsorption approaches saturation, as shown in Figure 9C. Such phenomenon is explained by adsorbate-assisted adsorption model. In this case, the incoming molecules stick better to the pre-adsorbed molecules than to the vacant adsorption sites due to a better mass-match leading to an efficient energy transfer. Adsorbate-assisted adsorption is more distinct at high impact energies but less distinct at high surface temperatures.

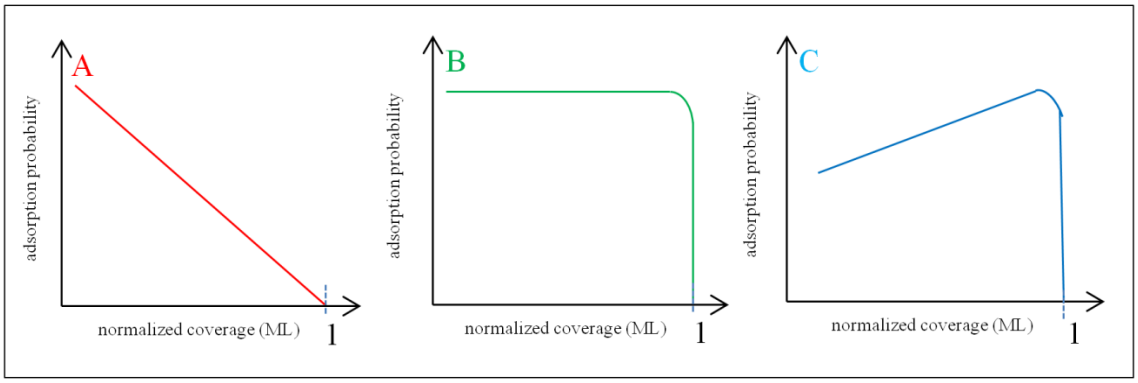

Figure 9. Schematic showing the coverage dependent adsorption probability, S(Θ) curves depicting the (A) Langmuirian, (B) Kisliuk, and (C) adsorbate-assisted adsorption. The coverage is expressed in monolayers (ML). When a surface is covered with exactly a single layer of adsorbate, the resultant surface coverage is called a monolayer.

The coverage dependent adsorption probability of CO on Cu clusters is shown in Figure 10. At low impact energies (E_i), S(Θ) remains constant up to the saturation coverage, where it drops to zero obeying the Kisliuk-like dynamics. This curve shape also indicates the effect of precursor states with the extrinsic precursor being predominant. At high impact energies, S(Θ) decreases linearly with Θ obeying the Langmuirian-like dynamics. A crossover from precursor-mediated Kisliuk-like dynamics to Langmuirian-like dynamics is seen for CO. This crossover is due to the decrease in the trapping probability of CO in the precursor state with increasing E_i. Thus, these adsorption models can be used to explain the experimental observations in molecular beam scattering.

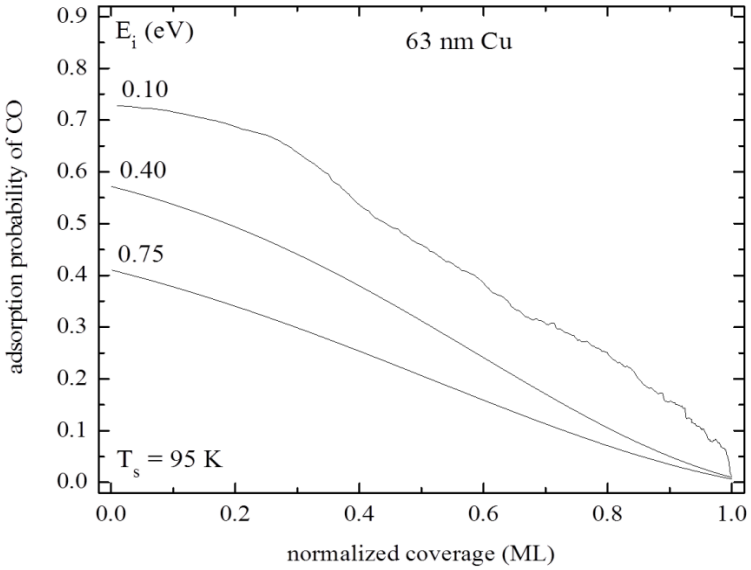

Figure 10. A set of coverage dependent adsorption probability, S(Θ) curves at different impact energies (E_i) for CO adsorption on 63 nm Cu clusters supported on silica.[48] T_s is the sample temperature. The coverage of CO is expressed in monolayers (ML).

2.4. Auger Electron Spectroscopy

Auger electron spectroscopy (AES) is the most important and popular chemical surface analysis tool used in surface science. The Auger process was described for the first time by

Pierre Auger in 1923,[75] when he observed the emission of β electrons during the ionization of gases by x-rays. The Auger process is based on the excitation of so-called 'Auger electrons' either by electrons or photons. Primary electrons in the energy range 3-5 keV are typically used in surface analytical AES. AES can analyze the elemental composition of the first 2-10 atomic layers of the matter. The process of Auger electron emission is briefly described below with the help of Figure 11.

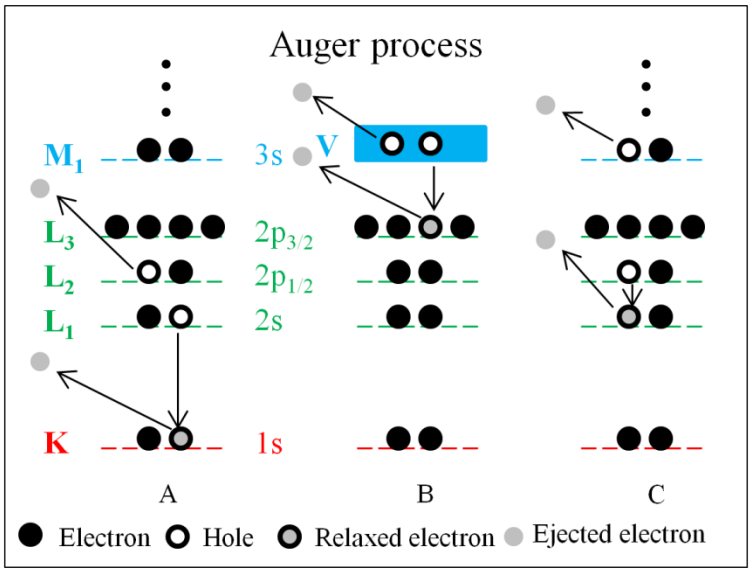

Figure 11. Schematic describing the Auger transitions. Transitions involving (A) three core levels and (B) a core level and the valence band, (C) Coster-Kronig transition.

Figure 11A describes Auger transition involving three core levels. As shown here, an incident radiation (electrons or x-rays) with energy larger than the binding energy of an electron in some core level, say the K shell, can displace an electron from the K shell to create a hole. A higher lying electron in either the core shell or valence shell tries to fill that hole. For example, if that higher energy shell is L_1, then the excess energy E_K-E_{L1} can be released as x-rays or given to an electron, say in the L_2 shell. The latter process emits an Auger electron with an energy equal to E_K-E_{L1}-E_{L2}-ϕ from the L_2 shell (ϕ is the work function of the surface). The electron must

overcome ϕ to get ejected into the vacuum. This Auger transition is labeled as KL_1L_2 transition because the Auger electron energy is a characteristic of the energy levels involved and hence of the parent atom.

AES can identify any element, apart from H and He. For surface analysis using AES, Auger transitions in the energy range 50-1500 eV are preferred. The types of Auger transitions in this energy range depend on atomic number, Z as shown Table 1. Figure 11B depicts Auger transition involving a core level and the valence band and is denoted as L_3VV transition, where V is the valence band electron. Figure 11C shows the Coster-Kronig transition, a special case of Auger process in which the initial hole is filled by an electron from the same shell. Several final state energies and electron effects make it difficult to accurately measure the energy of an Auger transition. Auger electron energy is independent of the energy used for excitation.

Table 1. Table showing the effect of atomic number (Z) on the type of shell ionized in the Auger process.

Atomic number (Z)	Shell ionized
Li(3) - Al(13)	K
Mg(12) - Br(35)	L
Br(35) - Yb(70)	M
Y(39)	N

Figure 12A shows a typical AES spectrum of Mo clusters supported on silica. This shows a plot of count rate N(E) against electron energy. The sloping background in the spectrum is due to the secondary electron background. Auger peaks are superimposed on the secondary electron background and appear as sharp peaks. The signal is differentiated to minimize such secondary electron background.

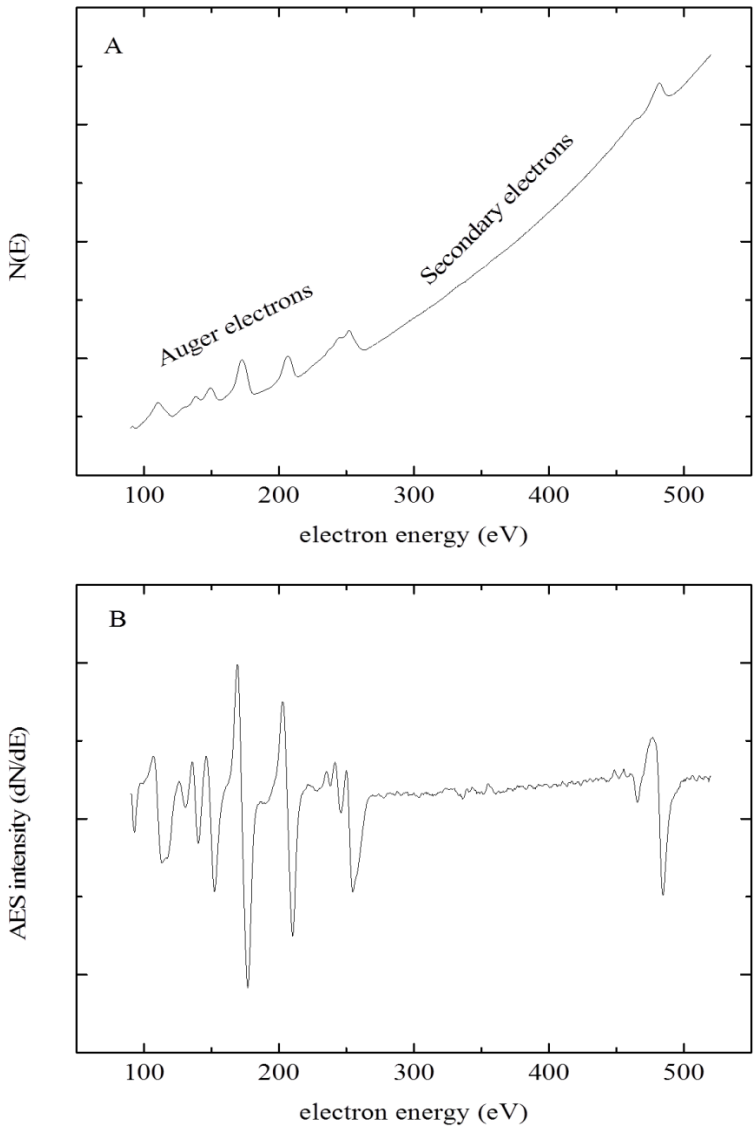

Figure 12. AES spectra of silica-supported Mo clusters. (A) plot of N(E) against energy and (B) plot of dN(E)/dE against energy. N(E) represents the number of electrons that possess an energy E.

Figure 12B shows the differentiated spectrum. Here, the derivative peaks are detected on a flat background. The Auger spectrum in Figure 12B provides three kinds of information. Auger peak positions give the qualitative information about the elemental composition in the surface and near surface region. The peak-to-peak height of the Auger peak is directly proportional to the atomic concentration and can be used to get quantitative information on

surface concentrations. Chemical state information can be obtained from Auger peaks that arise from transitions involving the valence electron states.

AES has four modes of operation: point analysis, line scan, mapping, and profiling. The typical survey spectrum shown in Figure 12A is a result of point analysis. AES can also be used for depth profile analysis. This is done by combining AES with ion beam sputtering. The process of bombarding the surface with ions to remove material from the surface is called sputtering. This method can be applied for layers of thickness ≤ 200-1000 nm. AES spectra are taken after each sputtering cycle. The sputter time is converted into depth and the peak-to-peak height of the derivative feature of each element is converted into elemental concentration. Thus, how the elemental composition varies with depth in thin layers can be studied. AES can be used to perform angular resolved analysis for layers of thickness ≤ 2-3 nm, which is non-destructive. This method involves the measurement of Auger intensity as a function of the emission angle, θ of the Auger electrons with respect to surface normal.

Line scan can be used to analyze the layers of large thickness (~ few μm). A typical example of a sample covered with a layer of other material is shown in Figure 13. While doing a line scan, an electron beam is scanned across a tapered section or a crater edge produced by ball cratering before reaching the substrate. Displacement of the electron beam (x), depth (z), radius of the ball used for cratering (R), and diameter of the crater (d) are related by the following equation:

$$z = \frac{1}{2}\left[(4R^2 - d^2 - 4x^2 + 4dx)^{1/2} - (4R^2 - d^2)^{1/2}\right] \qquad (18)$$

The variation of atomic concentration with the displacement of the electron beam using a line scan can be studied. Scanning or mapping is another working mode of AES. While making the Auger map of a sample, an electron beam of very small spot size of ~ 1 μm diameter is

scanned over a selected area of the surface of the sample using a rastering power supply. It is possible to map the elemental distribution at the sample surface by correlating the position of the electron beam with the emitted Auger electrons. Several AES scans are taken with different Auger peak energy settings of the analyzer. Thus, while scanning for an element x, bright spots indicating the high concentration of an element x will appear in the Auger map. AES has some advantages, such as good spatial resolution (< 1 μm) and surface sensitivity (~ 20 A^o), when compared to other surface analysis techniques. Moreover, it can easily detect light elements.

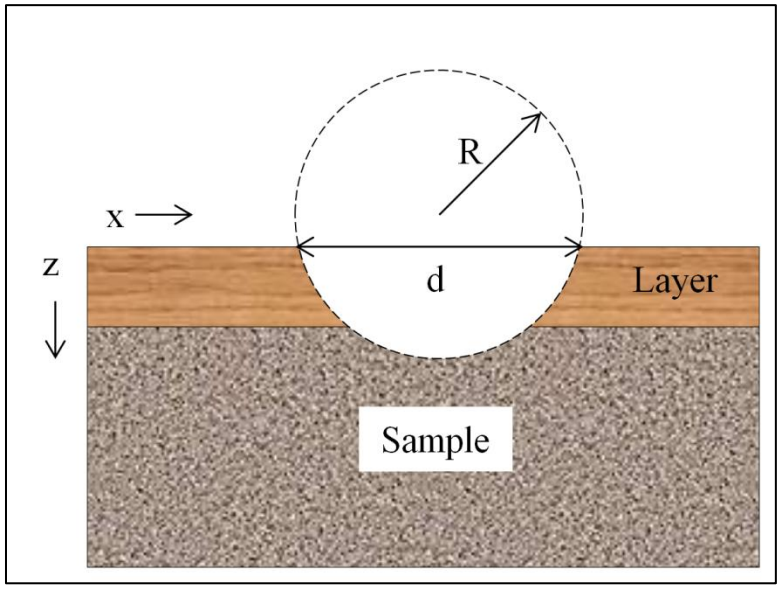

Figure 13. Schematic showing the Auger line scan process. Auger line scan of a sample covered with a layer of another material with x being the displacement of the electron beam; z being the depth; R being the radius of the ball used for cratering, and d being the diameter of the crater.

Almost all the projects covered in this dissertation utilize AES for the surface analysis. For example, the morphology and cleanliness of supported metal clusters of Mo and Cu were characterized by AES. AES was also crucial to monitor the cleaning processes for catalyst supports, nano HDS catalysts, model array nanocatalysts, and CNTs.

2.5. X-ray Photoelectron Spectroscopy

X-ray photoelectron spectroscopy (XPS), also known as electron spectroscopy for chemical analysis (ESCA), is a widely used technique to investigate the chemical composition of surfaces. XPS was developed in the mid-1960s by Kai Siegbahn and co-workers at the University of Uppsala, Sweden.[76] The XPS technique is based on the photoelectric effect. The principle of photoelectric effect and the important observations associated with it are given below.

When a photon impinges upon an atom and transfers its total energy to an atomic orbital electron, it causes the photoemission. Photoelectrons will be ejected from an atom only if the frequency of the excitation photon is greater than or equal to the characteristic threshold energy for each element. The number of photoelectrons emitted will be proportional to the intensity of incident light. The kinetic energy of the photoelectrons will be independent of light intensity, but linearly proportional to the frequency of the incident photons. Time between excitation and emission is extremely small (10^{-16} s). The process of photoemission can be described by Einstein's equation:

$$E_B = h\upsilon - KE \qquad (19)$$

where E_B is the binding energy of the electron and KE is the kinetic energy of the emitted photoelectron. The energy of the excitation x-ray photon is $h\upsilon$, where h is Planck's constant, and υ is the photon frequency.

The process of photoemission is shown in Figure 14A. Here an atom in n-electron initial state is considered. The incident x-ray photon transfers its total energy to a core-level electron and causes photoemission. As shown in Figure 14B, the atom that is in (n-1)-electron state undergoes a reorganization by dropping an electron from a higher level to fill core-level vacancy.

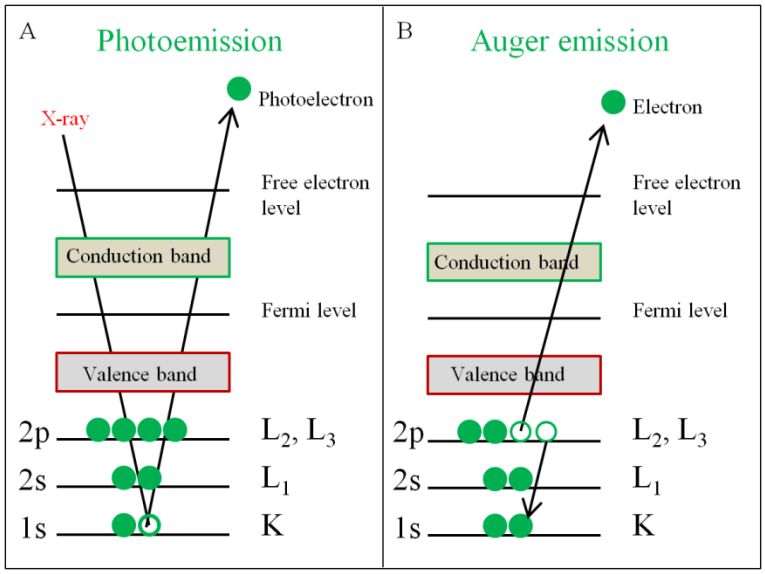

Figure 14. Schematic showing the process of (A) photoemission and (B) Auger emission when x-rays interact with matter.

The atom uses this excess energy either to eject an electron from the higher level (Auger emission) or emitting an x-ray photon (x-ray fluorescence). The E_B of the photoelectron is the energy difference between the initial (i) and final (f) states and is written as:

$$E_B = E_f(n - 1) - E_i(n) \qquad (20)$$

where $E_i(n)$ is the energy of the initial state and $E_f(n - 1)$ is the energy of the final state. E_B will be equal to the negative orbital energy ($- \varepsilon_k$) for the ejected photoelectron, provided there is no electronic rearrangement after photoemission. This approximation is derived from Koopmans' theorem and is written as:

$$E_B \approx - \varepsilon_k \qquad (21)$$

Typically, ε_k values are within 10-30 eV of the E_B values and are calculated by the Hartree-Fock method. However, the other electrons in the sample will undergo rearrangement to minimize the energy of the ionized atom. Such energy reduction is called the 'relaxation energy.' Relaxation is a final state effect, and that can occur in two ways: atomic relaxation or extra-

atomic relaxation. A more complete description of E_B is given by considering relaxation, electron correlation, and relativistic effects and is written as:

$$E_B = - \varepsilon_k - E_r(k) - \delta\varepsilon_{corr} - \delta\varepsilon_{rel} \qquad (22)$$

where $E_r(k)$ is the relaxation energy and $\delta\varepsilon_{corr}$ and $\delta\varepsilon_{rel}$ are corrections for the differential correlation and relativistic energies. A calibrated and suitably referenced x-ray photoelectron spectrometer is required to determine E_B accurately.

Electrically conducting samples, such as metals, are electrically contacted with the spectrometer and grounded as shown in Figure 15. Then, the Fermi levels (E_f) of the sample (E_f^s) and the spectrometer (E_f^{sp}) will be aligned ($E_f^s = E_f^{sp}$) so that the binding energy (E_B) is referenced with respect to E_f.

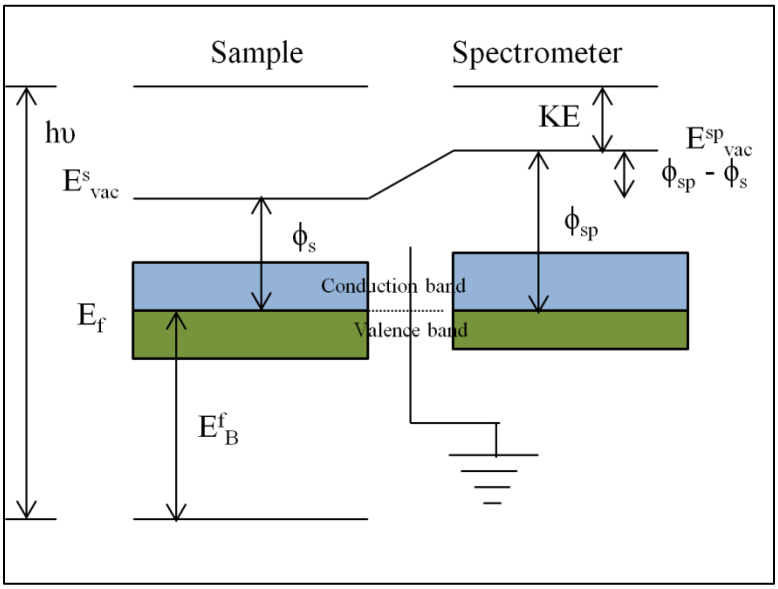

Figure 15. The energy level diagram for an electrically conducting sample that is grounded to the spectrometer. E_f is the Fermi level; E^s_{vac} and E^{sp}_{vac} are respectively the vacuum levels of the sample and the spectrometer; ϕ_s and ϕ_{sp} are respectively the work functions of the sample and the spectrometer; E^f_B is the binding energy (E_B) referenced with respect to E_f; hυ is the energy of the excitation x-ray photon, and KE is the kinetic energy of the emitted photoelectron.

The work function (ϕ) is the minimum energy required to remove an electron from the highest occupied level into vacuum and is given by:

$$\phi = E_f - E_{vac} \qquad (23)$$

where E_{vac} is the vacuum level. The Einstein equation is then modified as:

$$E_B^f = h\upsilon - KE - \phi_{sp} \qquad (24)$$

Here, E_B^f means E_B is referenced to E_f. The measurement of E_B is independent of sample work function (ϕ_s) but dependent on the spectrometer work function (ϕ_{sp}). Gold (Au) can be used as a standard to calibrate ϕ_{sp}.

Materials with low electrical conductivity (insulators) cannot be electrically contacted with the spectrometer. These samples acquire positive charge after the emission of photoelectrons. This positive charge can be compensated by an external source of monoenergetic (< 20 eV) electrons, such as a flood gun. Then, the vacuum level of the sample (E_{vac}^s) and the energy of the charge neutralization electrons (ϕ_e) are aligned, as shown in Figure 16 so that the binding energy (E_B) is referenced with respect to ϕ_e. The measured E_B depends on the sample work function (ϕ_s) and the energy of the charge neutralization electrons (ϕ_e) and is given by:

$$E_B^{vac} = E_B^f + \phi_s = h\upsilon - KE + \phi_e \qquad (25)$$

where E_B^{vac} is the binding energy (E_B) referenced with respect to E_{vac}.

It is difficult or impossible to measure accurate values of E_B for insulators, as is referenced to E_{vac} and ϕ_e. An internal reference is typically used to accurately determine the value of E_B.

XPS analysis is typically performed by first collecting a survey scan spectrum with a binding energy range of 0-100 eV. Later, high-resolution spectra of specific features observed in the survey scan spectrum are collected.

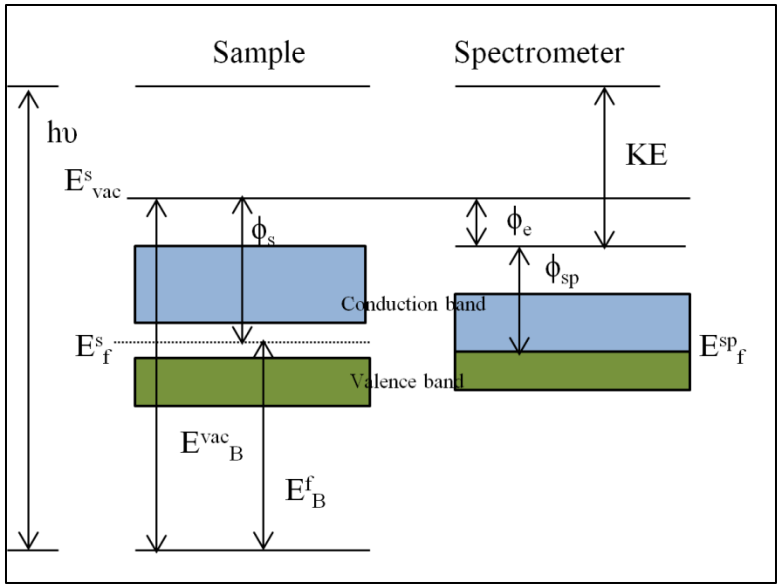

Figure 16. The energy level diagram for a sample that is electrically insulated from the spectrometer. E_f^s and E_f^{sp} are respectively the Fermi levels of the sample and the spectrometer; E_{vac}^s is the vacuum level of the sample; ϕ_s and ϕ_{sp} are respectively the work functions of the sample and the spectrometer; ϕ_e is the energy of charge neutralization electron; E_B^{vac} is the binding energy (E_B) referenced with respect to E_{vac}; E_B^f is the binding energy (E_B) referenced with respect to E_f; hυ is the energy of the excitation x-ray photon, and KE is the kinetic energy of the emitted photoelectron.

The survey scan spectrum of silica is shown in Figure 17. As shown in Figure 17, the intensity (counts) of photoelectrons is plotted against the binding energy. The "stepped" background in the spectrum is due to inelastic scattering. The background increases with increasing binding energy. Photoemission peaks and x-ray induced Auger electron emission peaks rise above the background. A high-resolution spectrum of Si 2p XPS peak is shown in the inset of Figure 17. If binding energy referencing is properly performed, the peaks can be easily compared to the reference data. Auger peak positions are not altered with a change in the x-ray source.

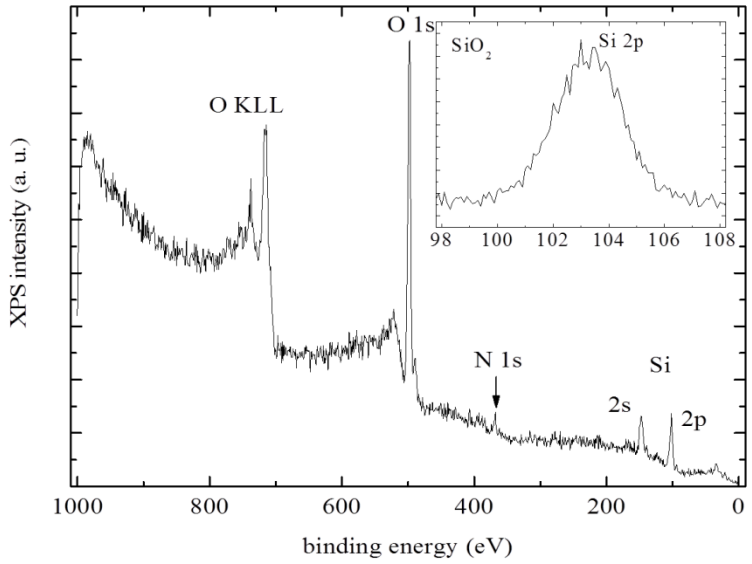

Figure 17. XPS spectra of clean silica.[39] XPS peaks of O, Si, and N (impurity) are observed in the XPS survey spectrum of clean silica. AES peaks (KLL) of O are also observed. The inset shows the high-resolution spectrum of Si 2p XPS peak.

For the orbitals with $l > 0$ (p, d, or f), two energetically equivalent final states 'spin up' or 'spin down' are possible after photoemission. A coupling between the magnetic fields of spin (s) and angular momentum (l) then occurs. This coupling can split the degenerate state into two components. This process is called spin-orbit coupling and is an initial state effect. Spin-orbit coupling often results in the splitting of photoemission peaks into subpeaks.

Methanol synthesis model nanocatalysts project utilizes XPS for the surface analysis. For example, the cleanliness and chemical state of silica-supported Cu clusters were characterized by XPS.

2.6. Gas Chromatography

Gas chromatography (GC) is the most widely used separation technique in analytical chemistry. Chromatography is a method of separation in which different components of a sample partition between stationary phase (bed with large surface area) and mobile phase (gas), where

the sample is vaporized and carried by mobile phase. Ramsey[77] used charcoal as an adsorbent to separate gaseous mixtures and vapors. Michael Tswett[78-79] used liquid chromatography (LC) to separate plant pigments. He introduced the term chromatography (color writing) and explained the process. Martin and James[80] introduced the technique of GC. GC is used to separate and analyze volatile materials. It can analyze solids (dissolved in volatile solvents), liquids, and gases. GC is so versatile that it can be used to analyze both organic and inorganic compounds. Automated systems with efficient capillary columns and sensitive detectors make GC the best analytical instrument.

Depending on the physical state of the mobile phase, column chromatography is mainly divided into gas chromatography (GC) and liquid chromatography (LC). GC is further divided into gas-solid chromatography (GSC) and gas-liquid chromatography (GLC), depending on the physical state of the mobile phase. Columns contain a stationary phase and are named after these phases. GC is schematically illustrated in Figure 18, and its simple description is also given.

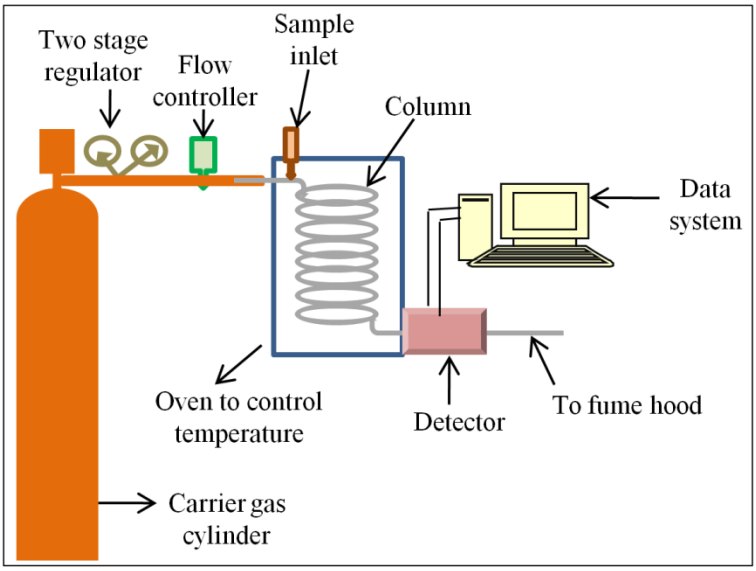

Figure 18. Schematic illustration of working of a gas chromatograph.

Carrier gas (He, Ar, or N_2, and sometimes H_2) flows continuously through the sample port, the column, and the detector. Inert carrier gas is used to avoid any interaction with the sample and stationary phase. A flow controller is used to control the flow of carrier gas. Retention time depends on the flow rate of carrier gas. A very small volume of the sample (µL) is injected into the heated sample inlet (sample port). The sample is vaporized in the sample port. Solid samples may be dissolved in volatile liquids and injected. Gaseous samples can be directly introduced, but they need special gas sampling valves. The vaporized sample is carried through the capillary column by the carrier gas. Capillary column length is typically in meters. High boiling liquid, which acts as a stationary phase, is coated like a thin film (0.2 µm) on the inside of capillary columns. Sometimes, capillary columns are enclosed in an oven and maintained at constant temperature. Each analyte of the sample partitions between stationary and mobile phases inside the column. The component with greater distribution in mobile phase is carried faster by the mobile phase through the column and reaches the detector first. The detector measures the quantity of each analyte and generates the corresponding electrical signal. It sends these signals to a data system. The data system generates the chromatogram. It also integrates the peak areas and gives details about retention times of analytes present in the sample.

An atmospheric flow reactor coupled to a GC was used to characterize the kinetics of thiophene HDS on the powder catalysts. A photograph and schematic of the experimental set up is shown in Figure 19. GC was used for the separation and detection of HDS products. Hydrogen gas (20 ml/min, 99.999%, Praxair), one of the reactants in HDS, was bubbled through 20 ml of liquid thiophene (≥ 99%, Sigma–Aldrich) contained in a 250 mL three neck flask. The temperature of thiophene was maintained at 30 ^{o}C using a saturator (Lauda Class RA 120). The flow rates of gases were measured and regulated using a flow regulator (Brooks SLA-5850S).

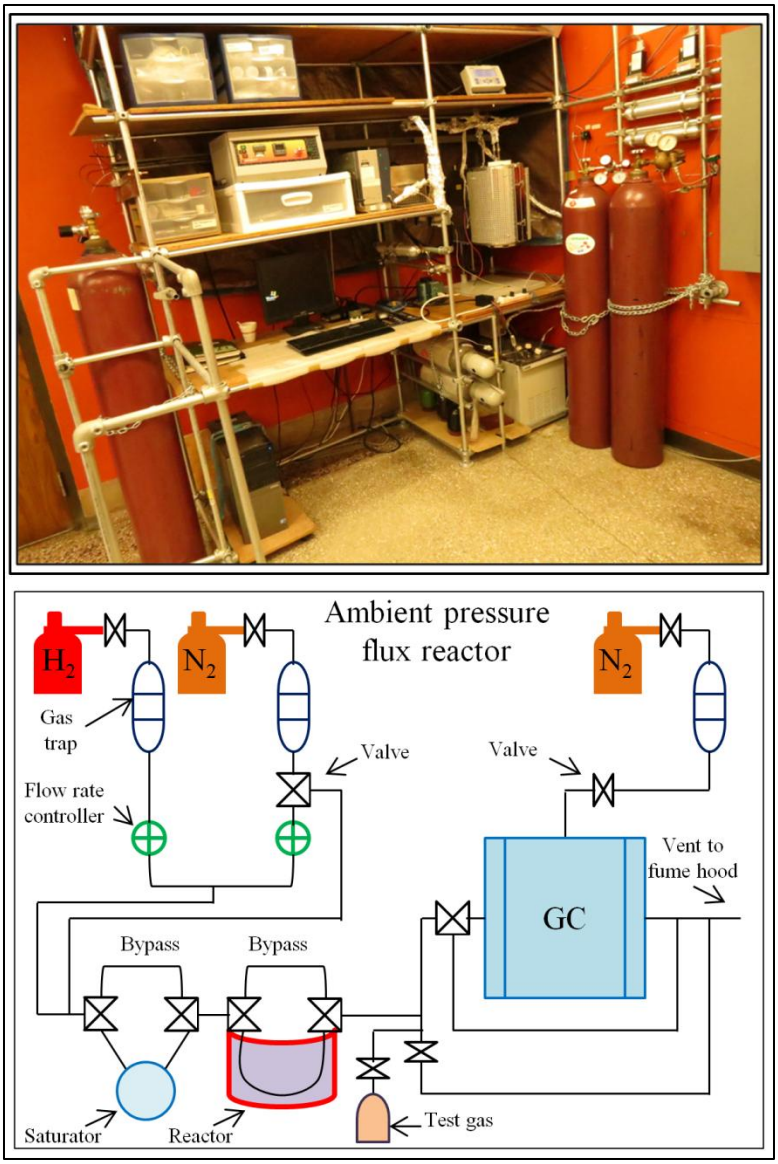

Figure 19. Photograph and schematic of an ambient pressure flux reactor that is coupled to a GC.

The HDS experiments were carried out in a mini reactor, consisting of a U-shaped quartz tube (Robinson Scientific, UK) inside a vertical split-hinge tube furnace (Carbolite VST 12/300). Typically, 27.5 mg of the catalyst powder was supported on 330 mg of glass wool plugs (Quartz Scientific, Inc.). These catalyst bearing glass wool plugs were gently inserted into the lower end of the glass tube. The catalyst was presulfided before the experimental runs at 600 K for 30 minutes in a flow of thiophene/hydrogen mixture. Gas lines were heated high enough using

heating belts to avoid condensation of thiophene. The reactor was heated to a desired temperature and the thiophene/hydrogen mixture was passed through the reactor. A 15-minute thermal equilibrium time was maintained. After this, the reaction products were sampled and analyzed by the gas chromatograph (GC) (Varian CP-4900) equipped with CP-Sil-5CB-4 m column and a thermal conductivity detector. Nitrogen (99.999%, Praxair) was used as the carrier gas. Agilent-Big Universal Traps were mounted in the N_2 and H_2 gas lines for the removal of moisture, oxygen, and hydrocarbons. HDS experiments with an empty reactor and one that contained only the glass wool were conducted. No reaction products were detected in those experiments.

CHAPTER 3. HYDRODESULFURIZATION MODEL NANOCATALYSTS

The hydrodesulfurization model nanocatalysts project is comprised of five interrelated sub projects. The main objective of this project is the characterization of the catalytic activity of novel nanomaterials towards HDS. The first project is concerned with the study of adsorption kinetics of thiophene on inorganic fullerene-like MoS_2 nanoparticles (IF-MoS_2).[57] The second project focuses on the adsorption and reaction kinetics of thiophene on inorganic nanotubes of WS_2 (INT-WS_2).[58] The third project is concerned with the fabrication of silica-supported Mo clusters and the adsorption kinetics and dynamics of thiophene on Mo clusters.[61] The fourth project focuses on the characterization of HDS catalytic activity of cobalt coated INT-WS_2 by UHV and ambient pressure kinetics experiments.[59] The fifth project primarily focuses on the characterization HDS catalytic activity of nickel coated INT-WS_2 by UHV and ambient pressure kinetics experiments, together with the first HDS catalytic screening of pristine and Re doped IF-MoS_2; pristine and Co, Ni, and Au coated INT-WS_2, and three other commercial catalysts: CoMo and NiMO (Haldor Topsoe, Denmark), and "nano MoS_2" (Impex Corp., USA).[60]

3.1. Adsorption of Thiophene on Inorganic Fullerene-like MoS_2 Nanoparticles

A brief introduction to inorganic fullerene-like MoS_2 nanoparticles (IF-MoS_2 NP) is presented first, followed by the fabrication of silica and sapphire-supported IF-MoS_2 NP. A combined results and discussion section is presented next. A summary of experimental results obtained in this study is given at the end.

3.1.1. Introduction

Inorganic fullerene-like MoS_2 nanoparticles (IF-MoS_2 NP) have been widely used for applications, such as solid lubricants and high-strength nanocomposites.[81-82] Exploring nanomaterials for applications in hydrodesulfurization (HDS) is a growing new field of research,

as evidenced by relevant research on CNTs,[83-85] IF-WS_2,[86] and MoS_2/WS_2 nanotubes.[87-88] This necessitates a study to investigate the possible application of IF-MoS_2 in HDS catalysis.[57]

Thiophene (C_4H_4S) is typically used as a probe molecule for this study to get insights into HDS process. This is because it is the smallest sulfur containing compound in crude oil. A number of proposed HDS mechanisms[89-91] assume the formation of sulfur vacancy (metallic) sites on MoS_2 catalyst in the presence of hydrogen. Desulfurization of thiophene at these sulfur vacancy sites fill the sulfur vacancies and form sulfur-free hydrocarbons. Thus, HDS can be interpreted as creation/filling of sulfur vacancies on the catalysts surface. Therefore, the present study on IF-MoS_2 aims to distinguish/characterize metallic and sulfur like adsorption sites on the catalyst by performing adsorption kinetics (TDS) experiments on fully sulfided (pristine) and hydrogen/oxygen annealed samples. Quasi-steady state HDS experiments were also conducted to test the catalytic activity of IF-MoS_2. HDS activity of fully sulfided edges of triangular single-layer MoS_2 nanoclusters has been recently observed.[92] Such unusual activity is attributed to the presence of brim sites with a metallic character. Cluster-support interactions also play a vital role in determining the catalytic activity of MoS_2 nanoclusters.[93] Therefore, two different materials - silica and sapphire are used as supports for the IF-MoS_2 in this study to understand/evaluate possible cluster-support interactions. Silica is used as a conventional support in nanoscience and sapphire (Al_2O_3) is typically used as a catalyst support material in industrial HDS process.

IF-MoS_2 synthesized at ApNano Materials[94-95] were used in this study. Aberration-corrected high-resolution transmission electron microscopy (HRTEM) backed by advanced modeling has recently been used to characterize the structure of IF-MoS_2.[96] Structural characterization showed that the IF-MoS_2 have a typical size of 50–70 nm and consist of closed MoS_2 layers. Each shell consists of a Mo layer sandwiched between two sulfur layers. Each Mo

atom has a sulfur coordination number of 6. Optical-absorption spectroscopy of IF-MoS_2 showed that they exhibited semiconductor behavior with a small band gap when compared to the corresponding bulk (2H) material.[97] MoS_2 nanooctahedra, the smallest closed hollow structures of IF-MoS_2 synthesized by LASER ablation,[98] have a typical size of 3–6 nm and consist of 3–5 MoS_2 stacked layers with weak inter-planar van der Waals forces. Bulk quantity production of such IF-like nanoparticles (IF-WS_2, NanoLub) is already made possible. Thus, fundamental studies that characterize the HDS catalytic activity of IF-MoS_2 are required for exploring their potential application in HDS.

Thiophene (99+%, Sigma-Aldrich) used in this study was cleaned by freeze-pump-thaw cycles. H_2/H (5.0, Praxair, USA) was dosed on the surface by a home-built, hot tungsten filament hydrogen doser. Unless specifically mentioned, a heating rate of 2 K/s was used for TDS experiments. The exposures, χ, were given in Langmuir (1L = 1 s gas exposure at $1x10^{-6}$ mbar).

3.1.2. Sample fabrication

IF-MoS_2 suspension was prepared by suspending IF-MoS_2 powder (~ 2 mg) in 20 mL isopropanol, followed by mild sonication at room temperature with a bench top sonicator.[99] Two 50 µL aliquots of the suspension were dropped-and-dried on each of the supports, silica [SiO_2/p-Si(111), MEMS nanotechnology Exchange, VA, USA][100-101] and sapphire [Al_2O_3(0001) from Crystal lab. Inc., FL, USA]. Scanning electron microscopy (SEM) and energy-dispersive x-ray spectroscopy (EDX) characterization was provided by R. Tenne's group at Weizmann Inst. (Israel).

3.1.3. Results and discussion

Figure 20 shows the SEM images of silica-supported IF-MoS_2 NP at different magnifications. SEM images clearly show that the surface of silica support is entirely covered

with the nanoparticles. As evident from the figure, the total surface area of the IF may be an order of magnitude greater than for the support.

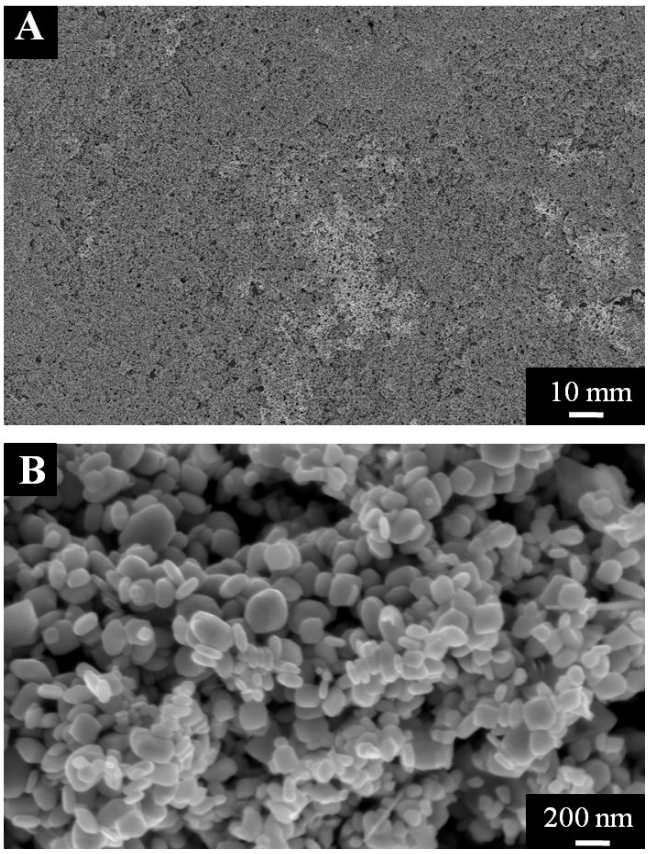

Figure 20. SEM images of silica-supported IF-MoS_2 NP at different magnifications.[57] The silica support is entirely covered with NP and the total surface area of NP is at least an order of magnitude greater than the support.

Figures 21A and B depict thiophene TDS data for IF-MoS_2 supported on (A) silica and (B) sapphire. The insets depict the data for small exposures. Figure 21C depicts the results of thiophene TDS on clean silica (control experiments).[101] The silica/sapphire-supported IF-MoS_2 samples were UHV annealed for 5 minutes at 800 K (labeled as pristine or as-received, hereafter). As evident from the figure, the three TDS peaks, labeled T, S, and Mo, appeared for both silica/sapphire-supported IF-MoS_2 samples. The peak positions for the two samples agree within ± 10 K, supporting the minimal effect of support on the adsorption kinetics of thiophene.

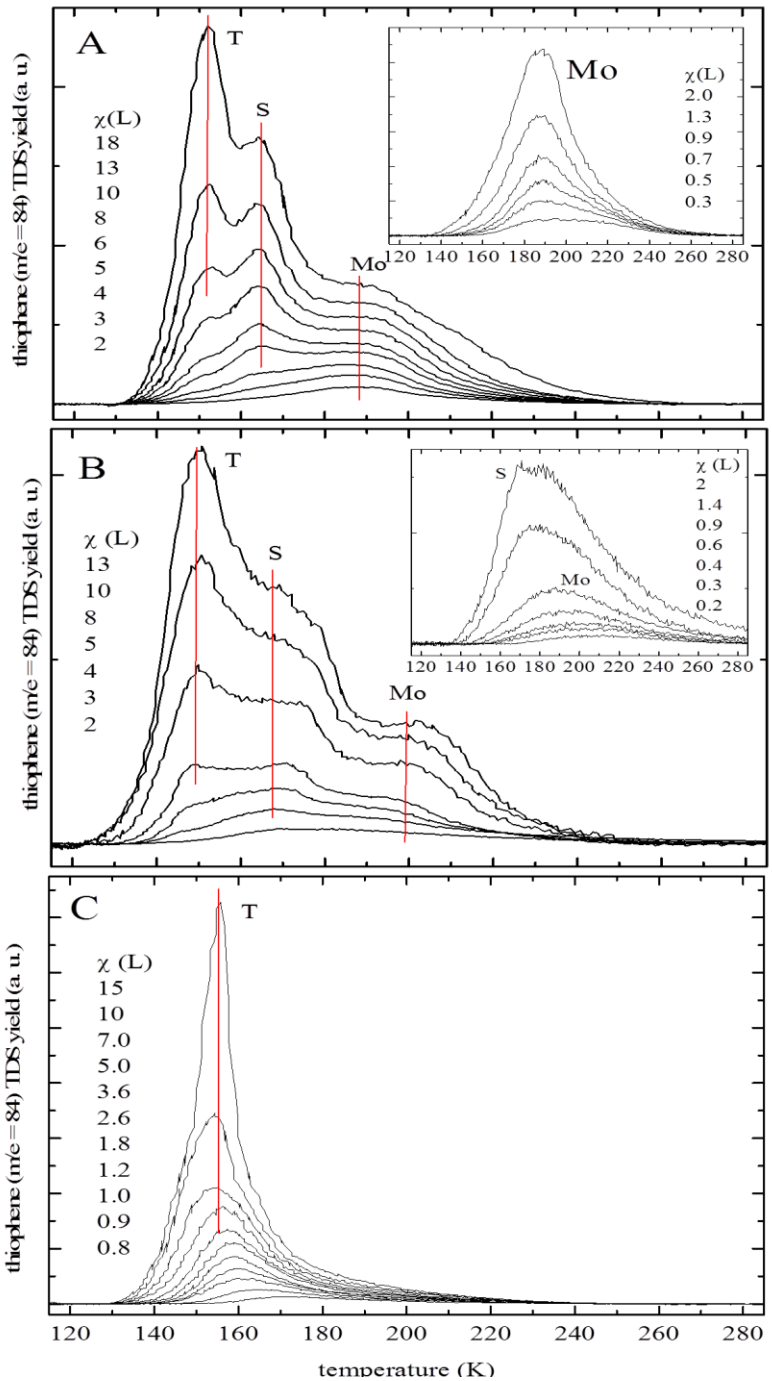

Figure 21. Thiophene TDS as a function of exposure, χ, in Langmuir (L) on (A) silica and (B) sapphire-supported IF-MoS_2 NP,[57] and (C) a clean silica support.[101] The S and Mo TDS peaks correspond to the adsorption of thiophene on S- and Mo/MoOx-like adsorption sites on IF-MoS_2 NP. The insets indicate the data for small exposures. T is the condensation peak of thiophene.

In addition, a single peak appeared in the blind experiments, and this ruled out the effect of non-covered areas of the support on the adsorption kinetics of thiophene. The lined up low temperature edges of the T peaks indicate thiophene condensation obeying 0th-order kinetics. The condensation peak appears only at low temperatures and large exposure. The position of the S and Mo TDS peaks are approximately independent of the thiophene exposure, indicating 1st-order kinetics and small effects of lateral interactions. This is further supported by the perfect match between the gas-phase fragmentation pattern of thiophene and the one obtained in multi-mass TDS experiments as shown in figure 22. Therefore, assuming a standard pre-exponential of 1x 10^{13}/s, the binding energies for the S (at ~ 180 K) and Mo (at ~ 200 K) TDS peaks were measured to be of 46 and 52 kJ/mol, respectively. Slightly larger binding energies (60 kJ/mol) were recently reported for thiophene adsorption on silica-supported IF-WS_2.[86]

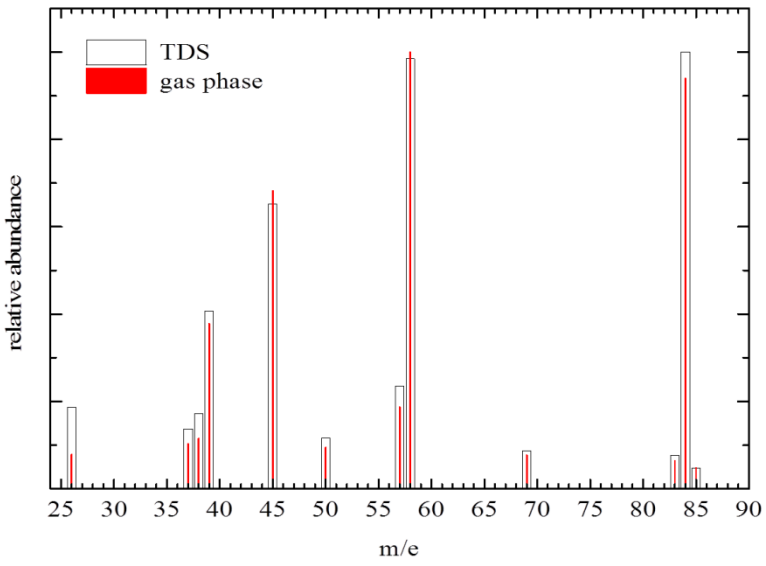

Figure 22. Thiophene multi-mass TDS experiment on IF-MoS_2 NP. Comparison of thiophene TDS peak intensities (open bars) on silica-supported IF-MoS_2 NP with the mass spectrometer signals (solid bars).[57] The intensity of peaks are normalized to m/e 84. A close match between the TDS and gas phase data indicates molecular adsorption of thiophene on IF-MoS_2 NP.

The samples were UHV annealed in H_2, O_2, and H_2S to identify the TDS peaks. The data of thiophene TDS experiments on these annealed samples are presented in Figure 23. As evident from Figure 23A, the TDS curves dominated by Mo TDS peak appeared for both the UHV annealed and hydrogen (H_2/H) annealed samples. It is important to note that H_2S was detected in the UHV chamber after annealing the samples in hydrogen. Interestingly, the Mo TDS peak shifted to lower desorption temperatures with increasing thiophene exposure. This peak shift is related to the repulsive lateral interactions of thiophene. However, no peak shift for Mo TDS peak was observed for the pristine sample. Therefore, the thermal annealing of IF-MoS_2 samples in hydrogen ambient (H_2/H) reduced the samples and formed kinetically distinct adsorption sites (S & Mo).

Similarly, as evident from Figure 23B, the thermal annealing of samples in oxygen ambient led to an enhancement in the intensity of Mo TDS peak when compared to the S TDS peak. In contrast, as evident from Figure 23C, the thermal annealing of samples in H_2S converted the reduced sample back to the pristine state. This observation is further supported by the similar TDS data obtained for H_2S annealed and pristine sample; cf. Figures 21A and B with Figure 23C. Thus, the reduction of the samples enhanced the Mo TDS peak intensity; whereas, sulfidation reduced the Mo TDS peak intensity compared to the S TDS peak.

AES data obtained for reduced/oxidized (H_2/O_2 annealed) and sulfided (H_2S annealed) samples provided further evidence supporting the peak assignments (Mo, S). Thermal annealing of samples in hydrogen (800 K, $2x10^{-6}$ mbar, 30 min) reduced the S AES peak intensity by 20% while subsequent H_2S annealing led to an increase in the intensity of S AES (compared to the pristine sample). Thus, it is reasonable to assign the S TDS peak to sulfur-like and the Mo TDS peak to Mo/MoO_x-like adsorption sites on the IF-MoS_2 samples.

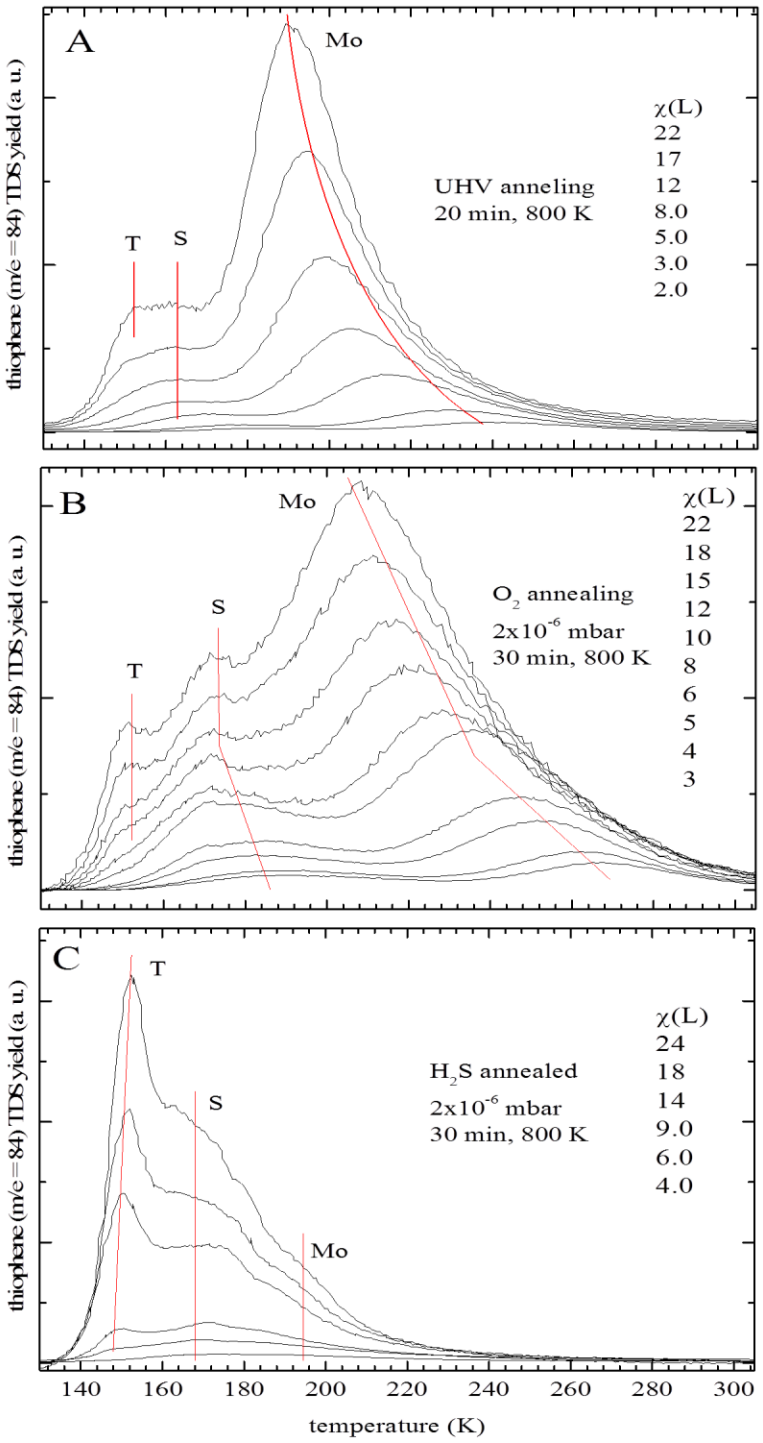

Figure 23. Thiophene TDS as a function of exposure, χ, in Langmuir (L) on (A) vacuum annealed, (B) oxygen annealed, and (C) H_2S annealed silica-supported IF-MoS_2 NP.[57] Annealing conditions are indicated in each case. Refer to Figure 21 for peak labeling.

Pressure jump experiments simulating the quasi-steady state conditions were also performed to characterize the HDS activity of the supported IF-MoS_2 samples. Typical pressure jump transients for the sapphire-supported IF-MoS_2 samples are summarized in Figure 24. It is therefore important to note that similar results were obtained for both the silica and sapphire-supported IF-MoS_2 samples.

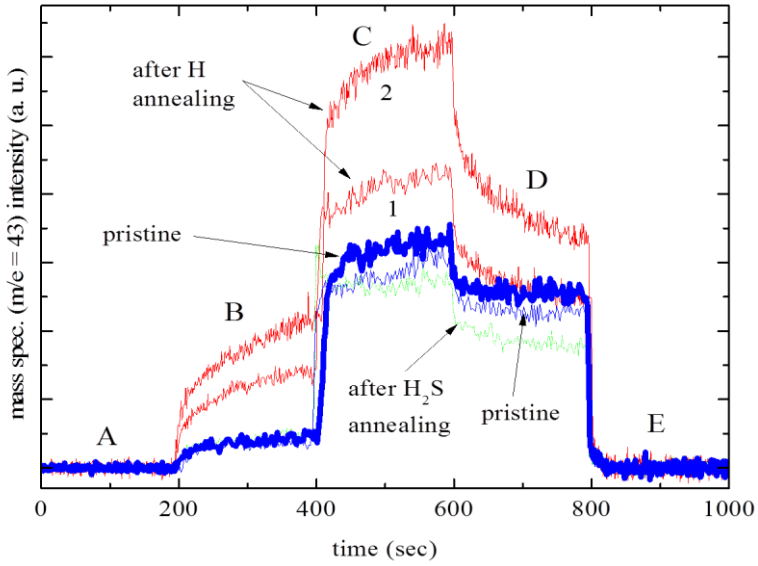

Figure 24. Pressure jump experiments at 350 K for reduced and sulfided IF-MoS_2 NP samples.[57] The formation of alkanes (m/e = 43) is monitored. Different sections in the plot indicate different experimental conditions: (A) valves closed, (B) $2x10^{-6}$ mbar H_2/H, (C) $2x10^{-6}$ mbar H_2/H and $1x10^{-6}$ mbar thiophene, (D) $1x10^{-6}$ mbar thiophene, and (E) valves closed.

Different sections in Figure 24, labeled A, B, C, D, and E, correspond to different experimental conditions. In section A (0-200 s) of the transient, UHV conditions were maintained. In section B (200-400 s), H_2/H was dosed at a pressure of $2x10^{-6}$ mbar starting at 200 s. In section C (400-600 s), thiophene was additionally dosed at $1x10^{-6}$ mbar starting at 400 s. In section D (600-800 s), the hydrogen flow was stopped right away at 600 s. In section E (800-1000 s), the thiophene flux was stopped right away at 800 s. Five different transients are

shown in Figure 24: two for the pristine samples, two for the reduced samples, and one for the sulfided sample, as indicated. The formation of alkanes (m/e = 43) and H_2S (m/e = 34) were monitored in situ using a mass spectrometer.

As evident from the results, IF-MoS_2 samples exhibited HDS activity at high pressure in a UHV chamber. As shown in section A, no HDS activity was observed in the absence of reactants. In section B, some HDS activity was observed in spite of dosing only H_2/H. This is due to an unavoidable background of thiophene in the UHV chamber. In section C, HDS activity was observed while simultaneously dosing H_2/H and thiophene. In spite of stopping the H_2/H flow, some HDS activity was observed in section D. This is due to a slow decrease in the background pressure of H_2/H in the UHV chamber. It is important to note that the reversal of the exposure order (first thiophene, next H_2/H) also led to some HDS activity mainly due to the background of hydrogen in the UHV chamber. Hydrogen is difficult to pump and therefore remains as the largest component of the residual gas in every UHV chamber. Moreover, some atomic hydrogen is always generated by the hot filaments used in sample heating, pressure gauges, and mass spectrometer.

Pristine samples showed distinct HDS activity. However, the hydrogen annealed samples formed approximately double the amount of alkanes when compared to pristine samples. H_2S annealed samples (sulfidation) showed a decreased HDS activity that is similar to pristine samples. Thus, it is evident that Mo/MoO_x sites enhanced the HDS activity that is consistent with traditional HDS mechanisms. Pristine samples (supposedly fully sulfided) also exhibited some catalytic activity. There was no evidence of catalyst poisoning in these experiments. However, as evident from the two different pressure transients for the pristine sample, some variation in the intensity was observed.

3.1.4. Summary

The catalytic activity of a novel nanomaterial, IF-MoS_2, towards thiophene HDS is characterized at UHV conditions. Thiophene adsorbed molecularly on IF-MoS_2 at low temperatures. Besides a condensation peak (150 K), two TDS peaks corresponding to binding energies of 46 and 52 kJ/mol ($1x10^{13}$/s pre-exponential) are observed in TDS experiments. TDS and AES data concerning the reduced and sulfided samples were utilized to assign the TDS peaks to S- and Mo/MoO_x-like adsorption sites. Quasi steady state experiments suggest that both reduced and sulfided samples exhibit HDS activity, with reduced samples being highly active.

3.2. Adsorption of Thiophene and Other Small Organic Molecules on WS_2 Nanotubes

A brief introduction to inorganic nanotubes of WS_2 (INT-WS_2) is presented first, followed by the fabrication of silica and indium-supported INT-WS_2. A combined results and discussion section is presented next. A summary of experimental results obtained in this study is given at the end.

3.2.1. Introduction

The synthesis of nanocatalysts utilizing novel nanofabrication techniques have received increased attention in catalysis and surface science.[102-103] Among the nanotubes synthesized so far, CNTs have been extensively investigated. However, few UHV model studies are available focusing on inorganic nanotubes. Conventional HDS catalysts consist of micro-sized Mo and W sulfide particles.[90-91]

This project is concerned with the study of adsorption kinetics (TDS) of thiophene and other small organic molecules on INT-WS_2, as well as the characterization of possible adsorption sites on INT-WS_2. Hollow nanoparticles and nanotubes clearly have interesting properties, such as enhanced surface area, confinement effects, and defects that make them interesting as

potential HDS catalysts. It is known from studies on single crystals that the catalytically active edges of metal clusters and surface defects are vital for HDS activity.[90-91, 93] A few recent studies indicate related effects for inorganic hollow nanoparticles[87] and nanotubes.[88] NTs can be considered as quasi one-dimensional systems with intriguing properties, such as confinement effects and unusual diffusion properties. In addition, NTs with chiral structure, functionalized NTs, and metal cluster deposited NTs are reported to have potential applications in catalysis.

The INT-WS_2 used in this study were synthesized at NanoMaterials Ltd. (Israel) according to published procedures.[94, 104] INT-WS_2 were very well characterized.[96, 104-105] According to the characterization, INT-WS_2 are multi-walled NTs with an empty core and are fully sulfided. INT-WS_2 have a purity of 90%. INT-WS_2 have a length of 10-50 μm with inner (~ 5 nm) and outer (20-180 nm) diameters.

As per Gaussian estimates, the maximum sizes of the probe molecules: n-pentane, thiophene, and benzene were estimated to be 0.7, 0.5, and 0.5 nm, respectively. So these probe molecules are also expected to adsorb inside INT-WS_2.

3.2.2. Sample fabrication

INT-WS_2 suspension was prepared by suspending two micro spatula tips of the INT-WS_2 powder in thiophene (1.8 mL), followed by mild sonication at room temperature with a bench top sonicator (PC 3, L& R Ultrosonics).[99] Ten 50 μL aliquots of the suspension were dropped-and-dried on silica (SiO2/p-Si(111) from MEMS nanotechnology Exchange, VA, USA).[100-101] In addition, solvent-free samples were fabricated by pressing the INT-WS_2 powder into a clean indium foil.[106] SEM characterization was provided by Tenne's group at Weizmann Inst. (Rehovot, Israel) and by M. Lu at Argonne National Laboratories (Chicago, USA).

3.2.3. Results and discussion

Similar results were obtained for both the silica and indium supported INT-WS_2, and therefore, only the results obtained for the silica-supported sample are presented. Figure 25 depicts a SEM image of the silica-supported INT-WS_2. The SEM image clearly shows that the surface of silica support is entirely covered with INT-WS_2. As evident from the figure, the total surface area of the INT-WS_2 may be an order of magnitude greater than for the support. Therefore, the TDS data will not be obscured by the non-covered areas of the support. Groove sites typically form between adjacent NT. Energy-dispersive x-ray spectroscopy (EDX) data of INT-WS_2 did not indicate any impurities. Figures 26–28 summarize the TDS data characterizing the adsorption kinetics of small organic molecules on the INT-WS_2 .

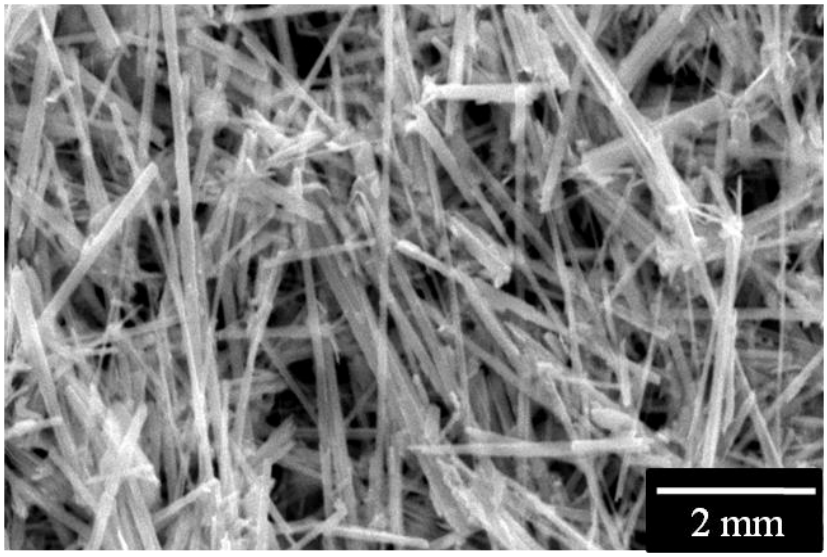

Figure 25. SEM image of silica-supported INT-WS_2.[58] The silica support is entirely covered with NT and the total surface area of NT is at least an order of magnitude greater than the support.

Alkanes are typically considered as prototype probe molecules in adsorption kinetics experiments on NTs at UHV conditions, as evident from several detailed studies conducted on CNTs.[107] Therefore, the adsorption kinetics experiments of n-pentane are presented here.

Figure 26A depicts the TDS data of n-pentane. The inset depicts the data for small exposures. Four distinct peaks, labeled A-D, are identified. The adsorption sites with the largest binding energy, e.g., A are typically first populated, followed by the sites with lower binding energy. This filling sequence (A-D) is clearly observed for some probe molecules when the TDS data is collected for small exposures, e.g., benzene TDS data in Figure 28.

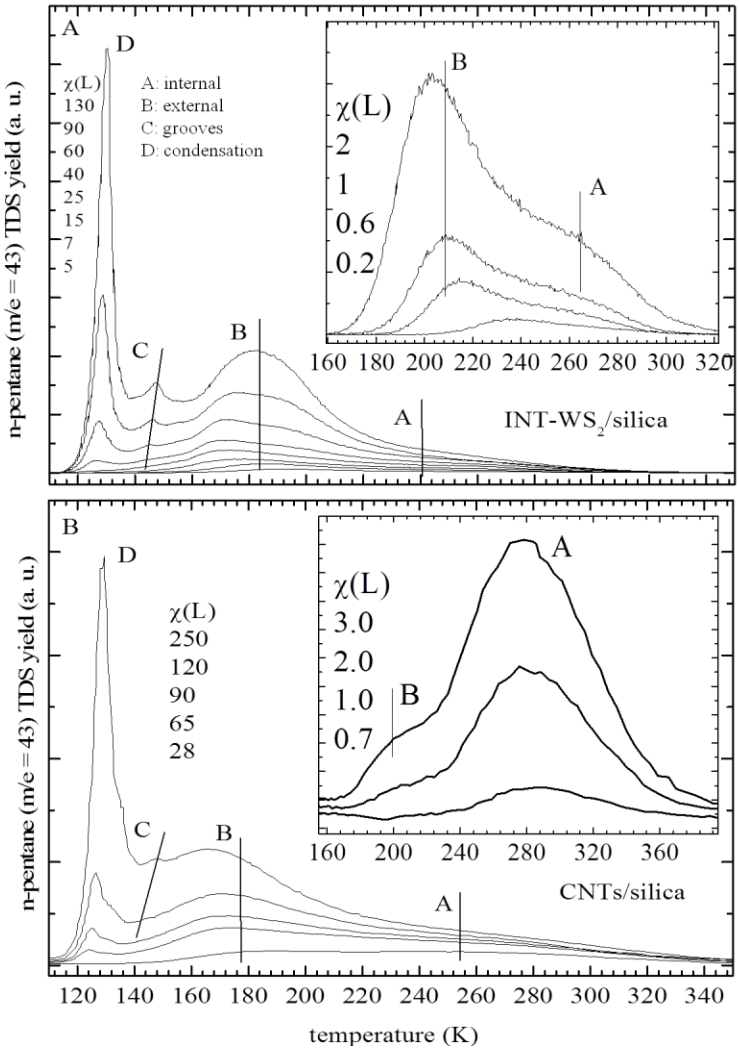

Figure 26. n-pentane TDS as a function of exposure, χ, in Langmuir (L) on silica-supported (A) INT-WS_2[58] and (B) CNTs.[74] The TDS peaks A, B, and C correspond to the adsorption of n-pentane on internal, external, and groove sites of nanotubes respectively. The insets show the data for small exposures. D is the condensation peak of n-pentane.

In the case of n-pentane, the intensity of A and B peaks increased simultaneously with exposure. This effect might be related to the molecular mobility and/or steric effects. The lined up low temperature edges of the D peaks indicate surface and adsorption site unspecific condensation of n-pentane. The condensation peak appears only at low temperatures and large exposures. The shape of the TDS peaks did not change when the TDS data was collected on H_2S annealed (1x 10^{-6} mbar, 50 min) samples. This rules out the possibility of TDS peaks arising due to the adsorption/desorption of n-pentane on defects in the side walls of the NT. The diffusion of the probe molecule is fast relative to the time scale of the experiment. This could rule out the adsorption/readsorption effects and Knudsen diffusion. Furthermore, as evident from Figure 25, the pore sizes between adjacent NT bundles are much larger than the NT diameters. Multi-mass TDS experiments concluded the molecular adsorption/desorption of probe molecule. Multiple TDS runs on the same sample give rise to similar TDS features and peak intensities, Therefore, no deactivation or poisoning of the catalyst is observed.

Interestingly, the TDS curves obtained on INT-WS_2 are very similar to those on CNTs;[74, 99, 108] cf. Figure 26A with 26B. It is important to note that the TDS data presented here is the first-of-its-kind for an inorganic nanotube system. Figure 26B depicts n-pentane TDS on silica-supported CNTs, collected in one of the previous projects on CNTs.[74] The similarity of the TDS data obtained on INT-WS_2 and CNTs is quite interesting. The TDS peak assignment for CNTs involved several measurements: infrared spectroscopy, filling factors measurement, coadsorption experiments, and the comparison studies on closed and open ended CNTs.[74, 99, 106, 109-110] Accordingly, the TDS peaks A, B, and C for CNTs were assigned to the adsorption/desorption of the probe molecule from the interior, exterior, and groove sites. It is therefore reasonable to have similar peak assignment for the TDS peaks obtained for INT-WS_2.

Some of the inorganic NTs may be close ended. In addition, some INT-WS_2 with much smaller diameters do not allow the probe molecule to enter inside the tubes. This assumption possibly explains the relatively small intensity of the A peak (internal sites) when compared to the B peak (external sites). The relatively small intensity of peak C (groove sites) could be due to steric effects that hinder the adsorption of the linear alkanes along the grooves of the NT. Relevant experiments on TiO_2 NT revealed only a monolayer peak.[111] TiO_2 NT have a relatively larger diameter but smaller aspect ratio when compared to INT-WS_2. Therefore, capture effects, as evident by the A TDS peak obtained for WS_2 NT, were not observed for TiO_2 NT. The TiO_2 NT walls consist of many nanocrystallites, which make the NT walls' surface areas larger than the highly crystalline INT-WS_2.

The adsorption kinetics data for thiophene, which is relevant for HDS studies on INT-WS_2, is depicted in Figure 27A. As evident from the figure, thiophene TDS on silica-supported INT-WS_2 reveals four different TDS peaks (A-D). However, these peaks do not appear in the TDS data collected on silica-supported IF-WS_2 NP.[86] In this case, a single TDS peak appears in the monolayer adsorption region (α peak) besides a condensation peak (D peak). This result further supports the conclusion that the distinct A-C TDS peaks (corresponding to different sites) are an intrinsic property of the NT. The same UHV system, including identical sample holder, has been used for all experiments. The C TDS peak (groove sites) for thiophene (Figure 27A) is more distinct when compared to n-pentane data (Figure 26A), which can be attributed to steric effects.

Benzene TDS on INT-WS_2 is depicted in Figure 28. Again, the characteristic features of the NT are present in the TDS curves. When the TDS data for all the probe molecules is analyzed, it becomes evident that the A (internal sites) and B peaks (external sites) have similar

intensity for thiophene and benzene; whereas, A peak has relatively small intensity when compared to B peak for n-pentane. This could be due to the sterical hindrance caused to n-pentane.

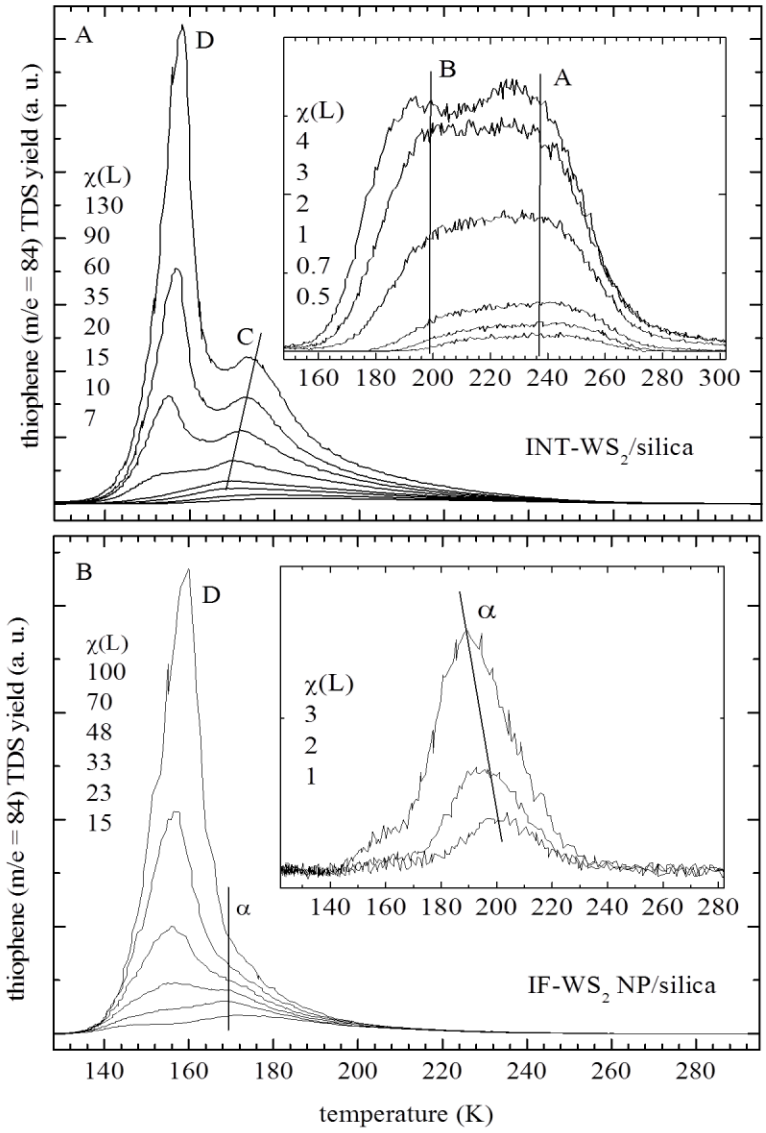

Figure 27. Thiophene TDS as a function of exposure, χ, in Langmuir (L) on silica-supported (A) INT-WS_2[58] and (B) IF-WS_2 NP.[86] The TDS peaks A, B, and C correspond to the adsorption of thiophene on internal, external, and groove sites of INT-WS_2 respectively. The insets show the data for small exposures. D is the condensation peak of thiophene. A single TDS peak (α) is observed in the monolayer region in the case of IF-WS_2 NP.

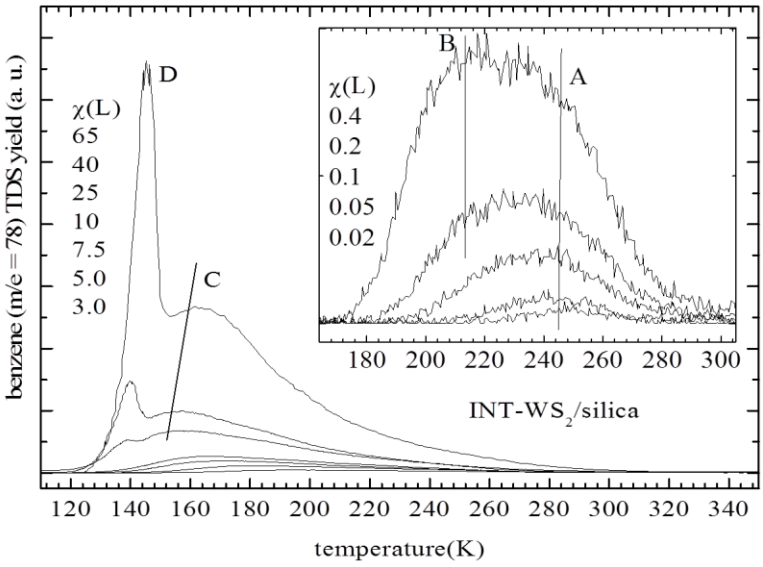

Figure 28. Benzene TDS as a function of exposure, χ, in Langmuir (L) on silica-supported INT-WS_2.[58] Refer to Figure 27 for peak labeling. The inset shows the data for small exposures.

HDS reactivity screening of INT-WS_2 NT was conducted by performing reactive TDS experiments. However, industrial HDS conditions cannot be simulated in UHV experiments. Large gas exposures typically lead to unavoidable/uncontrollable background effects. As a preliminary test, the sample temperature was increased while simultaneously leaking $2x10^{-6}$ mbar H_2/H and $1x10^{-6}$ mbar thiophene into the UHV chamber and the possible HDS fragments were detected with a mass spectrometer.

Figure 29 depicts the reactive TDS experiment. As evident from the figure, alkanes (m/e = 43) and H_2S (m/e = 34) formed well below room temperature. However, the reactive TDS experiments on WS_2 NP reveal HDS activity only above 500 K.[86] From a number of blind experiments conducted, it is concluded that a distinct HDS catalytic activity is exhibited by INT-WS_2 only when H_2/H and thiophene are simultaneously dosed. However, the intensity of reaction products is close to the detection limit of the mass spectrometer. These results led to a speculation that the HDS experiments conducted on Ni/Co coated INT-WS_2 at ambient pressures

would reveal greater catalytic activity. This speculation was indeed proved to be correct as evident from the studies conducted on Co and Ni coated INT-WS_2[59-60] and will be presented as the next subprojects.

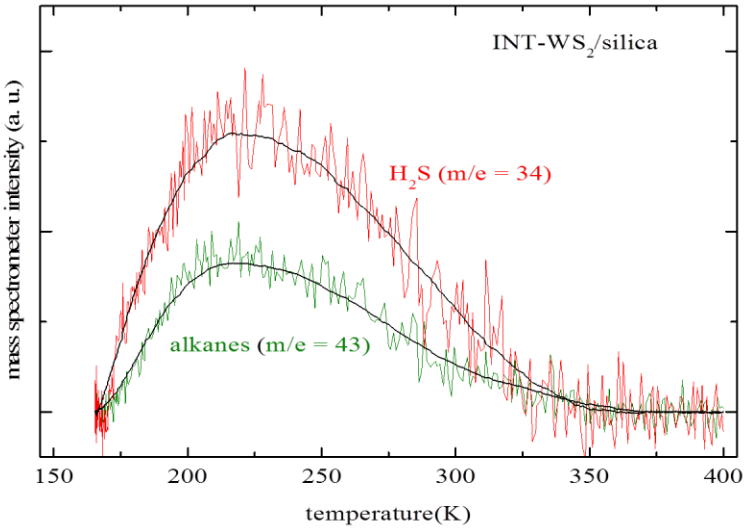

Figure 29. Reactive TDS experiments on silica-supported INT-WS_2. Reactive TDS experiments with the reactants at ambient pressure ($2x10^{-6}$ mbar H_2/H and $1x10^{-6}$ mbar thiophene) indicating the formation of alkanes (m/e = 43) and H_2S (m/e = 34) well below room temperature.[58]

3.2.4. Summary

Adsorption kinetics of thiophene on INT-WS_2 reveal the well-known characteristic TDS patterns observed for CNTs. Thiophene, n-pentane, and benzene adsorbed on internal, external, and groove sites of INT-WS_2. INT-WS_2 exhibit some HDS activity well below room temperature.

3.3. Adsorption of Thiophene on Silica-supported Mo Clusters

An introduction to hydrodesulfurization (HDS) process and Mo-based HDS catalysts is presented first, followed by the fabrication of silica-supported Mo clusters. A combined results and discussion section is presented next. A summary of experimental results obtained in this study is given at the end.

3.3.1. Introduction

Industrial HDS process involves the removal of sulfur from the sulfur-containing compounds present in the crude oil by treating them with hydrogen in presence of catalysts to obtain sulfur-free hydrocarbons.[89-91, 112-118] Molybdenum and tungsten-based catalysts with Ni/Co promoters are conventionally used in industrial HDS process. Recently, alumina-supported molybdenum carbide and nitride,[119] and molybdenum carbide single crystal[120] HDS catalysts have been considered. Thiophene (C_4H_4S) has been widely used as a probe molecule for HDS studies under UHV conditions to obtain mechanistic information which can constitute the basis for design of new catalysts. Extensive research comprising the HDS studies on single crystals was conducted in the 1980s and 1990s with regard to the development and commercialization of high-activity HDS catalysts. The renewed interest in HDS studies is related to the importance of studies focusing on the so-called model catalysts (supported metal clusters), as well as the development of nanofabrication techniques.[93, 121-122] However, very few studies have been devoted to HDS surface science kinetic studies on cluster systems and nanotubes.[57-58, 83-88, 123-124] Previous studies showed that the sulfur-terminated MoS_2 basal plane was fairly inactive;[125-126] whereas, the sputtered/annealed samples were fairly active.[125-139] Several different mechanisms were proposed for thiophene bond activation on sulfur vacancy sites (direct thiophene–Mo interaction).[89-91, 140] HDS activity of fully sulfided nanosized MoS_2 clusters was confirmed by recent scanning tunneling microscopy (STM) studies.[92-93, 116, 121-122] This activity was attributed to one-dimensional metallic states located at the perimeter of the MoS_2 nanoclusters (no direct thiophene interaction with Mo). Such fully sulfided model catalysts should be highly resistant to poisoning when compared to previously studied model catalysts. STM studies also confirmed the distinct catalytic activity of nanosized MoS_2 clusters, when

compared to the single crystal model systems. This necessitates an extension of HDS studies on single crystals to more realistic model systems, such as inorganic fullerene-like particles,[57-58, 86, 141] inorganic nanotubes, and nanosized clusters.[116, 123-124, 142] Despite the large number of STM studies concerning some cluster systems, only a limited number of studies concerning the reaction kinetics and dynamics on these novel systems are available. It is therefore important to characterize the catalytic activity of MoS_2 nanoclusters and compare it with Mo single crystal, an important model system for HDS studies. Accordingly, this study was aimed at investigating the adsorption kinetics/dynamics of thiophene on vapor-deposited Mo clusters supported on silica.

Thiophene adsorption, bond activation, and HDS on Mo single crystals were extensively studied by a variety of techniques. Thiophene decomposed completely on Mo(100) forming C and S impurities on the surface, which could be cleaned by annealing in oxygen.[143] TDS experiments revealed H_2 as the only product that desorbed from the surface.[143] High-resolution electron energy loss spectroscopy (HREELS) studies indicated the up-right thiophene adsorption (S-bonded) at small exposures. Different mechanisms for molecular decomposition were proposed based on the initial coverages of thiophene. At low coverage, the ring adsorbed parallel to the surface, and the molecular decomposition involved the C-S bond fission preceding the complete dehydrogenation in the 100-340 K temperature range. After saturation coverage, thiophene chemisorbed perpendicular to the surface, and the molecular decomposition involved stepwise dehydrogenation starting with a C-H bond activation at 230 K, followed by complete dehydrogenation until above 700 K. Even at saturation coverage, almost 20% of the molecules decomposed through the mechanism observed at low coverage. Some studies reported 50-66% decomposition of thiophene on Mo(100).[144] Based on TDS results, the binding energies between 16 and 22 kcal/mol were determined for molecularly adsorbed thiophene, depending on coverage

and adsorption site. Similar TDS features were observed in presence of sulfur. However, sulfur prevented further bond activation of thiophene. HDS studies at atmospheric pressure were also conducted on Mo(100) and high surface area MoS_2 powder, and the results were compared.[145] In this study, the single crystal exhibited a higher catalytic activity than the powder catalyst. The initial reaction step involved the C-S bond fission with the formation of butadiene, which was subsequently hydrogenated to form butenes and butane. The observed differences in the catalytic activity were attributed to the catalytic inactivity of the MoS_2 basal plane. Very recent XPS studies on Mo clusters supported on Au(111) revealed thiophene decomposition below 300 K.[123] STM and TDS studies on gold-supported Mo nanoparticles revealed the thermodynamic instability of Mo particles on Au(111) surface, and that gold encapsulated the Mo clusters above 300 K.[10, 124] Gold encapsulated Mo nanoparticles were relatively inert towards thiophene decomposition. Very recent electrocatalytic activity measurements for hydrogen evolution reaction on Au (111) supported MoS_2 nanoparticles revealed the correlation between hydrogen evolution and the number of edge sites on the MoS_2 catalyst.[146] The MoS_2 system has recently attracted great interest in theoretical studies.[147-152] Density functional theory (DFT) based bond activation energies for thiophene decomposition on Mo(100),[152] as well as the theoretical binding energies of thiophene on MoC nanoparticles, were also available.[138] Although the MoS_2 clusters are used in the industrial HDS process, the metallic Mo clusters are typically used as a preliminary system due to their simplicity. Moreover, it would be experimentally challenging to directly deposit the MoS_2 clusters. In addition, the experimental results detailing the effect of Mo cluster sulfidation on the adsorption kinetics and dynamics of thiophene are included in the present study.

3.3.2. Sample fabrication

Several supports of SiO_2/Si(111) (MEMS Nanotechnology Exchange, VA, USA) were used in this project. The supports were cleaned according to the published procedure.[153-154] AES was used to monitor the cleanliness of the support, as well as Mo clusters. Mo metal was dosed by a home-built metal doser by resistively heating a Mo wire (d = 0.25 mm). Photographs and schematic of the home-built metal doser is given in Figure 30.

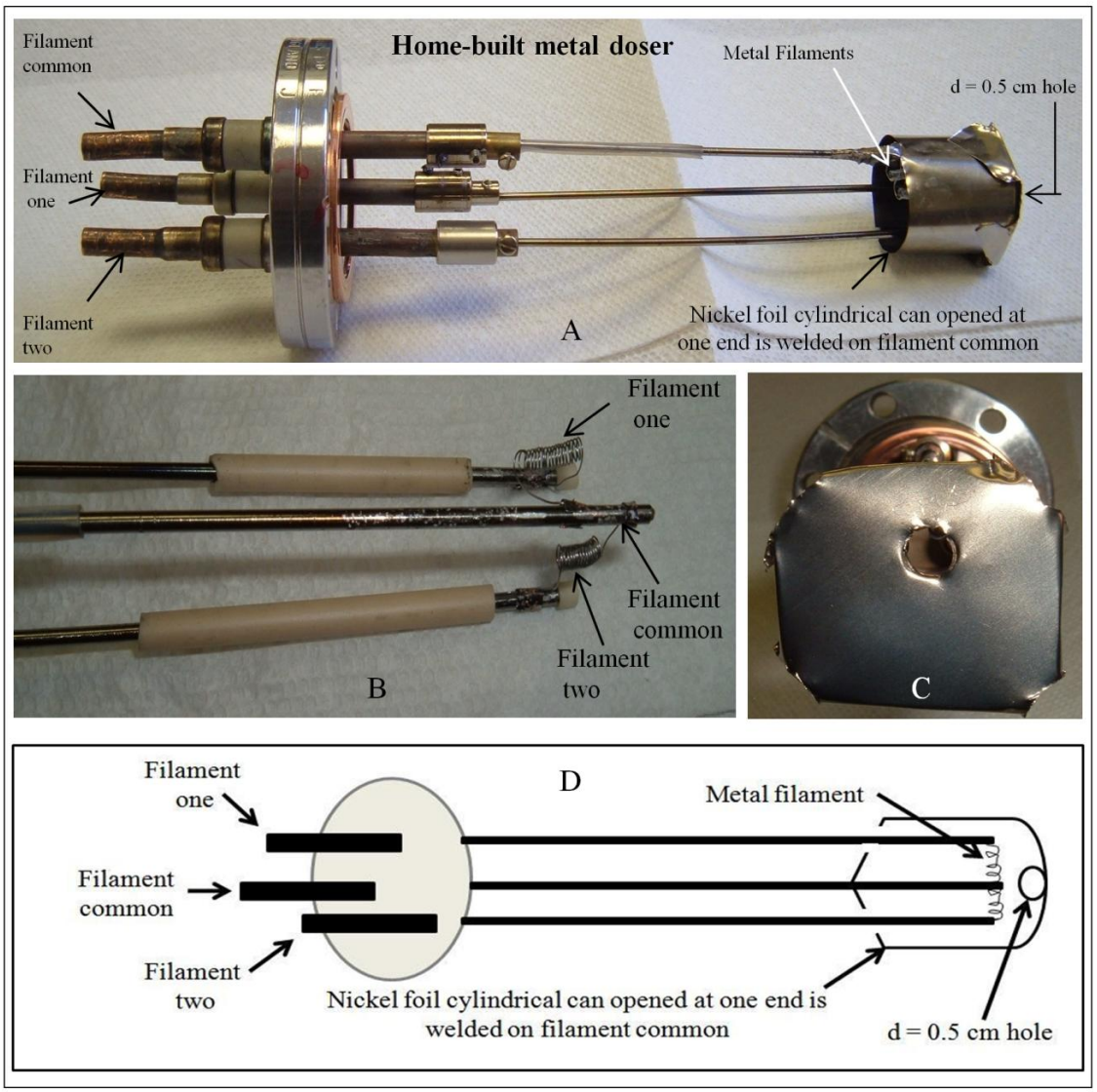

Figure 30. Photographs and schematic of the home-built metal doser. Photographs of (A) metal doser, (B) metal filaments, (C) nickel can, and (D) schematic of the metal doser.

The Mo coverage was calibrated by AES. Possible carbon contamination of Mo clusters were reported in the literature.[124] Carbon contamination was also expected in this project because of the nature of Mo to dissolve carbon to form carbides. In fact, industrial HDS catalysts contain a mixture of MoS_x and MoC_x during the catalytic process.[119-120] It is important to note that the carbon content of the sample used in this study was below 10% of a monolayer (ML). The Mo-to-S AES peak ratio, x, indicates the stoichiometry (MoS_x) of the clusters.

The TDS setup is described elsewhere.[109] The thermocouple reading was calibrated (± 5 K) in situ by TDS measurements of condensed hydrocarbons. A heating rate of 1.5 K/s was used in TDS experiments. Adsorption transients were collected by quickly (0.2 s) opening a leak valve to dose thiophene (E_i = 0.04 eV). The noise levels observed for the mass spectrometer reading and AES spectra were used to determine the uncertainties of individual measurements.

3.3.3. Results and discussion

The characterization of silica-supported Mo clusters is presented first, followed by the adsorption kinetics of thiophene on silica-supported Mo clusters. The kinetics of catalyst poisoning and activation is presented next, followed by the adsorption dynamics of thiophene on silica-supported Mo clusters.

3.3.3.1. Characterization of the Mo cluster sample

AES was used to characterize the morphology and cleanliness of the silica-supported Mo clusters. Figure 31A depicts a set of AES spectra of the Mo region as a function of Mo deposition time, χ_{Mo}. The inset depicts the oxygen AES region of the silica support. As evident from the Figure 31A, the Mo AES peaks (at 120, 148, 161, 186, and 221 eV) were very well resolved. The maximum carbon (peak at 273 eV) contamination was estimated to be less than 10% of a monolayer, taking into account the sensitivity factors[155] of the elements detected.

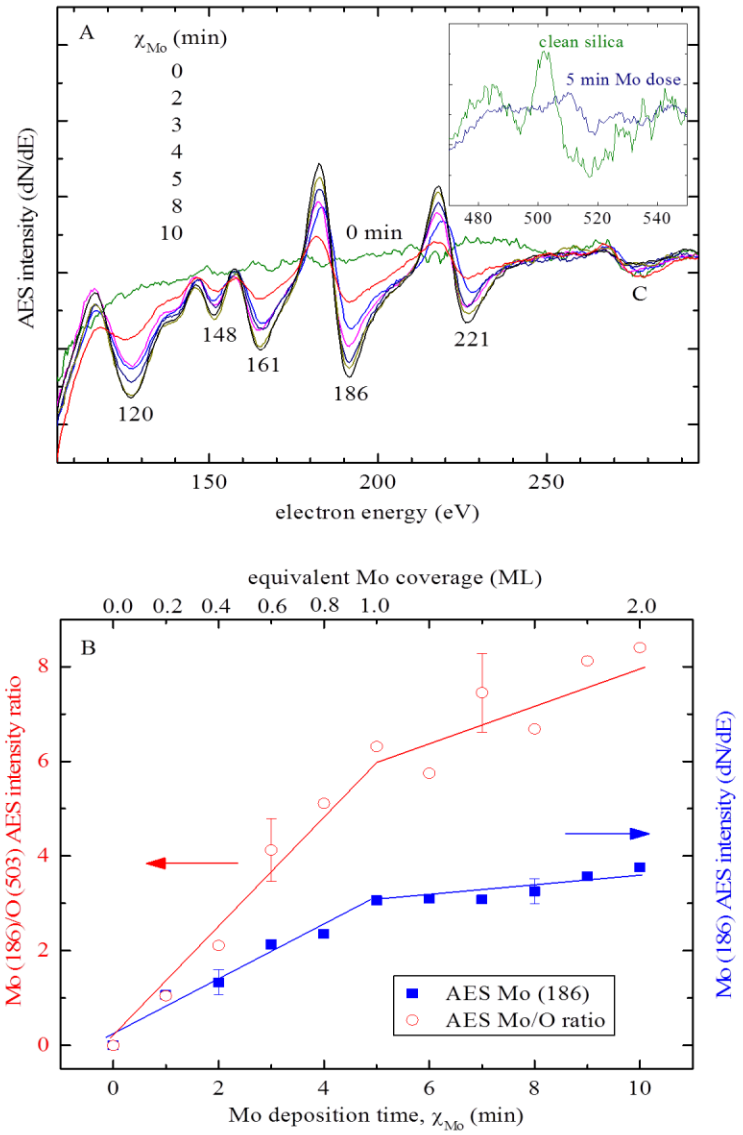

Figure 31. AES Mo coverage calibration. (A) AES spectra of Mo as a function of Mo deposition time (χ_{Mo}). The inset depicts the oxygen AES region.[61] (B) AES peak intensities as a function of $\chi_{Mo,}$ as indicated.[61]

Figure 31B depicts the Mo-to-O AES peak intensity ratio (left hand scale, open circles) and the Mo AES peak intensity (right hand scale, solid squares), as a function of Mo deposition time, χ_{Mo}. As typically observed for other model catalysts,[153-154] the AES peak intensity increased linearly with χ_{Mo} until a critical Mo coverage was reached, after which the AES intensity further increased linearly, but at a slower rate. This effect may be attributed to a change in the cluster

growth mode from two-dimensional (2D) clusters to three-dimensional (3D) clusters. While the 3D clusters being formed, the AES signal of the first Mo layer was shielded by the upper layers. This decreased its AES electron yield and resulted in a decrease of the slope of AES peak intensity vs. χ_{Mo} curve. These results concluded the 2D cluster formation for $\chi_{Mo} < 5$ min (labeled hereafter as "small clusters") and 3D cluster growth for $\chi_{Mo} > 5$ min (labeled hereafter as "large clusters"). As evident from the Figure 31B, the surface was saturated with 2D Mo clusters at $\chi_{Mo} = 5$ min. $\chi_{Mo} = 5$ min was considered as the equivalent of a monolayer (ML), and it was used to calibrate the Mo coverage in equivalent monolayer. SEM characterization of the cluster samples was not possible because of charging effects. However, an SEM image of the used sample showed the typical size of the smallest sulfided Mo clusters as ~ 10 nm.

3.3.3.2. Thiophene adsorption kinetics

The molecular adsorption of thiophene is discussed first followed by thiophene decomposition kinetics. The adsorption kinetics of thiophene on cleanest Mo clusters and sulfided Mo clusters (MoS_x) is presented next. Industrial HDS catalysts consist of MoS_2 particles and therefore thiophene adsorption kinetics on MoS_x is relevant for HDS catalysis.

3.3.3.2.1. Molecular adsorption of thiophene

Contamination of Mo/silica sample by S and C was unavoidable. So a typical TDS example for a used and partially poisoned catalyst is depicted in Figure 32A. Thiophene was adsorbed at 100 K. Thiophene TDS on a partially sulfided sample ($x > 0.2$ in MoS_x) revealed three distinct TDS peaks and a shoulder. The parent mass of thiophene (m/e = 84) was monitored in the TDS experiments. So, a fraction of thiophene was molecularly adsorbed/desorbed. The lined up, low temperature edges of the low temperature peaks (at ~150 K) indicate surface and adsorption site unspecific condensation of thiophene (labeled as multilayer peak). This peak

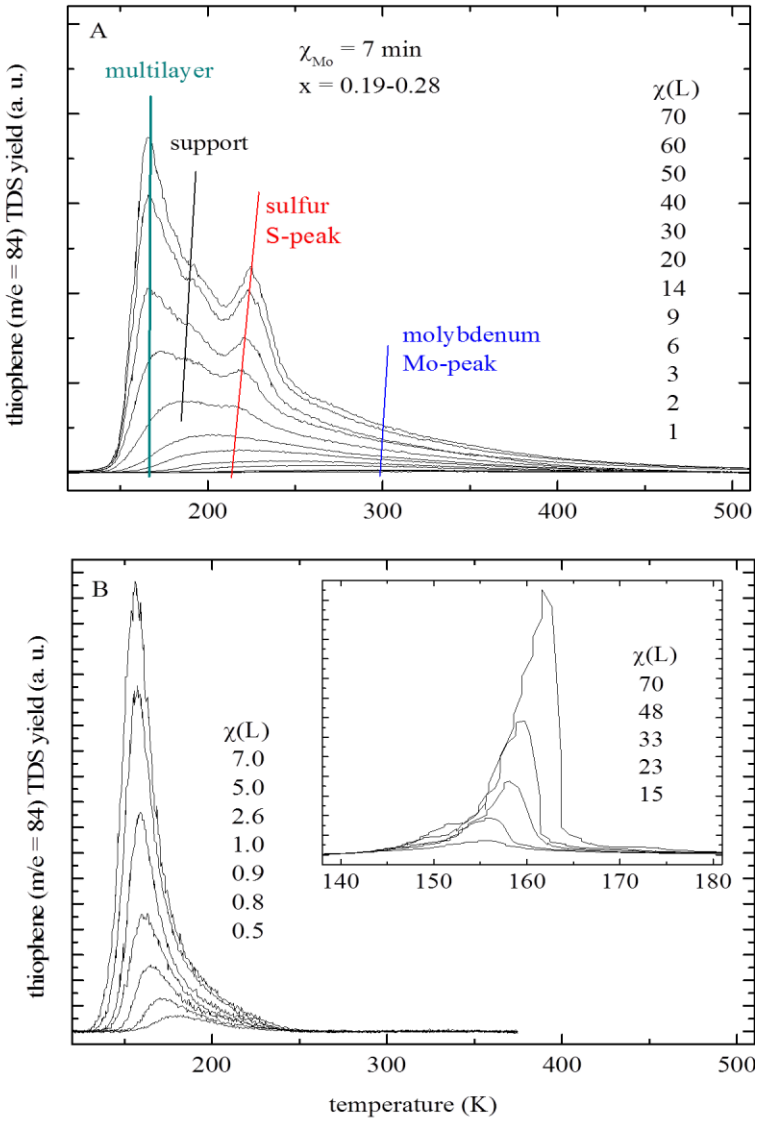

Figure 32. Thiophene TDS on silica-supported Mo clusters and clean silica. (A) Thiophene TDS as a function of exposure (χ) in Langmuirs (L) on silica-supported Mo clusters.[61] The S and Mo TDS peaks correspond to the adsorption of thiophene on sulfided Mo clusters/support and metallic clusters respectively. (B) Thiophene TDS on clean silica.[101] The inset depicts the data for large exposures.

shifted to higher temperatures with increasing thiophene exposure, $\chi_{thiophene}$. The other two distinct TDS peaks were labeled as sulfur (S peak) and molybdenum peaks (Mo peak), corresponding to the desorption of thiophene from sulfur-covered (S) and metallic (Mo) sites.

None of these TDS peaks were developed due to the desorption of thiophene from a clean silica support and is evident from Figure 32B. In this case, a single TDS peak appeared below 190 K.[101] It is important to note that similar thiophene TDS peaks were observed for IF-MoS_2 NP.[57] It is reasonable to assign the two TDS peaks to Mo-like and S-like adsorption sites. By comparing the areas of the multi layer and the S peak, it was concluded that the S peak originated from thiophene adsorbed on both the sulfided support and the sulfided Mo clusters. The Mo TDS peak was less intense compared to the S peak. In addition, the intensity of S peak was clearly correlated with the S AES signal. These observations further supported the TDS peak assignment. The weak shoulder at 190 K could be due the desorption of thiophene from either the support or the carbon covered adsorption sites.

3.3.3.2.2. Thiophene bond activation

The bond activation of thiophene was characterized by performing multi-mass TDS experiments which are summarized in Figure 33. A few examples of multi-mass TDS experiments are depicted in Figure 33A. Evidently, H_2, H_2S, and molecular thiophene desorbed in the same temperature range. The bond activation started at ~ 220 K. The hydrogen TDS signal was rather broad compared to the TDS peaks of other fragments. This is because of multiple decomposition reactions (with different activation energies) that occur during thiophene decomposition.

A histogram diagram depicting the peak areas of multi-mass TDS curves is shown in Figure 33B. The masses corresponding to the fragmentation pattern of gaseous thiophene in the mass spectrometer was subtracted. The observed fragmentation pattern could not be uniquely assigned to any one product due to the overlapping fragmentation patterns of different possible products. However, the detected masses m/e = 2 and 28 were not related to gaseous thiophene,

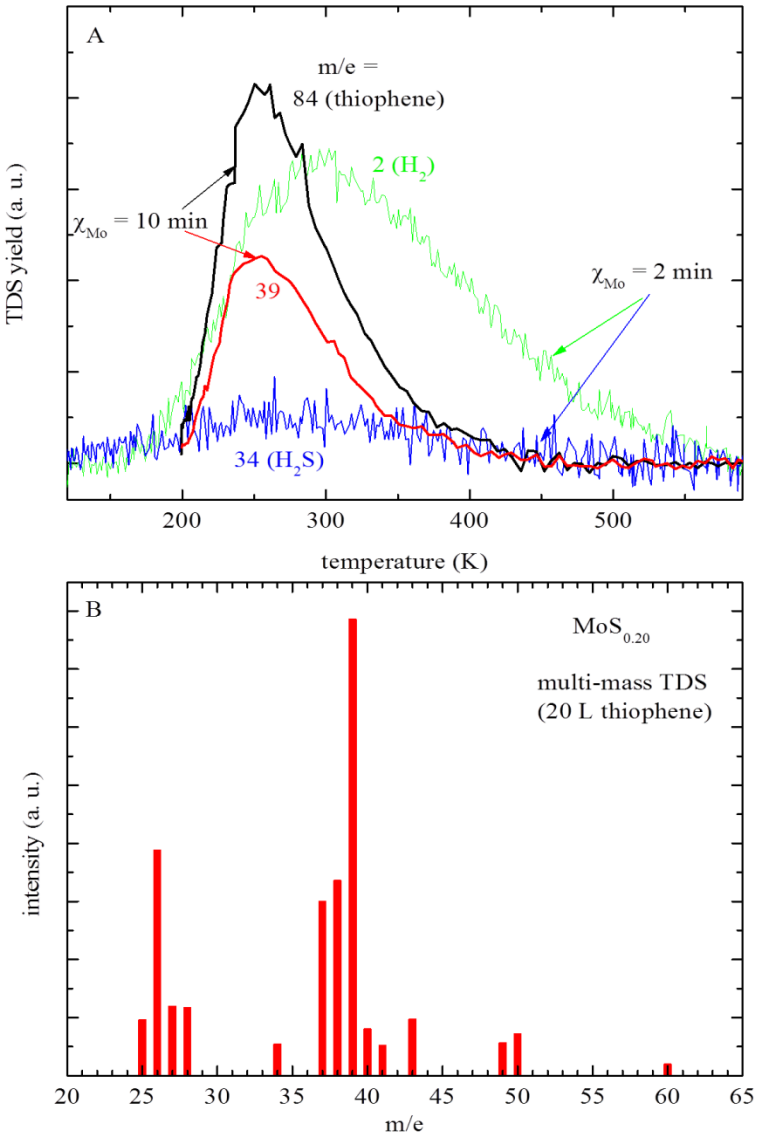

Figure 33. Thiophene decomposition on silica-supported Mo clusters. (A) TDS curves of major thiophene decomposition products. Thiophene bond activation started at ~ 220 K.[61] (B) Histogram depicting the integrated TDS intensities obtained from multi-mass TDS curves.[61] The observed multi-mass pattern mostly suits the fragmentation pattern of alkynes.

and that confirmed the decomposition of thiophene. In addition, AES spectra collected after the TDS experiments confirmed the presence of S and C impurities on the sample's surface. The observed multi-mass TDS pattern mostly suited the fragmentation pattern of alkynes[156] because

alkyne mass patterns contain m/e = 26 and 39 as the dominant peaks. A theoretical study supporting such a conclusion is available.[157]

3.3.3.2.3. Cleanest Mo clusters

As already described, the silica-supported Mo clusters were highly active toward thiophene bond activation, which resulted in catalyst poisoning by sulfur and carbon. Such catalyst poisoning prevented the characterization of pure Mo clusters. To overcome this problem, the experimental conditions were selected to keep the catalyst poisoning small. Small exposures of thiophene were used, and cleaning cycles were done in order to have low catalyst poisoning.

Thiophene TDS on χ_{Mo} = 10 min (2 ML Mo, large 3D Mo clusters) clusters is depicted in Figure 34. Thiophene was dosed at 190 K to avoid its condensation (cf., Figure 32). The data depicted in Figure 34A corresponds to the cleanest Mo clusters obtained (x = 0.10-0.14). Very similar data was obtained for small 2D clusters (e.g. χ_{Mo} = 2 min, 0.4 ML Mo). As depicted in Figure 34A, a broad peak centered at about 300 K was observed for clean Mo clusters. It is plausible to assign this peak to the adsorption of thiophene on Mo clusters or along the Mo/silica interface. This peak slightly shifted from 340 K to 274 K with increased thiophene exposure. Assuming first order desorption and a pre-exponential of 1×10^{13}/s, the activation energy of desorption (E_d = 90–76 kJ/mol) for thiophene was determined. The peak shift could be due to repulsive lateral interactions and/or different adsorption sites on the Mo clusters. Thiophene is a slightly polar molecule (0.51 Debye), and this could cause repulsive lateral interactions. Metal clusters typically have different adsorption sites (terrace sites, edges, and rim sites).

The Mo TDS peak shifted to higher temperatures with decreasing Mo exposure by about 50 K (ΔE_d = 14 kJ/mol) for 2.0–0.4 ML Mo, confirming the cluster size effects. It is concluded that the smaller clusters were more reactive than larger clusters for molecular adsorption of

thiophene. As depicted in Figure 34A, the stoichiometry of the clusters changed from x = 0.10 (for $\chi_{thiophene}$ = 0.1 L) to x = 0.14 (for $\chi_{thiophene}$ = 20 L).

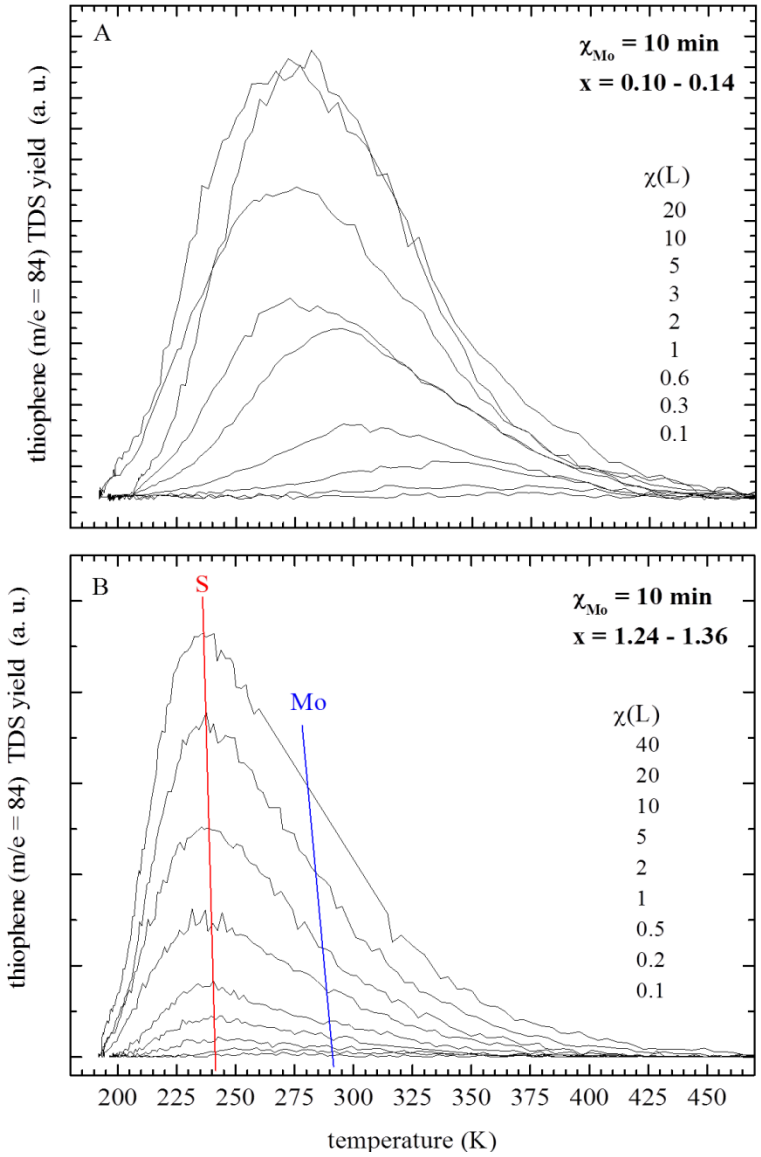

Figure 34. Thiophene TDS as a function of exposure (χ) in Langmuirs (L) on (A) the cleanest[61] and (B) strongly sulfided silica-supported Mo clusters.[61] The label "x" shown in the figure denotes the stoichiometry (x in MoS_x) of the sample, as determined by AES. Refer to Figure 32 for peak labeling.

Binding energies for molecular thiophene on Mo single crystals (16–22 kcal/mol)[144] are smaller than those obtained for Mo clusters (90–76 kJ/mol). This could be due to the large

number of defect sites present on the Mo clusters. The binding energy increases with an increase in the number of defect sites. As per DFT calculations, the binding energies of thiophene on Mo_8C_{12} are below 57 kJ/mol.[138] So it is concluded that MoC_x does not have a dominant effect in the kinetics experiments.

3.3.3.2.4. Sulfided Mo clusters

Thiophene TDS on strongly sulfided Mo clusters (x up to 1.36) is depicted in Figure 34B. The clusters were sulfided by dosing larger amounts of thiophene on the surface. Evidently, two peaks appeared in the TDS spectra. The position of the high temperature tail (Figure 34B) was in agreement with the Mo peak (Figure 32A) observed for the cleanest Mo clusters. It is plausible to assign that peak to thiophene adsorption on Mo sites. The low-temperature peak was only observed for sulfided samples (x > 0.2). In addition, the position of the S peak (~ 250 K, 66 kJ/mol) was independent of the Mo exposure within ± 10 K; whereas, the peak position of Mo depended on χ_{Mo} (cf. Figures 34 and 35).

The TDS peak assignment was supported by the experimental results summarized in Figure 35. The sample was annealed in oxygen after each TDS run and the data are depicted in Figure 35A. χ_{oxygen} denoted the oxygen annealing time. Thiophene exposure ($\chi_{thiophene}$ = 2 L), as well as the Mo coverage (χ_{Mo} = 2 min), was kept constant. A sulfided sample was used for the first experiment where χ_{oxygen} = 0. Therefore, both Mo and S peaks were initially present. When the sample was annealed in oxygen, the Mo peak almost entirely disappeared. The intensity of the S peak dropped by 50% for χ_{oxygen} = 30 min, and its position also shifted to lower temperatures. Sulfur burned off while annealing the sample in oxygen. Therefore, the intensity of S peak (mostly related to the sulfur-covered support) decreased. However, the Mo clusters were oxidized due to oxygen annealing. Mo oxide formation was previously reported in the

literature.[158] Therefore, the decrease in the intensity of Mo peak was attributed to the formation of MoO_x. The Mo peak also decreased at a greater rate than the S peak. This was attributed to the difference in the coverages of S (entire support) and Mo (~ 0.4 ML). No TDS peak related to the adsorption of thiophene on MoO_x appeared in the TDS curves. This was expected because

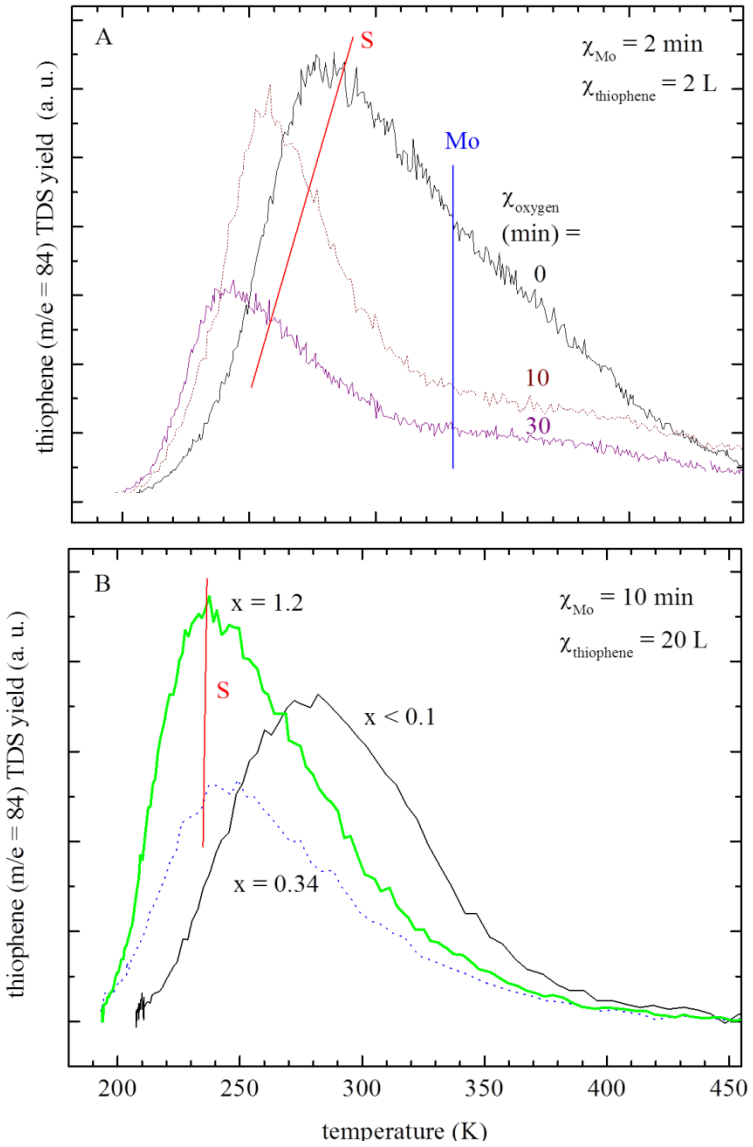

Figure 35. Thiophene TDS on oxygen and H_2/H annealed silica-supported MoS_x clusters. TDS of thiophene on a used catalyst annealed in (A) oxygen (at 600 K in $1x10^{-5}$ mbar for different times as indicated)[61] and (B) H_2/H (at 500 K in $1x10^{-7}$ mbar for a total of 2 hours).[61] Refer to Figure 32 for peak labeling.

oxides are usually less reactive toward thiophene adsorption than metals. It is also important to note that thiophene started to condense at 150 K and no additional peaks were observed up to 500 K.

The shift in the S peak with increasing oxygen exposure was attributed to the overlapping of S and Mo TDS peaks. The intensity of S peak increased while annealing the sample in H_2/H generated by an atomic hydrogen doser (Figure 35B). In addition, the AES measurements indicated an increase in the stoichiometry (x in MoS_x) of the sample due to H_2/H annealing. It is important to note the intensity of C AES peak remained relatively unchanged when compared to S AES peak. Therefore, the S peak was assigned to thiophene adsorption on sulfur sites.

3.3.3.3. Kinetics of catalyst poisoning and activation

The term "poisoning" in surface science studies typically refers to the blocking of adsorption (or active) sites on a surface. From a fundamental perspective, a better characterization and understanding of poisoning effects on a catalyst is pertinent to many applications. Results of a systematic kinetics study are depicted in Figures 36 and 37.

3.3.3.3.1. Poisoning/site blocking by sulfur

The changes in the stoichiometry (x) of the sample with thiophene exposure ($\chi_{thiophene}$) (lower scale) are depicted in Figure 36 A. It is important to note that the thiophene exposures used in subsequent TDS runs were added to get total $\chi_{thiophene}$. The data for small (open circles) and large (solid squares) Mo clusters are included. Evidently, x increased more slowly with $\chi_{thiophene}$ for large Mo clusters. Small and large Mo clusters were able to decompose thiophene. The yield of the gaseous reaction products as a function of the amount of deposited sulfur (x) is depicted in Figure 36B.

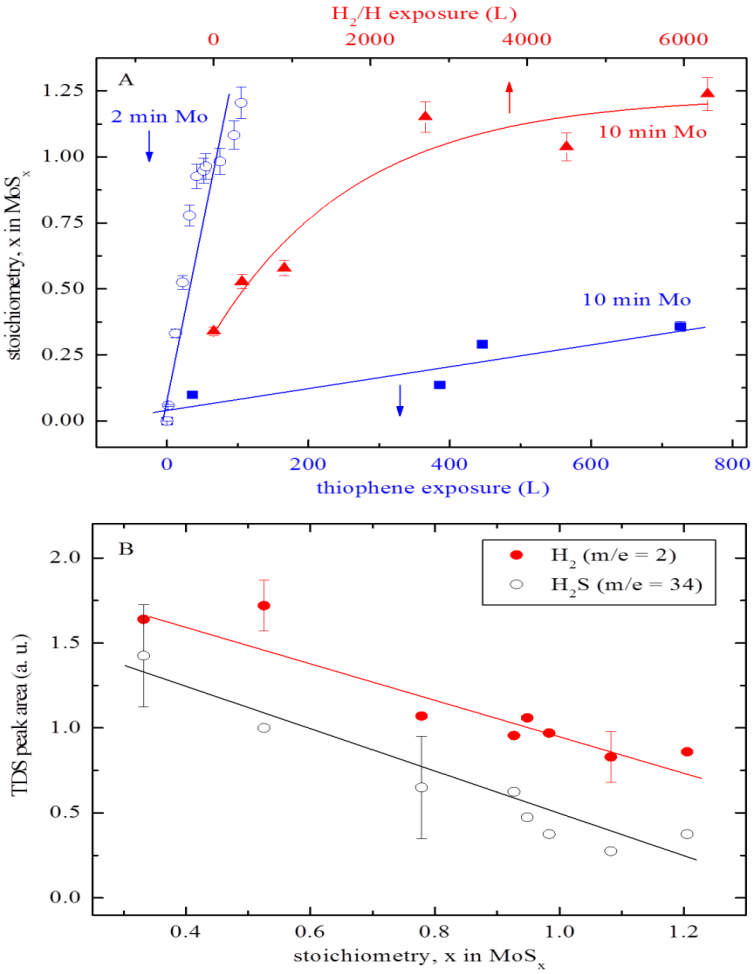

Figure 36. Catalyst poisoning and the effect of H_2/H annealing in the case of silica-supported Mo clusters. (A) uptake of sulfur (x) as a function of thiophene exposure for small (open circles) and large (solid squares) Mo exposures.[61] Exposures of thiophene (lower scale) and H_2/H (upper scale) are indicated. Adsorption/annealing temperature is 500 K. (B) catalyst poisoning as a function of sulfur uptake. The formation of H_2 and H_2S was monitored.[61]

As shown in figure 36B, the TDS peak areas of H_2 and H_2S obtained in subsequent multi-mass TDS experiments are displayed as a function of the MoS_x stoichiometry. It is evident from this figure that the yield of gaseous reaction products decreased with increasing x. Therefore, it is concluded that the strongly sulfided cluster catalyst is much less reactive than the metallic Mo cluster catalyst at UHV conditions.

3.3.3.3.2. Hydrogen annealing

Molecular hydrogen was inefficient to clean off sulfur at UHV conditions. When atomic hydrogen was used to clean off sulfur, it unexpectedly increased the amount of sulfur (x) significantly. A typical example is shown in Figure 36A (see upper scale, solid triangles). A partially sulfided sample was annealed in H_2/H, and the AES data was later collected. As evident from Figure 36A, the amount of sulfur (x) increased with H_2/H annealing time. A mechanism such as $H + S \rightarrow H_2S$ and $H_2S + Mo \rightarrow MoS_x$ could possibly explain the increase in the amount of sulfur.

3.3.3.3.3. Oxygen annealing

Some prior studies on Mo single crystals reported that oxygen annealing was efficient to clean off sulfur at UHV conditions.[143] The effect of oxygen annealing is illustrated in Figure 37. The amount of sulfur (x in MoS_x) increased with an increase in the total thiophene exposure (Figure 37A, solid squares, lower scale). When the sulfided sample was annealed in oxygen, it decreased the amount of x to a value that is similar to the one obtained for the fresh sample (Figure 37A, open circles, upper scale).

The carbon contamination that was produced by thiophene decomposition was also efficiently removed by oxygen annealing, as depicted in Figure 37B. A change in the O AES peak intensity with oxygen annealing time was not observed. This is because the total amount of Mo deposited was small (χ_{Mo} = 2 min) and the presence of oxygen in silica. However, the oxygen annealing of samples not only removed the S and C contaminants, but also oxidized the clusters as evident from Figure 35A. The formation of oxides was not observed in previous studies on Mo single crystals. However, nano-sized metal clusters are often very reactive toward oxide formation.[159]

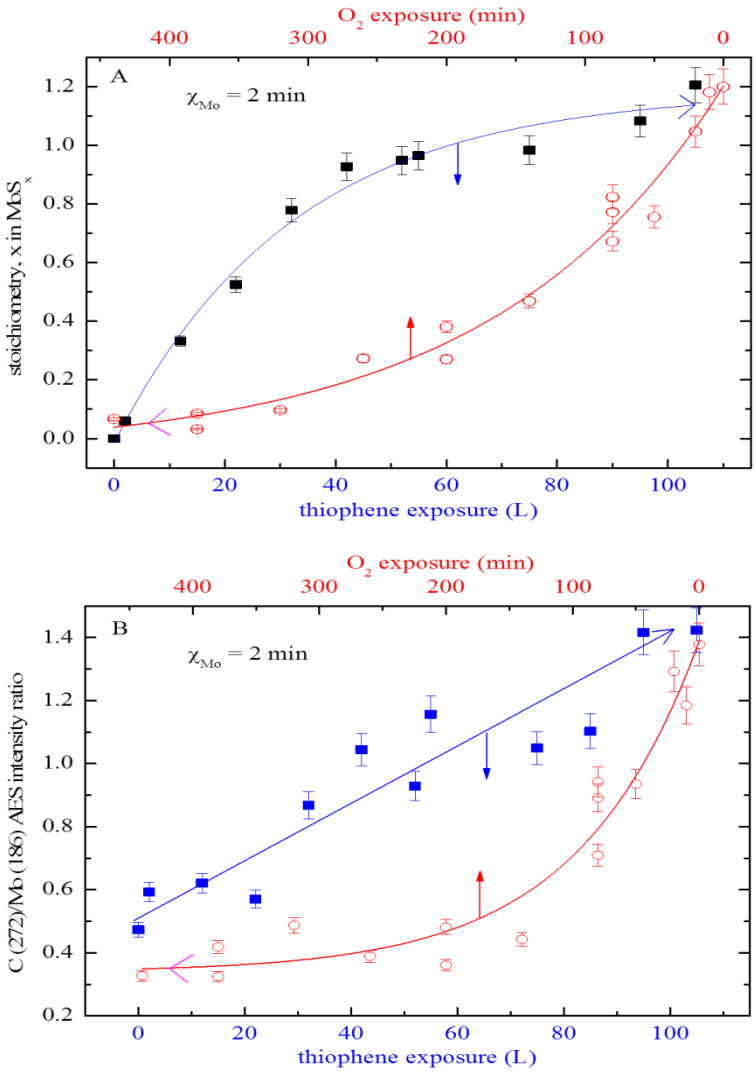

Figure 37. Catalyst poisoning and the effect of oxygen annealing in the case of silica-supported MoS_x clusters. (A) solid squares: change of x with $\chi_{thiophene}$ (lower scale). Open circles: change of x with oxygen annealing/exposure (upper scale).[61] (B) solid squares: change of C-to-Mo AES peak intensity ratio with $\chi_{thiophene}$ (lower scale). Open circles: change of C-to-Mo AES peak intensity ratio with oxygen annealing/exposure (upper scale).[61]

3.3.3.4. Thiophene adsorption dynamics

The adsorption dynamics of thiophene was studied by measuring the adsorption transients. A typical example is depicted in Figure 38. This figure depicts the pressure of thiophene (m/e = 84) in the vacuum chamber, P, as a function of thiophene exposure time, t.

Thiophene (1×10^{-8} mbar) dose started at t = 0 s and it was dosed by quickly (< 0.2 s) opening a leak valve. At low temperatures (T_s = 200 K), P increased slowly until a saturation level was reached. The area above the transient and below the saturation level is equal to the amount of molecularly adsorbed thiophene. At high surface temperatures (T_s = 380 K), a step like structure, indicating negligible thiophene adsorption was observed. Such transients were used to determine the initial adsorption probability, S_0, which is a measure of the reactivity of Mo clusters toward thiophene adsorption/decomposition in the limit of small thiophene coverage.

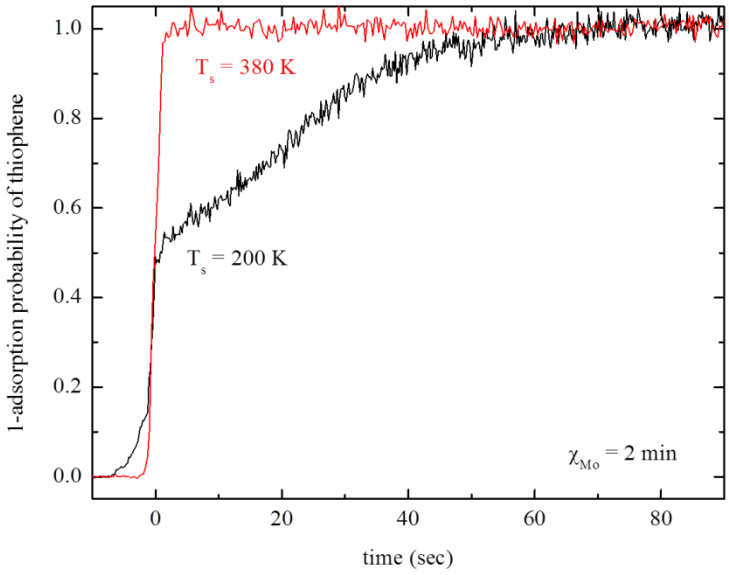

Figure 38. Thiophene adsorption transients on silica-supported Mo clusters (χ_{Mo} = 2 min).[61] Adsorption transients at two different sample temperatures, T_s are shown. The pressure of thiophene is $1x10^{-8}$ mbar.

Initial adsorption probability (S_0) of thiophene, as a function of Mo deposition time (χ_{Mo}), for a constant sample temperature (T_s) is depicted in Figure 39. A cluster size effect was evident. S_0 increased with χ_{Mo}, as expected, and was consistent with the capture zone model.[154, 160-161] S_0, as a function of T_s for small and large Mo exposures, is depicted in Figure 40A. Evidently, S_0 was independent of T_s for low temperatures (section I), indicating molecular and nonactivated adsorption of thiophene. The value of S_0 started to decrease with the initiation of bond activation

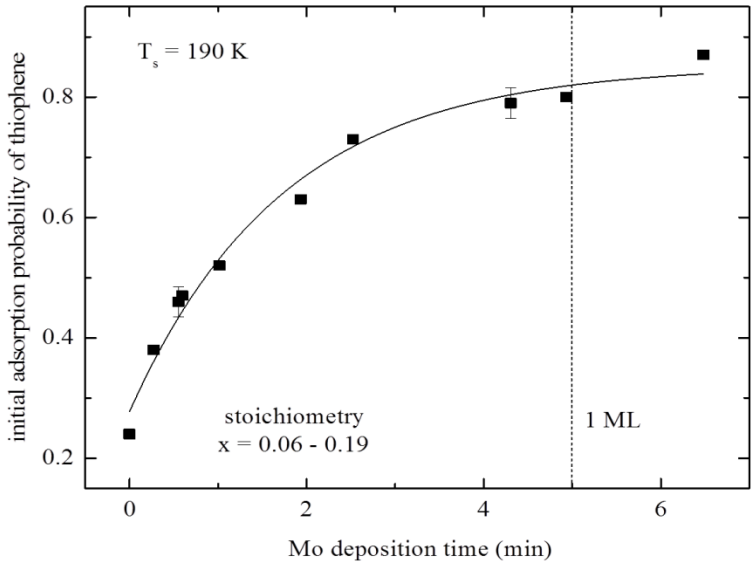

Figure 39. Initial adsorption probability of molecular thiophene as a function of Mo deposition time in the case of silica-supported Mo clusters.[61]

of thiophene on Mo clusters. In this temperature range (section II), S_0 is an apparent adsorption probability (i.e., a kinetic parameter). S_0 started to decrease above 240 K. This temperature was almost in agreement with the onset of H_2 and H_2S desorption (Figure 33A). Although the exact mechanism for thiophene decomposition on Mo clusters was not known, the C-S bond scission was assumed to be the first step by considering prior studies on single crystals.[162] Based on a methodology developed for analyzing the decomposition kinetics of alkanes,[163-165] the rate, r, of C-S bond fission was given by

$$r = F\xi\, k_{C\text{-}S}/(k_{C\text{-}S} + k_d) \qquad (26)$$

where F is the thiophene flux, and ξ (= 0.43 = S_0 for Ts < 240 K) is the probability for molecular adsorption. The initial decomposition probability was simply r normalized by the flux. Arrhenius form of the reaction rate coefficients for the C-S bond cleavage, $k_{C\text{-}S}$, and the thermal desorption of thiophene, k_d, were considered, and the apparent bond activation energy, $E_{app} = E_d - E_{C\text{-}S}$, was calculated from an Arrhenius type plot of S_0 vs. T_s (Figure 40B). E_d and $E_{C\text{-}S}$ are the activation

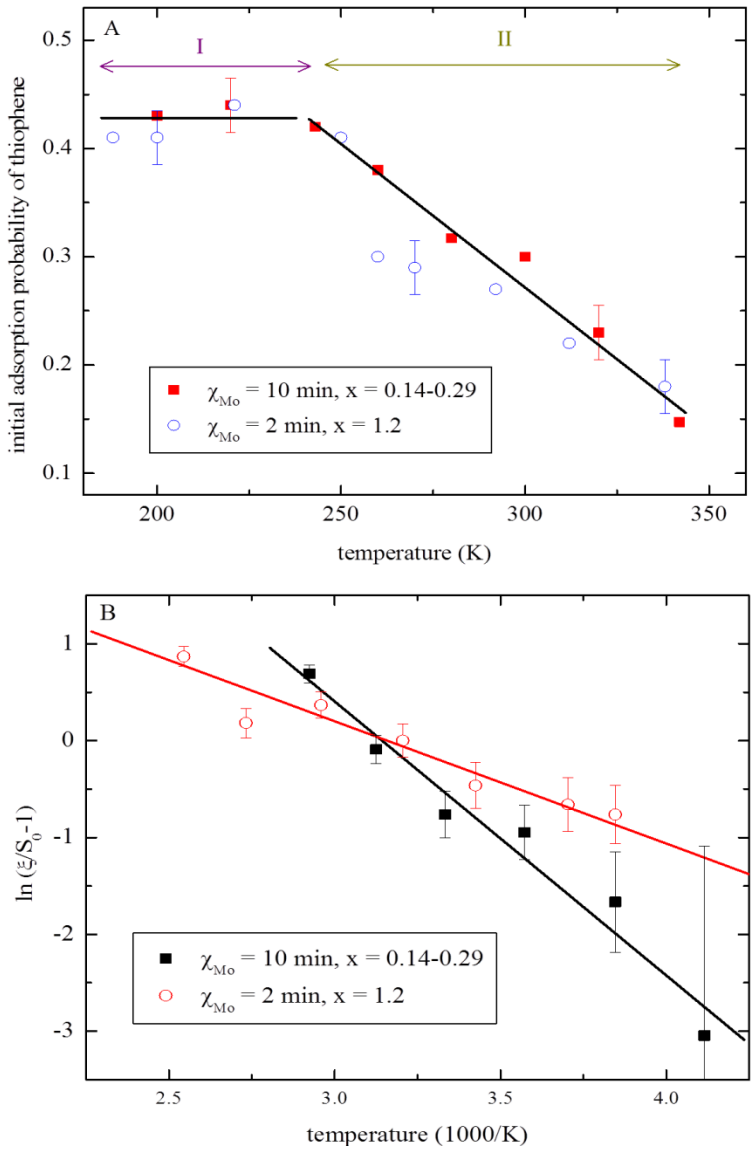

Figure 40. Thiophene reaction pathways on silica-supported Mo clusters and kinetic analysis. (A) Initial reactivity of thiophene adsorption/decomposition as a function of reaction temperature. Temperature ranges indicating molecular adsorption (Section I) and decomposition (section II) of thiophene are shown.[61] (B) Kinetic analysis of the data to measure the activation energy for the first elementary step in thiophene bond activation.[61]

energies for thermal desorption of thiophene and C-S bond activation, respectively. The slope of the Arrhenius plot equals negative E_{app}/R (R is the universal gas constant). Accordingly, apparent

activation energies, E_{app}, amounted to (11 ± 1) and (24 ± 3) kJ/mol for small (0.4 ML Mo) and large (2 ML Mo) clusters, respectively. E_d was determined from the TDS data on clean Mo clusters. Thus, the true activation energies, E_{C-S}, amounted to (79 ± 2) and (54 ± 4) kJ/mol for small and large Mo clusters, respectively. The experimental value was quite close to the energy barrier (46 kJ/mol) computed for C-S bond cleavage on Mo(100) by DFT.[152] Small clusters were more reactive for molecular thiophene adsorption than large clusters; whereas, the opposite held true for the bond activation. A similar trend was observed in a previous study.[145] Accordingly, the crystal structure of Mo clusters was more important than the small size of the clusters for thiophene decomposition. The molecular adsorption of thiophene may be favored on defect sites (kinks, steps). However, the relative number of these defects decrease with an increase in cluster size. Therefore, a decrease in E_d with increasing Mo exposure (cluster size) appears plausible.

3.3.4. Summary

The catalytic activity of silica-supported Mo clusters towards thiophene adsorption/bond activation was characterized by collecting TDS, AES, and adsorption transients. Two reaction pathways were evident: molecular adsorption and decomposition. Thiophene adsorbed molecularly at low adsorption temperatures but decomposed into H_2, H_2S, and small organic compounds (primarily alkynes) above 220 K. By assuming a pre-exponential of 1×10^{13}/s, the binding energies (E_d) for molecular adsorption of thiophene were calculated to be in the range of 90–76 kJ/mol, depending on Mo coverage and adsorption site. Thiophene bond activation energies were determined by collecting adsorption transients. The activation energies measured for the first bond scission (C-S) were in the range of 79–54 kJ/mol, depending on Mo cluster size, and were reasonably consistent with the theoretical values.[152] Thiophene bond activation led to the sulfidation of the Mo clusters (MoS_x), as well as carbon contamination. The S and C

contaminations poisoned the catalyst. The sulfided catalyst was found to be less reactive toward thiophene decomposition than the pristine system. The stoichiometry (x) of the sulfided clusters was controlled to some extent by changing the exposure of thiophene. H_2/H annealing of the sulfided sample significantly increased the amount of sulfur. In spite of efficiently removing the S and C contaminations, the oxygen annealing process led to the formation of Mo oxides, which further poisoned the catalyst. Mo clusters were highly reactive toward thiophene bond activation leading to S and C contamination, which made it difficult to characterize the intrinsic properties of clean (metallic) Mo clusters. The cleanest Mo clusters obtained had a stoichiometry of $x < 0.1$. The molecular adsorption/desorption pathway of thiophene resulted in two TDS peaks (Mo and S). The Mo peak was assigned to thiophene adsorption on metallic clusters; whereas, the S peak was assigned to thiophene adsorption on sulfided Mo clusters/sulfur covered support. Thiophene adsorbed more strongly on Mo sites than on S sites. The position of S TDS peak was approximately independent of the Mo coverage; whereas, the Mo TDS peak was shifted. Finally, the small (2D) Mo clusters were more reactive for molecular thiophene adsorption than the large (3D) clusters. The apparent activation energies decreased with an increase in cluster size; whereas, the true activation energy was smallest for the large clusters. The initial adsorption probability for molecular thiophene increased with Mo cluster size and was consistent with the capture zone model.

3.4. Characterization of Co Coated WS_2 Nanotubes for Hydrodesulfurization Catalysis

An introduction to hydrodesulfurization (HDS) process and industrial HDS catalysts is presented first, followed by the fabrication and characterization of Co coated WS_2 nanotubes (Co/INT-WS_2). A combined results and discussion section is presented next. A summary of experimental results obtained in this study is given at the end.

3.4.1. Introduction

Hydrodesulfurization (HDS) is a widely used industrial catalytic process for the removal of sulfur from organosulfur compounds present in crude oil feedstocks. These sulfur-containing compounds mainly consist of thiophenes, benzothiophenes, dibenzothiophenes, and their substituted derivatives, together with sulfides and thiols and several other complex molecules. Transition metal sulfide (TMS) catalysts[166-167] together with promoters such as Co and Ni are conventionally used as HDS catalysts. Co and Ni exhibit a strong promotion effect on HDS catalysis, when compared to the other first row (3d) transition metals.[168-169]

Nanoparticles of TMS with layered structure are known to form inorganic fullerene-like (IF) particles and inorganic nanotubes (INT). In the case of IF- MoS_2, the atoms within a layer are covalently bonded (S–Mo–S); whereas, the stacked layers are held together by weak van der Waals forces.[170-171] Among these novel nanomaterials, in view of their special structural properties and high surface area, IF-MoS_2, INT-WS_2, and polyhedral nanostructures were proposed as promising catalytic materials for the HDS process. MoS_2 nanotubes decorated with Ni nanoparticles were recently reported to be very effective for HDS of thiophene and thiophene derivatives at relatively low temperatures.[172]

As reported in the previous projects, thiophene adsorption kinetics (TDS) experiments on IF-MoS_2 NP[57] and INT-WS_2[58] revealed only low catalytic reactivity at UHV conditions. Therefore, in order to promote the catalytic activity of INT-WS_2 towards thiophene HDS, they were coated with Co nanoparticles using the electroless deposition process.[59] Cobalt NP were coated on INT-WS_2 by a surface activation process, followed by electroless plating. The catalytic activities of both the pristine and Co coated INT-WS_2 (Co/INT-WS_2) were characterized by UHV and atmospheric pressure kinetics experiments.

3.4.2. Sample fabrication and characterization

The fabrication of silica-supported Co/INT-WS_2 is described first, followed by the characterization of Co/INT-WS_2.

3.4.2.1. Sample fabrication

Co/INT-WS_2 synthesis was described elsewhere.[59] Co/INT-WS_2 suspension was prepared by suspending one micro spatula tip of Co/INT-WS_2 powder in benzene (2 mL), followed by mild sonication at room temperature with a bench top sonicator. A few 50 mL aliquots were dropped-and-dried on a silica support (SiO_2 with 1 mm thermal oxide layer from University Wafer, MA, USA).

3.4.2.2. Co/INT-WS_2 characterization

The morphology and topography of the synthesized Co/INT-WS_2 were analyzed by scanning electron microscopy (SEM) (LEO model Supra 7426). Transmission electron microscopy (TEM) (Philips CM-120) in conjunction with energy dispersive spectroscopy (EDS) (EDAX Phoenix Microanalyzer) were employed to determine the atomic-scale structure and chemical composition. Other instrumental details included: a high resolution transmission electron microscope (HRTEM) with a field emission gun (FEI Technai F-30) equipped with a parallel electron energy loss spectroscopy (EELS) detector (Gatan imaging filter, GIF; Gatan), TEM and scanning transmission electron microscope (STEM) equipped with high angle annular dark field (HAADF) detector (FEI Tecnai G2 F20). Phase analysis was performed by x-ray powder diffractometry (XRD) (Ultima III, Rigaku, Japan).

3.4.3. Results and discussion

The characterization of Co/INT-WS_2 morphology is presented first, followed by the ambient pressure kinetic experiments, i.e., thiophene hydrodesulfurization experiments. A

method to calculate the turnover frequency from the flow rates of reactants are explained next, followed by the adsorption and reaction kinetics of thiophene on Co/INT-WS_2 at UHV conditions. A summary of experimental results obtained in this study is given at the end.

3.4.3.1. Characterization of the sample's composition and morphology

Multiwall INT-WS_2 were coated with cobalt NP by electroless plating method. SEM image of the Co/INT-WS_2 is depicted in Figure 41A. As evident from Figure 41B, the surface of the nanotube was not entirely/uniformly covered by the cobalt NP. The incomplete coverage was attributed to the formation of nonhomogeneously distributed catalytic sites on the surface of nanotubes during the surface activation process. Subsequent nucleation of Co nanoparticles on these catalytic sites produced a non-uniform layer of Co nanoparticles on INT-WS_2 surface.

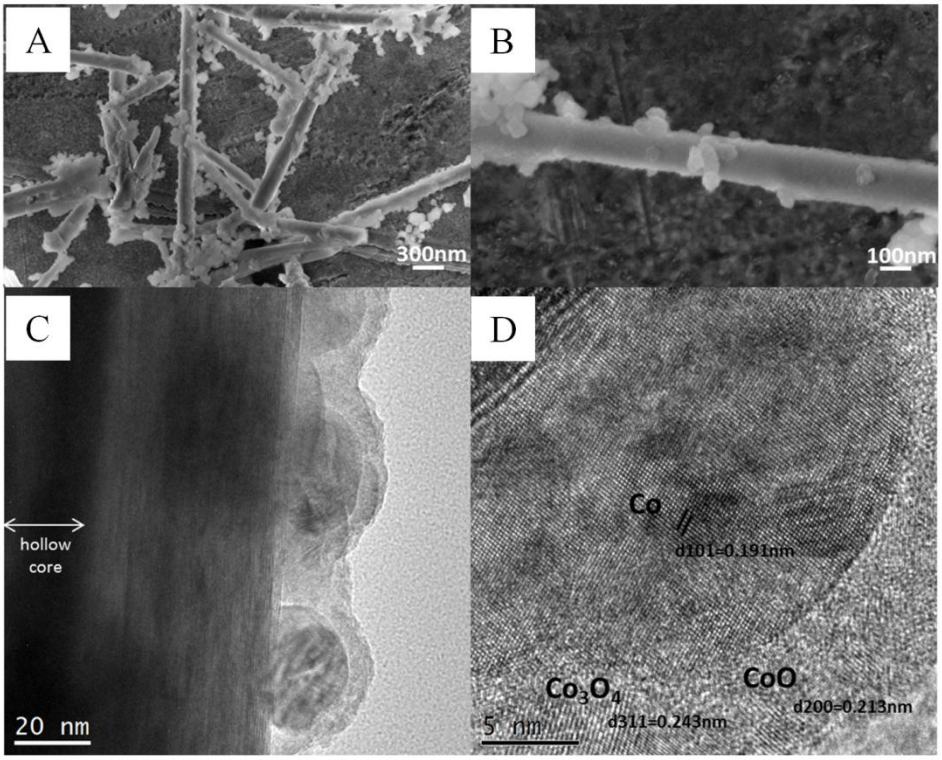

Figure 41. SEM and HRTEM images of Co/INT-WS_2. SEM images of (A) Co/INT- WS_2 and (B) close-up view of a single coated nanotube. HRTEM micrographs of (C) cobalt nanoparticles covering the nanotube and (D) a close-up of the image showing lattice spacings of Co, CoO, and Co_3O_4. Ref.[59]

Despite the rinsing process, non-attached agglomerates of cobalt nanoparticles were present in the final product. The crystalline structure of the cobalt NP was analyzed by HRTEM (Figures 41 C and D). The size of the Co nanoparticles was in the range of 10-20 nm. As evident from Figure 41C, cobalt NP were covered by a partially amorphous thin layer of cobalt oxide. As shown in Figure 41D, the cobalt NP exhibited hcp crystal structure with d-spacing of 0.191 nm corresponding to the (1 0 1) main peak of the hcp cobalt structure. The partially amorphous layer present on the cobalt NP consisted of two different sets of fringes: CoO d(2 0 0) = 0.213 nm and Co_3O_4 d(3 1 1) = 0.243 nm.

Elemental mapping of the surface of the Co/INT-WS_2 was performed by energy filtered TEM (EFTEM). As evident from Figure 42, an oxidation layer of few nm thickness covered the metallic cobalt particles. Cobalt oxide film was probably formed due to the open-air conditions during the reaction and the final drying (100 ^{o}C).

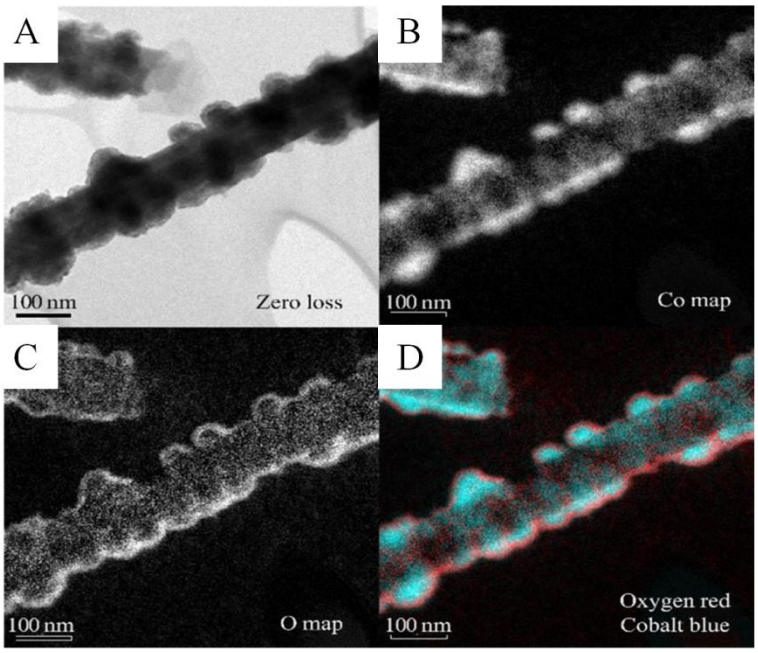

Figure 42. EFTEM elemental mapping of INT-WS_2. (A) image of a zero loss signal of single nanotube, (B) Co map, (C) O map, and (D) combined elemental map of Co and O. Ref.[59]

EDS analysis of Co/INT-WS_2 was carried out by STEM (Figure 43). STEM images of Co/INT-WS_2 are shown in Figure 43A, and the corresponding EDS line scan analysis is shown in Figure 43B. The red line and the cross indicated the location and the direction of the EDS line scan. As evident from Figure 43B, the cobalt peak rised at the edges of the nanotube and decreased at the center of the nanotube, confirming the nonuniform distribution of cobalt. The oxygen peak intensity almost remained constant while scanning across the coated nanotube. The HRTEM result was in good agreement with the XRD analysis.

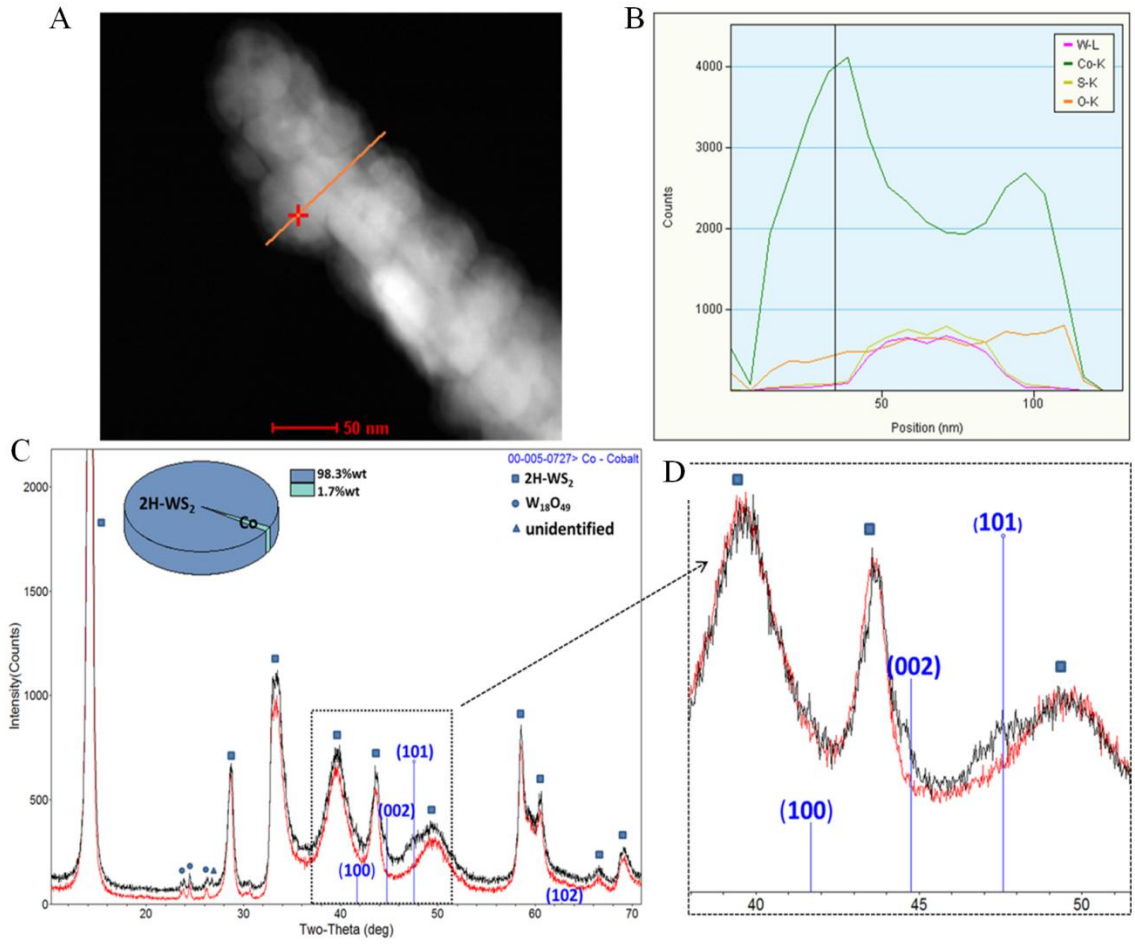

Figure 43. STEM/EDS analysis of Co/INT-WS_2 and XRD patterns of CO/INT-WS_2 and WS_2. STEM/EDS analysis of (A) Co/INT-WS_2 with the red line and cross indicating the location and direction of EDS analysis, (B) line scan analysis on the line, (C) XRD patterns of Co/INT-WS_2 (black) compared with that of WS_2 powder (red), (D) magnified Co diffraction peaks. Ref.[59]

The diffraction patterns of pristine INT-WS2 (bottom curve) and Co/INT-WS_2 (top curve) are depicted in Figure 43C. Co/INT-WS_2 consisted of WS_2 (2H phase) and cobalt. Figure 43D shows a clear distinction between the two curves. The coated Co nanoparticles had hcp crystal structure probably due to the low deposition temperatures (70 ^{o}C), which favored predominantly the hcp phase.

Cobalt oxide did not give rise to any XRD peaks due to its amorphous nature. The weight percentage of Co (1.7 %) calculated from the diffractogram (inset of Figure 43C) included both the deposited Co nanoparticles and the residual Co agglomerates. Therefore, the weight percentage of coated cobalt particles would be less than 1.7%. Residual $W_{18}O_{49}$ remaining from the synthesis was also detected.[104, 173] It is important to note that the BET specific area increased from 7.78 to 10.08 m^2g^{-1} after cobalt deposition, which would probably enhance the catalytic properties of Co/INT-WS_2. The relatively low BET areas were attributed to the inherent tendency of nanotubes to agglomerate and to the high atomic mass of WS_2.

3.4.3.2. Ambient pressure experiments

The catalytic activity of Co/INT-WS_2 toward thiophene desulfurization was characterized using an atmospheric pressure flow reactor. The experimental procedure for the ambient pressure catalytic experiments is detailed in the experimental section of this dissertation.

A typical survey spectra of GC transients for Co/INT-WS_2 is depicted in Figure 44A. The reactant gas mixture in HDS gave rise to the observed H_2 and thiophene peaks. H_2S and hydrocarbons were formed as the reaction products. The observed reaction products were consistent with the proposed HDS mechanism[174] for thiophene, as shown in Figure 45. Accordingly, HDS of thiophene occurred via two parallel pathways: hydrogenolysis and hydrogenation. The hydrogenolysis pathway involved the direct removal of sulfur atom from

thiophene. The hydrogenation pathway involved the removal of sulfur atom from thiophene by the hydrogenation of the aromatic ring. It was proposed that these two reactions occurred simultaneously using different active sites of the catalyst surface.

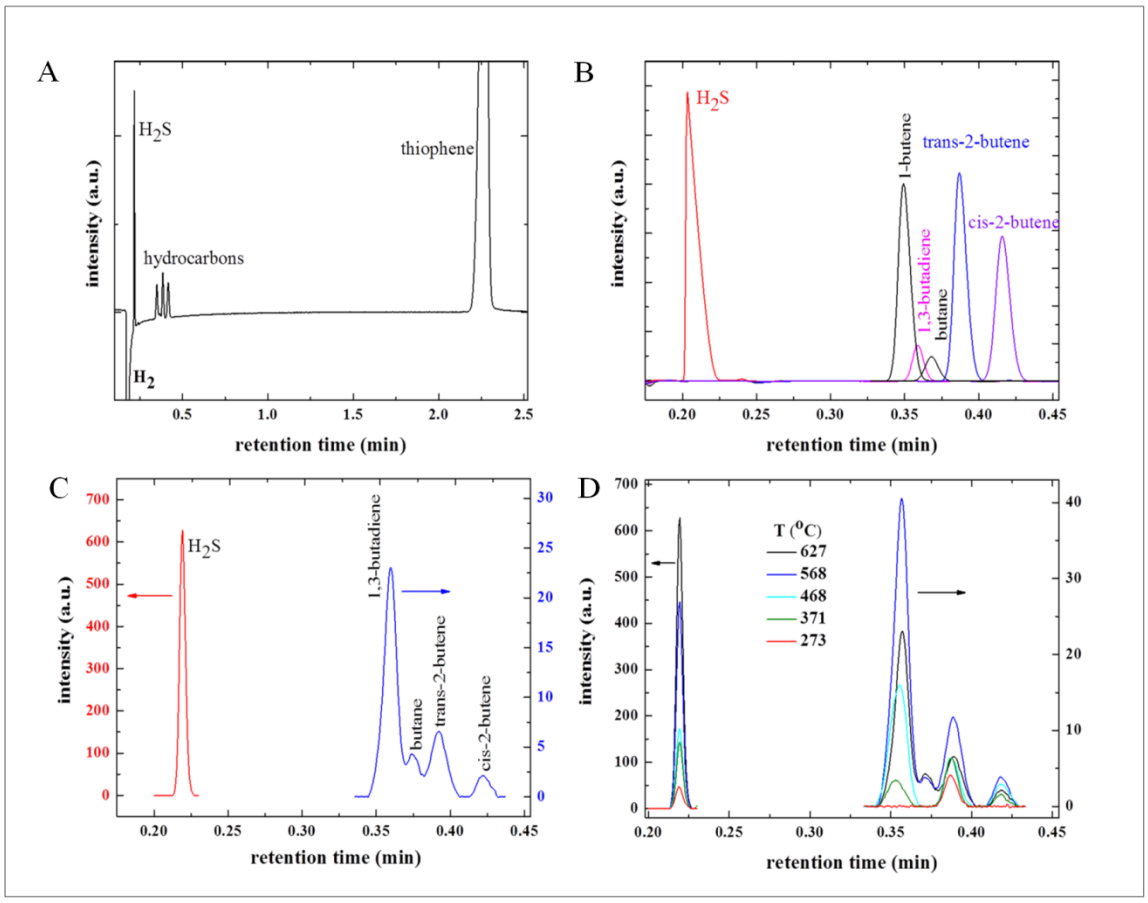

Figure 44. GC transients of Co/INT-WS_2 and reference compounds. (A) GC survey scan for Co/INT-WS_2, (B) GC transients of reference compounds, as indicated, (C) GC transients of Co/INT-WS_2, (D) H_2S and hydrocarbon regions of GC scans as a function of retention time at different reaction temperatures. Ref.[59]

In order to correctly identify the reaction products, GC transients of a number of reference compounds were collected. Reference compounds included H_2S, 1-butene, 1,3-butadiene, butane, trans-2-butene, and cis-2-butene and the corresponding data are depicted in Figure 44B. Figure 44C depicts a typical GC transient of the Co/INT-WS_2 sample showing only the HDS reaction products. Four GC peaks corresponding to the hydrocarbons,

1,3-butadiene, butane, trans-2-butene, and cis-2-butene appeared in the reaction products. Evidently, 1,3-butadiene was the predominant product; whereas, trans-2-butene and cis-2-butene were minor products. A trace amount of butane was also formed. It is therefore clear that sulfur-free reaction products were formed during the HDS reaction.

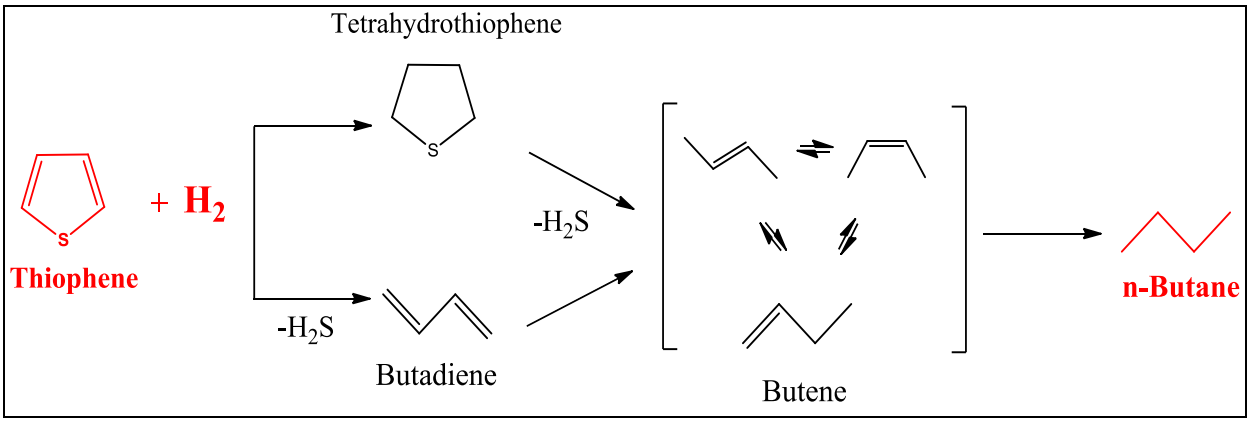

Figure 45. HDS mechanism for thiophene on Co/INT-WS_2. Ref.[59]

The GC transients of H_2S and hydrocarbons, as a function of reaction temperature, are depicted in Figure 44D. Evidently, H_2S dominated the product formation. Comparison of the GC peak areas of products (from the transients collected at 627 ^oC) revealed that the H_2S peak area was 7.6 times larger than the total hydrocarbon peak area. The dominance of H_2S in the products was attributed also to the hydrogenation of the less strongly bonded sulfur atoms from the edges of INT-WS_2. It was expected that hydrogen reacted with surface sulfur atoms to form H_2S and created sulfur vacancies at the edges of nanoparticles.[175] However, WS_2 nanotubes are very stable in the presence of hydrogen and their decomposition was not expected at the reaction temperatures used.[176] In spite of being catalytically active, these sites are not preferable for thiophene adsorption. The decrease in the formation of hydrocarbons was attributed to the depression in hydrogenolysis activity caused by the presence of H_2S.[177] Furthermore, the peak intensities of products increased with an increase in reaction temperature (Figure 44D).

The turnover frequency of the catalyst for thiophene conversion was calculated according to the procedure detailed by Sajkowski et al.[178] Figure 46 depicts an analysis of the GC traces obtained at different reaction temperatures. The conversion rate, r, of thiophene as a function of reaction temperature is depicted in this figure. The HDS conversion rates were calculated following the procedure outlined by Leliveld et al.[179] Accordingly, the conversion rate, r, is given by

$$r = \frac{\text{Sum of the peak areas of products}}{(\text{Sum of the peak areas of products} + \text{Peak area of thiophene})} \times 100 \qquad (27)$$

using the background corrected GC peak areas. H_2S was also included in the products to calculate thiophene conversion rates. Data for the Co coated and pristine INT-WS_2 were summarized. Two sequential experimental runs were conducted to evaluate the catalyst deactivation and the data is depicted.

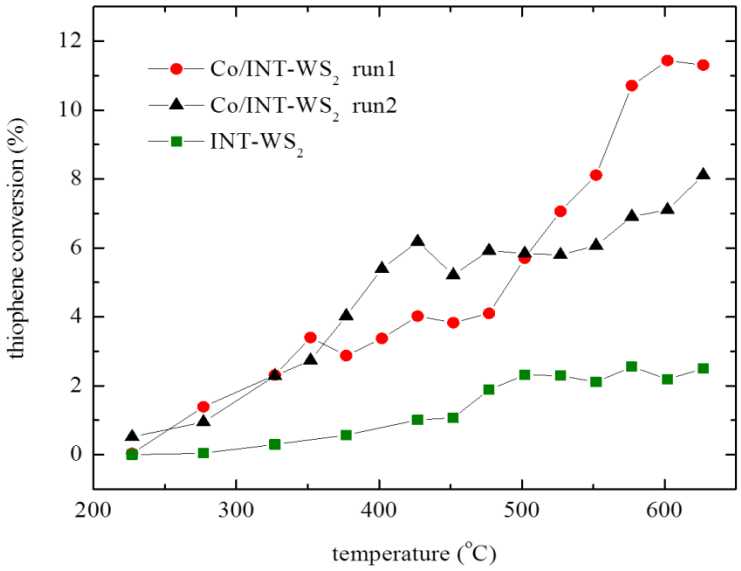

Figure 46. Thiophene conversion rates of Co/INT-WS_2 and INT-WS_2 as a function of temperature. Two sequential runs for Co/INT-WS_2 are shown. Ref.[59]

Thiophene conversion rates increased with the reaction temperature, indicating a thermally activated process. Thiophene conversion rate of 12% was obtained for Co/INT-WS_2 at

627 ^{o}C. Evidently, Co/INT-WS_2 catalyst was more reactive than the pristine INT-WS_2, which exhibited a conversion rate of ~ 2%. This result proved the promotion effect of cobalt in increasing the HDS catalytic activity. The prismatic (h k 0) edges of WS_2(MoS_2) and corners are catalytically more active than the basal (0 0 0 1) plane. Therefore, the low HDS reactivity of INT-WS_2 could be due to its high basal plane to edge area ratio.[180] But the coated cobalt NP increased the thiophene conversion rates by a factor of ~ 6. This suggested that the interface between cobalt NP and INT-WS_2 played a role in promoting the catalytic reaction.

A number of models explaining the promotion effect of cobalt were proposed. One model suggested that the promotion effect was due to the formation of catalytically active centers on WS_2 surface by the hydrogen spillover generated by segregated cobalt sulfide (Co_9S_8) phase.[181-182] Another model suggested that the promotion effect took place at ‘‘Co–Mo–S’ (Co–W–S) interaction phase. According to this model, the increased HDS activity was attributed to the low metal–sulfur bond energy that facilitated the formation of a large number of catalytically active sulfur vacancies.[168, 183-184] The "spillover" model does not explain the promotion effect of Co in Co/INT-WS_2, as the formation of cobalt sulfide phase needs very high temperatures and a long time.[167] Moreover, the catalyst consisted of only the metal cobalt NP but not the segregated cobalt sulfide phase. Therefore, the mechanism proposed in the second model was thought to be responsible for the increased HDS catalytic activity of Co/INT-WS_2. The size effect of the cobalt NP on the reactivity and selectivity of the catalyst was not investigated in the present study. Several studies explaining the size effects of the metal nanoparticles on the catalytic activity were available.[185]

As evident from Figure 46, there were small variations of the catalyst activity of Co/INT-WS_2 over time (compare 1st and 2nd run). It is important to note that the catalysts were

preserved under high vacuum conditions after the synthesis. However, several long time tests would be required to quantify the catalyst deactivation.

3.4.3.3. Turnover frequency as a function of thiophene conversion (%)

The turnover frequency (in molecules of thiophene converted per surface Co site per second) was calculated following the procedure detailed by D. J. Sajkowski et al.[178] According to this procedure, the turnover frequency (TOF) can be determined from the flow rate using the following equation:

$$N = (F_R/A_S)\alpha \qquad (28)$$

where N is the number of molecules of thiophene converted per surface Co site per second (TOF); F_R is the flow rate of thiophene in molecules per second; A_S is the number of Co atoms on the surface of the catalyst; and α is the fraction of thiophene converted in the reaction.

The fraction of thiophene converted (α) was obtained from thiophene conversion, e.g., 11.44% thiophene conversion was obtained at 592 ^{o}C. So $\alpha = 11.44/100 = 0.1144$. The number of Co atoms on the surface of the catalyst (A_S) was calculated using the weight percentage of cobalt and the weight of the catalyst. The weight percentage of Co in the catalyst was 1.7% and the weight of the catalyst used was 27.5 mg. Therefore, the total amount of Co present in the catalyst was equal to $(1.7/100)27.5\text{x}10^{-3}$ g = $4.675\text{x}10^{-4}$ g. Accordingly, the number of moles of Co was equal to $(4.675\text{x}10^{-4}/58.93) = 7.933\text{x}10^{-6}$ moles. Finally, $A_S = 7.933\text{x}10^{-6}$ x $6.023\text{x}10^{23}$ = $4.778\text{x}10^{18}$ atoms (where $6.023\text{x}10^{23}$ is the Avogadro number).

The flow rate of thiophene (F_R) was obtained indirectly from the flow rate of hydrogen. F_R was obtained from its partial pressure. The partial pressure of thiophene was calculated using the Antonie equation given below.

$$\log P^{sat} = A - \frac{B}{T+C} \qquad (29)$$

where P^{sat} is the vapor pressure of thiophene in mmHg; and T is the saturator temperature in ^{o}C (30 ^{o}C in the current project). The constants A, B, and C are 7.06944, 1296.79, and 225.437, respectively. The partial pressure of thiophene obtained from the Antonie equation was equal to 98.33 mmHg. Assuming that the hydrogen gas was at atmospheric pressure (760 mmHg), the mole fraction of thiophene was calculated to be equal to 98.33 mmHg/760 mmHg = 0.12938. Accordingly, the number of molecules of thiophene was equal to 0.12938 x 6.023×10^{23} = 7.793×10^{22} molecules. Hydrogen gas was bubbled through thiophene with a flow rate of 20 mL/min. Therefore, $F_R = (20/60) \times 7.793 \times 10^{22} = 2.5976 \times 10^{22}$ molecules/sec.

Finally, the turnover frequency in molecules of thiophene converted per surface Co site per second at 592 ^{o}C was calculated $N = (2.5976 \times 10^{22}/4.778 \times 10^{18}) \times 0.1144 \approx 622$. The turnover frequency of Co/INT-WS_2 as a function of reaction temperature is depicted in Figure 47.

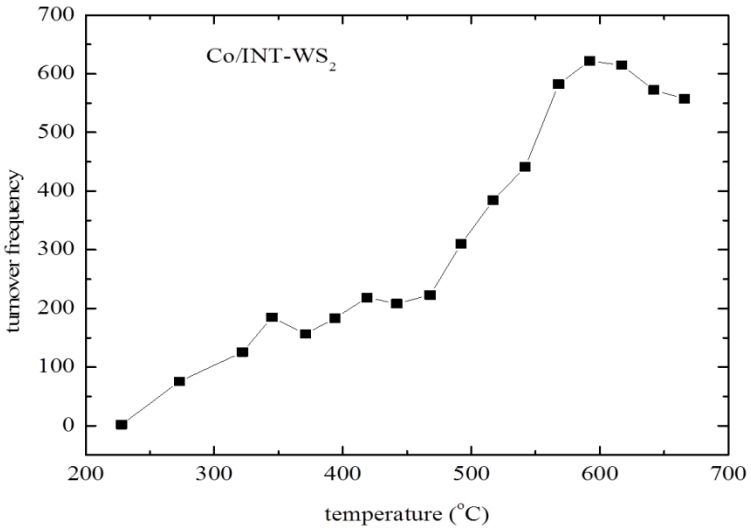

Figure 47. Turnover frequency (in molecules of thiophene converted per surface Co site per second) of Co/INT-WS_2 as a function of reaction temperature. Ref.[59]

Future studies concerning the HDS catalysis of Co/INT-WS_2 would investigate the size effects of Cobalt NP on catalytic activity to elucidate the catalytic mechanism. In addition, the effect of cobalt oxide film on the catalytic activity needs future investigation.

3.4.3.4. Adsorption and reaction kinetics

The adsorption and reaction kinetics of thiophene on Co/INT-WS_2 were studied using ultrahigh vacuum thermal desorption spectroscopy. A heating rate of 2 K/s was used in the TDS experiments. TDS data of thiophene on silica-supported Co/INT-WS_2 is depicted in Figure 48. As evident from the figure, four TDS peaks (labeled A-D) appeared in the TDS data. The lined up low temperature edges of the D peak indicated surface and adsorption site unspecific

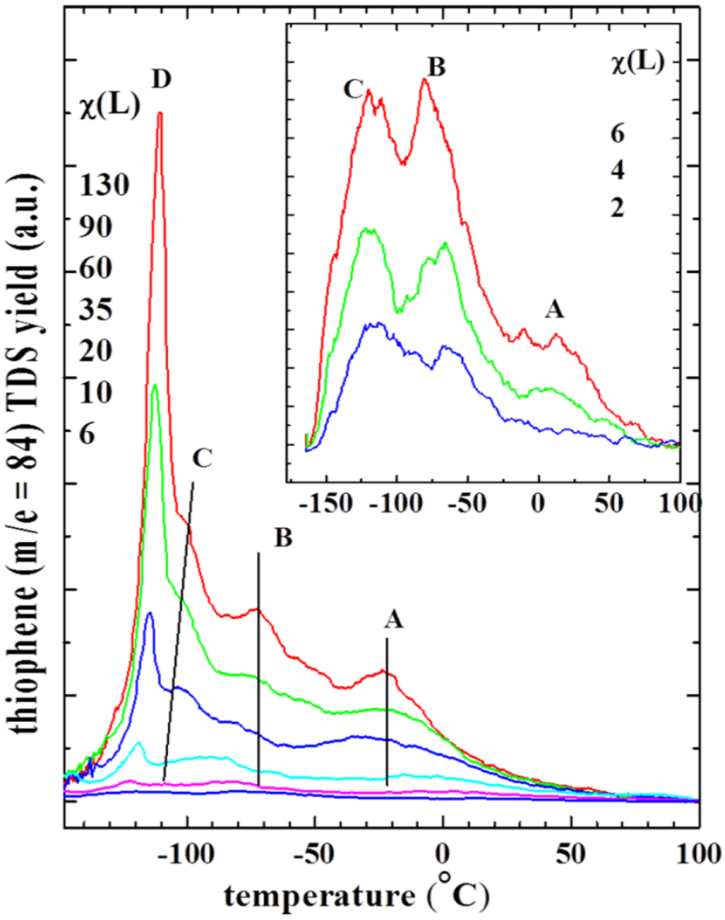

Figure 48. Thiophene TDS as a function of exposure (χ) in Langmuirs (L) on silica-supported Co/INT-WS_2.[59] The TDS peaks A, B, and C correspond to the adsorption of thiophene on internal, external, and groove sites of Co/INT-WS_2 respectively. The inset shows the data for small exposures. D is the condensation peak of thiophene.

condensation of thiophene. The condensation peak appeared only at low temperatures and large exposures and obeyed 0th-order kinetics. The A, B, and C peaks were similar to the characteristic adsorption features observed for the nanotubes. It is important to note that only two peaks, A and D were observed for thiophene TDS on clean silica.[61] In addition, only two TDS peaks were observed for thiophene TDS on IF-WS_2 nanoparticles.[86] TDS spectra were similar to those observed for CNTs[99, 108] and INT-WS_2.[58] Therefore, the A, B, and C TDS peaks were assigned to the adsorption of thiophene on internal, external, and groove sites of the Co/INT-WS_2 bundles. Interstitial sites would be too small to encapsulate thiophene. However, thiophene could be encapsulated in the interior of INT-WS_2 due to its smaller size (0.5 nm), when compared to INTs diameter (~ 5 nm).

By applying Redhead analysis and assuming a standard pre-exponential factor of $1x10^{13}$/s for 1st-order kinetics, the (low exposure/ coverage) binding energies were calculated: 74 kJ/mol (A peak, 11 ^{o}C), 52 kJ/mol (B, - 71 ^{o}C), and 39 kJ/mol (C, - 120 ^{o}C). Very similar TDS data were seen for thiophene TDS on INT-WS_2.[58] Therefore, it was concluded that the 1.7% Co coating did not have a significant effect on the molecular binding energies of thiophene.

The multi-mass TDS experiments for thiophene were also conducted on Co/INT-WS_2. The multi-mass TDS data for Co/INT-WS_2 deviated from the fragmentation pattern of gaseous thiophene, thus indicating a bond activation of thiophene by the catalyst. However, due to the overlapping fragmentation patterns in the mass spectra of possibly formed hydrocarbons, the products could not be identified. It is important to note that multi-mass TDS data obtained for pristine INT-WS_2 matched the fragmentation pattern of gaseous thiophene, thus indicating molecular adsorption of thiophene.[58] Therefore, thiophene adsorbed molecularly on pristine INT-WS_2, but decomposed on Co/INT-WS_2, even under UHV conditions.

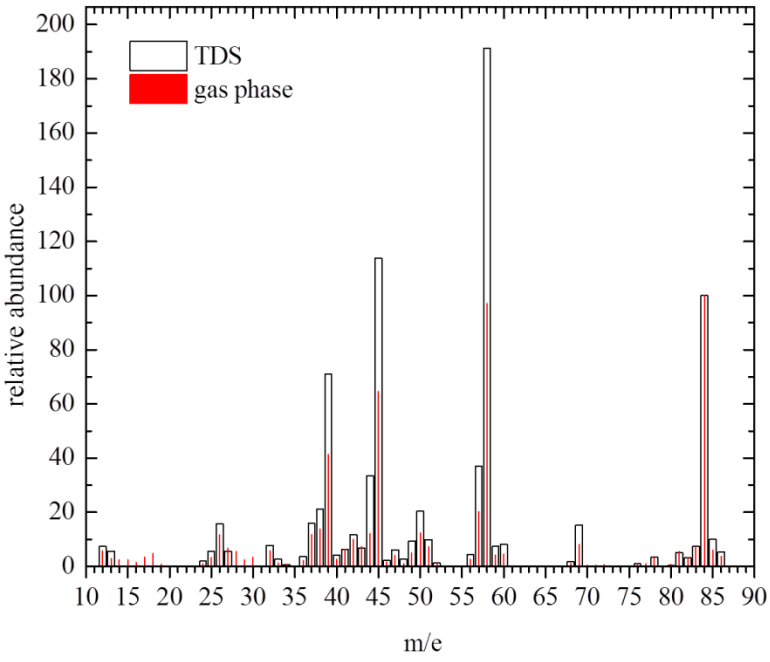

Figure 49. Thiophene multi-mass TDS experiment on Co/INT-WS_2. Comparison of thiophene TDS peak intensities (open bars) on silica-supported Co/INT-WS_2 with the mass spectrometer signals (solid bars). The intensity of the peaks are normalized to m/e 84. Ref.[59] The mismatch between the multi-mass TDS data and the gas phase fragmentation pattern of thiophene indicates thiophene bond activation on Co/INT-WS_2.

3.4.4. Summary

In the current project, Co/INT-WS_2, a novel HDS nanocatalyst was synthesized and its HDS catalytic activity was characterized. INT-WS_2 were coated with cobalt nanoparticles by the electroless plating method. The coated cobalt NP had hcp crystal structure and were covered by a thin cobalt oxide layer. The Co/INT-WS_2 catalyst was six times more reactive toward thiophene HDS than the pristine INT-WS_2, but ~ 4 times less active than commercial catalysts (CoMo from Haldor Topsoe). The adsorption kinetics of thiophene on Co/INT-WS_2 indicated the adsorption of thiophene on internal, external, and groove sites. Higher thiophene conversion rates were thought to be achievable with further optimization of the nanofabrication process.

3.5. Characterization of Ni Coated WS_2 Nanotubes for Hydrodesulfurization Catalysis

An introduction to the use of novel nanomaterials, such as nickel coated WS_2 nanotubes (Ni/INT-WS_2) for hydrodesulfurization (HDS) catalysis is presented first, followed by the fabrication and characterization of Ni/INT-WS_2. A combined results and discussion section is presented next. A summary of experimental results obtained in this study is given at the end.

3.5.1. Introduction

This project is concerned with the characterization of the HDS catalytic activity of novel nanocatalysts and their related surface chemistry, with the main focus being concerned with the nickel coated WS_2 nanotubes (Ni/INT-WS_2). It would be more advantageous to use Ni as a promoter due to its low cost and non-toxicity. However, very few studies concerning the HDS over novel nanocatalysts are available.[57-58, 83-88, 123-124, 141, 186]

Nanocatalysts consist of special adsorption sites and electronic structure that make them significantly different from their corresponding bulk materials, such as single crystals or micro-sized catalyst particles. Many HDS mechanisms were proposed,[89-91, 112-117, 187] mostly assuming a bond activation in thiophene on the S-vacancy sites of MoS_2 systems. However, according to UHV surface science studies on Mo clusters,[61, 93, 121-122, 188] fully sulfided Mo clusters exhibited high catalytic activity due to the formation of one-dimensional metallic edge states along the rim of the Mo clusters. Density functional theory calculations (DFT) suggested a more general effect.[116, 189-190] Therefore, it is suggested that the HDS mechanism for nanoclusters is different from single crystals.

In the current project, the HDS catalytic activity of ten powder catalysts was tested. The catalysts included seven new nanomaterials synthesized at the Weizmann Institute (Israel) and three commercial catalysts from Haldor Topsoe (Denmark)[191] and M K Impex Corp. (USA)[192].

3.5.2. Sample fabrication and characterization

The fabrication of silica-supported Ni/INT-WS2 is described first, followed by the characterization of Ni/INT-WS_2.

3.5.2.1. Sample fabrication

The clean multiwall INT-WS_2 were synthesized according to published procedures[104, 171, 173, 193-194] and were supplied by NanoMaterials Ltd. (Israel).[195] These nanotubes were 1-20 microns in length with 30-100 nm diameter. The IF-MoS_2 NP were prepared by R. Rosentsveig (Weizmann Inst.).[95] The INT-WS_2 were coated with nickel NP using electroless plating method. The same method was used to make Co/INT-WS_2 that were used in one of the prior projects.[59] The synthesized Ni/INT-WS_2 were annealed at 400 °C for one hr under a pressure of $1x10^{-5}$ torr.

Materials such as INT-WS_2, commercial HDS catalysts CoMo and NiMO (Haldor Topsoe, Denmark), and "nano MoS_2" (Impex Corp., USA) were studied as reference systems. In addition, the HDS catalytic activity of Au and Co-Ni coated INT-WS_2, un-doped IF-MoS_2 NP,[101] and Re-doped IF-MoS_2 NP (Re@IF-MoS_2 NP)[100] was also investigated.

The synthesis of the Au/INT- WS_2 was described in ref.[196] The catalyst loadings in weight percentage were 0.39%, 1.7%, 23%, 0.74%-0.63%, and 7.94% for Re, Co, Ni, Co-Ni, and Au functionalized catalysts, respectively. The composition of the commercial catalyst materials was not known. An amount of 27.5 mg of catalysts was typically used for catalytic experiments except for INT-WS_2 (200 mg) and Re@IF-MoS_2 NP (90 mg).

3.5.2.2. Ni/INT-WS_2 characterization

The synthesized Ni/INT-WS_2 were characterized using SEM, HRTEM, and XRD at the Weizmann Institute (Israel).

3.5.3. Results and discussion

The characterization of Ni/INT-WS_2 composition and morphology is presented first, followed by the ambient pressure HDS catalytic experiments on Ni/INT-WS_2. The promotion effect of Ni on the HDS activity of Ni/INT-WS_2 is presented next, followed by the catalyst screening of ten nanocatalysts towards thiophene HDS. The adsorption kinetics and reaction kinetics of thiophene on Ni/INT-WS_2 at UHV conditions is presented next. A summary of the experimental results obtained in this study is presented at the end.

3.5.3.1. Characterization of the sample's composition and morphology

Figures 50A and B depict the SEM images of Ni/INT-WS_2. As evident from Figure 50B, the surface of the nanotube was not entirely/uniformly covered by the nickel NP. The incomplete

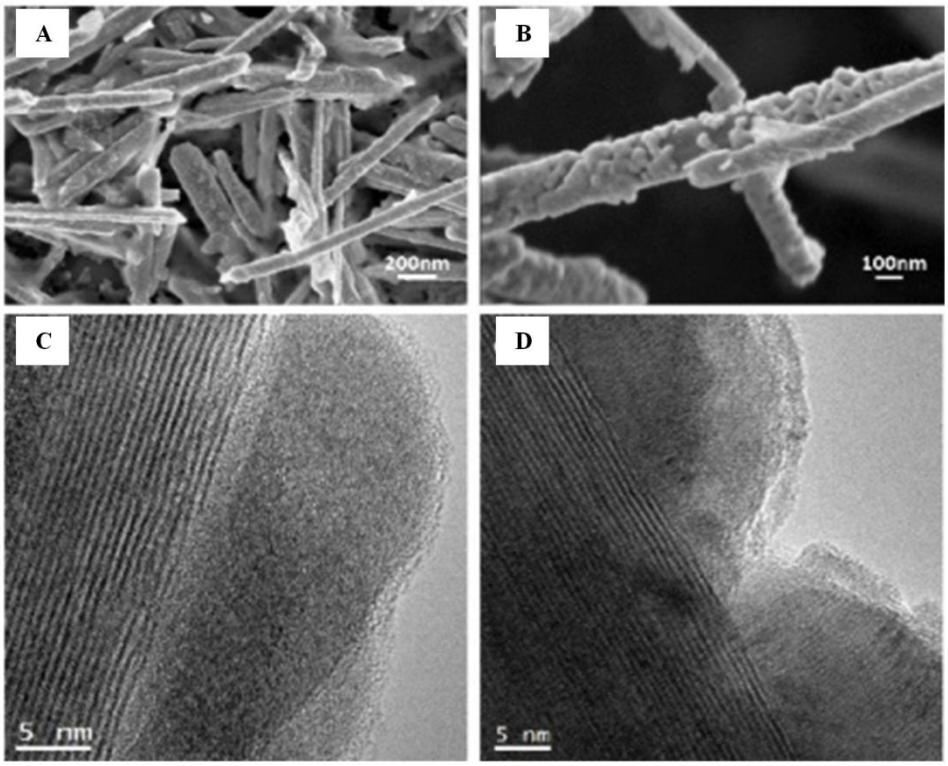

Figure 50. SEM and HRTEM images of Ni/INT-WS_2. SEM images of (A) INT-WS_2 decorated with Ni nanoparticles (B) close-up view of a single coated nanotube. HRTEM micrographs of nickel NP coated on INT-WS_2 (C) before and (D) after annealing. Ref.[60]

coverage was attributed to the formation of nonhomogeneously distributed catalytic sites on the surface of nanotubes during the surface activation process and was also observed in the case of Co/INT-WS_2.[59]

The crystalline structure of the Ni NP was studied by HRTEM. Figures 50C and 50D depict the HRTEM micrographs of the Ni NP. As evident from these figures, the size of Ni NP was in the range of 10-20 nm. Annealing of the synthesized Co/INT-WS_2 at 400 °C changed the crystalline structure of Ni NP from amorphous (Figure 50C) to crystalline (Figure 50D). As per previous studies,[197] nickel existed only in two stable phases (Ni and Ni_3P) at temperatures higher than 350 °C.

The results of XRD analysis of Ni/INT-WS_2 are depicted in Figure 51. Figure 51A shows the XRD pattern of Ni/INT-WS_2 before (bottom curve) and after (upper curve) the annealing

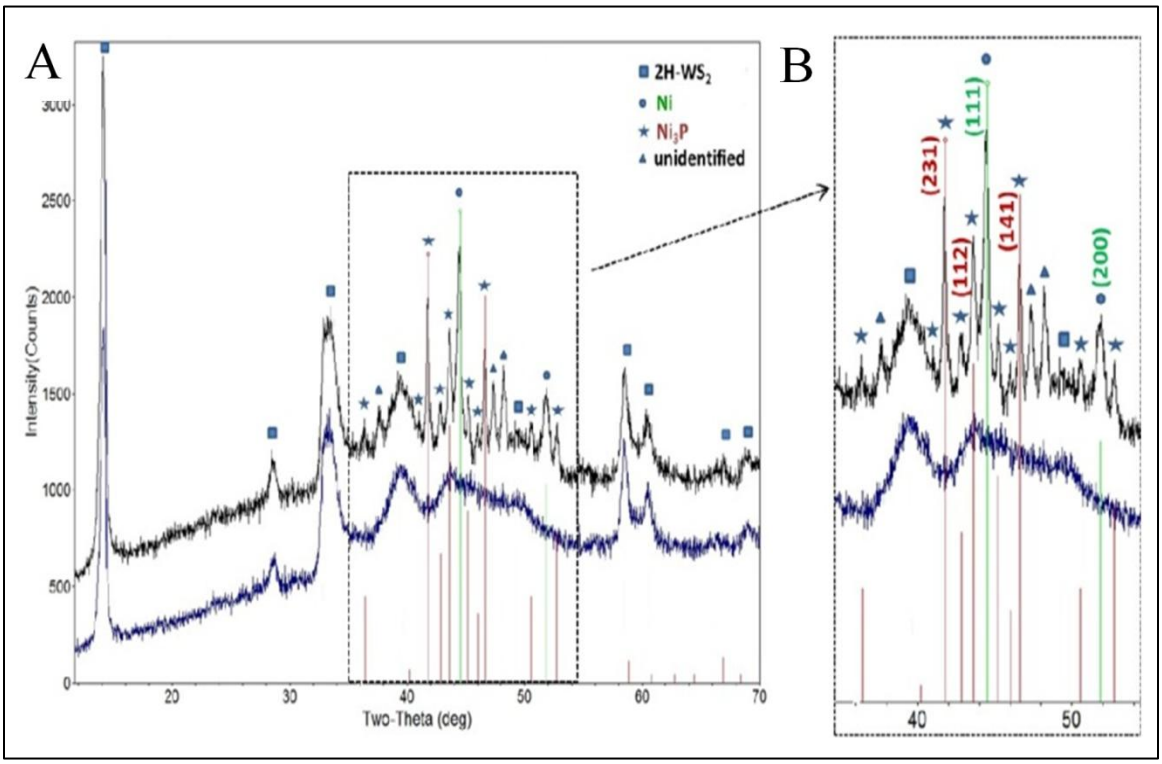

Figure 51. XRD patterns of Ni/INT-WS_2 before and after annealing at 400 °C. (A) XRD pattern of a nickel coated NT before (bottom curve) and after (upper curve) annealing (B) enlarged area of main peaks of Ni and Ni_3P phases. Ref.[60]

process. As evident from the figure, the diffraction peaks of the as-synthesized Ni/INT-WS_2 correspond only to the 2H-WS_2, indicating the amorphous phase of Ni. The diffraction peaks of the annealed Ni/INT-WS_2 correspond not only to the 2H-WS_2, but also to fcc Ni and Ni_3P phases. The diffraction peaks corresponding to Ni and Ni_3P phases are sharp (Figure 51B), confirming the crystalline nature of the annealed coating.

3.5.3.2. Ambient pressure experiments

Figure 52 depicts a typical GC survey scan for the NiMo catalyst (Haldor Topsoe) collected at 600 °C. As evident from the figure, the reaction products appeared in the retention time range of 0.2-0.45 min. Reference GC spectra of several compounds (Figure 53) were collected and were used to identify the products formed in HDS of thiophene.

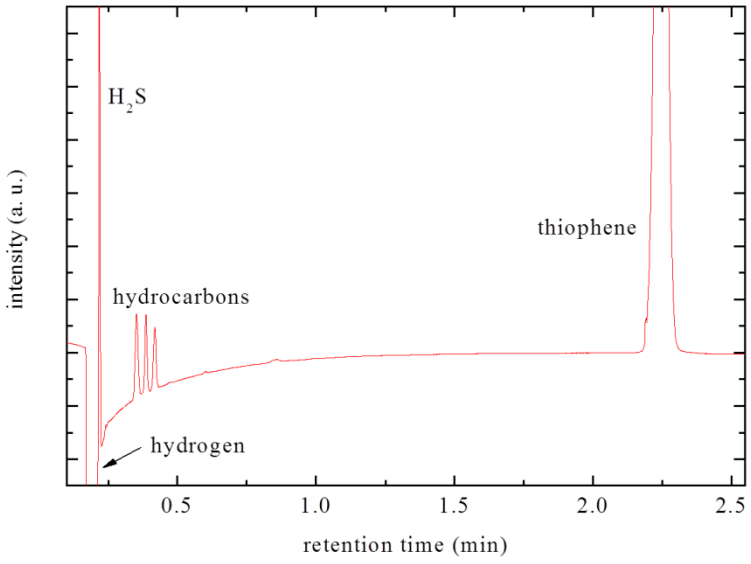

Figure 52. GC survey scan for NiMo powder sample (Haldor Topsoe). Ref.[60]

Figure 53A summarizes the GC scans of 1-butene, 1,3-butadiene, butane, trans-2-butene, and cis-2-butene which were used as reference compounds. Figures 53B and C depict the GC data collected at different reaction temperatures for the NiMo and Ni/INT-WS_2, respectively.

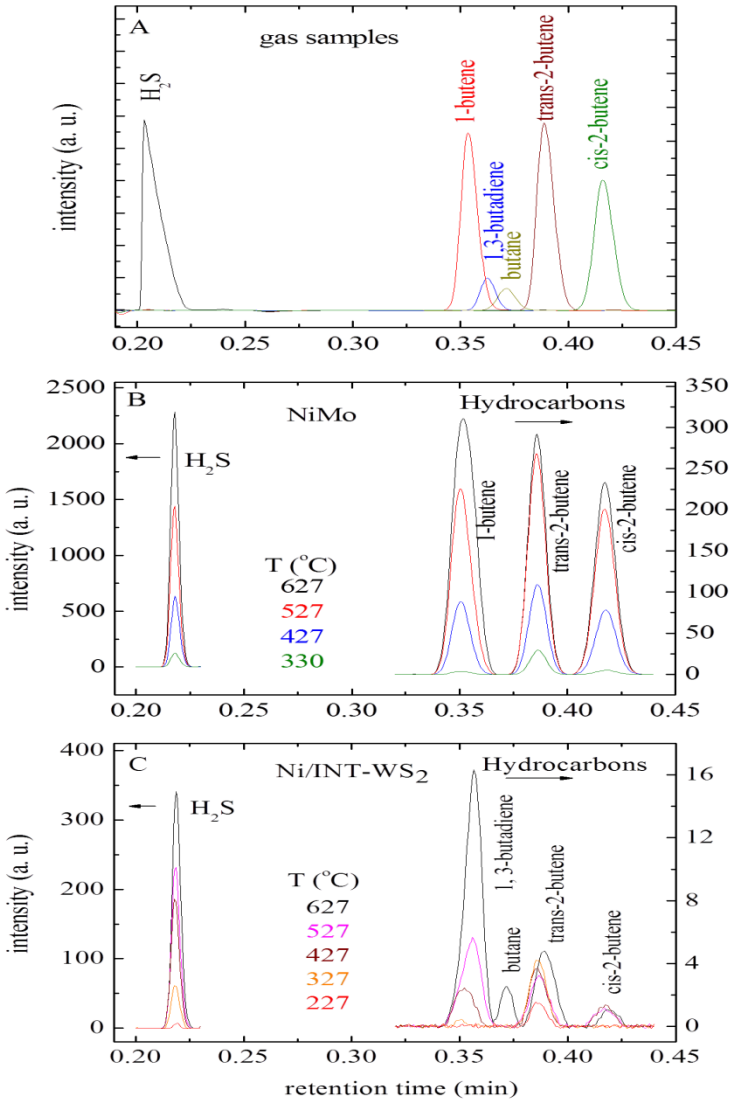

Figure 53. GC transients of reference compounds, NiMo, and Ni/INT-WS_2. (A) GC transients of reference compounds as indicated. H_2S and hydrocarbon region of GC scans as a function of reaction temperature for (B) NiMo (Haldor Topsoe) and (C) Ni/INT-WS_2. Ref.[60]

Quite similar GC scans were obtained for NiMo and Ni/INT-WS_2. In the case of Ni/INT-WS_2, the reaction products were dominated by H_2S formation. Four product GC peaks appeared in the case of Ni/INT-WS_2 catalyst; whereas, three GC product peaks appeared for the commercial catalyst (NiMo). The HDS products formed were recognized by comparing their GC peak retention times (Figures 53B and C) with that of reference compounds (Figure 53A).

Similar data for the other nanomaterials is depicted in Figure 54 and the HDS products formed for all the catalysts are summarized in Table 2. The percentage of H_2S in the HDS reaction products (Figure 53) amount to 53% and 87% for NiMo and Ni/INT-WS_2 at 627 ^oC, respectively. Thus, NiMo, the commercial catalyst, forms about 34% less H_2S than Ni/INT-WS_2. The total hydrocarbon yield increases with reaction temperature for all the catalysts studied, indicating an activated HDS process.

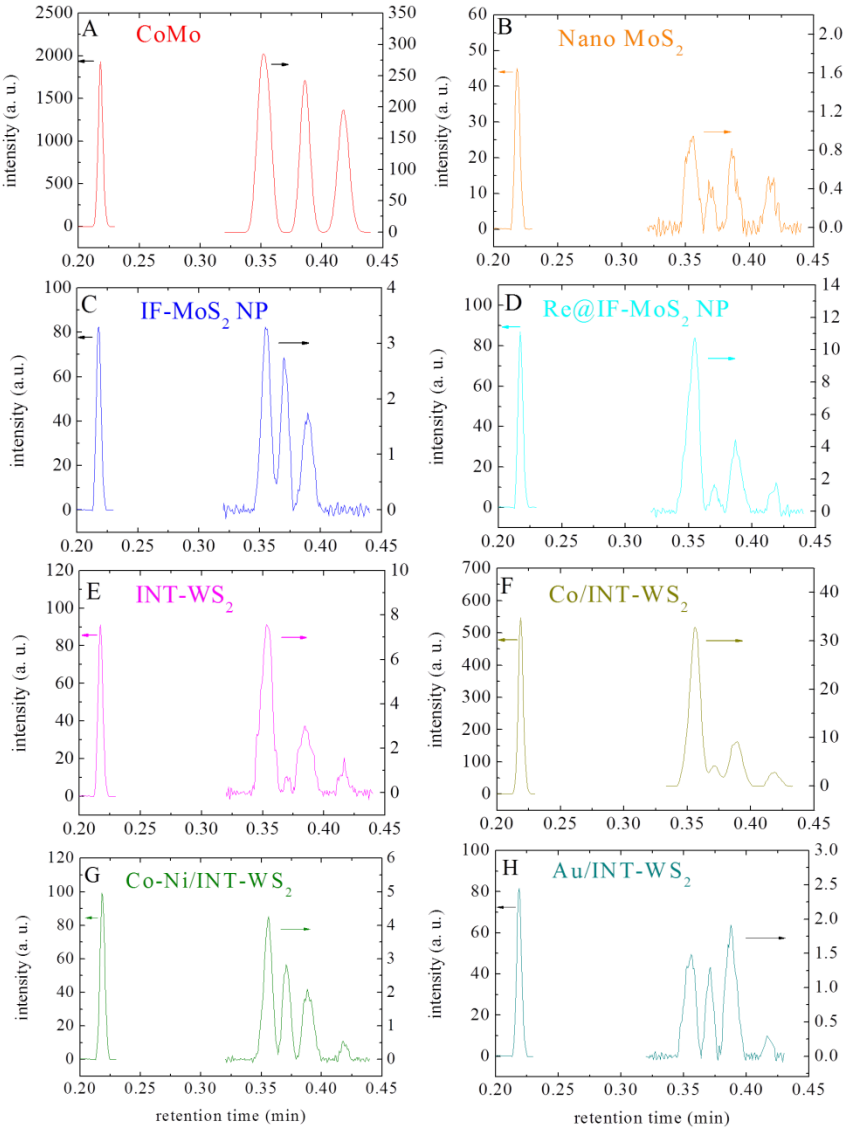

Figure 54. H_2S and hydrocarbon region of GC scans for commercial and novel nano HDS catalysts, as indicated. Ref.[60]

Table 2. Products formed by the commercial and novel nano HDS catalysts in thiophene HDS. Retention times in minutes for different products are indicated. Ref.[60]

Catalyst	H_2S 0.218	1-butene 0.348	1,3-butadiene 0.357	Butane 0.366	trans-2-butene 0.385	cis-2-butene 0.41
NiMo (Haldor Topsoe)	✓	✓			✓	✓
CoMo (Haldor Topsoe)	✓	✓			✓	✓
Nano MoS_2 (M K Impex Corp)	✓		✓	✓	✓	✓
IF-MoS_2 NP	✓		✓	✓	✓	
Re@IF-MoS_2 NP	✓	✓		✓	✓	✓
INT-WS_2	✓		✓	✓	✓	✓
Co/INT-WS_2	✓		✓	✓	✓	✓
Ni/INT-WS_2	✓		✓	✓	✓	✓
Co-Ni/INT-WS_2	✓		✓	✓	✓	✓
Au/INT-WS_2	✓		✓	✓	✓	✓

3.5.3.3. Effect of Ni functionalization of the INT-WS_2

The total HDS conversion rates were calculated according to the procedure described in a prior project on Co/INT-WS_2.[59]

The pristine and Ni coated INT-WS_2 decomposed thiophene into the same reaction products (Table 2). The catalytic activity of INT-WS_2 was increased by a factor of 4 with Ni NP deposition as depicted in Figure 55.

Catalyst deactivation of Ni/INT-WS_2 was evaluated by repeating the experimental runs. The data for two subsequent experimental runs are shown in Figure 55A. Catalyst deactivation was not observed in the duration of HDS experiments. Long duration experiments would be required to correctly evaluate catalyst deactivation.

The TOF values, shown in Figure 55B, were calculated according to the procedure described by D. J. Sajkowski, et al.,[178] which was discussed in detail in a prior project on

Co/INT-WS_2. As evident from the figure, the temperature dependence of TOF follows the trend observed for thiophene conversion rates.

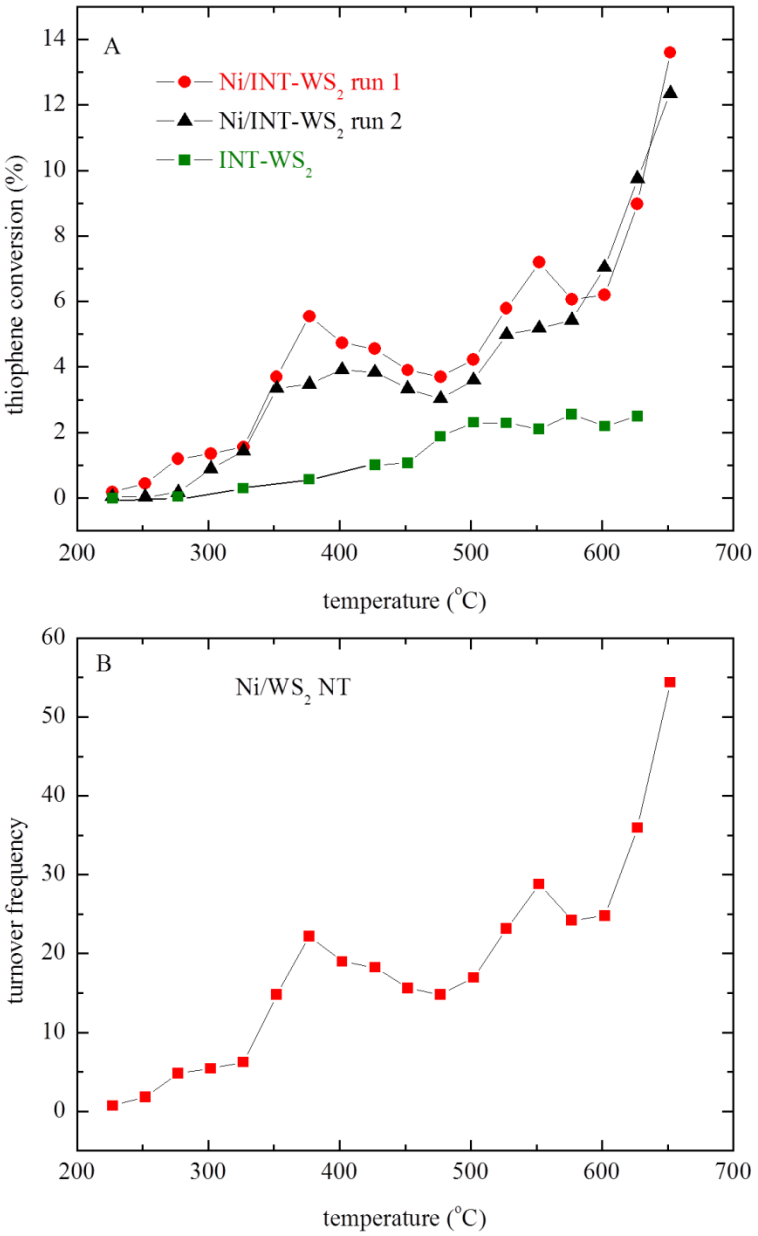

Figure 55. Thiophene conversion rates of INT-WS_2 and Ni/INT-WS_2, TOF data for Ni/INT-WS_2. (A) Thiophene conversion rates of Ni/INT-WS_2 (first and second runs) and pristine INT-WS_2 as a function of temperature (B) turnover frequency of Ni/INT-WS_2 as a function of reaction temperature. Ref.[60]

3.5.3.4. Catalyst screening

Figure 56 depicts the temperature dependence of the thiophene conversion rate for all ten powder catalysts studied. As evident from Figure 56A, NiMo and CoMo (Haldor Topsoe) have high thiophene conversion rates up to 50% and exhibit the highest HDS activity among all the catalysts studied. The next best systems are the Ni/Co coated INT-WS_2 catalysts with approximately similar thiophene conversion rates of ~ 11% at 650 °C. Ni and Co coated INT-WS_2 catalysts form the same products (Table 2). The rest of the catalysts show smaller conversion rates below 4% (Figure 56B). Despite the prominent promotion effect of Ni in the

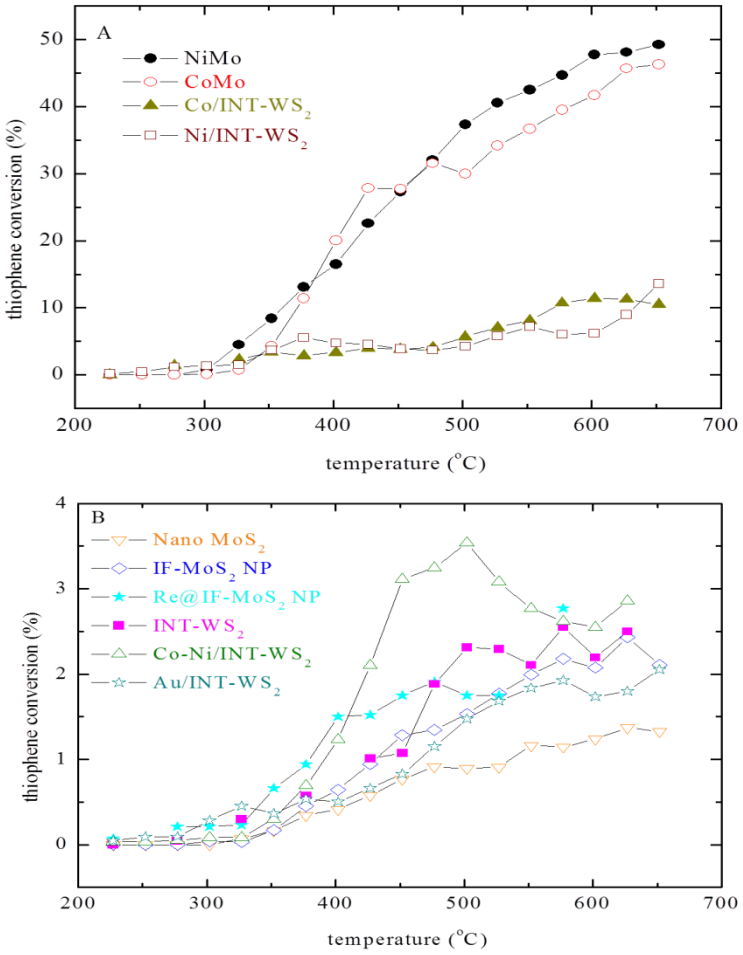

Figure 56. Thiophene conversion rates of (A) highly active and (B) less active HDS catalysts as a function of reaction temperature. Ref.[60]

case of Co/Ni coated INT-WS_2, the Re doped IF-MoS2 NP[198] does not exhibit high thiophene conversion rates when compared to pristine IF-MoS2 NP. Similarly, Au deposition on INT-WS_2 does not enhance the thiophene conversion rates, when compared to pristine INT-WS_2.

H_2S is a toxic and undesirable product in HDS reactions, and its formation has to be minimized by optimizing the catalyst's selectivity. Accordingly, the ratio of the GC peak areas of non-sulfur containing hydrocarbons (HC) to H_2S for different catalysts in the temperature range of 227-652 ^oC are depicted in Figure 57. HC to H_2S ratio of greater than 1 indicates the dominance of hydrocarbons in the HDS products; whereas, the ratio below 1 indicates the dominance of H_2S in the reaction products. Among the catalysts studied, only the commercial catalysts from Haldor Topsoe exhibit a HC to H_2S ratio of approximately 1:1. The rest of the catalysts form more H_2S than hydrocarbons, except Re and Au systems; however, their HDS activity was very small.

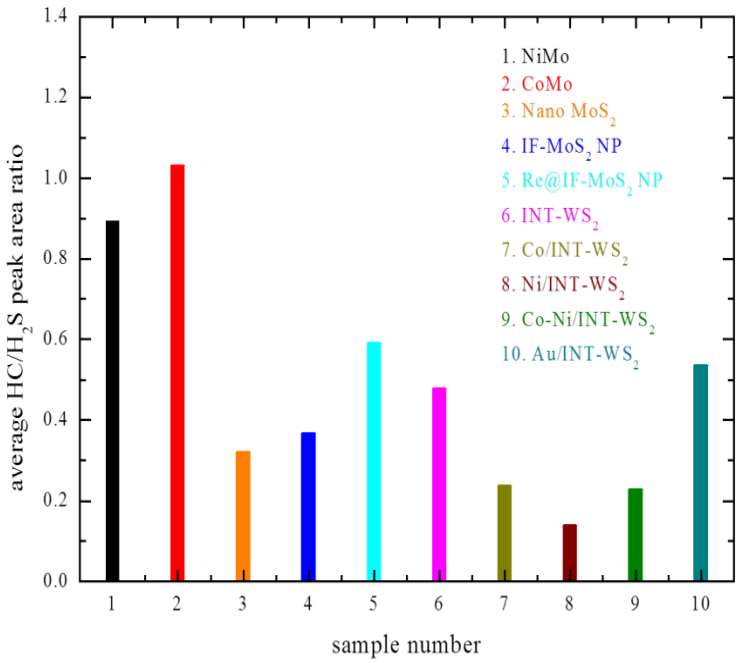

Figure 57. Average HC/H_2S peak area ratio for the commercial and novel nano HDS catalysts in the temperature range 227-652 ^oC. Ref. [60]

Finally, the thiophene conversion rates calculated by excluding H_2S in the reaction products for all catalysts are depicted in Figure 58. As expected from the data already discussed, the Ni/INT-WS_2 and Co/INT-WS_2 exhibit similar and greater performance among the novel nanocatalysts studied. Although Re is an uncommon promoter used in HDS, Re@IF-MoS_2 NP exhibits the next best performance. Unexpectedly, the prominent Au/INT-WS_2 exhibits very low catalytic activity. The low catalytic activity of Co-Ni/INT-WS_2, when compared to either Co or Ni coated INT-WS_2, is also similarly unexpected.

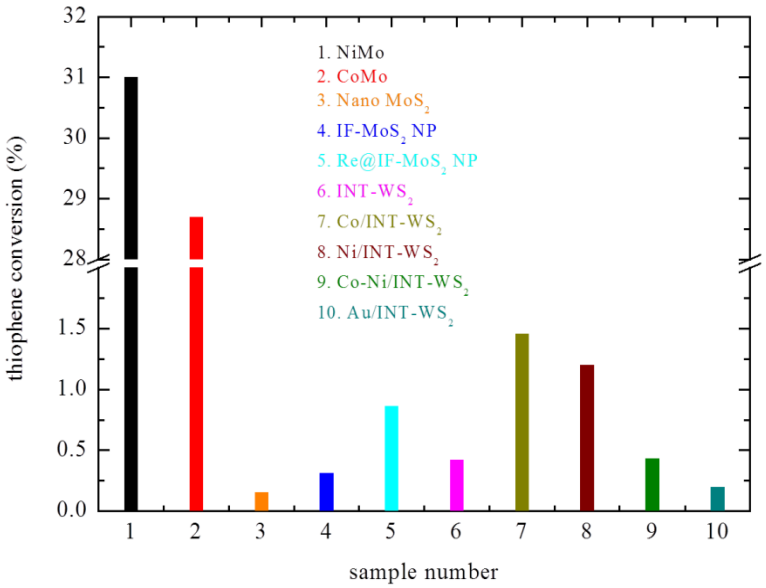

Figure 58. Thiophene conversion rates of the commercial and novel nano HDS catalysts at 627 ^oC calculated by excluding H_2S in the reaction products. Ref.[60]

3.5.3.5. UHV kinetics data

Ni and Co coated INT-WS_2 exhibit good HDS catalytic activity among the nanocatalysts studied. Therefore, additional UHV kinetics experiments on Ni/INT-WS_2 were conducted. Thiophene TDS data on silica-supported Ni/INT-WS_2 together with the TDS data for clean INT-WS_2[58] and IF-WS_2 NP[86] is depicted in Figure 59. Thiophene adsorption on clean silica and the silica-supported IF-WS_2 NP sample (Figure 59A) reveal only two TDS peaks, one of these

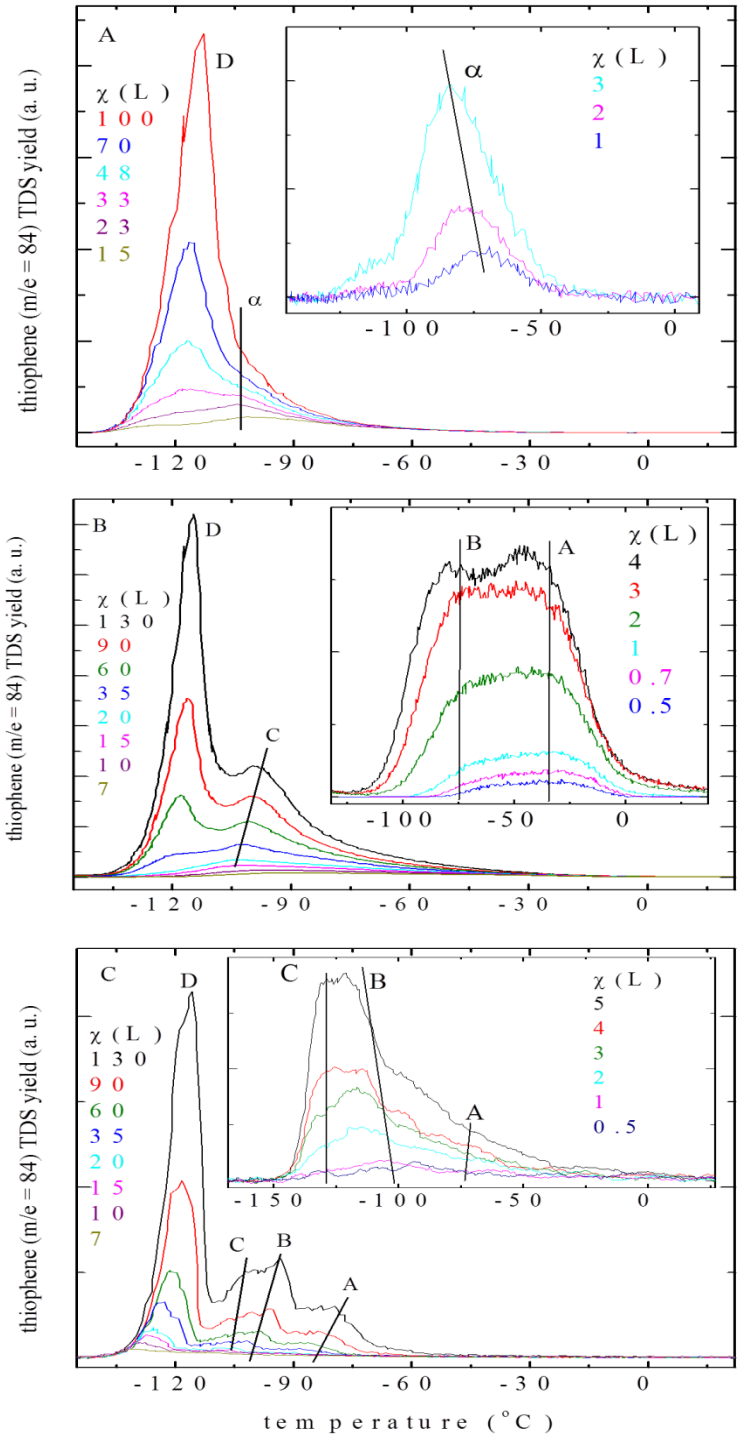

Figure 59. Thiophene TDS on (A) IF-WS_2 NP,[86] (B) INT-WS_2,[58] and (C) Ni/INT-WS_2.[60] The peaks A through C are assigned to thiophene adsorption on internal, external, and groove sites of INT-WS_2 bundles; the D peak refers to thiophene condensation. The insets show the data for small exposures.

(D peak) was only detectable at large exposures. In contrast, the TDS data for silica-supported INT-WS_2 shows four TDS peaks (A-D), depending on the thiophene exposure (χ). UHV kinetics data for the Co/INT-WS_2 catalyst can be found also in ref.[59]

The parent mass of thiophene (m/e = 84) is detected in the TDS experiments (Figure 59). Thus, the molecular adsorption/desorption pathway is monitored. The lined up low temperature edges of the D peaks indicates the condensation of thiophene. The remaining peaks (A, B and C) are unique adsorption features of NT (Figures 59B and C) and are also seen for CNTs.[99, 107-108, 199] Therefore, the A, B, and C peaks are assigned to the adsorption of thiophene on internal, external, and groove sites of the Ni/INT-WS_2 bundles. Thiophene is weakly bonded to the Ni/INT-WS_2 than to the pristine INT-WS_2. By applying Redhead analysis and assuming a standard pre-exponential factor of $1x10^{13}$/sec for 1st-order kinetics, the binding energies (low exposure/coverage) of thiophene on the pristine INT-WS_2 are calculated to be 62, 51, and 43 kJ/mol for the A, B, and C adsorption sites, respectively. The binding energies of thiophene on Ni/INT-WS_2 are ~10 kJ/mol smaller, when compared to pristine INT-WS_2 (Table 3).

Table 3. Binding energies of thiophene on pristine INT-WS_2[58] and Ni/INT-WS_2.[60]

	INT-WS_2			Ni/INT-WS_2		
	A internal	B external	C grooves	A internal	B external	C grooves
T_{max} (K)	239	199	169	200	170	144
T_{max} (^oC)	-34	-74	-104	-73	-103	-129
BE (kJ/mol)	62	51	43	51	43	37

The multi-mass TDS experiments are summarized in Figure 60. Multi-mass TDS scans (open bars) for the IF-WS_2 NP,[86] INT-WS_2,[58] and Ni/INT-WS_2 are depicted in panels A, B, and

C of Figure 60, respectively. The fragmentation pattern of the gaseous thiophene is additionally depicted (solid bars).

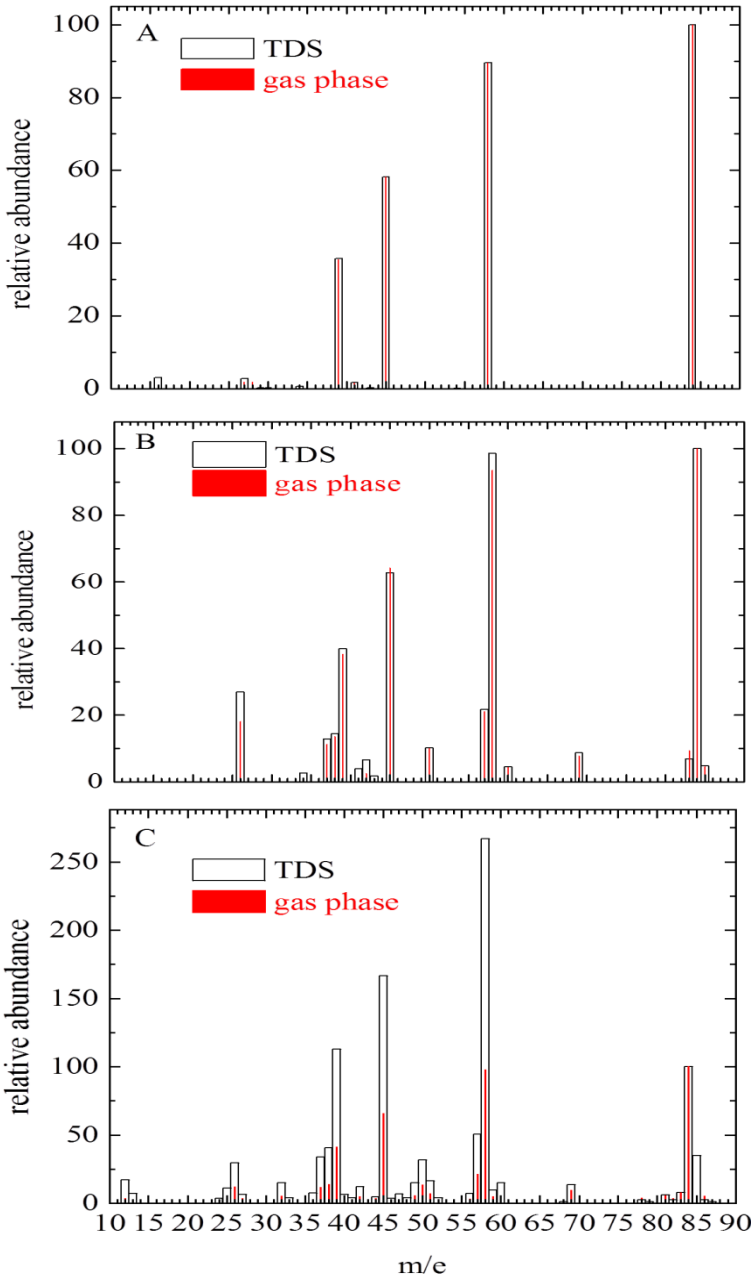

Figure 60. Thiophene multi-mass TDS experiments on IF-WS_2 NP, INT-WS_2, and Ni/INT-WS_2. Comparison of thiophene TDS peak intensities (open bars) on (A) IF-WS_2 NP,[86] (B) INT-WS_2,[58] and (C) Ni/INT-WS_2[60] supported on silica with the mass spectrometer signals (solid bars). The intensity of the peaks is normalized to m/e 84.

The deviation of the multi-mass TDS data from the gas phase fragmentation pattern of thiophene indicates the bond activation of thiophene during TDS experiments at UHV conditions. Molecular adsorption of thiophene on IF-WS_2 NP (Figure 60A) and INT-WS_2 (Figure 60B) is clearly evident. Bond activation of thiophene on Ni/INT-WS_2 is clearly observed (Figure 60C) below room temperature (Figure 59C) at UHV conditions. This is in contrast to the ambient pressure catalytic experiments, where the HDS products formed only by the simultaneous presence of hydrogen and thiophene over the catalyst. No reaction products are evident when HDS experiments are conducted with an empty reactor or a reactor with glass wool.

Pressure and material gaps were extensively discussed in the catalysis and surface science literature.[11, 200-201] However, some recent studies proposed the non-existence of pressure gap for some catalysts.[202] In the current study concerning the HDS nanocatalysts, the discrepancy between the ambient pressure and UHV kinetics can be explained by one or more of the following factors: (1) Ni NP were covered by a thin oxide layer that resulted from synthesis.[59] The oxide might have been reduced at high temperature in presence of ambient pressure hydrogen gas used in the HDS experiments. (2) The difference in the degree of sulfidation of the catalyst. (3) Catalysts are typically contaminated by carbon when exposed to air. However, AES data of Co/INT-WS_2 did not indicate significant amount of carbon. The catalyst was preserved under high vacuum conditions in sealed glass vials after the synthesis. (4) Same catalyst material was used for UHV and ambient pressure experiments. However, the catalyst was supported on silica for UHV kinetics experiments; whereas, unsupported catalysts were used in ambient pressure kinetics experiments. (5) Water dissolved in liquid thiophene is removed by freeze-pump-thaw cycles for the use in UHV experiments. However, water contamination was unavoidable at ambient pressure catalysis experiments.

The thin oxide film would likely be present also at UHV. Unfortunately, AES cannot distinguish between the oxygen present in the silica support and oxygen in the oxide layer. The thin oxide layer might be reduced at high temperature in presence of ambient pressure hydrogen in the ambient pressure catalysis experiments. Although unlikely, the oxide phase might be more reactive than the metallic phase. The degree of sulfidation of the metal surface did not affect the catalytic reactivity and was evident in the sequential HDS experiments. In spite of annealing the samples in H_2, H_2S, and O_2, the Co and Ni coated INT-WS_2 catalysts decomposed thiophene at UHV conditions. It is important to note that similar experiments done on pristine INT-WS_2 did not reveal any thiophene decomposition. Therefore, neither the oxide formation nor the degree of sulfidation has a significant effect on the observed catalytic activity at UHV conditions. AES and EDS data of the samples does not reveal any impurities. Catalyst-support interactions are typically present. However, our previous studies on similar materials supported on sapphire and silica as supports did not indicate support effects on kinetics.[57, 86] Water might dissociate and hydroxylate the catalyst at ambient pressure and have a significant influence on the HDS catalytic activity. This hypothesis needs further investigation. Unfortunately, no in-situ spectroscopy experiments were done to support this hypothesis.

3.5.4. Summary

A first HDS catalytic screening of WS_2 and MoS_2 nanomaterials with nanotube (INT) and fullerene-like (IF) structure was done. Catalysis, surface science, and kinetics techniques were used in this study. The INT are crystalline and the NP have fullerene-like structures.[171, 193-194] IF and INT-WS_2 are already commercially available, making this study more relevant for possible catalytic applications, such as HDS. They are being used as lubricants[100-101] and for reinforcing various polymer nanocomposites.[203] NiMo, a commercial catalyst (Haldor Topsoe),

exhibited 4.5 times higher thiophene conversion rates than the best HDS nanocatalyst used in this study. Nickel and cobalt exhibit similar promotion effects on the HDS catalytic activity of INT-WS_2.[59, 204]

Sulfur free hydrocarbons and H_2S were formed as the products in the HDS reaction. Commercial catalyst is less than a factor of 2 better than the novel HDS catalysts in the formation of H_2S, which is an undesirable product. It is speculated that the Ni decorated INT-WS_2 with Re-doping or Au nanoparticle deposition could possibly have higher thiophene conversions with lower H_2S formation.

The UHV kinetics experiments indicate that thiophene adsorbed more weakly on Ni/INT-WS_2 than on pristine INT-WS_2. This result might provide a clue for possible mechanisms in thiophene HDS on this catalyst. Interestingly, thiophene did not decompose on Ni/INT-WS_2 in ambient pressure catalytic experiments, but it decomposed below room temperature at UHV conditions. This could be due to the change in the chemical composition of the catalyst under different experimental conditions.

CHAPTER 4. METHANOL SYNTHESIS MODEL NANOCATALYSTS

The methanol synthesis model nanocatalysts project is comprised of two interrelated sub projects. The main objective of this project is to characterize the catalytic activity of silica-supported Cu nanoclusters towards the adsorption of CO and CO_2. The first project is concerned with the fabrication of physical vapor deposited (PVD) Cu clusters on silica and characterize their catalytic activity towards CO adsorption.[39] The second project is focused on the characterization of the catalytic activity of electron beam lithography (EBL) fabricated silica-supported Cu nanoclusters towards CO and CO_2.[48] In addition, the results of CO adsorption on Cu PVD clusters are also compared to those obtained on silica-supported Au PVD clusters in order to understand the cluster size effects.[72]

4.1. Adsorption Dynamics of CO on Silica-supported Cu Clusters

An introduction to the supported Cu model catalysts is presented first, followed by the experimental details that include the fabrication and characterization of silica-supported Cu clusters. A combined results and discussion section is presented next. A summary of experimental results obtained in this study is given at the end.

4.1.1. Introduction

The use of nanoparticles for promoting catalytic processes is an active area of research.[102-103, 205-206] Several studies have been devoted to understand the effect of particle size, rim, shape, and chemical composition of metal clusters on the catalytic activities of metal clusters.[16, 21, 201, 207] Silica-supported PVD Cu clusters is studied as a reference system to characterize the catalytic activity of EBL fabricated Cu nanoclusters.[40, 153, 208] Supported Cu model catalysts are of practical interest for water gas shift reaction and methanol synthesis reactions.[28, 154, 209-212] Furthermore, metal coated silica has applications in microelectronics.[213]

Among the silica-supported systems, amorphous silica-supported PVD Cu clusters were studied with a variety of techniques, such as Cu TDS,[213-214] XPS,[215] Fourier transform infrared spectroscopy (FTIR),[216-217] and on-air scanning tunneling microscopy (STM).[8] Chemical vapor deposition (CVD) was often used to grow thin films of copper.[218] Despite a large number of studies available on Cu/silica model catalyst,[8] no molecular beam scattering studies on Cu/silica are available. Cluster-support interactions were also reported for the Cu/silica system.[213, 219] The adsorption probability of Cu on silica, S_{Cu}, at room temperature is only ~ 0.2 in the monolayer deposition range. However, the adsorption probability of Cu on the Cu clusters (near saturation of the support with Cu clusters) may approach one.[216, 220] The growth of Cu clusters on silica was studied using FTIR and STM. Briefly, low temperature deposition of copper resulted in the formation of highly dispersed 2D Cu clusters that were characterized by a single CO TDS peak and a single IR band. When the sample was annealed at 300 K, the 3D clusters formed. In the case of annealed Cu/silica, at least two TDS peaks and several IR absorption bands were observed, indicating the presence of different copper surfaces on clusters.[216] A typical cluster size of 10-30 Å was observed for low Cu coverages; whereas, a continuous Cu grain structure (∼200 Å) was observed for high Cu coverages.[8, 216]

4.1.2. Experimental procedures, sample fabrication, and characterization

Experimental details of AES, XPS, molecular beam scattering, and TDS are presented first, followed by the fabrication of silica-supported Cu clusters and blind experiments.

4.1.2.1. AES/XPS

Mg Kα line (1253.6 eV) was used for XPS measurements with an analyzer pass energy of 100 eV (survey spectrum) and 50 eV (individual peaks). The XPS spectra were referenced with respect to the O 1s XPS line at a binding energy (BE) of 532.9 eV.[221] XPS peak shift of 2.6

eV occurred due to charging. The electron energy used for AES measurements was 2 keV with a modulation voltage of 2 eV. Signal-to-noise ratio of the AES spectra was used to measure the uncertainties in the AES peak intensities.

4.1.2.2. Adsorption transients

The impact energy (E_i) of CO molecules was varied in the range of 0.09-0.98 eV by using pure and seeded (3% CO in He) CO gases and controlling nozzle temperature (300-700 K). E_i was determined using time of flight spectroscopy (TOF). Initial adsorption probabilities (S_0) and coverage dependent adsorption probabilities, $S(\Theta)$, were measured using the King and Wells uptake technique. Signal-to-noise ratio of the transients were used to measure the uncertainties in S_0, which amounted to $\pm$ 0.05 in the current project. Several individual measurements were also averaged for certain experiments to minimize the statistical error, which amounted to $\pm$ 0.02.

4.1.2.3. UHV kinetics data

CO was dosed onto the sample's surface with the supersonic molecular beam. The reading of the thermocouple was calibrated in situ within $\pm$ 5 K by recording the condensation peaks of the alkanes. The heating rate of 1.7 K/s was used for TDS measurements.

4.1.2.4. Cu deposition and sample cleaning

Silica supported Cu clusters sample was prepared by depositing copper on a clean silica support, using physical vapor deposition.

4.1.2.4.1. Cleaning of silica

A Si(111) wafer with a 1 μm thick thermal oxide layer (MEMS nanotechnology Exchange, VA, USA) was used as the support. The silica sample was cleaned with several Ar^+ sputtering cycles (2 μA, 2 keV, 20 h). As per prior studies,[40] sputtering also reduced Si^{4+} to Si^0. Therefore, the sample was annealed in oxygen ($2x10^{-5}$ mbar, 8 h) to oxidize the support.

4.1.2.4.2. Copper deposition

Copper was deposited at room temperature on silica by a home-built Cu metal doser. However, Cu filaments were not directly used due to the low melting point of Cu. In this case, a tungsten wire (d = 0.15 mm) wrapped around a high purity copper wire (d = 0.25 mm, 99.9%, Goodfellow) was resistively heated to evaporate copper. Several different silica supports were used in this project. It is important to note that the flux of Cu metal doser changes with filament (W/Cu) replacement. The Cu clusters were never annealed above 350 K.

4.1.2.5. Blind experiments

Blind experiments were done by recording the adsorption transients on clean silica supports.[40, 100] Both the fully oxidized and partially reduced supports were used for blind experiments. No significant uptake of CO by the support was observed in molecular beam scattering experiments at the lowest sample temperature (T_s) achievable.

4.1.3. Results and discussion

A characterization of silica support and silica-supported Cu cluster growth is presented first, followed by the CO initial adsorption probability measurements and its dependence on Cu cluster size, sample temperature, CO impact energy, and CO initial coverage.

4.1.3.1. Characterization of the silica support

The prime objective of this study is to characterize the adsorption dynamics of CO on silica-supported Cu clusters. However, the surface cleanliness and the growth of the Cu clusters were monitored with AES and XPS. Figure 61A depicts the AES survey scans of silica before/after cleaning. Several different silica supports used in this study were characterized using AES and XPS. However, very similar AES and XPS data were obtained. As evident from Figure 61A, the impurities (C, N), initially present in silica support were reduced to a level below the

detection limit of AES due to sputtering/annealing cleaning cycles. However, N AES peak of very low intensity (N to O AES peak intensity ratio of 0.02) was present even after extensive cleaning. The inset of Figure 61A shows AES silicon region of silica and partially reduced silica. Evidently, the absence of AES peak at 92 eV,[222] corresponding to Si^0, indicates a fully oxidized silica support.

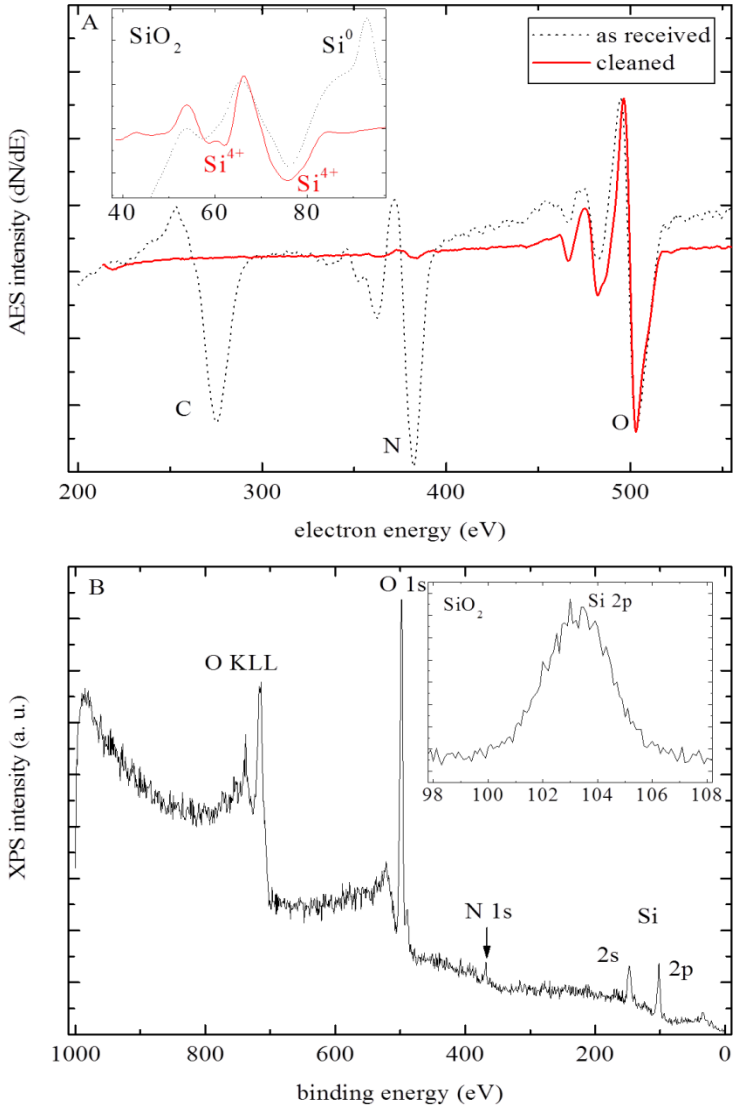

Figure 61. AES and XPS spectra of silica. (A) AES spectra of the silica support. The inset shows the AES silicon region of silica and partially reduced silica. (B) XPS survey spectrum of clean silica. The inset shows Si 2p XPS peak. Ref.[39]

This result is very important because fully oxidized silica is chemically inert; whereas, partially reduced silica (Si^0) is reactive towards certain compounds. CO does not adsorb on fully oxidized silica, and its adsorption is not significant, even at 90 K on partially reduced silica.[100-101] Figure 61B depicts an XPS survey spectrum of clean silica that shows an excellent agreement with the reference spectra.[223] Again, a very low intensity N 1s XPS peak was present. N 1s XPS peak's intensity was larger than it actually was, because of the sensitivity factors (0.477 for N 1s and 0.283 for Si 2p).[223] The inset of Figure 61B shows the silica 2p XPS region. Evidently, Si 2p XPS peak appears as a single peak, corresponding to a fully oxidized silica sample. In addition, the peak position also supports this conclusion. XPS and AES data collected for the clean silica support are in good agreement.

4.1.3.2. Characterization of the supported Cu cluster growth

Figure 62A summarizes the AES data collected as a function of Cu deposition time, χ_{Cu} (lower scale). Cu-to-O AES peak intensity ratio as a function of χ_{Cu} is depicted. Examples of the corresponding Cu AES spectra are depicted in Figure 62B. The inset of Figure 62B depicts the oxygen AES peaks originating from the silica support. The results of two independent experiments are depicted in Figure 62A. Different silica supports and Cu dosers were used in these experiments. As mentioned earlier, Cu flux depends on the metal doser. The inset of Figure 62A depicts the original Cu exposure time scale for the second Cu doser. The Cu exposure time scale for the first Cu doser is depicted in the main panel. The Cu flux of the first Cu doser was 10 times larger than the second. Therefore, a scaling factor was used to match the Cu exposure times for two different dosers and compensate the flux differences. As evident, the calibration curve shapes are identical. Therefore, the exact Cu flux is unimportant for the deposition of Cu clusters. Cu-to-O AES peak intensity ratio as a function of $\chi_{Cu,}$ is depicted in Figure 62A.

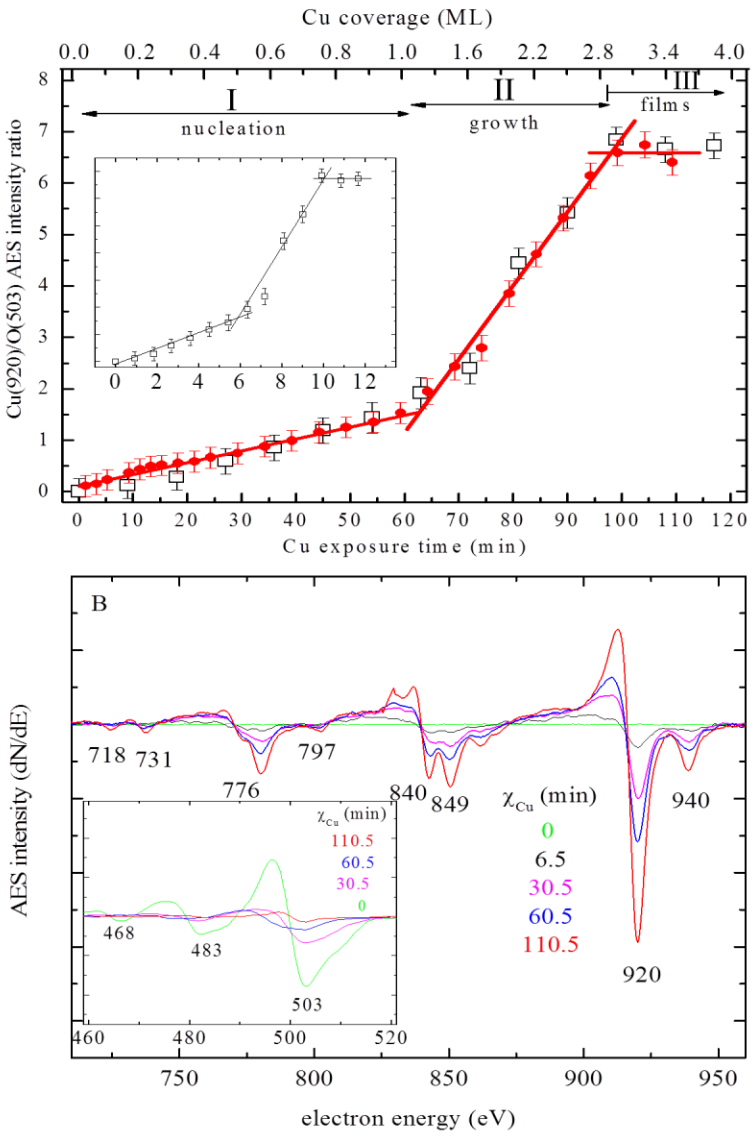

Figure 62. AES Cu coverage calibration. (A) Cu-to-O AES peak intensity ratio as a function of Cu exposure. Two dosers, high flux (open squares) and low flux (solid circles) have been used for dosing Cu. The Cu exposure time of the low flux doser is increased by a factor of 10 for comparison with that of high flux doser. Cu coverage in monolayers (ML) is indicated on the upper scale. (B) AES spectra of copper and oxygen (inset) as a function of Cu exposure. Ref.[39]

Initially, the Cu-to-O AES peak intensity ratio, increased linearly until a critical exposure (Section I) and then, suddenly, increased (section II) to a saturation level (section III). This type

of calibration curve shape is uncommon for supported cluster systems. An abrupt change in the slope of AES vs. χ_{Cu} was not observed on metal oxides[40, 224] and metal supports.[225] Two linear segments in AES growth curves are typically expected,[154] but not a step-like shape. AES spectra (Figure 62B) collected during Cu deposition does not reveal any unusual features. All peaks shown in Figure 62B are assigned to copper.[226] As evident from the inset of Figure 62B, the O AES peak intensity decreases with increasing χ_{Cu}. Similarly, the XPS spectra of Cu clusters collected for different χ_{Cu} (Figure 63) also look normal.

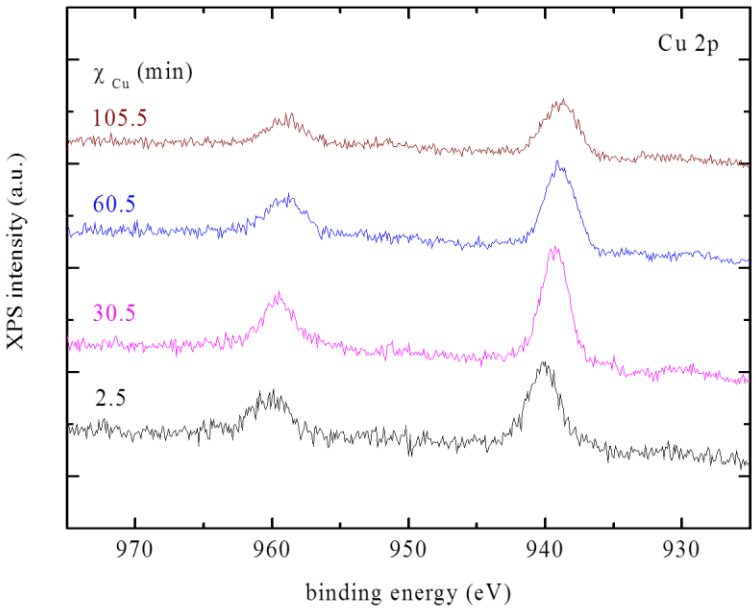

Figure 63. Cu 2p XPS region for different Cu exposures at 300 K as indicated. Ref.[39]

Therefore, neither AES nor XPS provides an explanation for the uncommon shape of the AES growth curve. Cu 2p XPS region for different χ_{Cu} is depicted in Figure 63. As evident from the Cu 2p XPS peak shapes, the Cu clusters are metallic for all the Cu exposures. In contrast, copper oxides give rise to distinct XPS shake-up satellite peaks.[227] Thus, the formation of CuO_x can be ruled out. However, certain metal nanoclusters have a distinct affinity for oxide formation.[159]

Several XPS studies on Cu systems indicated the difficulty in interpreting the Cu XPS core-level shifts. Cu 2p XPS peak shift of 1 eV (939-940 eV) is typical for supported clusters. However, the 2.6 eV XPS peak shift observed in the present study could be due to charging. Intermixing and alloy formation were also safely ruled out by considering the low adsorption temperatures used during Cu deposition. Unusual growth behavior of Cu on silica was reported earlier in a study concerning the TDS of Cu on silica.[213] Cu had a very low adsorption probability (S_{Cu}) on silica; whereas, the adsorption probability of Cu on Cu was equal to one.[213] It is therefore concluded that the step-like feature observed in the AES data (Figure 62A) is due to the variations in the adsorption probability of Cu on silica. The conclusion is that the silica support was decorated with Cu atoms for $\chi_{Cu} < 60$ min. According to previous studies, a very low adsorption probability ($S_{Cu} = 0.2$) was observed for the room-temperature deposition of copper. All the nucleation sites were filled (section I) prior to the growth Cu clusters (section II). At this instance, Cu started to adsorb on Cu islands and resulted in a sudden increase in the adsorption probability of Cu ($S_0^{Cu} = 1$) and corresponding AES intensity.

The spectroscopic (AES and XPS) data obtained is consistent with a standard cluster growth of Cu on silica (nucleation → 2D/3D cluster growth → film formation). This conclusion is also supported by the TDS data of CO on small (Figure 64A) and large (Figure 64B) Cu clusters. Consistent with prior studies,[216] the CO TDS on Cu clusters (Figure 64) reveal two TDS peaks at 150 and 200 K.[216] The observed peak temperatures are close to the TDS peaks (160 and 180 K) reported earlier.[216]

Different TDS peaks indicate chemically distinct adsorption sites and Cu cluster growth. Unfortunately, neither STM nor TDS data are available for the silica-supported Cu clusters of submonolayer coverage. The presence of different adsorption sites (rim, corner, and terrace sites)

in the nucleation regime were also expected. For example, different CO TDS peaks, independent of Cu exposure, were also present in the case of Cu/ZnO(0001).[154] Thus, the CO TDS data are consistent with the cluster growth of copper.

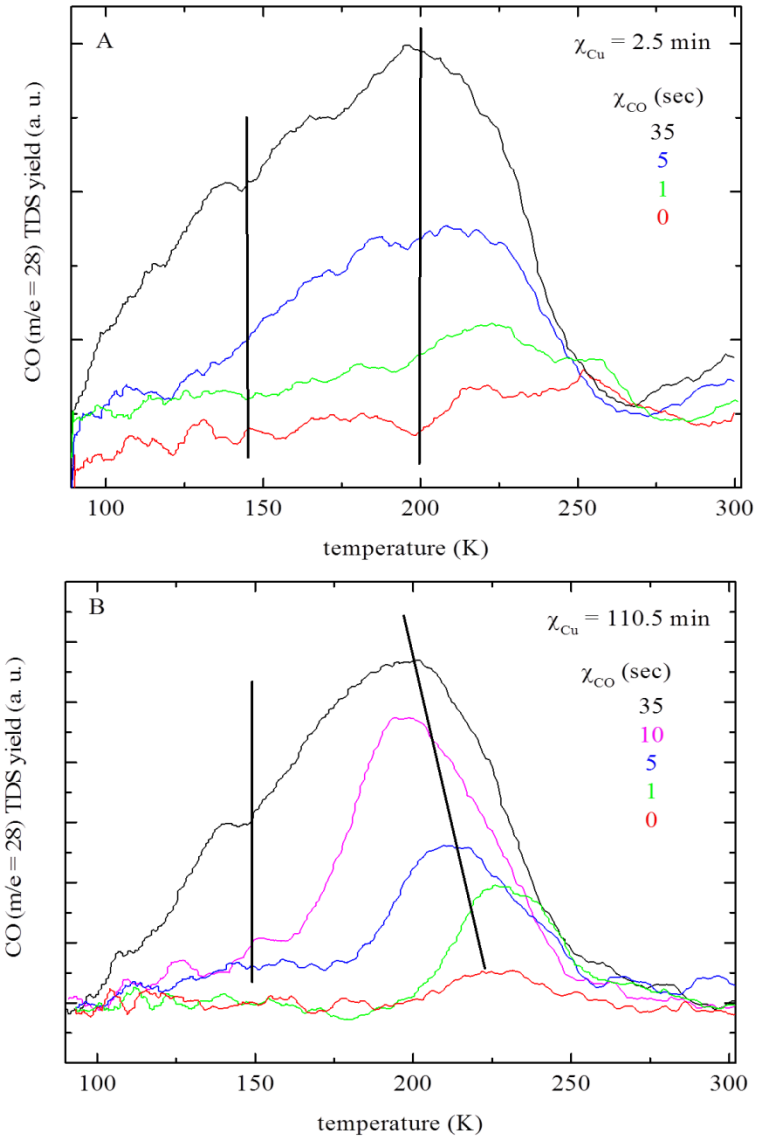

Figure 64. CO TDS on silica-supported Cu clusters with Cu exposure times (A) 2.5 min and (B) 110.5 min. CO was dosed with the molecular beam. Ref.[39]

CO TDS peak shifts were only observed in the case of large clusters. This is expected for large Cu clusters because they lead to high coverages of CO that cause the repulsive lateral

interactions, which decrease the binding energies. In fact, the integrated CO TDS peak areas for large clusters were about a factor of 3 greater than the small clusters (Figure 64). Therefore, different sections of the AES growth curve (Figure 62A) were assigned different stages of the Cu cluster growth: section I to the nucleation regime, section II to the cluster growth regime, and section III to the formation of a film that consists of large 3D clusters. Accordingly, 60 min of Cu deposition (χ_{Cu} = 60 min) was considered equivalent to one monolayer (Θ_{Cu} = 1 ML) of copper, i.e., the nucleation phase of the Cu growth was completed and $S_{Cu} \rightarrow 1$. Accordingly, a Cu coverage scale was added to Figure 62A (upper scale). Cu coverage estimation will be further explained.

As per prior studies[220] concerning the adsorption of Cu on silica, the change from low ($S_0^{Cu} \sim 0.35$) to high ($S_0^{Cu} \sim 1.0$) adsorption probabilities of Cu correspond to a Cu coverage of $\sim 7.8 \times 10^{15}$ Cu atoms/cm^2. It is therefore concluded that the step feature in Figure 62A corresponds to 1 ML Cu = $\Theta_{Cu} \sim 7.8 \times 10^{15}$ atoms/cm^2. S_0^{Cu} is assumed to remain constant at 0.35 until the coverage corresponding to Δt = 60 min is reached. The Cu flux (F) is given by the following equation:

$$F = \Theta / (S_0^{Cu} \Delta t) \qquad (30)$$

Flux (F) = 6.2×10^{12} Cu atoms/cm^2 s. The estimated Cu flux is consistent with prior studies[213, 215, 220] that used a similar Cu metal doser. However, some studies[213, 215] estimated S_0^{Cu} to be 0.2 that would result in a Cu flux of 1.1×10^{13} Cu atoms/cm^2 s. The Cu flux was constant, but beyond the step feature, $S_0^{Cu} \sim 1.0$. Therefore, the Cu coverage corresponding to χ_{Cu} = 120 min is estimated to be ~ 4.0 ML according to the following equation.

$$\Theta = (F \times S_0^{Cu} \times \Delta t) + 1 \qquad (31)$$

where F = 6.2×10^{12} Cu atoms/cm^2 s, S_0^{Cu} = 1.0 and Δt = 60 min. No carbon was detected by

AES/XPS after dosing CO on silica-supported Cu clusters, indicating the molecular adsorption/ desorption of CO.[228]

4.1.3.3. Typical adsorption transients

The adsorption dynamics of CO on silica-supported Cu clusters was characterized by collecting adsorption transients with molecular beam scattering.[229] Typical adsorption transients of CO on silica, partially reduced silica, and silica-supported Cu clusters (χ_{Cu} = 60 min, i.e., 1ML) is depicted in Figure 65. CO pressure, as a function of CO exposure time (t), is depicted.

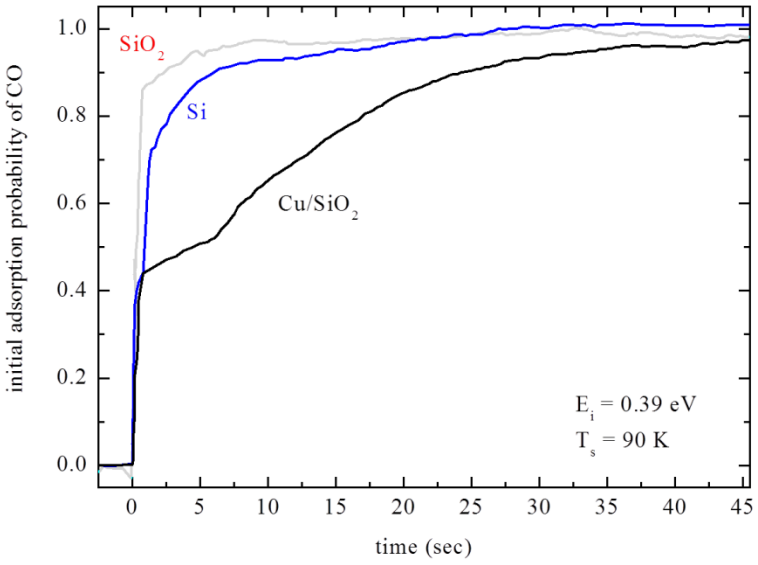

Figure 65. King and Wells up-take curves of CO on bare supports and Cu/silica (χ_{Cu} = 60 min). Ref.[39]

As evident from the figure, CO adsorbed on silica-supported Cu clusters but not on clean supports. The beam flag was opened at t = 0 s to start dosing CO onto the surface of the sample. A step-like function was observed in the adsorption transient of CO that were collected on clean supports. However, in the case of model catalyst, the CO pressure initially increased at t = 0 and then gradually increased until the saturation level was reached. The pressure increase was delayed due to the adsorption of CO on the catalyst surface. After filling all the adsorption sites available, all CO molecules were backscattered. Thermal desorption and condensation of CO

were neglected at the chosen sample temperature (~ 90 K). The data is depicted such that the adsorption transient corresponded to 1-S, with S being the coverage (time) dependent adsorption probability. Therefore, the initial adsorption probability (S_0) could be directly read from the transients at t = 0. The area which is above the transient and below the saturation level corresponded to the total number of adsorbed CO molecules. Therefore, it is evident that the CO coverage on the clean supports is very small/negligible, since the adsorption transient is a step-like function. This conclusion is consistent with a prior study[215] that used different measuring techniques. Coverage dependent adsorption probability, $S(\Theta)$, was obtained by integrating the adsorption transient. The coverage of CO obtained at the lowest surface temperature is typically considered to be one monolayer, and that is used to calibrate the saturation coverage at higher surface temperatures.

4.1.3.4. Initial adsorption probabilities of CO: Cluster size effect

Initial adsorption probability (S_0) of CO, as a function of $\chi_{Cu,}$ for constant surface temperature (T_s), and CO impact energy (E_i) is depicted in Figure 66.

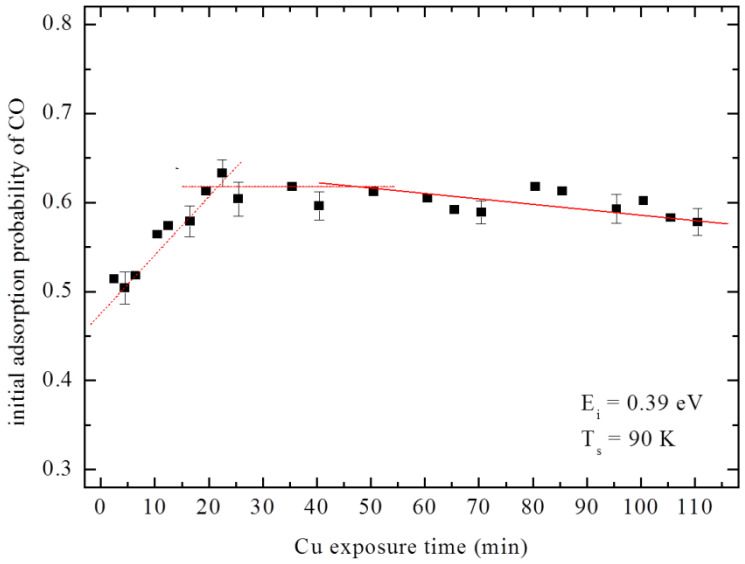

Figure 66. S_0 of CO on Cu/silica as a function of Cu exposure. Ref.[39]

S_0 initially increased linearly and then leveled out at $S_0 = 0.6$ for $\chi_{Cu} \sim 20$ min (0.33 ML). This is typically observed for supported cluster systems. This result can be explained by the so-called capture zone model (CZM).[160] CZM was introduced early on by Boudart et al.[160] and was also used by others[154, 230] to account for such kinetic effects. Molecular beam scattering experiments were conducted at a surface temperature ($T_s = 90$ K) that favors only negligible coverage of CO on the clean support (cf., Figure 65). However, even in such a case, the probe molecules (CO) have a life time long enough to diffuse from the support to the metal clusters. CZM is used to explain the catalytic activities of various supported cluster systems.[154, 231-232] CZM takes the effect of the supported clusters into account and provides information about the precursor lifetime. Accordingly, several adsorption/desorption pathways were considered: (1) direct adsorption of probe molecules on the support or the metal deposits, (2) thermal desorption of probe molecules from the deposits or the support, (3) trapping of the adsorbates on the deposits and subsequent diffusion to the support (spillover), and (4) trapping of the adsorbates on the support and subsequent diffusion to the deposits (inverse spillover). The desorption pathway can be neglected due to low surface temperatures used ($T_s < 100$ K, cf., Figure 64). The inverse spillover path way was mostly expected because the coverage of Cu was small.

The size of the capture zone around a metal cluster is given by the ratio of the surface residence time of adsorbates to their characteristic diffusion time. In the case of a cluster ensemble, the capture zones of different clusters overlap with each other. The size of the capture zone decreases with increasing surface temperature.

Initial adsorption probability (S_0) of CO, as a function of Cu exposure time, is depicted in Figure 66. The S_0 of CO initially increased with Cu coverage. This is due to an increase in the total capture zones formed around all Cu clusters. After reaching a critical coverage, the capture

zones of different Cu clusters overlapped with each other and caused no further increase in S_0, i.e., reactivity. As evident from Figure 66, a model catalyst with χ_{Cu} = 10 min (0.17 ML) has nearly the same reactivity towards CO adsorption as the one consisting of large 3D Cu clusters. However, the steps observed in Figure 62A and Figure 66 do not coincide. The step-like feature in Figure 62A is related to the variations in the adsorption probabilities of Cu on Cu/silica. The step-like feature in Figure 66 is related to the kinetics effect caused by the diffusion and inverse spillover of CO molecules.

In contrast to the CZM, a small but decreasing trend in S_0 is observed for large Cu exposures (see the solid line in Figure 66). This might be due to a dynamics effect caused by the variations in gas-surface energy transfer processes that depend on the morphology of Cu layer. According to the AES data presented in Figure 62A, dispersed clusters for χ_{Cu} > 50 min (0.83 ML) and a thick film of copper for χ_{Cu} > 90 min (2.5 ML) formed. The thick Cu film is typically smoother (less corrugated) than dispersed clusters. Considering a simple hard sphere model, an efficient gas-surface transfer (higher S_0) is expected for a corrugated surface, when compared to a less corrugated surface (lower S_0).[233] This could possibly explain the decreasing trend observed in S_0 (Figure 66).

S_0 vs. Cu exposure time curves ("growth curves", Figure 66) were also obtained for other supported cluster systems. However, the shape of growth curve obtained for Au/silica system was different from the one obtained for Cu/silica.[40, 153, 208] In the case of Au/silica, the reactivity of the clusters dramatically changed with their size, resulting in more complex growth curves. Thus, the growth curves would reflect the differences in cluster growth morphologies and reactivity trends.

4.1.3.5. Initial adsorption probabilities of CO: Temperature effect

In the case of nonactivated adsorption of CO, the initial adsorption probability (S_0) of CO would be unaffected with the changes in surface temperature (T_s).[225] However, the capture zones surrounding the Cu clusters generate the temperature dependence of S_0. Both the surface residence time and diffusion time decrease with an increase in T_s. Therefore, even for nonactivated molecular adsorption, an increase in T_s reduces the size of the capture zones and leads to a decrease in S_0. This is indeed observed from the data depicted in Figure 67. S_0 vs. T_s curves at constant E_i and parametric in Cu deposition time are depicted .

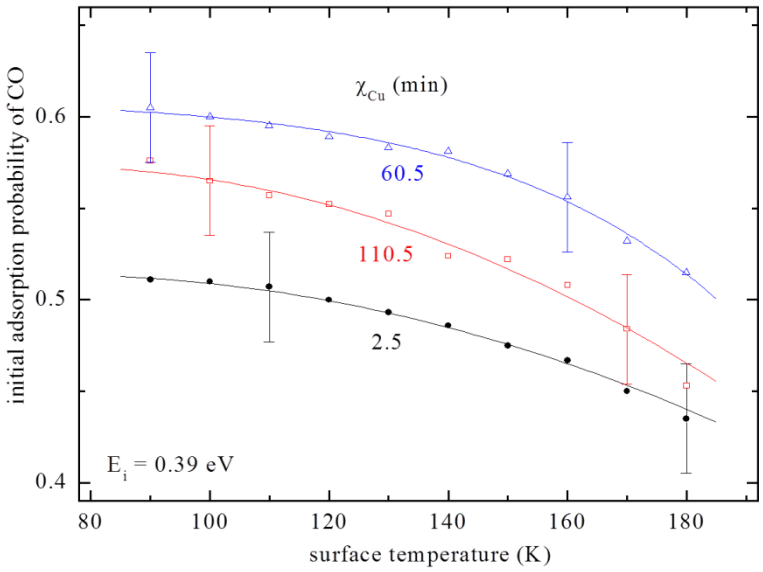

Figure 67. S_0 of CO as a function of surface temperature, T_s for different Cu exposures. Impact energy of CO, E_i was kept constant. Ref.[39]

S_0 of CO decreases (for constant χ_{Cu}) with T_s due to the decrease in the size of the capture zone. As described earlier, cluster size effects are evident while varying χ_{Cu}. S_0 initially increases with an increase in χ_{Cu} [see curves for 2.5 min (0.04 ML) and 60.5 min (1 ML) deposition time]. This is attributed to an increase in the capture zone that results from increased dispersion and increased number of Cu clusters. A small but decreased trend in S_0 is observed for

large Cu coverages [see curves for 60.5 min (1 ML) and 110.5 min (3.7 ML) Cu deposition time]. As discussed earlier, this trend is attributed to a dynamic effect caused by variations in Cu cluster morphology.

4.1.3.6. Initial adsorption probabilities of CO: Impact energy effect

The impact energy (E_i) dependence of S_0 at low T_s is depicted in Figure 68 for different Cu deposition times. Two independent measurements conducted on two different samples that have the same coverage [χ_{Cu} = 110.5 min (3.7 ML)] are depicted. However, a different Cu doser was used for the second sample. The data of these two measurements match perfectly. The corresponding single crystal [Cu(111)][234] data is also depicted.

The decrease in S_0 with E_i is clearly evident. This is typical for nonactivated molecular adsorption of CO.[235] In simple terms, the gas-surface energy transfer is not efficient in the case of probe molecules with large E_i due to their short interaction times with the surface. Therefore, S_0 decreases with an increase in E_i.

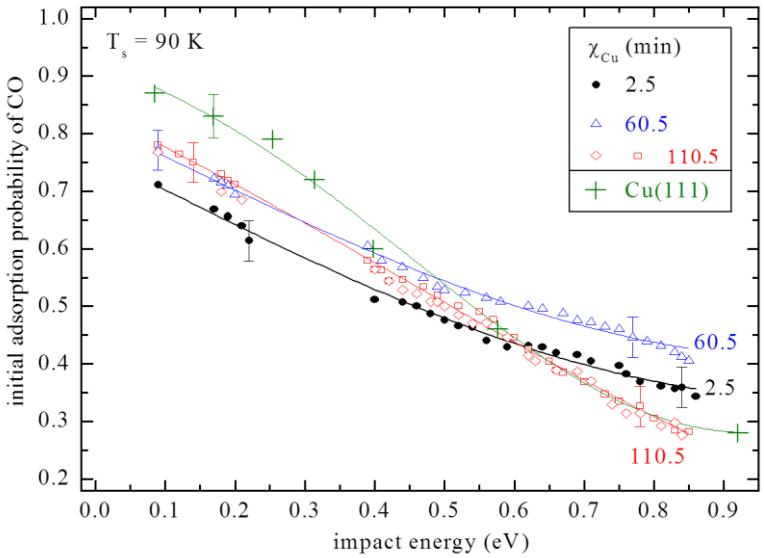

Figure 68. S_0 of CO on Cu/silica as a function of impact energy for different Cu exposures[39] and Cu(111).[234] The surface temperature, T_s was kept constant.

At constant E_i, the observed changes in S_0 for clusters with different χ_{Cu} are within (or close to) the experimental uncertainties. However, larger effects are observed for other supports.[154] At low E_i (slow-moving CO), similar S_0 values are obtained for clusters with different χ_{Cu} because the gas-surface energy transfer details are not important in gas-surface interaction. At large E_i (fast-moving CO) , the differences in S_0 are larger because the details of the gas-surface energy transfer processes become crucial in determining the fate (adsorption vs. desorption) of CO molecules. The variation in S_0 for clusters with different χ_{Cu} at E_i = 0.85 eV were due to the cluster size effects. S_0 initially increases with χ_{Cu} due to an increase in the number and size of Cu clusters. This results in an increase of the total capture zone and S_0. However, S_0 decreases with the formation of a thick Cu film. This is attributed to the smoothness of Cu film. The conclusion is further supported by a close match between the $S_0(E_i)$ values obtained for clusters with large χ_{Cu} and Cu(111) single crystal.[234]

4.1.3.7. Coverage dependence of CO adsorption probabilities

Examples for the CO coverage dependent adsorption probabilities, $S(\Theta)$, are given in Figure 69. $S(\Theta)$ vs. E_i curves (at low T_s) for small (Figure 69A) and large (Figure 69B) χ_{Cu} are depicted. The capture zone model (CZM) assumes the trapping of adsorbates on the surface and subsequent diffusion to the clusters, i.e., the CZM is a special case of precursor mediated adsorption. Therefore, Kisliuk-like shapes of $S(\Theta)$ curves were expected and are indeed seen here (Figure 69). The molecules are initially trapped in an extrinsic/intrinsic precursor state. Therefore, $S(\Theta)$ remains constant until the CO coverage reaches a saturation level, after which it drops to zero. $S_0 = S(\Theta \rightarrow 0)$ scales with E_i, T_s, and χ_{Cu}, as already described.

A kinetic model for methanol synthesis was presented in prior studies based on the reaction mechanisms deduced from Cu single crystal studies.[28] Therefore, it is necessary to

compare different model catalysts.[28] A single molecular beam scattering study concerning the CO adsorption on Cu model catalyst [Cu/ZnO(0001)] was available.[154] Molecular beam scattering of CO_2 on Cu/ZnO(0001), a traditional methanol synthesis model system, was also investigated.[109] Other metal and support combinations were also investigated and were reviewed in refs.[21, 236-239] S_0 of CO on Cu/silica was slightly larger ($\Delta S_0 \sim 0.1$) than on Cu/ZnO(0001)[224] for large E_i of CO. Higher S_0 values are a prerequisite for high catalytic activity in surface reactions. Cu/ZnO(0001) was significantly more reactive ($S_0 \rightarrow 0.1$) than Cu/silica for small E_i.

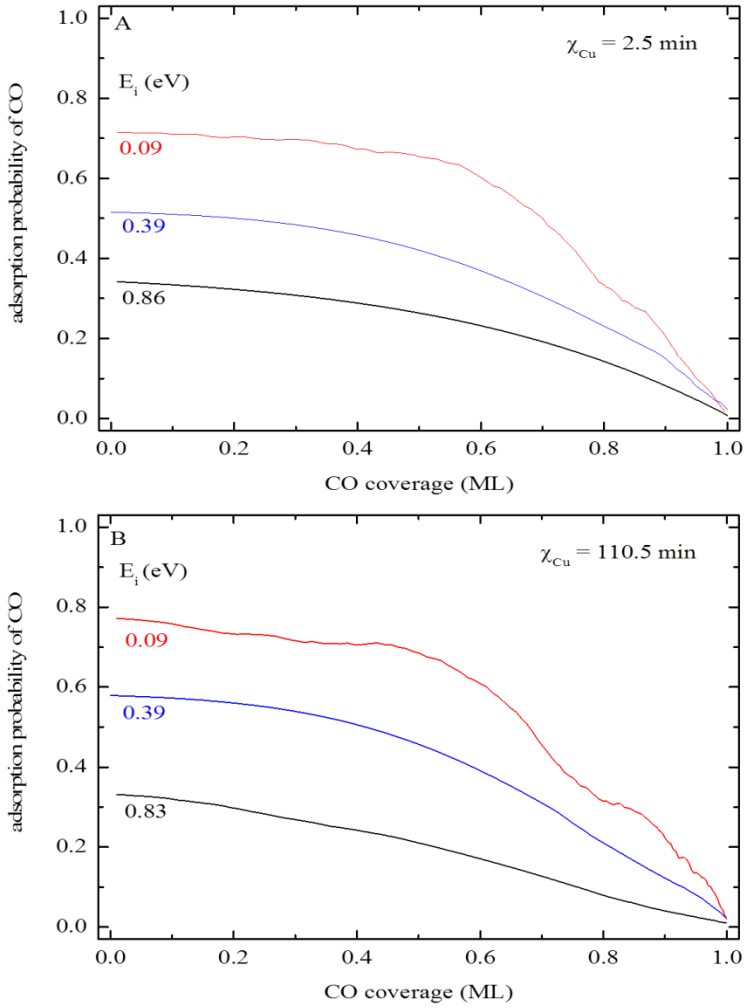

Figure 69. S(Θ) curves of CO on Cu/silica for (A) small (2.5 min) and (B) large (110.5 min) Cu coverages. The impact energy (E_i) of CO was varied as indicated. Ref.[39]

4.1.4. Summary

The adsorption of CO on silica-supported Cu clusters was studied using spectroscopic (Auger electron spectroscopy and x-ray photoelectron spectroscopy), kinetic (Thermal desorption spectroscopy), and dynamics (Molecular beam scattering) techniques. Morphology characterization of the system was available from prior studies.[8, 213, 215-216] In agreement with prior studies, the AES, XPS, and TDS data obtained for Cu/silica indicates three stages in the AES growth curve of Cu clusters: nucleation of Cu clusters on silica for short time Cu deposition, formation of 3D clusters (cluster growth regime), and thick film formation for long time Cu deposition. The beam scattering data indicates smooth surface morphology of Cu films. The unusual growth dynamics of Cu on silica is explained by coverage-dependent adsorption probabilities of Cu. XPS data confirms the metallic state of Cu clusters at UHV conditions.

The adsorption dynamics of CO on Cu/silica was modeled within the framework of capture zone model (CZM). Accordingly, the CO molecules that adsorbed on the silica support subsequently diffuse to the Cu clusters, the high-binding energy sites. Thus, the CZM is a precursor model consistent with the Kisliuk-like shaped coverage dependent adsorption probability, $S(\Theta)$ curves of CO observed in the present study. The capture zone's size decreases with surface temperature, T_s, explaining the observed decrease in initial adsorption probability (S_0) with T_s. Similarly, the total area of the capture zone increases with an increase in the number and size of Cu clusters, explaining the observed increase in S_0 with Cu deposition time. S_0 of CO on Cu clusters with large Cu deposition time, χ_{Cu} approached a value that was obtained in prior studies on Cu(111), indicating the formation of less corrugated Cu films. S_0 decreased with impact energy, E_i, indicating the molecular and nonactivated adsorption of CO on Cu/silica.

4.2. CO Adsorption Dynamics on Silica-supported Cu & Au Clusters: Cluster Size Effects

An introduction to the significance of catalytically active sites in heterogeneous catalysis is presented first, followed by the fabrication of silica-supported Au and Cu clusters. A combined results and discussion section is presented next. A summary of the experimental results obtained in this study is given at the end.

4.2.1. Introduction

The idea that different adsorption sites exist on surfaces dates back at least as far as Irving Langmuir. The concept of catalytically active sites was first introduced in heterogeneous catalysis by Taylor in 1925.[240] The concept of active sites is still being used in the modern era of surface science, catalysis, and nanoscience.[102-103, 241-242] A recent example of the 'active site' concept is the correlation of active edge sites on MoS_x nanocatalysts with the catalytic activity towards hydrodesulfurization[93] and electrochemical hydrogen evolution.[146] Despite a growing number of studies on the nanogold system,[49, 102-103, 207] only a few studies investigating the effect of supported nano-clusters on the adsorption dynamics are available.[243-246] The adsorption of gas-phase species is the first step in gas/solid heterogeneous catalysis. Therefore, the adsorption dynamics can affect the reaction mechanisms. Initial adsorption probability (S_0) measurements are useful to quantify the number of active sites on a catalyst surface.

The adsorption of CO is the first step in converting CO to CO_2, which is an important prototype reaction. Both the gold [$Au/TiO_2(110)$] and copper [Cu(110)] systems exhibited low temperature activity for CO oxidation.[246-247] However, distinct cluster size effects for supported gold clusters are very well-known.[49] The atomistic details of these cluster size effects and the unique catalytic activity of gold are still being debated.[9, 55, 243, 248-251] In contrast to the standard adsorption dynamics on Cu/silica, CO exhibited unusual adsorption dynamics on Au/silica. The

unusual reactivity of Au clusters was attributed to the role of defect sites. Molecular beam scattering technique was used to measure S_0 of CO on silica-supported Au and Cu clusters. The data for silica-supported gold clusters were recently presented.[40] A direct comparison of the adsorption dynamics data obtained on silica-supported Au and Cu clusters provide clear evidence for the presence of active sites on a catalyst surface.

4.2.2. Sample fabrication

Silica-supported Au[40] and Cu clusters[39] were made by physical vapor deposition process.

4.2.3. Results and discussion

The beam scattering data shown here were collected at an adsorption temperature of negligible CO uptake on the silica supports.[153-154]

4.2.3.1. Cluster growth mode

The cluster growth mode for gold[252-254] and copper[8, 213-217, 255-256] on silica were very similar. The cluster growth mode involved three stages: nucleation, growth, and film formation. This growth mode is also confirmed by AES, XPS, and SEM data collected on silica-supported Au clusters.[40] The labels 'nucleation phase,' 'growth phase,' etc., in Figure 70, are based on the AES data[39] and the reference data from prior studies. The formation of very small clusters (0.1–0.3 nm) for low coverage and a continuous copper grain (~ 20 nm) structure for high coverage were reported for silica-supported Cu clusters.[8, 216] Similarly, the formation of sub-10 nm Au clusters was also reported for Au/silica model catalysts.[40]

CO typically adsorbs on rim, edge, and the terrace sites of supported nanoclusters. However, in contrast to Cu and other systems, the large Au clusters are catalytically inactive. Terrace sites are dominant when compared to rim sites in the case of large Au clusters. CO does not adsorb on the terrace sites of Au. As an example, the total coverage of CO on small Au

clusters was found to be large when compared to large clusters.[250] The number of adsorption sites on a catalyst surface can be determined using initial adsorption probability (S_0) measurements.

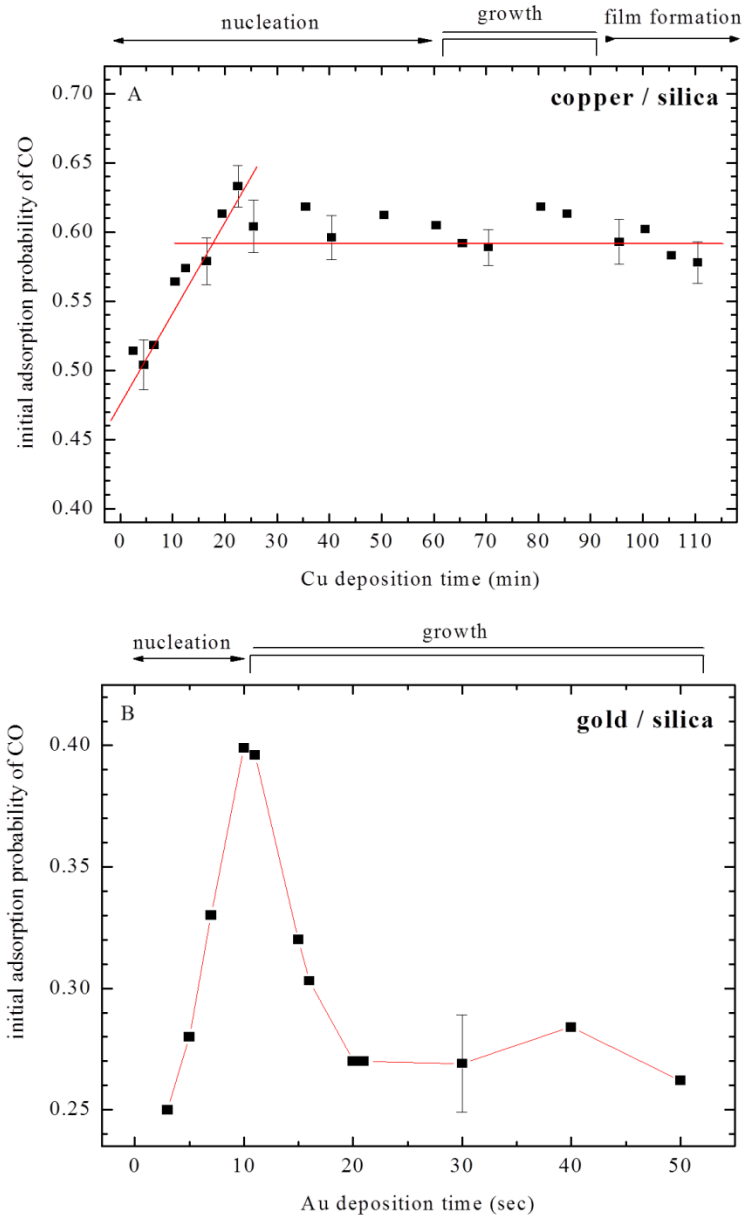

Figure 70. S_0 of CO as a function of metal deposition time for (A) Cu/silica[39] and (B) Au/silica[40] (T_s ~ 90 K and E_i = 0.39 eV). The growth mode was determined by AES in comparison with the literature.

4.2.3.2. Copper clusters

Initial adsorption probability (S_0) is depicted as a function of cluster deposition time (Ŧ) for silica-supported copper (Figure 70A) and gold (Figure 70B) clusters. The S_0(Ŧ) curves obtained for the Au and Cu systems were different. S_0(Ŧ) curve for Au clusters showed a peak maximum at Ŧ = 10 s; whereas, it appeared like a smooth step-like function for Cu clusters. The observed shape of S_0(Ŧ) for copper was predicted by the CZM. However, the S_0(Ŧ) data obtained for Au was unusual. The initial increase in S_0, as a function of Cu coverage (Figure 70A), was predicted by the CZM. Accordingly, S_0 initially increased with Cu coverage in the nucleation regime due to an increase in the total capture zone formed around all Cu clusters. Assuming the size independent catalytic activity of Cu clusters however, once the coverage and dispersion of clusters became large enough, the individual capture zones overlapped with no further increase in S_0 with Ŧ. As described earlier, the initial increase in S_0 is a kinetics effect. The S_0 value obtained for large Cu coverages is very close to that obtained on Cu single crystals.[257]

4.2.3.3. Gold clusters

As evident from Figure 70B, the density of Au clusters increased rapidly for Ŧ < 10 s during the nucleation phase. Therefore, S_0 of CO initially increased with Ŧ due to an increase in the number of catalytically active sites (similar to Cu clusters). This effect was in contrast to the site blocking effects observed for CO adsorption on Ir(110).[235] In this case, S_0 decreased linearly with an increase in O precoverage due to the blocking of catalytically active sites. In the present case, S_0 initially increased due to the formation of active sites during Au cluster deposition. However, the Au cluster size further increased (growth regime) with Ŧ after the nucleation regime. The cluster density remained essentially constant.[253-254] This resulted in a decrease in the relative fraction of low-coordinated Au sites, which can also be theoretically proved using the

so-called Wulf construction of clusters.[258] Therefore, S_0 of CO decreased within the cluster growth regime (Figure 70B) due to a decrease in the number of low-coordinated sites. In other words, the large 2D Au clusters were less reactive than small ones. Interestingly, the maximum in $S_0(Ŧ)$ corresponded to a cluster size of ~ 2 nm (the Au cluster size was determined by performing statistical analysis of SEM images).[153] Au particles of this size have been found to exhibit the highest catalytic activity in prior studies.[52] However, the variations in S_0 were rather small. Obviously, the catalytic activity of gold is not governed by adsorption dynamics alone, but several other factors such as electronic, structural, and support effects.

4.2.4. Summary

Supersonic molecular beam scattering was used to determine the adsorption probabilities of CO on silica-supported Cu and Au clusters. The variation in $S_0(Ŧ)$ observed for these clusters nicely reflects the variation in the density of catalytically active sites. Nano Au clusters exhibit unusual adsorption dynamics for CO. Unlike the weak cluster effects observed for Cu/silica system, the Au/silica system exhibits clear cluster size effects on CO adsorption. dynamics.

4.3. Adsorption Dynamics of CO on EBL-fabricated Silica-supported CuO_x Clusters

An introduction to the EBL fabricated silica-supported Cu clusters and their significance in studying the cluster size effects on catalytic activity is presented first, followed by the sample fabrication, cleaning, and characterization. A combined results and discussion section is presented next. A summary of the experimental results obtained in this study is given at the end.

4.3.1. Introduction

The introduction includes the motivation for using EBL-fabricated Cu clusters for studying the cluster size effects in catalysis and a brief literature survey about copper-containing catalysts and CO adsorption on supported Cu catalysts.

4.3.1.1. Motivation

The use of nanoparticles for promoting catalytic processes is a fast growing field. The influence of clusters' sizes, shapes, rims, and the chemical compositions on the chemical/catalytic activity of metal clusters are currently being investigated.[16] Electron beam lithography (EBL) could be used to nanofabricate the so-called model nanoarray catalysts,[40, 46, 259-261] i.e., nearly monodisperse cluster samples with a predetermined pattern on a substrate. EBL could be used to nanofabricate the clusters with predetermined size, shapes and height. This avoids the time consuming morphological characterization of the samples. However, the EBL samples used in the current project were analyzed by SEM. In addition, AES and XPS were used to characterize the cleanliness and chemical state of the samples. Although the smallest size of the clusters that can be made covering a macroscopic surface is still technically limited, the cluster size effects can be studied in a unique way by utilizing EBL. Silica is conventionally used as a support for nanostructures. In addition, SiO_2 supported catalysts have practical applications in methanol steam reforming[262] and hydrogenation reactions.[263] In the present study, the cleaning cycles used for Cu EBL samples also oxidized the Cu clusters to form CuO and Cu_2O moieties. However, AES and XPS were used to characterize different Cu oxides both before and after each kinetics/dynamics experiment. This made it possible to compare the chemical activities of Cu and CuO_x clusters. The electronic structure of clusters may affect kinetics and dynamics properties, as reported in prior studies.[264-265] Owing to the abundance and low cost of copper, it has been used extensively for catalytic applications, such as methanol synthesis,[28, 210] low-temperature CO oxidation,[266] water-gas shift reaction,[267] and water splitting under visible light irradiation.[268] Cu is also being used for several applications in materials science, such as solar cells[269] and high-temperature superconductors.[270] In the current study, CO is used as a probe

molecule due to its relevance for a number of catalytic processes. CO is also a standard surface science probe molecule. The adsorption dynamics of CO was characterized using molecular beam scattering technique. Utilizing beam scattering techniques is advantageous to study EBL samples that typically have small clusters with a large dispersion (small total coverage) because the molecular beam can directly be focused onto the surface while keeping the background pressure low.

4.3.1.2. Brief literature survey

Copper-containing catalysts are useful for a variety of chemical reactions. Supported copper nanoclusters, in particular, have been widely used in heterogeneous catalysis. The copper cluster literature is dominated by studies that focused on Cu nanoparticle powders that were synthesized by wet-chemical/electrochemical methods.[219, 271-273] Most of the investigations on these powder samples focused on surface reactions. Several techniques such as infrared spectroscopy (IR), XRD, XPS, and SEM, were used to characterize the supported powder systems. Despite the importance of Cu catalysts, very few UHV kinetics/dynamics studies concerning the adsorption of small molecules on Cu system are available. The Blyholder model for CO adsorption on metal surfaces has to be modified for metal oxides.[274] As evident from the TDS data, the differences in the electronic structure lead to larger binding energies of CO on $Cu_2O(100)$.[275] According to prior studies, CO adsorbed/desorbed molecularly on Cu metal oxide single crystals, indicating no CO_2 formation.[275] However, CO was oxidized to CO_2 on silica-supported Cu_2O nanoparticles,[272] as well as Cu single crystals.[247]

The so-called capture zone model (CZM) is considered to explain the dependence of S_0 on cluster size of the nanoparticles. In certain cases, depending on binding energies, the size of the capture zone can be significant even at high surface temperatures.[154, 160, 230] Prior studies

concerning the adsorption dynamics of CO and CO_2 on Cu/ZnO and Cu single crystals are known.[154, 225, 276-277] However, surface chemistry studies of CuO_x cluster systems, the molecular beam scattering[154] in particular, are rare. In addition, very few studies have utilized EBL technique for the fabrication of model catalysts.[40, 46, 259-261]

4.3.2. Sample fabrication and cleaning

The details of sample fabrication will be presented first, followed by the sample cleaning procedures and Cu cluster oxidation/reduction procedures.

4.3.2.1. Sample fabrication

The Cu nanoclusters were fabricated by EBL at Molecular Foundry (Lawrence Berkeley National Laboratory). The nanofabrication procedures of the EBL cluster samples is described elsewhere.[40] Cu cluster samples with d_s = 12 nm and d_l = 63 nm diameter were fabricated with a lattice constant of a_s = 100 nm and a_l = 150 nm, respectively. A Cu layer of thickness, h = 5 ± 2 nm was used in the fabrication process and a 5x5 mm area on a 10x10 mm silica support was covered with the clusters.

4.3.2.2. Sample cleaning

As discussed in the pioneering works of Somorjai and Kasemo on EBL samples,[259-260] the cleaning of EBL samples without changing the morphology and/or the chemical composition is a challenging task. In the present study, the 12 and 63 nm Cu/SiO_2 model nanoarray catalysts were annealed in a flux of atomic hydrogen [$p(H_2) = 7x10^{-8}$ mbar, Ts = 480 K] generated by a thermal hydrogen doser (Tectra) to remove impurities, following the procedures used in our prior projects.[40, 153] Atomic hydrogen annealing removed the surface carbon as judged by AES. In some cases, sulfur impurities were also present and the atomic hydrogen annealing was not efficient in removing S. Therefore, the samples were annealed in molecular oxygen

[$p(O_2)$ = 2x 10^{-5} mbar, Ts = 500 K] to remove S. However, molecular oxygen annealing also oxidized the Cu nanoclusters.

4.3.2.3. Reduction of copper oxide

In the present study, the metallic and oxidic-like Cu clusters were considered. The CuO_x was reduced to Cu by annealing the CuO_x/SiO_2 sample in molecular hydrogen [$p(H_2)$ = 5x10^{-5} mbar, 420 K]. The chemical state of Cu nanoclusters was monitored by XPS throughout the project. The presence/absence of oxide satellite features indicate CuO_x/Cu chemical state of Cu nanoclusters. The Cu nanoclusters were found to be very stable at UHV conditions, as confirmed by the reproducible AES, XPS, and molecular beam scattering data. The EBL samples were never annealed above 500 K, well below the Tammann temperature of Cu (678 K)[278] in order to avoid the sintering of Cu clusters. Sintering effects were observed in one of our prior studies on Au EBL samples.[208] In the prior study, when annealed above 600 K, the Au clusters sintered and reduced the adsorption probability of CO. However, the sintering effects were not observed for the Cu EBL samples due to the low temperatures used for cleaning and measurements.

4.3.3. Results and discussion

The morphological characterization of EBL-fabricated silica-supported Cu clusters will be presented first, followed by a spectroscopic characterization of the chemical state of Cu clusters. Adsorption kinetics and dynamics of CO on Cu EBL samples will be presented next.

4.3.3.1. Sample morphology

The sample morphology was studied by SEM. SEM images were collected using Zeiss Ultra 60 field-emission SEM that has a nominal resolution of ~1.2 nm at an acceleration voltage of 20 keV. The SEM image of 12 nm Cu clusters is shown in Figure 71A. The particle size distributions for 12 and 63 nm Cu cluster samples are shown in Figures 71 B and C respectively.

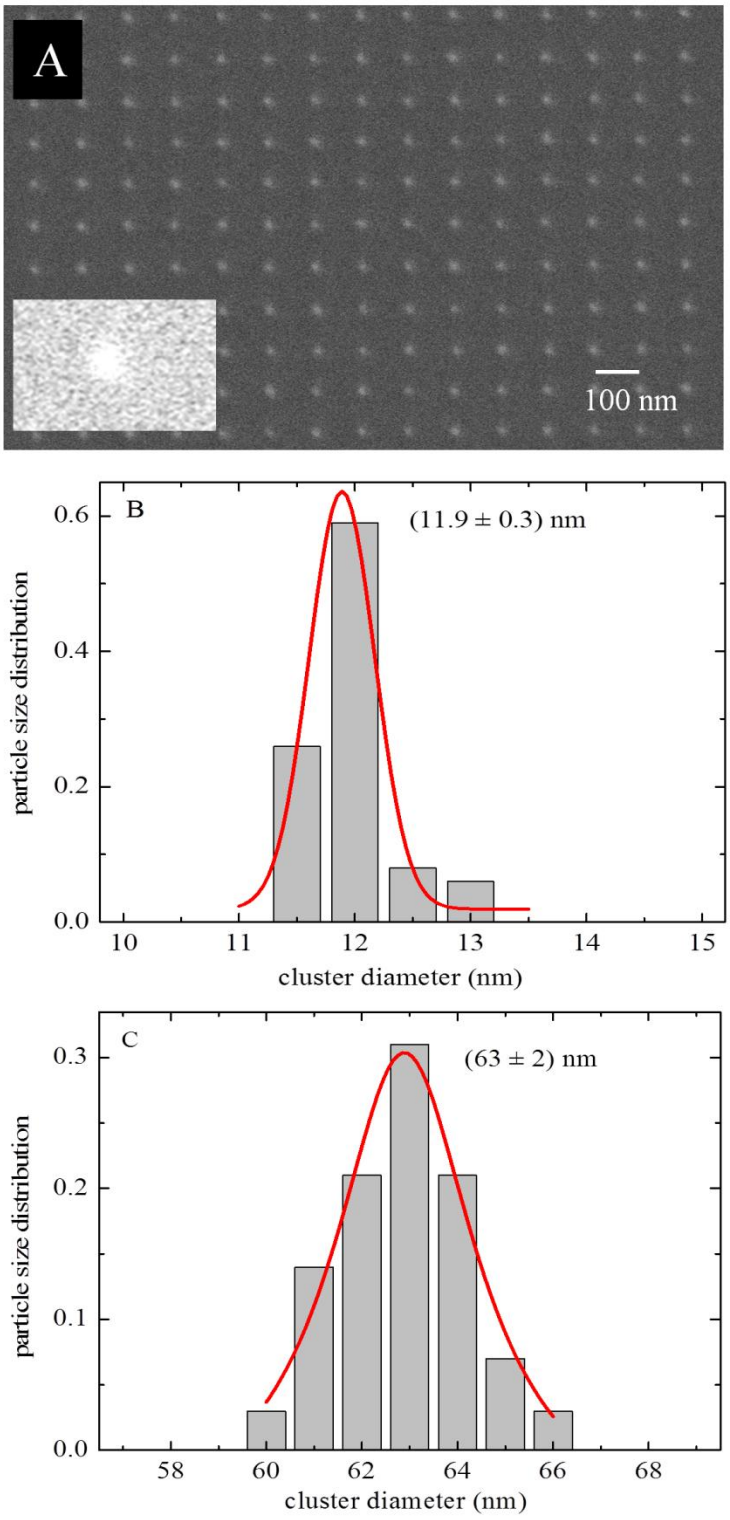

Figure 71. (A) SEM image of 12 nm Cu EBL sample and particle size distributions for (B) 12 nm and (C) 63 nm Cu cluster samples. The inset of A shows a close-up SEM image of a single Cu cluster. Ref.[48]

As evident from Figure 71A, the clusters had a predetermined square pattern and were separated by a_s = 100 nm. The inset of Figure 71A shows an enlarged image of a single Cu cluster. The SEM image did not reflect the actual shape of the cluster and appeared rather like a structureless spot. This might be due to the resolution/contrast limits of scanning electron microscope.

Figures 71B and C depict the size distribution of Cu clusters obtained (using the software tool Pixcavator) by analyzing an area of 1.4x1 μm section. Accordingly, the most probable diameter (cluster size) for the small (s) and large (l) clusters amounted to $d_s = 11.9 \pm 0.3$ nm and $d_l = 63 \pm 2$ nm, respectively, with a lattice constant of $a_s = 100 \pm 1$ nm and $a_l = 150 \pm 4$ nm. A very narrow cluster size distribution was observed for EBL samples, e.g., 0.3/11.9 ≈ 2.5% using the full width at half maximum of the Gaussian fit shown in Figure 71B.

Assuming the circular shape for Cu clusters, the calculated Cu coverage (ratio of Cu area to support area, $= \frac{1}{4}\pi d^2/a^2$ amounted to 0.011 ML and 0.139 ML for the small (12 nm) and large (63 nm) clusters, respectively. The Cu coverage for large clusters was by a factor of 12.6 ± 1.0 larger than the small clusters. It is important to note that the uncertainties in the theoretical predictions are related to the cluster size variations. Thus, if the adsorption dynamics is dominated by terrace sites, the saturation coverage of CO, Θ_{sat}, for large clusters should also be a factor of 12.6 ± 1.0 larger than the small clusters. Relative Θ_{sat} can be determined using the beam scattering data and will be explained later in the discussion. However, the total rim length was given by $\rho A \pi d$, where A is the total area covered by Cu clusters and ρ is the cluster density (particles per area). Therefore, the ratio (large/small clusters) of the rim lengths amounted to $d_l\rho_l/d_s\rho_s = 2.3 \pm 0.4$. Thus, if the rim effects dominate the adsorption dynamics, the Θ_{sat} for 63 nm clusters should also be a factor of 2.3 ± 0.4 larger than the 12 nm clusters. (The assumption is

that the rim length and surface area of Cu clusters are proportional to the number of adsorption sites and that the rim is a 1-D structure.) The former assumption was trivial. The latter was a good assumption considering the small aspect ratio of the clusters. The cluster density ($=1/a^2$) decreased from $\rho_s = 1\times10^{-4}/nm^2$ to $\rho_l = 4\times 10^{-5}/nm^2$ when comparing the 12 nm vs. 63 nm cluster samples. If CO adsorbed on both the rim and terrace sites, then Θ_{sat} should increase by a factor of 6 ± 0.8 when comparing the 12 nm vs. 63 nm cluster samples. In order to do such estimation, a 2D rim with a height of h = 5 nm was considered. This assumption might have overestimated the area of rim sites. The total area of terrace and rim sites was given by $\pi A\rho d(\frac{1}{4}d + h)$. Similarly, the calculated ratio of the rim area to cluster size (= 4h/d) is 1.66 and 0.32 for 12 and 63 nm clusters, respectively. Therefore, the special properties of rim adsorption sites (if present) should be most distinct for the small Cu clusters. It is more advantageous to use EBL samples for model studies because such estimates are possible without very time-consuming characterization, e.g. STM.

4.3.3.2. Spectroscopic characterization of the chemical state of the Cu clusters

AES and XPS are used to characterize the chemical state of Cu clusters. Spectroscopic data for the 12 nm Cu cluster sample is not explicitly shown.

4.3.3.2.1. Brief literature survey

A large number of XPS studies on copper systems are available. In the present study, XPS is only used to characterize the chemical state of catalyst before and after the reactivity tests with CO. Although, each of the Cu oxides has a distinct LMM AES peak position, the bulk CuO (powders, single crystals) is characterized by the presence of intense Cu 2p XPS shakeup satellites and a broad O 1s peak.[227] In contrast, Cu_2O and metallic Cu show weaker/no Cu 2p XPS satellites and a narrow O 1s peak.

It is experimentally challenging to distinguish the oxidation state of Cu based on the LMM AES peak position due to the charging effects. Unfortunately, whether or not the inspection of LMM AES signature is required to distinguish the oxidation state of Cu is controversial. According to an XPS study on Cu oxides,[279] the Cu 2p shakeup satellite peaks are formed due the charge transfer into 3d bands (Cu^0 has a fully filled 3d orbital). Therefore, the presence of small Cu 2p satellite peaks indicates Cu_2O, and their complete absence indicates Cu^0. The same holds true for Cu clusters. However, the XPS peak positions of Cu^0 also depend on clusters' morphology (primarily on coverage) and support. Therefore, a correct assignment of the Cu clusters' oxidation state based on XPS/AES peak positions is quite challenging.[221, 280] In this study, the absence of XPS satellite peaks indicate nearly metallic (Cu^0-like) Cu clusters; whereas, the presence of intense XPS satellite peaks indicate fully oxidized (CuO-like) Cu clusters.

4.3.3.2.2. AES/XPS measurements

AES scans of the as received and cleaned 63 nm Cu cluster samples are depicted in Figure 72A. XPS data of the cleaned sample is depicted in Figure 72B. The XPS spectra were referenced with respect to Si 2p XPS peak corresponding to a binding energy of 103.4 eV. Evidently, only the XPS peaks arising from the support and Cu clusters were present for a cleaned sample. The observed peak positions are consistent with the data obtained in prior studies[8, 213-217, 255-256] and the reference data.[222-223] The inset depicts the Si 2p XPS region. The presence of a single peak confirmed the fully oxidized state of silica support.[223] It is important to note that a partially reduced silica exhibits two features in the Si 2p XPS region.[48] Therefore, the cleaning procedures did not reduce the support. The cleaning procedures affected the oxidation state of Cu clusters. However, the support remained fully oxidized throughout the project. This is

an important result because silicon (Si^0) is more reactive towards certain probe molecules than silica (Si^{4+}), e.g., silica is inert towards hydrogen, which enables one to distinguish between cluster and support effects.

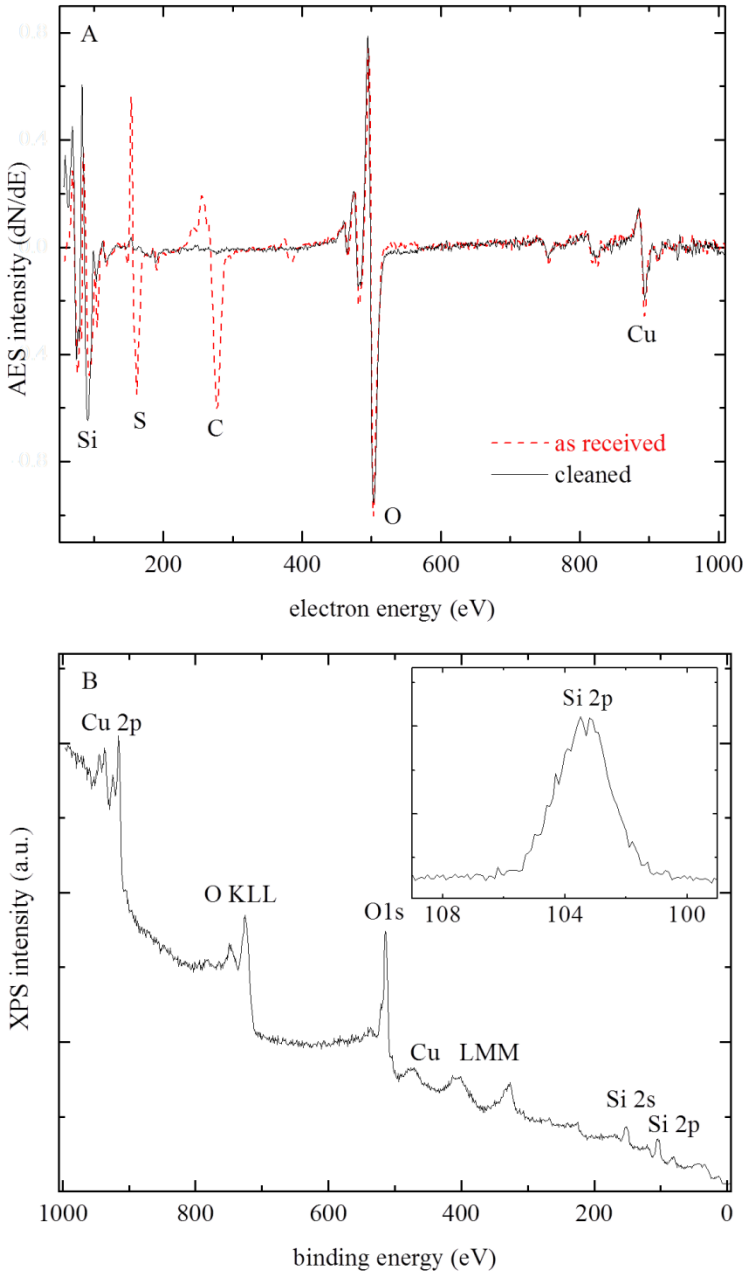

Figure 72. AES and XPS spectra of 63 nm Cu EBL sample. (A) AES spectra of 63 nm Cu EBL sample. (B) XPS survey spectrum of the clean 63 nm Cu EBL sample. The inset shows the Si 2p XPS peak. Ref. [48]

4.3.3.2.3. Oxidation state of the Cu clusters

The silica-supported Cu EBL samples were annealed at 500 K in oxygen [$p(O_2) = 2x\ 10^{-5}$ mbar] to oxidize them to CuO_x nanoclusters. The CuO_x was reduced to Cu by annealing the CuO_x/SiO_2 sample at 420 K in hydrogen [$p(H_2) = 5x10^{-5}$ mbar]. The chemical state of Cu nanoclusters was monitored by XPS throughout the project. The presence/absence of oxide satellite features indicate CuO_x or Cu chemical state of Cu nanoclusters.

Figure 73 depicts typical examples of the Cu 2p XPS region of the metallic and fully oxidized silica-supported 63 nm Cu clusters. Similar results were obtained for the 12 nm Cu clusters. These results were in good agreement with the literature (see Table 4). Thus, the nearly metallic, partially oxidized, and fully oxidized Cu clusters were prepared by following specific cleaning procedures. The oxidation-reduction of Cu clusters is reversible at UHV conditions as evident from Figure 73. The Cu cluster oxidation/reduction was reversible, as supported by the AES/XPS.

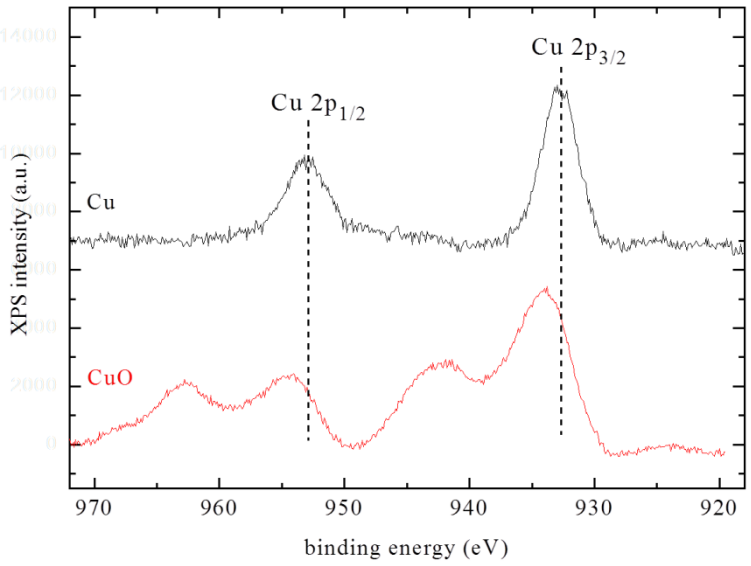

Figure 73. Cu 2p XPS data for the metallic (Cu) and fully oxidized (CuO) 63 nm Cu EBL sample. Ref.[48]

Table 4. Cu $2p_{3/2}$ XPS line positions for Cu and Cu oxides.[a] Ref.[48]

	This wok	Other studies	System	ref
Cu	932.7	932.8	Single crystal	[279]
		933.1-932.7	Cu/Zr	[221]
		932.6	Metallic Cu	[227]
Cu_2O	932.8	932.6	Single crystal	[279]
		932.3	Thin films	[281]
		933.0-932.4	Cu_2O/SiO_2	[221]
		932.4	Nanocrystals	[282]
		932.4	Powder	[227]
CuO	934	933.8	Single crystal	[279]
		933.9	Thin films	[281]
		935.5-933.8	CuO/SiO_2	[221]
		933.5	Nanocrystals	[282]
		933.6	Powder	[227]
[a]The Cu_2O data refers to 12 nm Cu clusters sample, and the rest of the data is for 63 nm Cu sample.				

4.3.3.3. Kinetics

Figure 74 summarizes CO TDS data on 63 nm Cu EBL samples for metallic (panel A) and fully oxidized (panel B) Cu clusters. CO gas was dosed with the molecular beam (the intensities are given in arbitrary units). A heating rate of 1.7 K/s was used for TDS experiments. In the case of metallic clusters (Figure 74A), a very broad TDS peak appeared. This peak shifted slightly to low temperatures with an increase in CO exposure. TDS signals were weak and noisy due to the small overall Cu coverage.

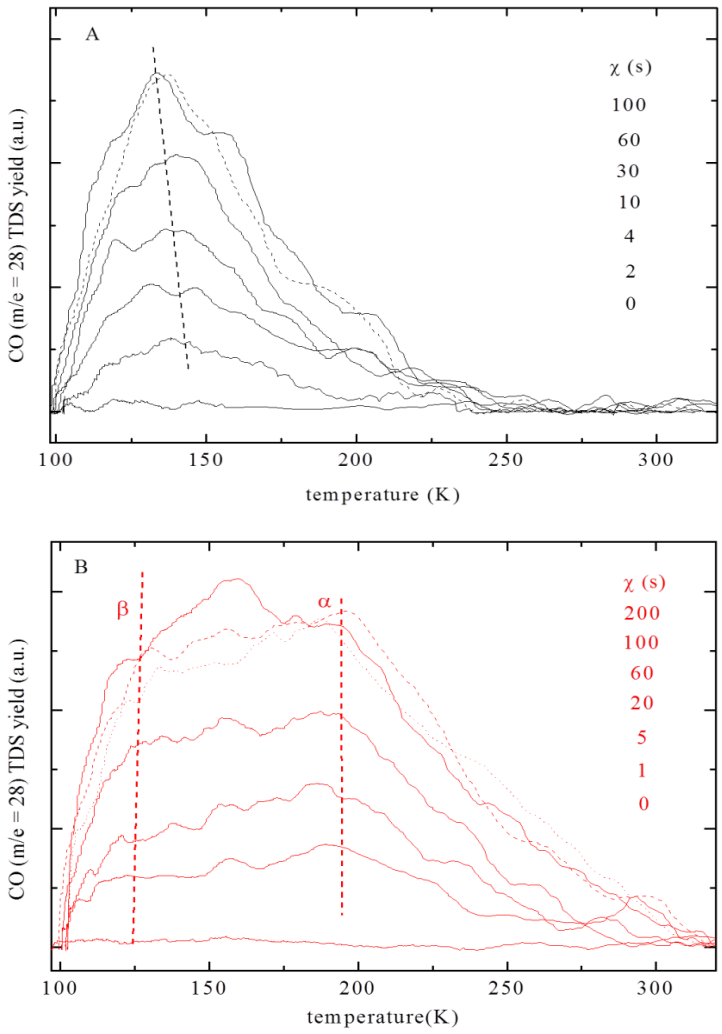

Figure 74. CO TDS on silica-supported 63 nm Cu clusters that are (A) metallic and (B) oxidic. CO gas was dosed with the molecular beam. Ref.[48]

Distinct adsorption sites, repulsive interactions, or a combination of both might cause the observed TDS peak width and shift. The lateral interactions of CO were ruled out because the total coverage of CO was small, even on the large Cu clusters. However, the small clusters have a large rim-to-surface area ratio. This further supported our conclusion that the presence of different adsorption sites caused the peak broadening. By assuming a pre-exponential of $1x10^{13}$/s, the binding energies of CO were calculated using the Redhead equation. TDS peak positions and binding energies of CO are given in Table 5.

Table 5. Binding energies of CO on Cu and CuO clusters (EBL) as compared to literature values.[a] Ref.[48]

	T_{peak} (K)	E_d (kJ/mol)	system	ref
Cu^0	203	49.4	Cu(311)	[283]
	430	107.5		
		58.6	Cu(110)	[284]
		54.3	Cu(111)	[285]
CuO	132-143	33.6-36.5	63 nm EBL clusters	This work
	(α) peak	50.2	63 nm EBL clusters	This work
	(β) peak	31.7		
[a]The uncertainty is temperature calibration amounts to ± 5K, which results in an uncertainty of ± 1.3 kJ/mol in binding energies.				

The TDS peak width was similar to the data collected in our prior study on Cu PVD clusters.[39, 154] However, the TDS peak appeared at significantly lower temperature. This might be due to the morphological differences of the clusters' structure and/or electronic properties. Similar deviations were also observed when comparing the TDS data collected on Au PVD and Au EBL cluster systems.[40] As mentioned in prior studies,[154] a definite assignment of TDS peaks to certain crystallographic phases is rarely possible. CO TDS data on oxidic Cu clusters is depicted in Figure 74B. As evident from the figure, two very broad TDS peaks, consisting of two structures (α and β), were present. There were no adsorption kinetics studies of CO on CuO_x clusters. However, the CO TDS data collected on single crystals of TiO_2 and ZnO also contained two TDS peaks.[286-287] It is typical to assign different TDS peaks to different types of adsorption sites, e.g., the high temperature (larger binding energy) feature may correspond to defect sites (rim sites, edges, etc.); whereas, the low temperature peak corresponded to pristine (terrace) sites. Similarly, the binding energies of CO on O and Cu sites of the oxidic clusters would also be different. In the case of iron oxide clusters,[159, 288] different CO TDS features were assigned to

different Fe oxides. In the present study, the presence of different Cu oxides was ruled out by the XPS results. It is important to note that no CO_2 formation was observed in TDS and molecular beam scattering studies of CO.

4.3.3.4. Adsorption dynamics

Figures 75−79 summarize the results of molecular beam scattering of CO on silica-supported Cu EBL cluster samples in comparison with blind experiments on the clean supports and Cu PVD cluster data.[39] Data for Cu-like and CuO-like EBL clusters are shown.

4.3.3.4.1. Brief literature survey

Several reviews concerning the molecular beam scattering experiments on model catalysts are available in the literature. The PVD deposition of Cu on silica was studied before using spectroscopic and kinetic techniques.[28, 209-210] Cu PVD clusters' morphology was characterized using STM.[8, 213, 215-216] The data indicated that the growth of Cu PVD clusters consisted of nucleation and cluster growth regime. According to our prior beam scattering study on Cu PVD clusters,[39] the Cu PVD clusters remained metallic at UHV conditions. The adsorption dynamics of CO could be modeled with the CZM. S_0 of CO decreased with an increase in impact energy indicating the molecular and nonactivated adsorption of CO.

In some prior studies concerning the CO adsorption on ZnO(0001) supported Cu PVD clusters,[154, 277] a crossover from direct adsorption dynamics (Langmuirian-like) to more precursor assisted adsorption dynamics (Kisliuk-like) was observed, but that clearly depended on the size of the metal clusters. Some of the observed trends were consistent with simple CZM, but not the shape of the $S(\Theta)$ curves, which were obtained at small Cu coverages and large impact energies. These results suggested a weak effect of precursor states. Molecular beam scattering studies of CO on Cu(110) are also available.[289] There were no studies in the literature concerning the

molecular beam scattering studies on CuO_x single crystals, supported CuO_x clusters, or Cu EBL system.

4.3.3.4.2. Examples of typical CO adsorption transients: Rim vs. terrace sites

The beam flux of CO was determined by measuring the equivalent beam pressure using the mass spectrometer aligned with the beam. The beam flux of CO amounted to $F = (1.8 \pm 0.1)x10^{13}$ molecules.cm^{-2}.s^{-1} for the seeded CO beam (3% CO in He). A constant beam flux was maintained (within 6%). Typical examples of CO adsorption transients on silica-supported EBL clusters, together with blind experiments on silica and partially reduced silica are depicted in Figure 75. The results for metallic clusters are depicted in Figure 75A and the results for oxidic clusters are depicted in Figure 75B. The curves were normalized such that $1 - S(t)$ vs. t was depicted (t is the exposure time and S(t) is the adsorption probability). Evidently, the adsorption transients of CO approached the saturation level (where S = 0 or 1-S = 1) much slower on the supported cluster samples than on the clean supports. Thus, the clusters clearly affected the adsorption dynamics of CO and CO adsorbed on the clusters and/or along the clusters' rim. Evidently, the CO coverage on the bare supports (silica and reduced silica) was negligible at the given T_s. Therefore, the total CO uptake (or saturation coverage Θ_{sat}) amounted to $\Theta_{sat} = \int FS(t)\,dt \approx 1.8 \times 10^{14}$ molecules/cm^2 or ($1.8x\ 10^{14}/1.9x10^{15} = 0.09$ ML) for 63 nm Cu clusters. [Using the bulk lattice constant of Cu (3.6 Å), the calculated Cu atom density of, e.g., a (111) plane amounted to 1.9×10^{15} atoms/cm^2.] The experimental saturation coverage (0.09 ML) was reasonable since the calculated Cu coverage was 0.139 ML. The calculated CO coverage amounted to 0.07 ML = (0.139 × 0.52). (A saturation coverage of 0.52 ML for CO adsorption Cu(111) was experimentally determined.) More interesting, when comparing large and small clusters, the experimental ratio of $\Theta_{sat,l}/\Theta_{sat,s}$ amounted to 5.5 ± 0.9 and 4.5 ± 0.7 for metallic and

oxidic clusters, respectively. (The experimental uncertainties were obtained by averaging the independent experimental runs.) As described earlier, the ratios of 2.3 ± 0.4, 12.6 ± 1.0, and 6.0 ± 0.8 would be expected for the adsorption of CO on the rim sites, terrace sites, and both (rim + terrace), respectively. These results led to the following conclusions.

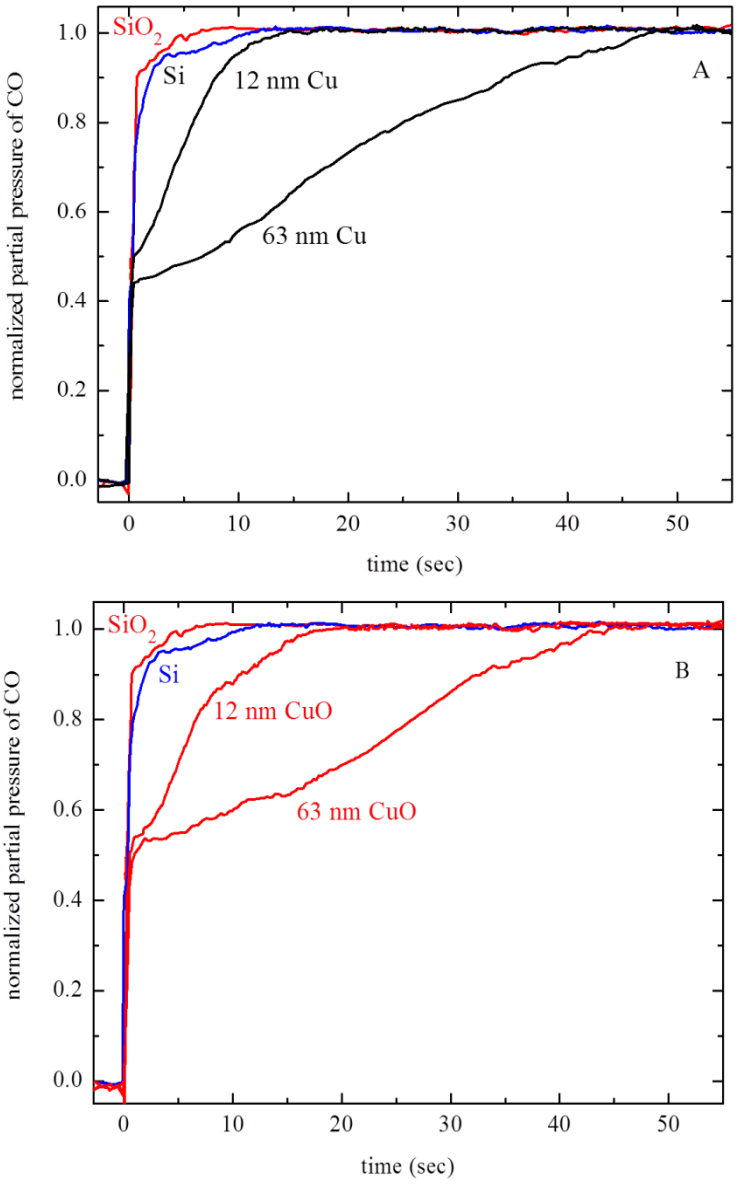

Figure 75. Adsorption transients of CO on (A) metallic and (B) oxidic 12 and 63 nm Cu clusters depicted together with the blind experiments on clean bare supports (T_s = 95 K and E_i = 0.39 eV). Ref.[48]

Nearly the same saturation coverage ratios were obtained irrespective of the oxidation state of Cu clusters. Therefore, it appeared that geometrically similar adsorption sites might be present on both the metallic and oxidic Cu clusters. The experimentally determined ratio matched within uncertainties the calculated value for CO adsorption on both the rim and terrace sites. Therefore, CO also adsorbed on the clusters' rim as expected. The rim sites on the EBL clusters provided additional adsorption sites that were not kinetically much different than terrace sites. For example, if the kinetics was dominated by the rim sites (as it was for Au clusters[49, 72]), a different ratio of the saturation coverages would be expected.

4.3.3.4.3. Energy dependence of initial adsorption probability: Cluster size effects

Figure 76 depicts the $S_0(E_i)$ curves at constant T_s. This plot summarizes the results for metallic Cu EBL and Cu PVD clusters of different cluster sizes or Cu exposures. The lines were presented as a guide for the eye.

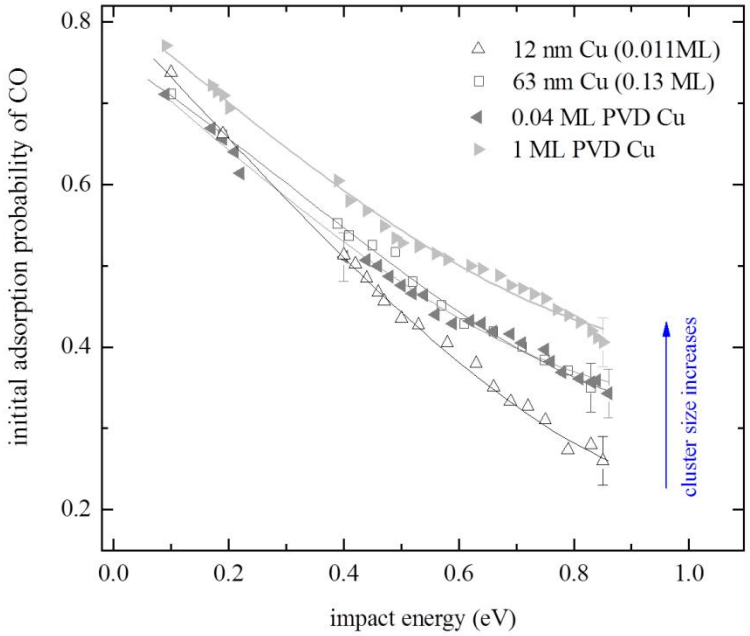

Figure 76. S_0 of CO as a function of E_i for 12 and 63 nm metallic Cu clusters[48] as well as for selected Cu PVD depositions (T_s = 95 K).[39]

In all cases, S_0 of CO decreased with E_i, indicating the nonactivated and molecular adsorption. This was supported by AES/XPS results, which indicated no carbon formation after the adsorption/desorption cycles. The adsorption probabilities of CO were large for small E_i, similar to its adsorption on a variety of other systems.[235, 257, 290] Cluster size effects were also evident for certain data sets. Figure 77 shows an increase in S_0 of CO with Cu cluster size (or coverage). Here, S_0 of CO on Cu PVD data, as a function of Cu exposure, were compared with S_0 of small and large Cu EBL clusters. The E_i and T_s of CO were kept constant. Evidently, the results obtained on Cu EBL samples and Cu PVD clusters[39] matched. In the case of Cu PVD clusters, for large Cu coverages, S_0 appeared to approach the values obtained on Cu single crystals or Cu films.[257, 289] The same trend was observed for ZnO supported Cu PVD clusters.[154] Briefly, the Cu clusters with a small total coverage (percent range) were as reactive as Cu single crystals mainly due to the capture zone effect.[160, 291] The initial increase in S_0 of CO (Figure 77) with cluster size/coverage was due to an increase in the number of available adsorption sites.

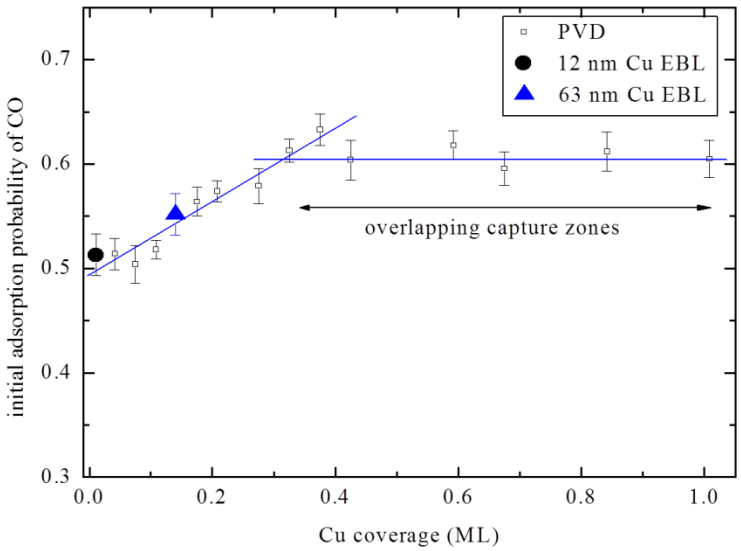

Figure 77. S_0 of CO as a function of Cu coverage (T_s = 95 K and E_i = 0.39 eV) for 12 and 63 nm metallic Cu clusters[48] as well as for selected Cu PVD depositions.[39]

(However, for large Cu coverages large Cu cluster density), the capture zones surrounding different metal clusters overlap with each other. At that point, S_0 did not increase further with an increase in cluster size and dispersion. Therefore, the S_0 vs. Cu coverage plot leveled out.

4.3.3.4.4. Effect of oxidation state on initial adsorption probability

Figure 78 depicts S_0 (E_i) curves of metallic and oxidic Cu EBL clusters of different sizes. Differences in S_0 were evident, depending on the oxidation state of the clusters; metallic Cu clusters were more reactive than oxidic Cu clusters for CO adsorption. This trend was clearly observed at large E_i. This trend was explained by considering simple mass matching models, taking into account the site blocking effects. The CO molecule could interact only with Cu sites in the case of metallic clusters but with Cu and O sites in the case of oxidic clusters. The CO-to-Cu mass match is worse than the CO-to-O mass match. Therefore, an efficient gas-to-surface energy transfer (and larger S_0) are expected in the latter case (oxidic clusters). However, a contradicting result was obtained for CO adsorption on oxidic clusters. This result suggested that CO did not adsorb on oxygen sites of the oxidic clusters. Because S_0 is the ratio of adsorption

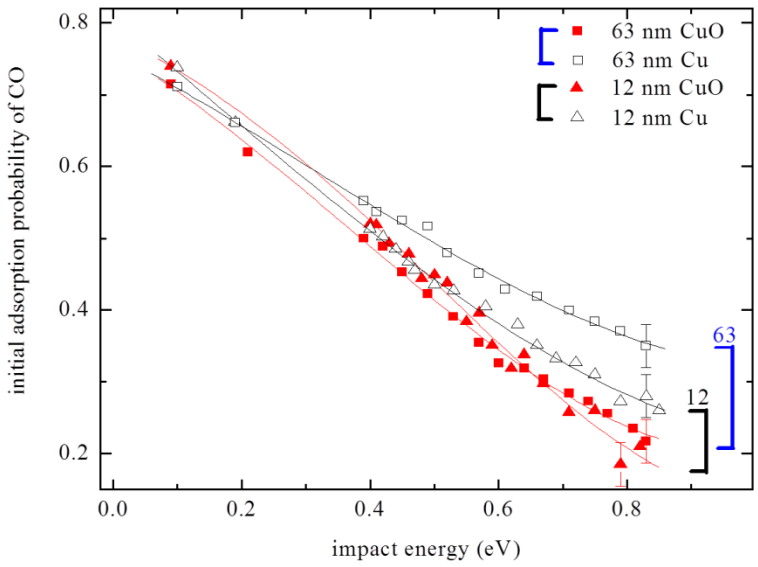

Figure 78. S_0 of CO as a function of E_i for 12 and 63 nm metallic and oxidic Cu clusters (T_s = 95 K). Ref.[48]

rate to impinging rate of probe molecules, the site blocking effects (or poisoning) resulted in smaller S_0 values. The O sites on the CuO_x acted as poisoned adsorption sites and decreased S_0.

Therefore, all these assumptions conclude that the number of available adsorption sites on oxidic clusters are smaller than those on metallic clusters. However, the adsorption of CO on oxidic clusters might also be influenced by carbonate formation or the defects, such as oxygen vacancy sites. The S_0 of CO (within experimental uncertainties) is independent of cluster size for oxidic clusters (Figure 78); whereas, it depends on cluster size for metallic clusters (Figures 77 and 78). Electronic effects should be present. However, the oxidation of Cu clusters should also increase the size of the clusters. The dominant crystallographic phase in the oxidic clusters was not known. However, the unit cell of Cu(111) amounts to 6.5 $Å^2$ and is by a factor of 2.5 larger than the unit cell of bulk CuO is with 16 $Å^2$ (= a × b, see ref[292]). Therefore, as evident from Figure 77, no cluster size effects on S_0 are present for oxidic clusters due to the possible overlapping of capture zones of the clusters during the oxidation process. In addition, the CO binding energies on the oxidic clusters are larger than those for the metallic clusters (Figure 74), i.e., the longer precursor lifetimes for oxidic clusters result in larger capture zones, which quickly overlap.

4.3.3.4.5. Coverage-dependent adsorption probabilities

Adsorption transients are integrated to calculate the relative coverage (Θ) and coverage dependent adsorption probabilities, S(Θ). Figure 79 depicts S(Θ) of CO, as a function of E_i at constant T_s, for the 63 nm Cu-like (Figure 79A) and CuO-like clusters (Figure 79B). The coverage was normalized to 1 ML, which corresponded to 1.8×10^{14} molecules/cm^2, as described earlier. S(Θ) obeyed reasonably well the traditional Kisliuk shape at low E_i, i.e., S(Θ) initially remained large until CO reached the saturation coverage and then dropped to zero. The

curve shape indicated the effect of precursor states, as expected from the CZM. S(Θ) of CO decreased almost linearly with Θ for large E_i, i.e., S(Θ) obeyed Langmuirian-like adsorption dynamics. This crossover from precursor-mediated Kisliuk-like dynamics to direct Langmuirian-like dynamics is also typical for CO on planar catalysts, and that reflects the decrease in the trapping probability in the precursor state with increasing E_i.

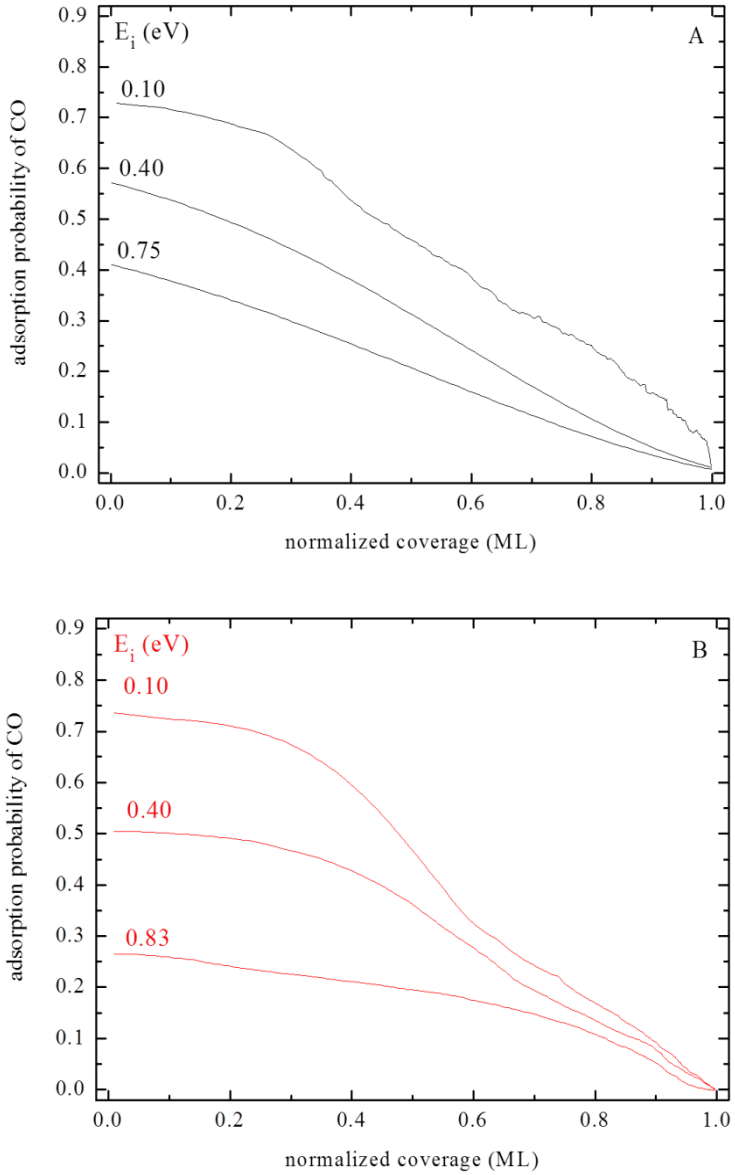

Figure 79. S(Θ) curves for (A) metallic and (B) oxidic 63 nm Cu EBL clusters (T_s = 95 K). The impact energy (E_i) was varied as indicated. Ref.[48]

4.3.4. Summary

Kinetics (TDS), dynamics (Molecular beam scattering), microscopic (SEM), and spectroscopic (AES, XPS) techniques were used to characterize the reactivity of Cu and CuO_x clusters toward CO adsorption. The silica-supported 12 and 63 nm Cu cluster samples were fabricated using EBL. Interestingly, the saturation coverage of CO did not simply scale with the area of the clusters, but, rather, the rim effects clearly increased the saturation coverage. The decrease in S_0 of CO with an increase in E_i, and the indication of no surface carbon after CO experiments concluded the nonactivated molecular adsorption of CO. S_0 of metallic Cu clusters depended on cluster size, and the results could be described in the framework of the CZM. Interestingly, the adsorption dynamics of CO varied with the oxidation state of the clusters. S_0 of CO on the metallic clusters were larger than on oxidic clusters. These results can be explained by simple mass matching models, although the electronic effects are expected. In addition, distinct cluster size effects are only present in the case of metallic clusters, and that would be consistent with cluster size expansion during the oxidation process and larger binding energies.

4.4. Identifying Catalytic Active Sites on EBL-fabricated Silica-supported CuO_x Clusters

An introduction to the significance of identification of catalytically active sites in catalysts is presented first, followed by a discussion on the special properties of EBL-fabricated clusters that allow one to identify the catalytically active sites using simple kinetics techniques. A combined results and discussion section is presented next. A summary of experimental results obtained in this study is given at the end.

4.4.1. Introduction

The identification of active sites is useful to build structure-activity relationships at the atomic level, which can eventually be used for catalyst optimization.[293] It still remains

scientifically challenging to clearly identify the active sites on a solid catalyst. Very few studies utilizing sophisticated microscopic techniques were able to clearly identify the active sites on catalysts.[93, 146]

The so-called model catalysts are extensively studied in surface science because they serve as models for industrial, real-world catalysts. One proposal associated the catalytically active sites with the rims of the clusters and claimed that the clusters' top surface (terrace sites) was catalytically less reactive.[294] This idea was detailed in the discussion concerning the formation of minute Schottky junctions at the interface between metals and oxides and their correlation with catalytic activity in the case of methanol synthesis model systems.[294] However, no clear experimental proof is available for most of the systems. In the present study, the first experimental evidence for catalytically active rim sites along Cu clusters in the case of CuO_x/silica methanol synthesis model catalyst is presented. EBL can be used to nano-fabricate nearly mono-disperse clusters with a predetermined pattern on a substrate (Model nanoarray catalysts).[40, 46, 259-261]

In the current study, silica-supported CuO clusters of size 12, 35, and 63 nm silica were considered. Molecular beam scattering technique can be used to precisely measure the saturation coverage, Θ_{sat}, of probe molecules. Θ_{sat} quantifies the maximum number of gas phase species that can adsorb on a catalyst surface. The morphology of EBL samples is known a priori, so it is possible to predict the possible adsorption sites on EBL nanoclusters from some simple geometrical considerations and the values of Θ_{sat} . In so doing, it is experimentally proved that CO_2 adsorbed only along the rim of CuO clusters; whereas, CO populated both the rim and terrace sites. Thus, the active sites were identified using simple kinetics techniques. These conclusions were further supported by the SEM, TDS, AES, and XPS results.

SiO_2 supported catalysts are of practical interest for methanol steam reforming,[262] as well as hydrogenation reactions.[263] CO is the main component of syngas synthesized by steam methane reforming with CO_2 as the byproduct. Syngas is also used for the synthesis of methanol. Methanol has potential applications, such as an alternative fuel and a feed stock for chemicals. Sustainable methanol production could be possible by using hydrogen and recycled CO_2.[295] CO and CO_2 are also involved in Fischer-Tropsch synthesis. As the current study is mostly focused on CO_2 adsorption, some prior studies related to CO_2 adsorption will be summarized.

4.4.1.1. Brief literature survey about CO_2 adsorption

CO chemisorbs on most metal surfaces; whereas, CO_2 interacts rather weakly with most metal surfaces, i.e., it physisorbs. CO_2 dissociates on Ni and Fe surfaces at UHV conditions. In the case of silver, the coadsorption of CO_2 and oxygen formed carbonates (CO_3^{ads}). Carbonate formation was not reported on Cu. However, molecular beam scattering experiments with CO_2 were only conducted for Pt(111), Pd(111), Cu(110), and Ni(100).[224, 296-298] Except for Ni(100), non-dissociative and non-activated molecular adsorption was observed for CO_2 in all other cases. CO_2 adsorption dynamics was dominated by the extrinsic precursor states (trapping of adsorbates above the occupied sites) for all the systems. The binding energy of CO_2 on metal oxides is much larger than on metals. The effect of defects was extensively discussed, i.e., trapping of CO_2 on O vacancy sites.[154, 287] No CO_2 beam scattering experiments are available for oxides except the one conducted by our research group.[154] CO_2 beam scattering on ZnO-supported Cu PVD clusters is the only other study available for supported Cu cluster system.[211]

4.4.2. Results and discussion

A method to calculate the saturation coverages of probe molecules on rim and terrace sites of EBL-fabricated cluster samples is presented first. The kinetics of CO_2 and CO adsorption

on CuO EBL clusters is presented next. Next, the theoretical and experimental relative saturation coverages of CO_2 and CO for three different CuO EBL sample combinations are presented. The effects of impact energy and sample temperature on the initial adsorption probability of CO_2 on CuO EBL clusters is presented next.

4.4.2.1. Rim vs. terrace sites - calculated saturation coverages

The Cu coverage calculations were discussed in detail in the prior project.[48] Briefly, Small (12 nm) Cu clusters have $d_s = (11.9 \pm 0.3)$ nm $a_s = (100 \pm 1)$ nm. Large (63 nm) clusters have $d_l = (63 \pm 2)$ nm and $a_l = (150 \pm 4)$ nm. Calculated Cu coverage for 12 and 63 nm EBL samples were 0.011 ML and 0.139 ML, respectively. If the adsorption is dominated by terrace sites, the Θ_{sat} for 63 nm cu clusters should be 13 ± 1 times larger than the Θ_{sat} for 12 nm Cu clusters. Similarly, the ratio of the rim lengths of large-to-small clusters amounted to 2.3 ± 0.4. Therefore, if the adsorption is dominated by rim effects, then the Θ_{sat} for 63 nm cu clusters should be 2.3 ± 0.4 times larger than the Θ_{sat} for 12 nm Cu clusters. Finally, if there is simultaneous adsorption on both rim and terrace sites, then the Θ_{sat} for 63 nm cu clusters should be 6.0 ± 0.8 times larger than the Θ_{sat} for 12 nm Cu clusters. Although the size of surface unit cell of CuO is not precisely known, the estimates will also hold true for oxidic Cu clusters. While oxidizing the clusters, the expansion factor (e.g., ratio of metallic-to-oxidic unit cell area) should be independent of cluster size.

4.4.2.2. Rim vs. terrace sites - measured saturation coverages

The Θ_{sat} were precisely determined by measuring adsorption transients using molecular beam scattering technique. The molecular beam is focused onto the surface. Therefore, the sample holder effects were excluded.

Typical examples for CO_2 adsorption transients on CuO are shown in Figure 80. The measured S_0 determines the reactivity towards CO_2 adsorption in the limit of zero CO_2 coverage. Evidently, the CO_2 coverage on the bare supports is negligible because the transients resemble a step function.

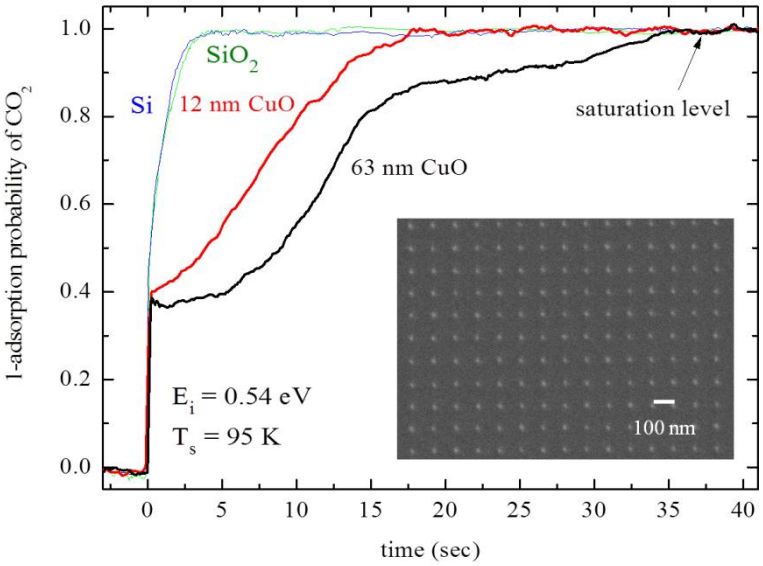

Figure 80. Adsorption transients of CO_2 on 12 and 63 nm CuO clusters depicted together with the experiments on clean bare supports. The inset shows the SEM image of a 12 nm Cu EBL sample. Ref.[73]

Several independent experimental runs were averaged, and a third sample with a cluster size of 35 nm was studied (Table 6). When comparing the large and small clusters, the experimental ratio of $\Theta_{sat,l}/\Theta_{sat,s}$ amounted to 2.0 ± 0.3 (red in Table 6) for CO_2 adsorption and 4.5 ± 0.7 (green in Table 6) for CO adsorption on CuO clusters, respectively. CO_2 did not adsorb on metallic clusters even at T_s = 85 K. (The data for CO is described in the previous project.[48]) First of all, different saturation coverage ratios ($\Theta_{sat,l}/\Theta_{sat,s}$) were obtained for CO and CO_2 adsorption on CuO clusters (compare red and green labeled data in Table 6). Interestingly, for CO adsorption on CuO clusters, the experimentally determined ($\Theta_{sat,l}/\Theta_{sat,s}$) value is close to the

predicted value for adsorption on rim sites plus terrace sites. Interestingly also for CO_2 adsorption on CuO clusters, the experimentally determined ($\Theta_{sat,l}$ / $\Theta_{sat,s}$) value is close to the predicted value for adsorption on highly coordinated rim sites.

Table 6. Theoretical and experimental saturation coverage ratios of CO and CO_2 for three different CuO EBL sample combinations. Note that also the lattice constant differ. (Experimental CO_2/CuO [**red**], Experimental CO/CuO [**green**], Theoretical [**black**]) Ref.[73]

	63 nm/12	63nm/35	35nm/12
Terraces	**13 ± 1**	**1.2 ± 0.3**	**10 ± 2**
Rims	**2.3 ± 0.4** **2.0 ± 0.3**	**0.6 ± 0.1** **0.8 ± 0.2**	**3.9 ± 0.6** **2.7 ± 0.3**
Both	**6.0 ± 0.8** **4.5 ± 0.7**	**1.0 ± 0.2** **1.2 ± 0.3**	**6 ± 1** **4.0 ± 0.6**

Therefore, it is concluded that CO_2 adsorbs preferentially along the rim of the CuO clusters. In the case of 35 nm CuO clusters (which was of a low quality), the predicted and measured ($\Theta_{sat,l}$ / $\Theta_{sat,s}$) values do not match perfectly. However, the adsorption of CO_2 on terrace sites can be easily ruled out.

More generally, a simple kinetics technique combined with EBL samples allowed us to identify different types of adsorption sites. This methodology could also be applied to other systems. The unique catalytic properties of rim sites were also reported in a recent study concerning the scanning tunneling microscopy (STM) measurements of thiophene on MoS_x nanoclusters.[93] In the case of CO adsorption on CuO clusters, the rim sites on Cu clusters provide additional adsorption sites. However, the terrace sites are not kinetically much different from terrace sites. This is consistent with the data obtained on various Cu single crystals, where

no significant differences in initial adsorption probability, S_0 and coverage dependent adsorption probability, $S(\Theta)$ are observed for CO adsorption on different crystallographic planes of Cu. Nearly the same ($\Theta_{sat,l}/\Theta_{sat,s}$) values have been obtained for CO on metallic and oxidic Cu clusters. In the case of CO, it appears that identically similar adsorption sites are present on metallic and oxidic clusters.

4.4.2.3. Kinetics of CO_2 and CO adsorption

The ($\Theta_{sat,l}/\Theta_{sat,s}$) results obtained for three different EBL samples are further supported by the TDS data. Figure 81 depicts the CO_2 and CO TDS on CuO clusters. A single desorption peak appeared in CO_2 TDS data; whereas, two desorption peaks appeared for CO. The latter is a typical result for oxidic systems. The appearance of two TDS features is an indication for the adsorption of probe molecules on different adsorption sites, rather than the effects of lateral interactions.[299-301] The latter can be ruled out due to the small coverages of copper (Calculated Cu coverage for 63 nm Cu clusters was 0.18 ML.) Furthermore, it is well known that CO and CO_2 are ideal probe molecules to differentiate pristine and defect adsorption sites.[286, 302] Condensation temperatures of CO and CO_2 are well below 100 K.[303-304] Thus, the observed TDS peaks correspond to the adsorption in monolayer range.

Interestingly, a single peak appeared in the TDS data for CO_2. It is known that CO_2 does not adsorb on the close packed surfaces of copper.[305-307] The terrace sites of the Cu clusters in the current study most likely have the close packed structure. Therefore, a single CO_2 TDS peak appeared. Copper oxides will have Cu and O adsorption sites. The interaction of CO_2 with O sites is likely repulsive and carbonates are not formed on copper oxides.[297, 308-309] Therefore, it appears plausible that CO_2 adsorbs solely on defect (rim) sites and results in a single TDS peak. A heating rate of 1.7 K/s was used for TDS experiments.

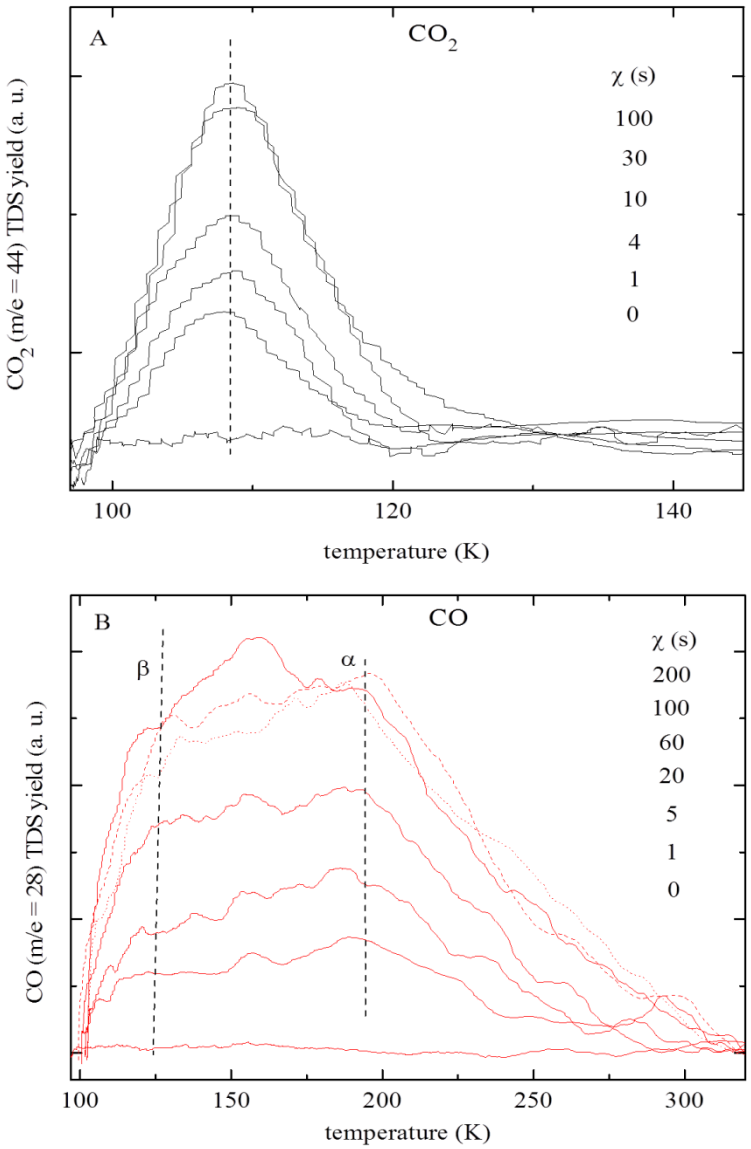

Figure 81. TDS data of (A) CO_2 and (B) CO on 63 nm CuO clusters. β = 1.7 K/s in TDS experiments. The gases were dosed with the molecular beam. Beam exposure time is also indicated. Beam fluxes are measured to be $8x10^{12}$ molecules.cm^2.s^{-1} for CO_2 and $1.8x10^{13}$ molecules.cm^2.s^{-1} for CO. Ref.[73]

Assuming a standard pre-exponential factor of $1x10^{13}$/s for first order molecular adsorption/desorption, the Redhead equation yielded the binding energies of 27 kJ/mol for CO_2 as well as 50 kJ/mol and 33 kJ/mol for the α and β CO TDS peaks. The binding energies of CO are rather smaller (see Table 1 in ref.[154, 310]). However, they are close to the binding energies

obtained on a stepped copper surface which would be consistent with the clusters consisting of a large defect density.

According to the prior studies on metal oxides, such as TiO_2 and ZnO, it was known that the adsorption of CO on defect sites (oxygen vacancies) was characterized by higher binding energies when compared to pristine sites. Therefore, it is plausible to assign the two CO TDS peaks, α and β to defect (rim sites, step edges, etc.) and pristine (terrace) sites, respectively. Similarly, a single TDS peak is expected for the preferential adsorption of probe molecule along the rim sites, as observed here for CO_2. The database for copper oxide clusters, in particular for CO_2 adsorption, is small.[239] CO_2 interacts weakly with metal surfaces.[225, 308-309]

4.4.2.4. Energy dependent adsorption probabilities of CO_2

Figure 82 depicts the $S_0(E_i)$ curves parametric in cluster size, as indicated. The measurements were conducted at constant surface temperature (and precursor life times). Accordingly, S_0 decreases with an increase in E_i and cluster size.

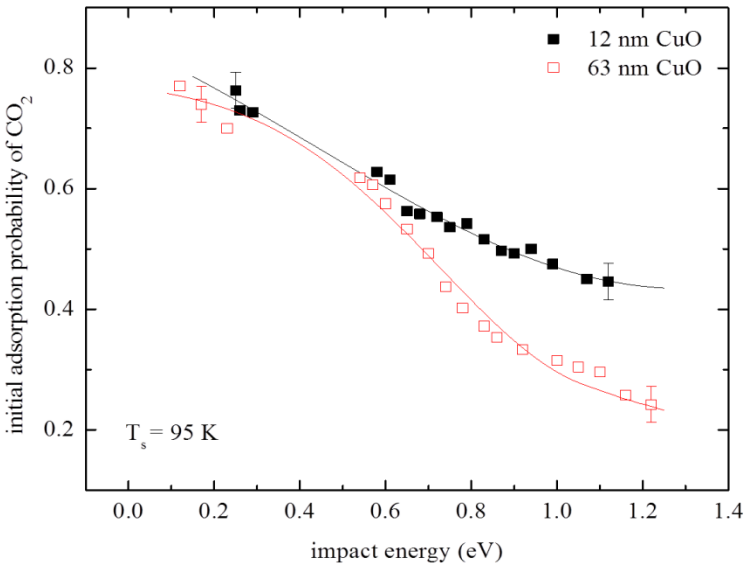

Figure 82. S_0 of CO_2 on 12 and 63 nm CuO EBL samples as a function of impact energy, E_i at constant surface temperature, T_s. Ref.[311]

In the case of molecular and non-activated adsorption, the trapping probability in precursor states decreases with an increase in E_i. Therefore, S_0 decreases with E_i, consistent with the TDS and XPS results, which indicate molecular adsorption. The trapping probabilities in precursor states are large at low E_i, as observed in Figure 82. The details in the adsorption dynamics become clearly evident at large E_i.

Unexpectedly, the small CuO clusters appeared to be more reactive than large clusters, in contrast to the CZM. The terrace sites on the Cu clusters may most likely consist of close packed Cu surfaces, i.e., similar to Cu(111). As described earlier, the unit cell of bulk CuO is 2.5 times larger than the unit cell of Cu(111). Therefore, while oxidizing the Cu clusters, the cluster size increased such that the sample contained dominant terrace sites. It is well known that the terrace sites are less reactive for CO_2. Therefore, it is not surprising that the large CuO clusters were less reactive (smaller S_0) than small clusters. In addition, the total CZ of 63 nm oxidic clusters would be smaller due to its large size, resulting in smaller S_0 values. In the case of 12 nm Cu clusters, the capture zone effects would be dominant, even after oxidizing the clusters, and allow the diffusion mediated adsorption of CO_2 along the clusters' rim.

4.4.2.5. Temperature dependent adsorption probabilities of CO_2

Figure 83 depicts the S_0 as a function of T_s for CO and CO_2 adsorption on 63 nm CuO clusters. S_0 would be independent of T_s for nonactivated molecular adsorption. S_0 decreased due to a decrease in the capture zone with T_s. In addition, the binding energy of CO_2 is smaller than that of CO (Figure 81). When approaching the desorption temperature of the adsorbates, a kinetic adsorption probability would be determined, which depends on adsorption/desorption equilibrium. Therefore, $S_0(T_s)$ for CO approached zero at much lower temperature when compared to CO_2. This result further confirms the TDS data presented in Figure 81.

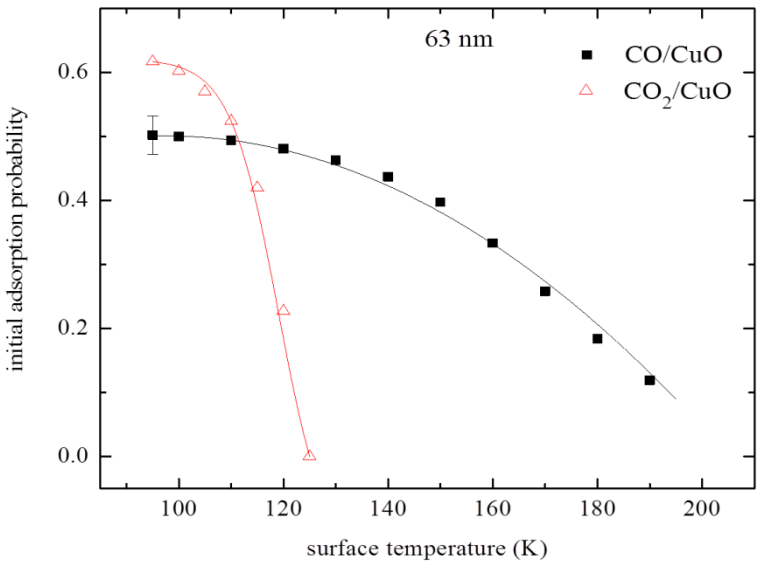

Figure 83. S_0 of CO and CO_2 as a function of T_s for 63 nm CuO sample. Ref.[311]

4.4.3. Summary

Identification of catalytically active sites in chemical transformations is a vital part of research in heterogeneous catalysis.[16] The information about the active sites is crucial to optimize the performance of existing catalysts or to design efficient catalysts. Model catalysts with predetermined morphology could be prepared using EBL. This unique feature of EBL samples was combined with a simple kinetics technique to identify the active sites on a catalyst.

In the current study, this method is illustrated for a methanol synthesis model catalyst; however, it could possibly be applied to other systems. The implications of the current study to catalysis may be to synthesize the catalysts that have maximum rim length for supported metal clusters in order to have high coverages of reactants and large conversion rates. In fact, the highly active "brim site" (i.e. rim site) MoSx catalysts from Haldor Topsoe are currently being used for hydrodesulfurization applications. The hypothesis that rim sites along catalysts have special catalytic properties is evident,[212] but it is rather difficult to provide experimental proof. The method used in the present study could be easily applied to other catalysts.

CHAPTER 5. CARBON NANOTUBES

The carbon nanotubes (CNTs) project is comprised of three sub projects. The main objective of this project is to study the adsorption kinetics of small organic molecules on CNTs and investigate the effect of CNT crystal structure on chemical activity, i.e., structure activity relationship (SAR). The first project is concerned with the study of adsorption kinetics of n-pentane and benzene on thick and thin layers of CNTs. The second project is focused on the effect of CNTs' crystal structure on adsorption kinetics of methanol. The effects of solvent and flash temperature on the adsorption kinetics of methanol are additionally investigated. The third project is focused on the study of SAR of benzene, n-pentane, and water on CNTs.

5.1. Adsorption Kinetics of Small Organic Molecules on Carbon Nanotubes

5.1.1. Introduction

Carbon nanotubes (CNTs) have a tendency to form bundles due to van der Waals interactions. This gives rise to the formation of geometrically different adsorption sites, such as grooves and interstitials in addition to the already existing internal and external sites on isolated (open-ended) CNTs. Therefore, both the thin (monolayer, Figure 84-I) and thick films (Figure 84-II) of CNTs should consist of geometrically identical adsorption sites (internal, external, and grooves) except the interstitial sites. Interstitial sites are typically too small to facilitate the adsorption of most of the molecules. However, using TDS, an unexpected experimental evidence that thick layers of CNTs exhibit kinetically distinct adsorption sites compared to those of thin CNT films is presented. It is well known that the isolated CNTs have distinct electronic structure compared to bundled CNTs.[312-315] In fact, the inherent tendency of CNTs to form bundles has been a major hurdle that prevented the application of optical spectroscopy, e.g., bundles of metallic CNTs quench the photoluminescence of semi-conducting CNTs. This can be

prevented by using surfactants in the preparation of CNT suspensions. Interestingly, the adsorption kinetics of gas-phase molecules on isolated and bundled CNTs are also affected by their electronic structure, as observed in the current study. This is similar to the behavior of bimetallic surface alloys that exhibit different chemical activity compared to their individual alloy constituents.[316] In the case of, e.g., random surface alloys, the geometrical structure of adsorption sites remain the same except the electronic structure. Variations in the density of states ('isolated' vs. bundled CNTs) of a surface can lead to an efficient overlap with the orbitals of adsorbates and result in higher binding energies. This has implications in catalysis, since adsorption of at least one reactant is the first elementary step in all heterogeneously catalyzed reactions. Large binding energies lead to large coverages of reactants that often increase the rate of product formation. In addition, it would be fundamentally useful to find a correlation between the adsorption kinetics and electronic structure of CNTs.

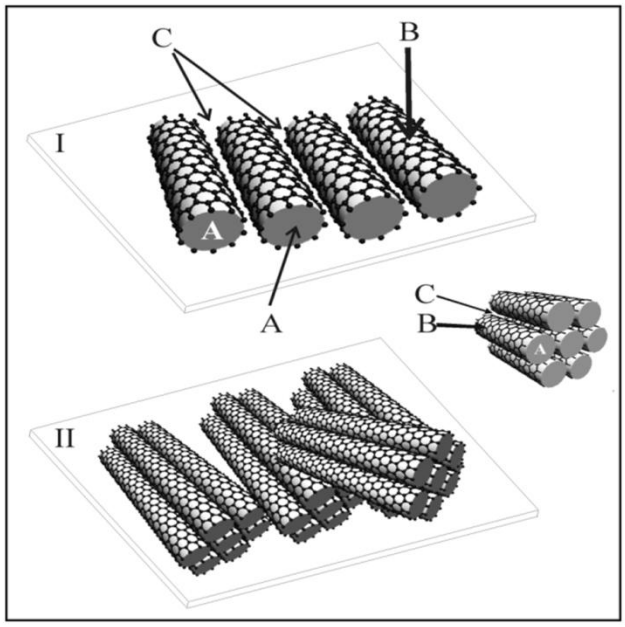

Figure 84. Schematic showing the possible adsorption sites on (I) a monolayer and (II) a thick layer of CNTs.[317] The graphics were made using the software from ref.[318]

In the current study, we used TDS to characterize the adsorption of probe molecules on different CNT samples. n-pentane and benzene were used as probe molecules.[108, 110] Alkanes are used as a standard reference system for UHV kinetics experiments on CNTs.[108, 110] Benzene adsorption on CNTs so far has not been studied with UHV experimental surface chemistry techniques. The binding energies of the Π-stacking interactions in the case of benzene/CNTs system would be useful for theoretical studies. TDS experiments on CNT samples resulted in fingerprint adsorption spectra (as observed in prior studies[99, 110]) that allowed us to distinguish between internal, external, and groove adsorption sites on CNTs deposited on a support.

5.1.2. Sample fabrication

Commercial HiPco (lot SPO0322, 2006, Carbon Nanotechnologies) and CoMoCAT (lot SG-000-0005, 2007, South-West Nanotechnology) CNTs were used. These CNTs have perhaps the best characterized crystal structure to date.[319-323] A micro spatula tip of the CNT powder was suspended in 1% w/v SDS (sodium dodecyl sulfate/ionized water) suspension. The CNT suspension was sonicated using a sonication probe (Branson sonifier 450, 50W for 25 min, ice bath) and centrifugated at 5125g for 4.5 hours. The sonication exfoliates the CNT bundles and opens up the tube ends. The centrifugation removes amorphous graphite particles, carbonaceous materials, and catalyst particles.[324] The supernatent solution after centrifugation is supposed to consist of isolated single wall CNTs.[325] The supernatent was used for making the samples. CNT samples were made by drop-and dry-technique, i.e., a few 50 μL aliquots of CNT suspension was dropped and dried on a 1x1 cm gold foil (Good fellow, USA). Thin and thick films of CNTs were prepared by varying the number of drops of CNT suspension used in the fabrication process. In addition, thick films of agglomerated CNTs were obtained from CNT/isopropanol suspensions. The SDS-based samples were annealed under N_2 at 600 K in a tube furnace for 30

minutes in order to remove SDS surfactant. However, some Na_2SO_4 crystals might remain on the surface, as observed in prior studies.[99] Prior to the TDS experiments, the CNT samples were degassed in the UHV chamber by flashing them to 1200 K. AES data of the annealed CNT samples indicated clean surfaces.

5.1.3. Results and discussion

Figure 85 depicts three sets of n-pentane TDS data for adsorption on gold-supported HiPco CNTs. Panel one (Figure 85-I) shows the TDS data obtained for a thin layer of CNTs (two aliquots of CNTs/SDS suspension). Four TDS peaks (A-D) appear in the TDS data. As per prior studies, the IR spectroscopy measurements and the determination of filling factors allow us to assign the TDS peaks to the adsorption of alkanes on internal (A), external (B), and groove (C) sites (cf. Figure 84). The adsorption sites are filled up in the sequence of their binding energies (A → D) with increased n-pentane exposure, i.e., the site corresponding to the highest binding energy (A) is occupied first. The adsorption sites' unspecific low temperature D-peak, which appears at large exposures indicated the condensation of the alkanes. The observed TDS features are in agreement with prior studies.

Unexpectedly, additional high temperature peaks appear in the TDS data for the samples fabricated either with higher amount of CNTs (Figure 85-II) or the solutions containing agglomerated CNTs (Figure 85-III). As a typical example, Figure 85-II depicts the TDS data for a thick layer of CNTs (CNT/SDS suspension). Figure 85-III depicts the TDS data for a thick layer of CNTs (ten aliquots of CNT/isopropanol suspension). The TDS data for both of these thick CNT film samples contain very broad (200-450 K) and dominant TDS peaks. The greatest desorption temperatures are observed for the samples fabricated from CNT/isopropanol suspension. In this case, the large CNT bundles dominate the adsorption kinetics. In addition, the

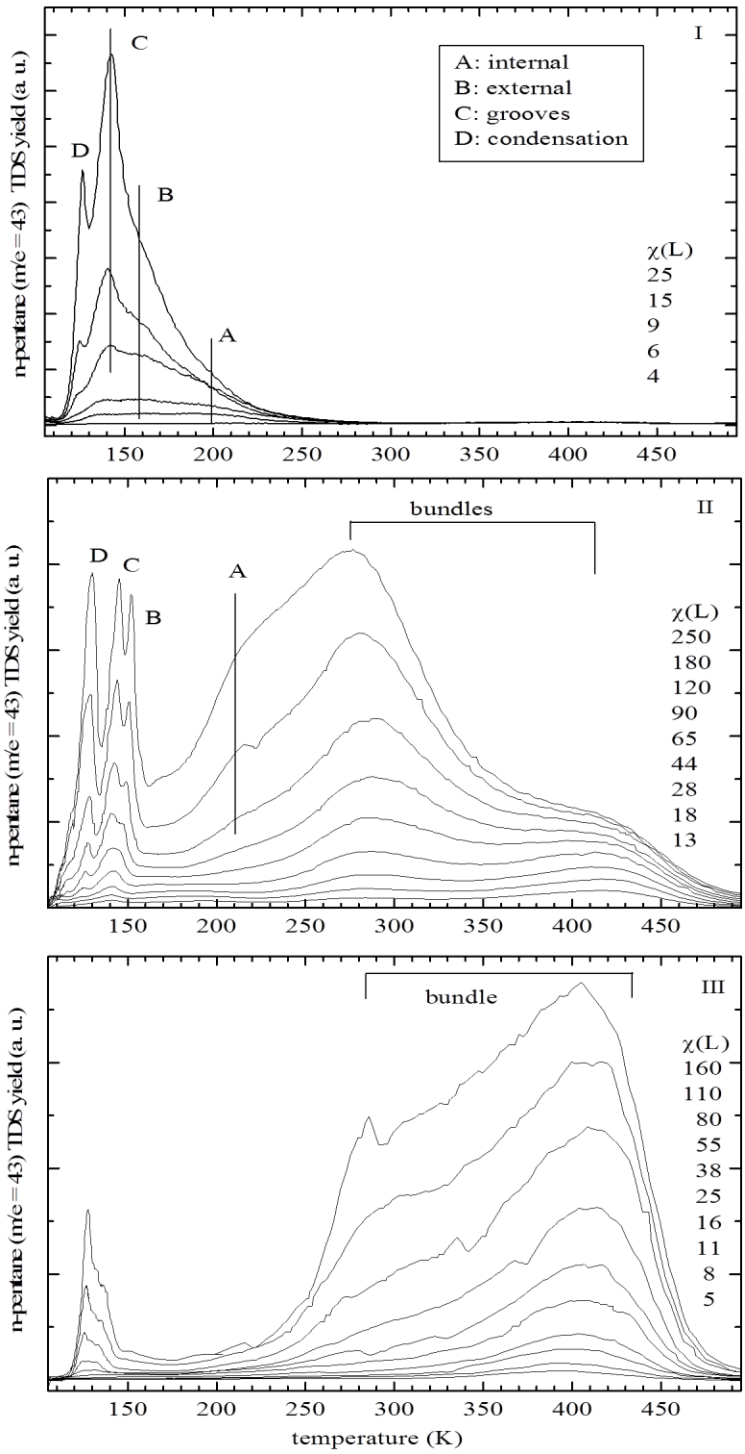

Figure 85. n-pentane TDS on (I) thinner and (II/III) thicker HiPco CNT layers. Solvents used: SDS/water (for I/II) and isopropanol (for III). TDS peaks A, B, and C correspond to the adsorption of n-pentane on internal, external, and groove sites of CNTs respectively. D is the condensation peak of n-pentane. Ref.[317]

low temperature (100-200 K) TDS features that result from thinner CNT films are also present and are clearly detected in the case of samples fabricated from CNT/SDS suspension (Figure 85-II). Similar results are obtained for benzene adsorption on CoMoCAT CNTs, and the results are depicted in Figure 86.

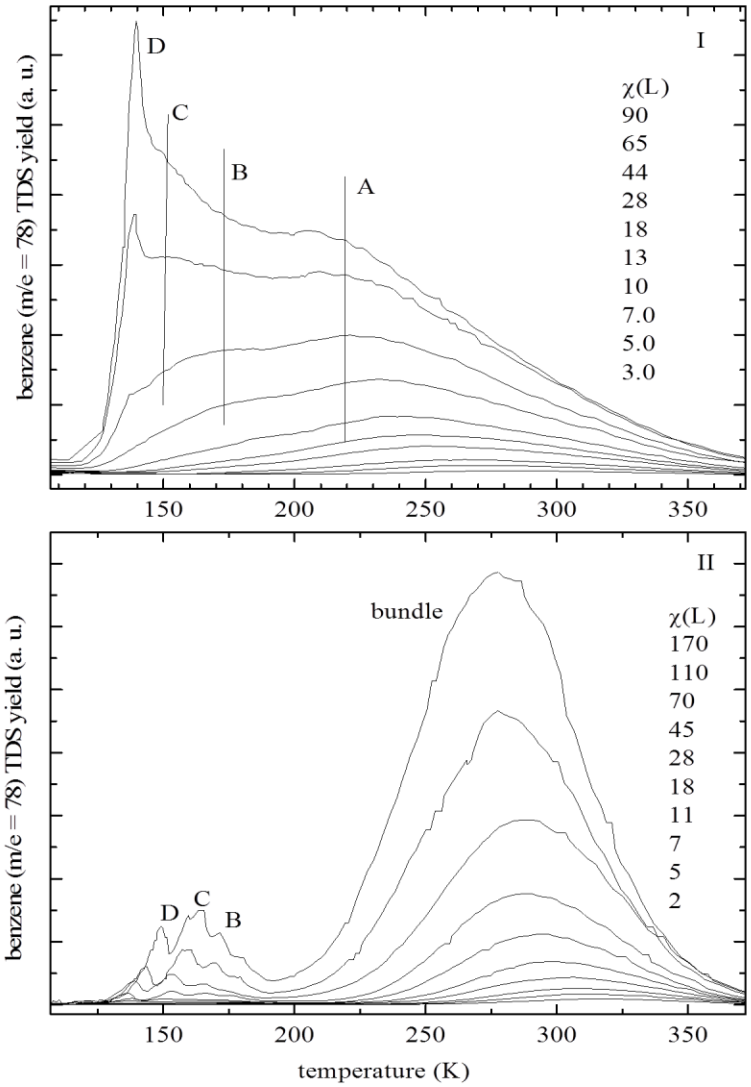

Figure 86. Benzene TDS on (I) thinner (SDS/water solvent) and (II) thicker (isopropanol solvent) CoMoCAT CNT layers. Ref.[317]

Again, the thinner monolayer CNT samples reveal only the well known A → D TDS features (Figure 86-I); whereas, the thick layers of agglomerated CNTs (Figure 86-II) reveal high

temperature TDS features. Similarly, monolayer and bundle TDS peaks (depending on the film thickness) are also observed in the case of n-pentane adsorption on CoMoCAT CNT samples (not explicitly shown). Additional high temperature peaks are also observed in the experiments that use water and methanol as probe molecules. However, they are not as distinct as for n-pentane and benzene. Several CNT samples were studied that consistently reveal high temperature desorption features for thick and/or agglomerated CNT films. The schematics in Figure 84 illustrate the different possible adsorption sites on thick and thin (monolayer) layers of CNTs. However, despite the differences in the overall morphology, the internal, external, and groove sites are present in both thin and thick CNT films.

SEM images of the CNT samples are shown in Figure 87. CNTs in thick films (Figures 87-I and 87-II) appear to form a matrix structure, with large pores connecting the CNT bundles (see the circle in Figure 87-II). CNTs that were deposited in smaller amounts (Figures 87-III and 87-IV) on the support appear to be arranged in sheets (see the circle in Figure 87-IV). Thus, both the thin and thick CNT layers consist of geometrically similar adsorption sites (internal, external, and groove sites). Therefore, the high binding energies observed for thick CNT films are attributed to the electronic effects, rather to the geometric effects.

The TDS technique applied in this study allowed us to distinguish between the well-known TDS features in thin CNT films and the features resulting from thick CNT layers. Diffusion-limited kinetics was ruled out, because the diffusion of probe molecules is fast within the timescale of a TDS experiment.[110] In addition, the pore sizes between adjacent CNT bundles were also much larger (Figure 87). Thus, similar diffusion effects were expected for both the thick and thin CNT layers.

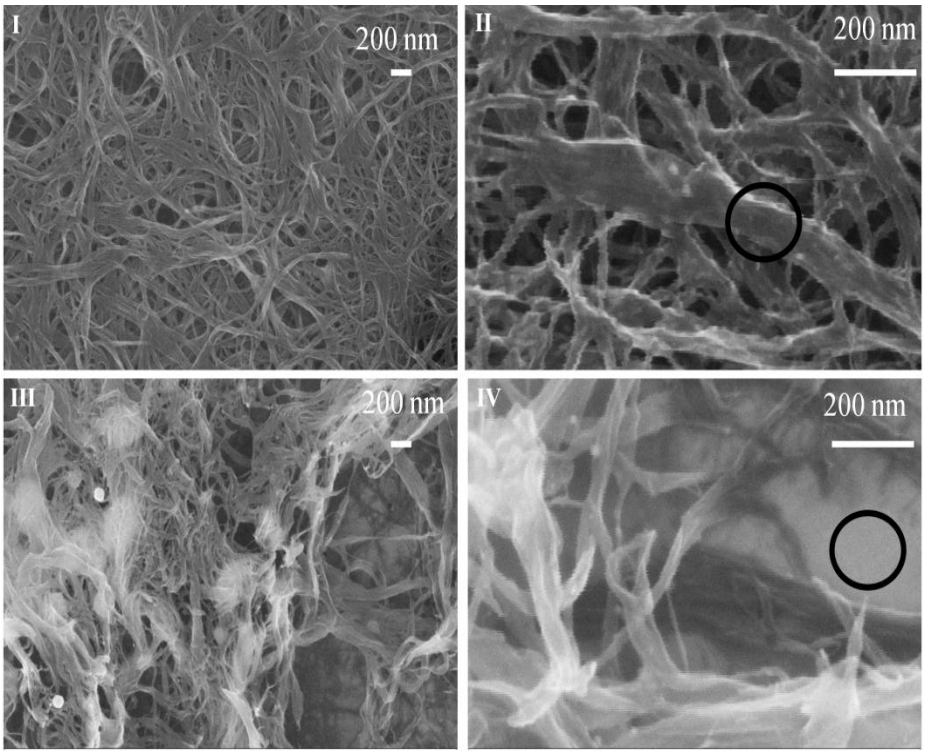

Figure 87. SEM images of (I/II) thicker (isopropanol solvent) and (III/IV) thinner (SDS/water solvent) CNT layers. Ref.[317]

We ruled out the possibility that the high temperature bundle TDS peaks, α_b, are caused due to the impurities, because the high temperature TDS features were also evident for the samples fabricated from CNT/isopropanol suspensions. In the case of CNT samples fabricated from CNT/isopropanol suspensions, no solvent-related impurities were expected because alcohols evaporate without leaving any residue. This was further supported by the AES data collected on CNT samples made from CNT/isopropanol suspensions, which showed no indication of impurities. If CNTs had impurities, then it should have resulted in α_b peaks for all the samples, in contrast to the experimental results. In addition, different catalysts were used to nanofabricate HiPco and CoMoCAT CNTs and α_b peaks are present for both systems. The samples made from centrifugated (CNT/SDS) and non-centrifugated (CNT/isopropanol) suspensions both showed α_b peaks. Therefore, amorphous graphite particles are not responsible

for α_b peaks. Other artifacts, such as contributions from the sample holder were ruled out, because the same sample holder was used for thin CNT samples, that showed no α_b peaks.

According to prior studies concerning the adsorption of alkanes[108] and benzene[326] on gold single crystals, alkanes have quite different adsorption temperatures. Thus, the support effects were ruled out. In addition, even in the case of thin CNT layer samples, the total surface area of the CNTs is at least by a factor of 6 larger than the support (assuming a single and close packed layer of CNTs with 1 nm diameter). These results have important implications for catalysis, e.g., CNTs are used as catalyst supports in fuel cells,[327] desulfurization catalysis,[84, 186] and Fischer-Tropsch synthesis. CNT powders or thick (pressed) films of CNTs are typically used in these applications. Thus, the presence of high binding energy sites in CNT bundles would lead to large surface coverage of reactants at ambient temperature and probably increase the chemical conversion.

5.1.4. Summary

An ultra-high vacuum kinetics technique (TDS) was used to investigate the adsorption kinetics of n-pentane and benzene on thick and thin layers of CNTs. Despite the presence of geometrically similar adsorption sites on both the thick and thin CNT layers, the thick CNT layers shows kinetically distinct adsorption sites compared to thin CNT layers. The effects of CNT film thickness on the binding energies of probe molecules are attributed to electronic effects, rather than to geometric effects. These results are significant to gain an understanding about the electronic effects on adsorption kinetics that could have possible applications in catalysis.

5.2. Adsorption Kinetics of Methanol in Carbon Nanotubes-Solvent Effects

5.2.1. Introduction

The bulk production of CNTs has further reinforced the basic research on CNTs to understand their electronic, optical, elastic , and diffusion properties.[312, 314-315] In most experimental studies, CNT suspensions were analyzed using optical spectroscopy. Several ambient pressure catalysis studies were also conducted on CNT powders. However, the adsorption kinetics and dynamics of gas-phase molecules on CNTs is still unexplored, e.g., adsorptions kinetics and dynamics of very few molecules (alkanes, alcohols, thiophene, CCl_4, Xe)[99, 107-108, 186, 328-331] on internal/external sites of CNTs were investigated at UHV conditions.

Interestingly, TDS technique was used to distinguish various adsorption sites in supported CNTs.[108] In the case of CNTs, four features typically appear in the TDS data, which can be assigned to the adsorption/desorption of probe molecules on internal (A), external (B), groove (C) sites of CNTs. A surface and adsorption site unspecific TDS peak appears at high exposures and low temperature, indicating the condensation of probe molecules on the surface(D). Thus, A simple kinetics technique can be used to obtain very specific kinetic information. This initiated several experimental studies to obtain structure-activity relationship (SAR) information that can be combined with theoretical studies on CNTs. Density functional theory (DFT) studies typically consider a single molecule adsorbed on isolated CNTs for calculations. Therefore, UHV experiments can provide reliable data that can be matched with theoretical studies on CNTs.

The cleaning and preparation of CNT samples for UHV surface science experiments is not trivial. The cleaning of CNTs is probe molecule specific, as detailed in this study. The sample preparation and cleaning processes are important for the fabrication of samples for the

experimental studies. The CNT samples used for surface science experiments are typically prepared from the sonicated and centrifugated suspensions of high grade CNTs.[99, 108] A few drops of CNT suspensions are dropped and dried on a support, such as silica or metal foils, to obtain a thin but closed layer of CNTs.[99] High temperature annealing in UHV is believed to remove the solvent-related impurities, as well as the functionalities blocking the CNT tube ends. This is indeed evident from the previous studies on CNTs, where the TDS intensities increased after annealing the samples in UHV.[99, 328] In addition, the characteristic A→D TDS peaks were detectable for alkanes and CCl_4 using solvents, such as SDS/water.[108]

Unexpectedly, in one of our prior studies on CNTs, the characteristic A→D adsorption peaks were revealed for alkanes but not for MeOH.[330-331] It is important to note that the same CNT sample was used for both the alkanes and MeOH. However, the MeOH–alkane coadsorption experiments provided an evidence for MeOH adsorption on internal, external, and groove sites of CNTs. This behavior was previously attributed to the dipole moment effects, i.e., the characteristic A→D TDS peaks appeared for non-polar molecules (alkanes, CCl_4) but not for polar molecules (alcohols,[330-331] thiophene[186]), when adsorbed on non-polar CNTs. As part of a long term project concerning the SAR of CNTs, several different probe molecules were studied and different solvents/surfactants/supports were used.

Unexpectedly, the solvent and flash temperatures appear to strongly affect the TDS data of MeOH and other polar molecules as well. As described in our previous study, the solvent effects were not evident for the adsorption of alkanes and benzene on CNTs.[74] One of our prior studies also indicated the effect of CNT layer thickness on the adsorption kinetics of probe molecules.[317]

5.2.2. Sample fabrication

The samples were fabricated by the drop-and-dry technique, as described in the previous project. Gold foil (Goodfellow) was used as the support material. The details about the CNTs, solvents, and flash temperatures are given here. Different commercial CNTs were used (see the figure captions) in order to study the effect of CNTs' crystal structure on the adsorption kinetics. HiPco (lot SPO0322, 2006, Carbon Nanotechnologies) consists of 2/3 semiconducting (s-CNTs) and 1/3 metallic CNTs (m-CNTs) and CoMoCAT (lot SG-000-0005, 2007, South-West Nanotechnology) is dominated by s-CNTs. In addition, we used m-CNTs synthesized by Y.P. Sun's group. Diameters of CNTs: CoMoCAT < HiPco < m-CNTs from 0.8 to 1.4 nm.[319-323] SDS, NMP (n-methylpyrrolidone) (99.9%, Sigma Aldrich), and isopropanol were used as solvents. SDS is one of the most popular surfactants used for debundling CNTs.[319, 332] NMP is used for the formation of real ($\Delta G_{mix} < 0$) CNT solutions.[333] Both SDS and NMP may contaminate the CNTs. Alcohols form clean samples but do not debundle CNTs. In addition, all samples were flashed to high temperatures in the range of 600-1200 K (see the figure captions for details).

5.2.3. Results and discussion

Figure 88 depicts the AES data for gold foil-supported CNTs that used SDS (Figure 88-I), isopropanol (Figure 88-II), and NMP (Figure 88-III) solvents. As evident from Figure 88-I, SDS based samples were contaminated by sulfur and sodium, which resulted from Na_2SO_4 crystals (consistent with SEM data) that formed due to the thermal decomposition of SDS. Flash temperatures of about 1200 K were required to significantly reduce the sulfur contamination. It is important to note that the CNTs supported on silica (used as a support in our previous projects) started to desorb at 600 K.[99] As evident, the CNTs stuck more strongly to Au support. However, the samples appeared to degrade with prolonged annealing at 1200 K. On the

other hand, the isopropanol and NMP-based CNT samples did not show any impurities, as judged by the AES data shown in Figures 88-II and 88-III. No differences in AES data were observed for HiPco, CoMoCAT, and m-CNTs samples.

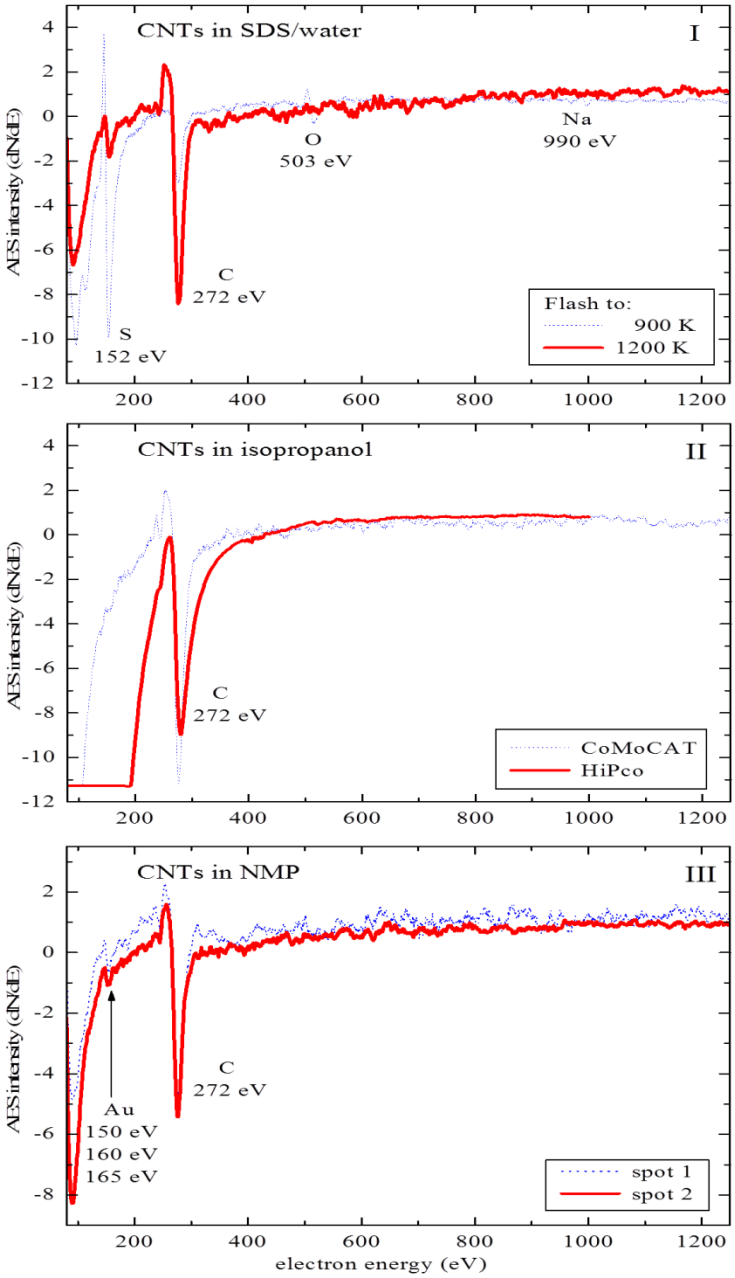

Figure 88. AES characterization of CNTs/gold foil: (I) m-CNTs (SDS/water solvent) flashed to 900 K and 1200 K, (II) HiPco/CoMoCAT CNTs (isopropanol solvent) flashed to 900 K, and (III) HiPco CNTs (NMP solvent) flashed to 1200 K. Ref.[106]

Figures 89I-III summarize the effect of the flash temperature on MeOH TDS on SDS-based CNT sample. The characteristic peaks (A→D) for MeOH adsorption appear only after flashing the CNT sample to 1200 K. Interestingly, in the case of n-pentane and benzene adsorption on the same CNT sample, the A→D peaks appear for flash temperatures below 600 K.[317] However, the prior coadsorption experiments[330] confirmed that the open ends of CNTs were not blocked by SDS residuals. Thus, we conclude that it is possible to obtain CNT samples that are clean enough for surface science experiments using SDS.

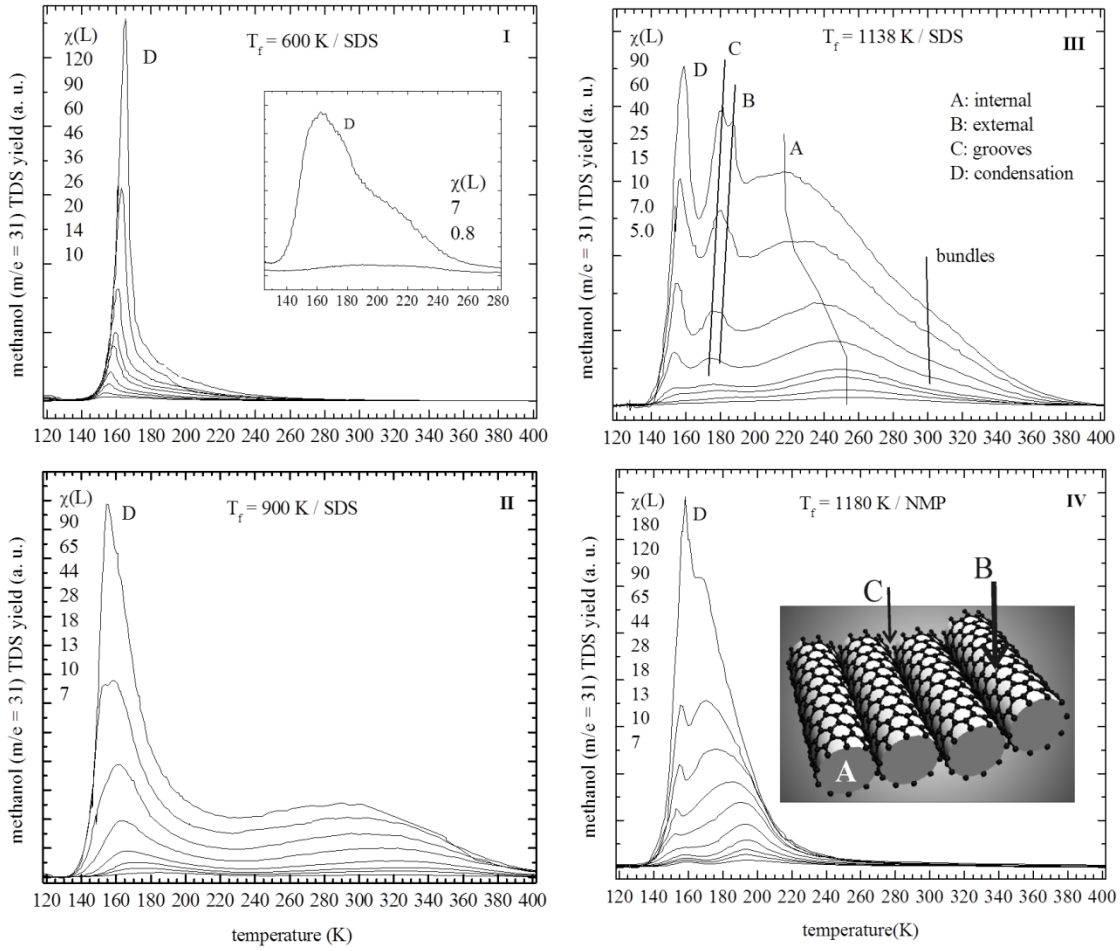

Figure 89. Flash temperature and solvent effects on methanol TDS on (I) HiPco, (II) CoMoCAT, (III) HiPco, and (IV) HiPco CNTs. The flash temperature and the type of solvent used in each case are indicated. The inset of IV shows the three possible adsorption sites on CNTs. TDS peaks A, B, and C correspond to the adsorption of methanol on internal, external, and groove sites of CNTs respectively. D is the condensation peak of methanol. Ref.[106]

However, flash temperatures (1200 K) close to the desorption temperatures of CNTs from Au support were required. Unexpectedly, the NMP-based CNT samples, which had no solvent related impurities (Figure 88-III), revealed featureless MeOH TDS curves (compare Figures 89-III and 89-IV). It is important to note that the same CNT materials and similar flash temperatures were used, except the solvents. Similar results were obtained for water TDS experiments. However, the non-polar probe molecules, such as alkanes and benzene, reveal the A→D TDS peaks for NMP based samples. These effects are seen for several samples studied. Thus, NMP appear to 'functionalize' the CNTs such that the adsorption kinetics of polar molecules is obscured. Therefore, it is concluded that the detection of the CNT-induced TDS features is a better tool than AES to check the cleanliness of the sample.

Figure 90 depicts the common solvent and all the samples were flashed to ~ 950 K. As expected, the alcohol did not contaminate or strongly functionalize the CNTs, because the characteristic A→D TDS peaks are detectable. The positions of A TDS peak (internal sites) for these three different samples agree within ± 10 K. This temperature variation is within the uncertainty of absolute temperature measurements in this study, i.e., no SAR is evident for adsorption on internal sites. However, MeOH desorbs systematically at low temperatures, when adsorbed on external and groove sites (B and C TDS peaks) of m-CNTs compared to HiPco and CoMoCAT CNTs. The TDS features strongly overlapped. Peak shifts of about 30 K, corresponding to a variation in the binding energies of ~ 8 kJ/mol ($1x10^{13}$/s pre-exponential factor, first order desorption), are evident for the B TDS peak for these three different samples. Thus, SAR for MeOH adsorption on external sites of CNTs is evident. This is the first example of SAR on CNTs in an experimental UHV study.

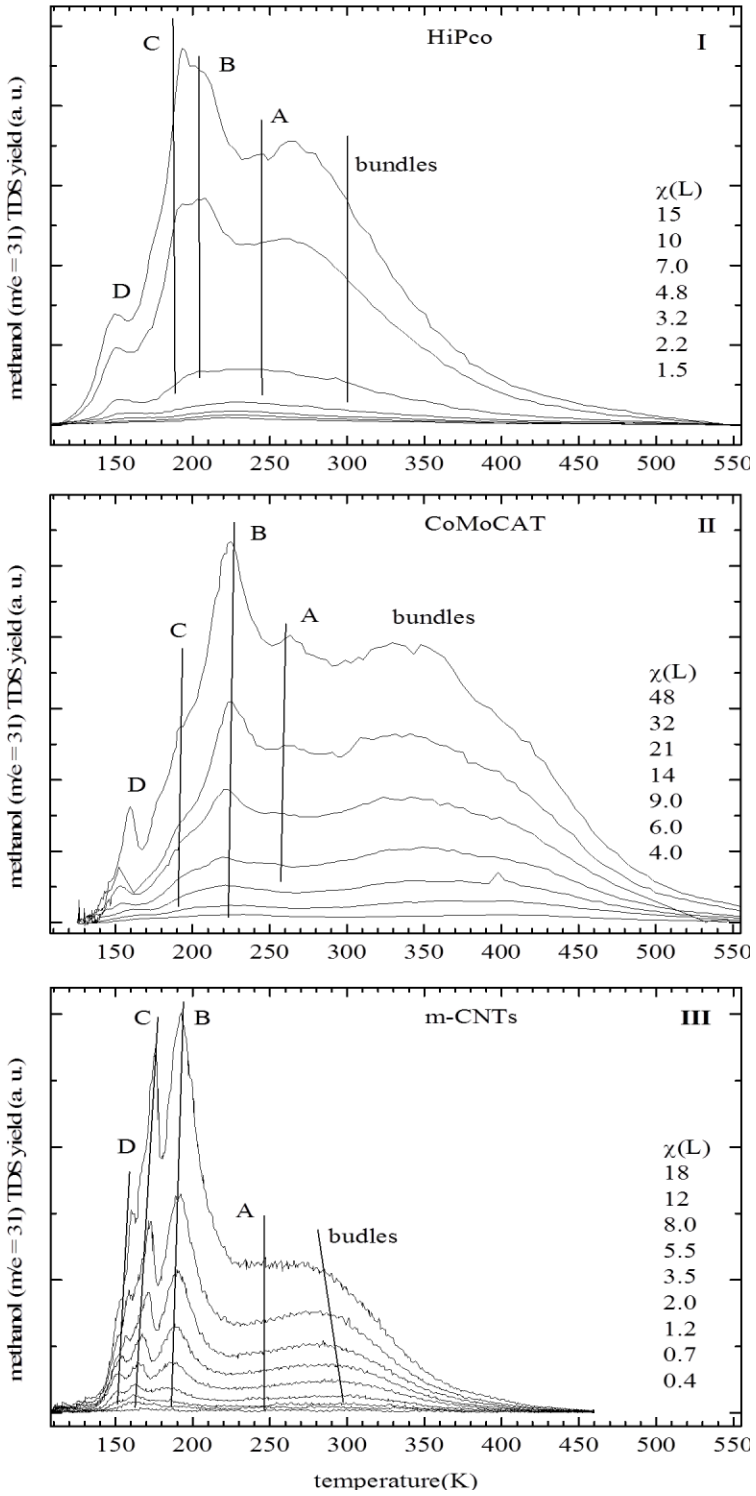

Figure 90. Methanol TDS on different CNT samples (isopropanol solvent and 950 K flash temperature): (I) HiPco CNTs (metallic/semiconducting), (II) CoMoCAT CNTs (semiconducting), and (III) m-CNTs (metallic). Ref.[106]

The results are in agreement with DFT calculations for non-covalently bonded molecules, which predicted an increase in reactivity with CNT diameter. MeOH physisorbs (at least on HOPG),[331] and the m-CNTs have larger diameters than the CoMoCAT and HiPco CNTs. However, the binding energies of MeOH on CNTs are larger than those obtained for HOPG,[334] which is consistent with the trend observed in DFT for non-covalently interacting probe molecules.[335]

The CNTs' intrinsic impurities were not expected to affect the results, because the solvent-related artifacts were independent of the type of CNTs. When isopropanol was used as a solvent, it led to the formation of CNT bundles and resulted in high temperature TDS features (Figure 90). Similar bundle TDS peaks are also evident in the case of thick CNT films made from CNT/SDS suspensions.[317]

5.2.4. Summary

TDS was used to study the effect of CNT crystal structure on the adsorption kinetics of probe molecules such as MeOH. In the case of MeOH adsorption on CNTs, a clear SAR was observed for its adsorption on external sites. No SAR was evident for MeOH adsorption on internal sites. The kinetics results were also obscured by solvent effects. The CNT samples that appeared clean for the adsorption of non-polar molecules, such as alkanes and benzene, were not clean enough for the adsorption of polar molecules such as MeOH. TDS experiment was a better tool to characterize the cleanliness of CNT samples than AES. Selection of solvents and flash temperatures were considered important in UHV surface science studies to avoid subtle solvent effects.

5.3. Effect of Carbon Nanotube Diameter on Gas-surface Interactions

5.3.1. Introduction

The crystal structure of carbon nanotubes (CNTs) influences their electronic, optical, and diffusion properties and this triggered massive efforts to develop special nanofabrication and separation procedures. In turn, a structure–activity relationship (SAR) in solutions was well investigated for several systems, including the bandgap-selective protonation of the CNT side walls[319] and their functionalization.[336-337] Unfortunately, too little attention has so far been paid to the effect of CNTs' crystal structure on their catalytic properties in gas–surface adsorption processes. This is of fundamental interest that can lead to the optimization of gas-sensors. In addition, adsorption of gas-phase reactant molecule is considered as the first step in gas/solid heterogeneous catalysis. CNTs have been used as catalyst supports for a number of applications that include fuel cell catalysts,[327] Fischer–Tropsch synthesis,[338] and desulfurization catalysis.[84] CNTs, owing to their enhanced surface area and binding strength, can result in large coverages of reactants on the CNT surface. Furthermore, the qualitative/quantitative information gained from SAR will be useful for the theoretical studies on CNTs. The separation of CNTs also utilizes the SAR. However, the UHV surface science studies concerning the gas-CNTs interactions are still rare.

In this study, we used TDS to characterize the catalytic activity of CNTs. TDS experiments on CNTs revealed the finger print adsorption spectra of probe molecules that allowed us to distinguish different adsorption sites such as the internal, external, and groove sites on CNT surface.[99, 110] The adsorption energies obtained could be used to refine quantum chemical models. In order to study the effect of CNTs crystal structure on the chemical activity, well characterized commercial HiPco (1/3 metallic 2/3 semiconducting CNTs) and CoMoCAT

(dominated by (6,5) and (7,5) semiconducting CNTs, hereafter s-CNTs) were studied. In addition, the metallic CNTs (hereafter m-CNTs)[337] synthesized by Ya-Ping Sun's group at Clemson University following the arc discharge method were also studied. HOPG (highly-oriented pyrolytic graphite) is used as a reference system. Overall, four different materials with different crystal structure were studied.

The catalytic activity of the CNTs was characterized by TDS of n-pentane, benzene, and water on s-, m-, and HiPco-CNTs. In addition, TDS data for NO and H_2S were also collected. Alkanes are considered as a standard (reference) system in UHV studies concerning the gas–CNT interactions. However, so far only the surface science studies of HiPco CNTs are known.[110] The results of noncovalent p-stacking interactions in the benzene/CNT system can have implications for quantum chemical modeling. However, no UHV experimental data have so far been available. Despite an extensive research on the structure of water ice in CNTs,[339] very little is known about the adsorption kinetics of water on/in CNTs at UHV conditions. Quantitative/qualitative information about the water–CNT interaction is crucial for a variety of applications. More covalent interactions are expected for NO and H_2S.

A brief description of theoretical predictions will be given followed by the experimental results. The expected trend in the catalytic activity of carbon nanostructures is fullerenes > m-CNTs > s-CNTs > graphene. This trend is expected due to a decrease in the curvature induced strain from spherical fullerenes to planar graphene. Therefore, the reactivity of the exterior surface of CNTs is expected to increase with diameter. In addition, the interior sites of CNTs are expected to be more reactive than exterior sites due to their ability to provide nearest-neighbor sites for adsorbates. Furthermore, m-CNTs may have higher catalytic activity than s-CNTs in analogy to studies on single crystal surfaces.

Unexpectedly, the theoretical studies predict an increase in binding energy with CNT diameter for noncovalent interactions. According to theoretical predictions, benzene adsorbs more strongly on HOPG than on CNTs.[340] Very small binding energies (hereafter E_d – heat of adsorption) of about E_d = 19 kJ/mol corresponding to desorption temperatures as low as ~ 65 K were calculated. Theoretical studies predicted only a small effect of CNT crystal structure on E_d.

Recently, similar predictions have been made for alkanes.[341] However, no experimental evidence has so far been available. However, the noncovalent functionalization of CNTs can have a significant effect on the electronic and transport properties.[342] In the case of covalent interactions, the smaller-diameter CNTs are expected to be more reactive than CNTs with large diameter, e.g., according to the theoretical studies on artificially bent CNTs, the high chemical activity of bent CNTs was attributed to their high curvature.[343] Possible differences in the reactivity of the outer and inner surfaces of CNTs were also studied by quantum chemical techniques.[344]

In the case of covalent interactions, the binding energies for adsorption on the inner CNT surface decrease with an increase in CNT diameter. In contrast, the binding energies for adsorption on the outer surface of CNTs are much smaller and rather independent of the CNT diameter, except for very narrow CNTs. Similar trends were predicted by donor–acceptor models based on DFT calculations.

No experimental studies verifying such predictions have so far been available. In the present study, benzene was used as the probe molecule. The characteristic adsorption features for CNTs (internal, external, and groove sites) were revealed for all the probe molecules (benzene, water, alkanes) studied.

The theoretical predictions did not explain certain experimental results in the present study. In the case of benzene adsorption on CNTs, no variations in E_d for the adsorption on external sites are evident, consistent with theoretical studies; whereas, a small trend of increasing E_d with decreasing CNT diameter is observed for adsorption on internal sites. In addition, the experimental E_d values, in particular for adsorption on internal sites, are much larger than those expected from theoretical studies. Therefore, in the case of benzene adsorption on CNTs, CNTs are catalytically more active than HOPG, in contrast to theoretical predictions. No SAR is evident in the case of water and alkanes adorption on CNTs. However, higher E_d values are obtained for adsorption on internal sites.

5.3.2. Sample fabrication and characterization

The sample fabrication procedure was outlined in the prior project. Overall, 15 CNT samples were studied. SEM characterization of the CNT samples were conducted at Argonne national laboratories using a JEOL JSM7500F FESEM. The CNT crystal structure of m-CNTs was characterized by Raman spectroscopy (Jobin Yvon T64000, 633 nm excitation, a triple monochromator, an Olympus BX-41 microscope, and a cooled Symphony detector) at Clemson University.

5.3.3. Results and discussion

Figure 91-I depicts the SEM image of gold-supported m-CNTs. As evident from the SEM image, the surface of gold support was completely covered with a thin layer of CNTs. Figure 91-II depicts the Raman spectrum for m-CNTs. The diameter of m-CNTs was determined to be 1.4 nm, consistent with the studies on SWCNTs (single wall carbon nanotubes) produced by arc-discharge method. The diameters of the CNTs studied here decreases from 1.4 nm to 0.8 nm as m-CNTs > HiPco > s-CNTs.

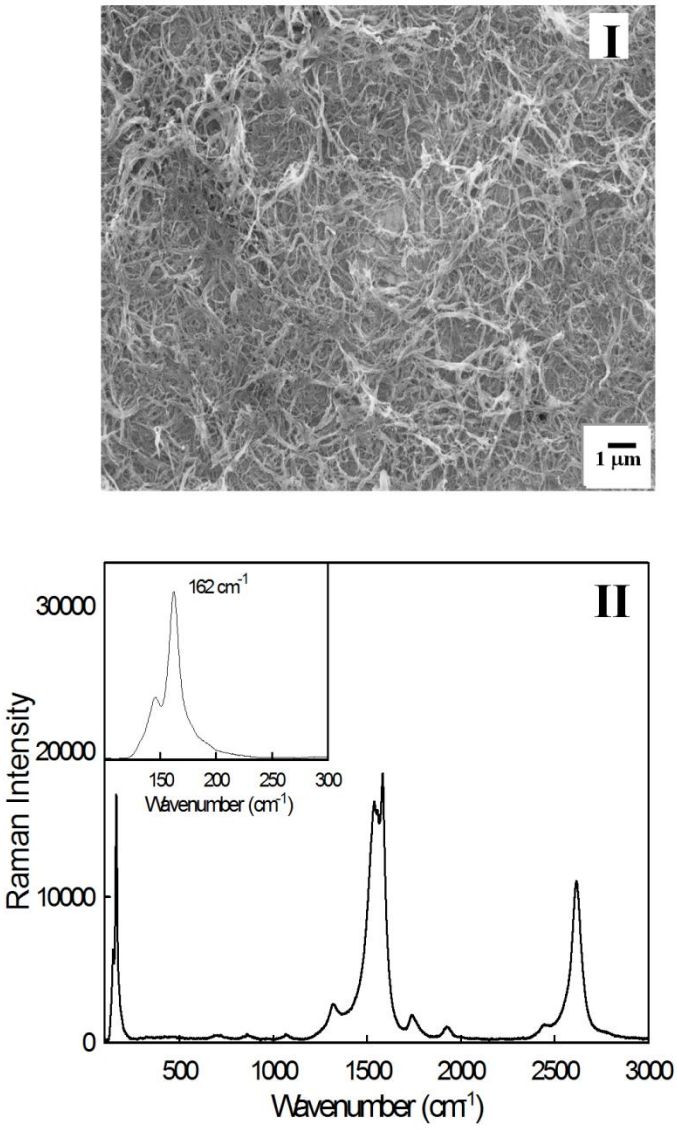

Figure 91. (I) SEM image of m-CNTs/gold foil and
(II) Raman spectrum of m-CNTs. Ref.[74]

Figure 92 depicts benzene TDS on different CNTs together with reference data of HOPG (Figure 92-IV). HOPG is used as a standard reference system for CNTs. Benzene TDS data for s-CNTs (Figure 92-I), HiPco CNTs (Figure 92-II), and m-CNTs (Figure 92-III) are depicted. The insets show the data for small exposures. The TDS peak temperatures determined in the limit of very small exposures (zero coverage) are indicated.

Desorption temperatures as high as 300 K were obtained for the CNTs corresponding to binding energies of ~ 80 kJ/mol (assuming 1st order kinetics and a standard pre-exponential of $1x10^{13}$/s). Theoretical binding energies are much smaller.

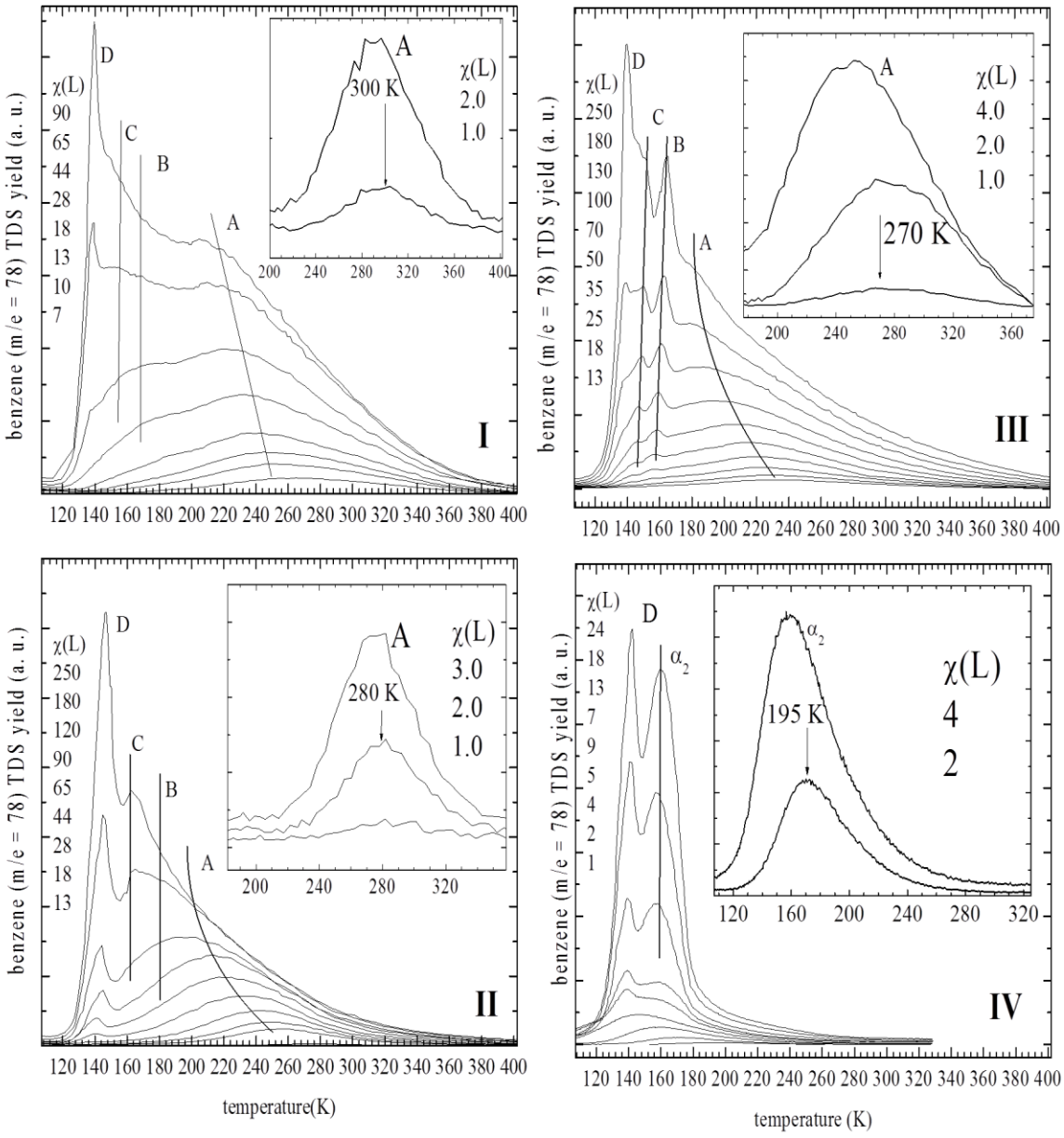

Figure 92. Benzene TDS on (I) CoMoCAT (semiconducting, small diameter), (II) HiPco (metallic/semiconducting), (III) m-CNTs (metallic, large diameter), and (IV) HOPG. TDS peaks A, B, and C correspond to the adsorption of benzene on internal, groove, and external sites of CNTs respectively. D is the condensation peak of benzene. Ref.[74]

Figure 92-IV depicts benzene TDS on HOPG. The low exposure α_2 TDS peak corresponding to benzene adsorption in the monolayer coverage range and the condensation peak (D-peak) are evident. The TDS peak positions agreed within 7 K with prior surface science studies.[345] As evident, the desorption temperature of benzene on HOPG is smaller than those obtained for CNTs (Figure 92). In a prior study concerning the benzene adsorption on MWCNTs (multi-wall CNTs) at high gas pressure conditions, a binding energy of 60 kJ/mol was measured.[346] In the case of benzene adsorption in liquid phase on carbon nanohorns, desorption features in the range of 380-440 K were determined.[347]

Interestingly, four distinct adsorption features were detected for benzene adsorption on different samples (Figures 92 I–III). Prior surface chemistry studies concerning the adsorption of alkanes on HiPco CNTs[99, 110] indicated the presence of kinetically different adsorption sites. In these prior studies, the filling sequence of adsorption sites were determined by the measurements of filling factors, coadsorption experiments, and by using IR (infrared spectroscopy). Accordingly, A, B, and C were assigned to the benzene adsorption/desorption from the interior, groove, and exterior sites of the CNTs. D is the condensation peak of benzene. The smaller size of benzene (0.5 nm) allowed it to adsorb in the interior sites of CNTs. Despite the overlapping of TDS peaks, the positions of the C and B peaks (grooves and external sites) agreed within 10 K for all the CNT samples studied. This result is consistent with DFT calculations that predicted only a small increase in the binding energies (0.9 kJ/mol corresponding to a 3 K TDS peak shift)[335, 340] with increasing CNT diameter. Interestingly, a trend of decreasing binding energy with increasing diameter is observed for the adsorption on internal (A) sites. The position of A TDS peak shifts from 300 K (s-CNTs, small diameter) to 270 K (m-CNTs, large diameter), corresponding to a variation in the binding energy of 78–70 kJ/mol. In the case of HOPG, the α_2

TDS peak appears at 200 K (52 kJ/mol). Thus, the binding energies of benzene on internal sites of CNTs are larger than those obtained for HOPG. Unfortunately, all the available theoretical studies were only related to the adsorption of benzene on exterior sites, predicting the higher activity of HOPG than CNTs.

In the case of alkanes (Figure 93) and water (Figure 94) adsorption on CNTs, the characteristic adsorption features are very well distinguished. No SAR is evident for alkanes and water, consistent with theoretical studies.[341, 348]

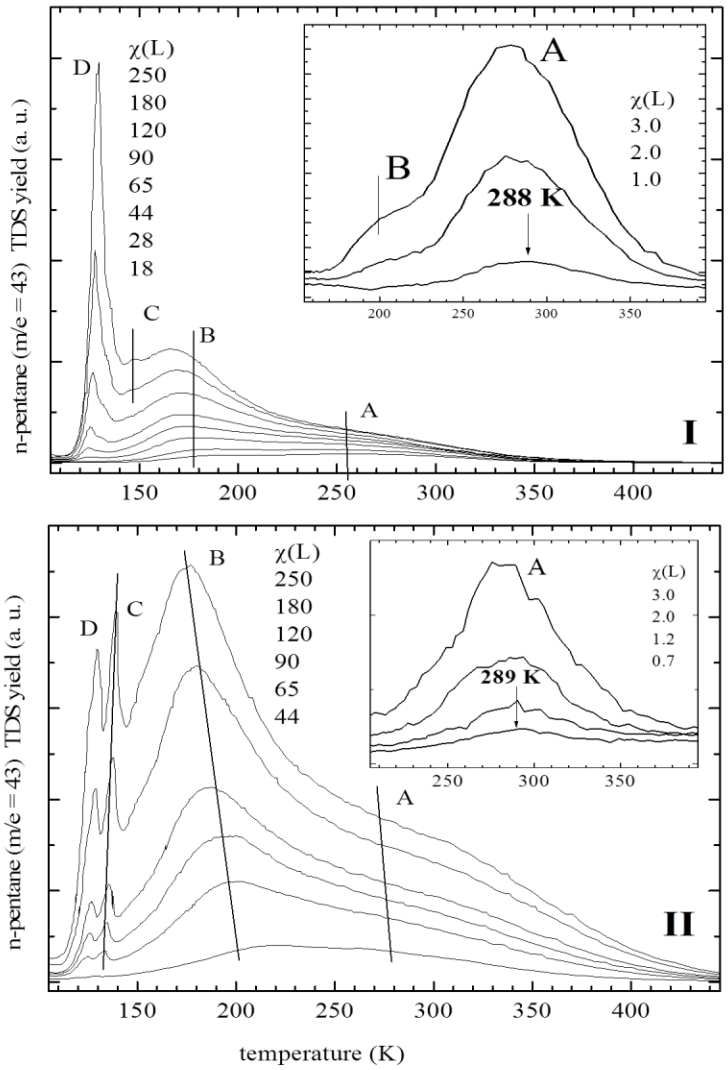

Figure 93. n-pentane TDS on (I) CoMoCAT CNTs and (II) m-CNTs. Refer to Figure 92 for peak labels. Ref.[74]

In the case of NO and H_2S adsorption on CoMoCAT and HiPco CNTs, very broad and structureless TDS curves are observed. Thus, the DFT calculations are partly in agreement with experimental results. A number of possible explanations are considered.

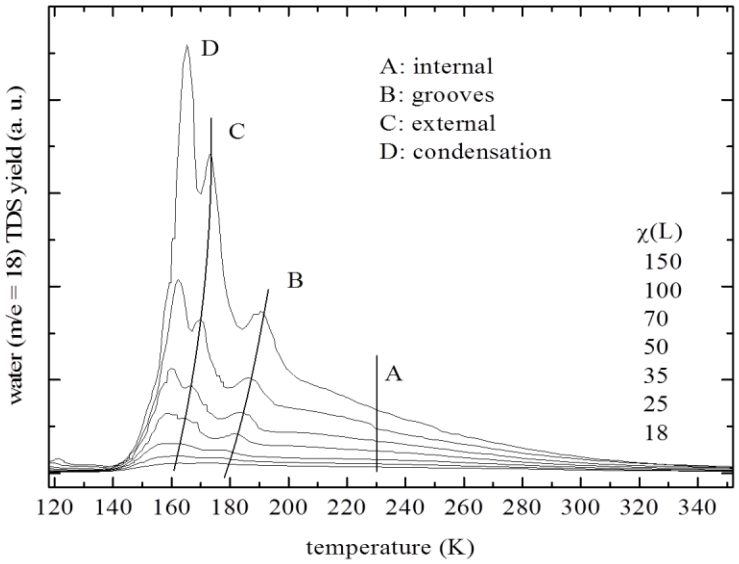

Figure 94. Water TDS on metallic (m) CNTs. Refer to Figure 92 for peak labels. Ref.[74]

DFT is known to be problematic in treating long range van der Waals (dispersion) interactions, which are important for noncovalent bonding. It often leads to an overestimation of binding energies. The choice of basis sets is also limited because the CNTs as macromolecules are considered as large systems for DFT calculations. Although most DFT calculations predict weak Π–Π interactions of aromatic molecules with CNTs, considerable variations in theoretical binding energies are evident. Possible distortions of benzene on CNTs are not included. In theoretical studies, a single molecule on an isolated (defect free) CNT is often considered to have reasonable computational time. Although the low coverage binding energies measured in this study match these conditions better than those conducted at high pressure or in liquid phase, the effects of lateral interactions, interactions with adjacent CNTs, and the effects of side wall defects were rarely considered in theoretical studies. The adsorption of probe molecules on

internal sites are definitely affected by lateral interactions, as evident from the peak shift of the A TDS peak. The CNTs used possibly have a wide distribution of diameters and chiral angles. However, DFT calculations were also performed on CNTs with different crystal structures (not on internal sites), but the theoretical binding energies and trends (HOPG more reactive than CNTs) did not perfectly match our experimental results. We hope that the experimental binding energies obtained for different probe molecules in this study will be useful for theoretical studies on CNTs.

5.3.4. Summary

TDS was used to characterize the catalytic activity of CNTs (s/m/HiPco) towards the adsorption of probe molecules, such as benzene, n-pentane, and water. In the case of benzene, a weak SAR is evident for the adsorption on internal sites; however, no SAR is evident for the adsorption on external sites. In the case of n-pentane and water, no SAR is evident. The experimental data are in part consistent with theoretical predictions.

CHAPTER 6. CONCLUSIONS AND IMPLICATIONS

Heterogeneous catalysis plays a major role in environmental protection and sustainable development. The utilization of nanomaterials for catalytic applications is a key area of research. Nanomaterials exhibit special physical and electronic properties compared to their bulk analogs that could possibly be exploited to develop highly active and highly selective catalysts. Nanocatalysis has the potential to address the principles of green chemistry, which can have direct influence on human society and development.

Surface chemistry studies on model catalysts contributed significantly to heterogeneous catalysis. The developments in nanotechnology, surface science, and surface-sensitive spectroscopic techniques greatly advanced a molecular-level understanding of heterogeneous catalysis. Recently, the oxide-supported metal cluster model catalysts facilitated the study of particle size/shape effects and cluster-support interactions. The oxide-supported metal cluster model catalysts provide a suitable replicate for industrial catalysts. For a number of catalytic reactions, there has been a good correlation between the activity and selectivity of model and industrial catalysts. These model catalysts also allow for building structure-activity relationships at an atomic level that leads to the development of efficient catalysts.

Adsorption kinetics (TDS) and dynamics (Molecular beam scattering) measurements were conducted on novel hydrodesulfurization and methanol synthesis model nanocatalysts. In addition, the ambient pressure kinetics experiments were also conducted on HDS powder catalysts. A variety of material characterization techniques, including SEM, HRTEM, STEM, EELS, XRD, and Raman were used for the characterization of nanocatalysts. Surface science studies on hydrodesulfurization model nanocatalysts finally led to the fabrication of active HDS catalysts, such as Ni/Co coated INT-WS_2. Our research on methanol synthesis model

nanocatalysts allowed us to identify the active sites of a model catalyst, silica-supported CuO_x nanoclusters. These model catalysts also facilitated our understanding of the cluster size effects in gas-surface interactions. A summary of results will be given below.

Adsorption kinetics studies of thiophene on IF-MoS_2 NP confirm the molecular adsorption of thiophene. In addition, the adsorption sites of the catalyst are characterized as S- and Mo/MoO_x-like sites. HDS studies reveal higher catalytic activity for the reduced samples.

Adsorption kinetics studies on INT-WS_2 reveal the first evidence for the adsorption of probe molecules on internal, external, and groove sites of inorganic nanotubes. Such characteristic adsorption peaks are also evident for CNTs. The catalyst shows some HDS activity below the room temperature.

In the case of silica-supported Mo clusters, the Mo cluster growth mode reveals 2D → 3D transition with increasing Mo exposure. The adsorption/decomposition kinetics/dynamics of thiophene on silica-supported Mo clusters reveals the molecular adsorption and decomposition pathways. Smaller Mo clusters are more reactive than larger clusters for molecular adsorption of thiophene. Larger clusters are more reactive for thiophene decomposition. Fully sulfided Mo clusters are less reactive than Mo clusters for thiophene decomposition. Bond activation energy for the first elementary decomposition step has been determined from adsorption dynamics studies. In addition, the adsorption sites of MoS_x are characterized as Mo- and S-like sites.

The results of these three projects allow us to nanofabricate novel HDS catalysts, including Co/Ni coated INT-WS_2, which shows good catalytic activity towards thiophene HDS. The TDS experiments on these metal coated nanotubes reveal the characteristic TDS features for a nanotube system. Thiophene decomposes on Co/Ni coated INT-WS_2 at UHV conditions. Ambient pressure catalytic experiments were conducted on a number of novel HDS catalysts,

including pristine and Re doped IF-MoS_2 NP, pristine and metal (M) coated INT-WS_2 (M = Co, Ni, Au), commercial catalysts NiMo, CoMo from Haldor Topsoe, and nano MoS_2. The Ni and Co promoted INT-WS_2 exhibit the highest HDS activity among the novel catalysts studied. A clear promotion effect of Ni, as well as Co, was observed. Commercial NiMo and CoMo catalysts are ~ 4.5 times highly reactive than Ni/Co coated INT-WS_2. It is anticipated that the use of additional promoters, such as Re or Au to Ni/Co coated INT-WS_2, will reduce H_2S formation.

In the case of silica-supported Cu clusters, the Cu cluster growth mode reveals nucleation → 2D/3D cluster growth → film formation. The adsorption dynamics of CO on Cu/silica was modeled within the frame work of capture zone model. Nonactivated and molecular adsorption of CO was observed. For large coverages of Cu, the adsorption probability of CO approach the value of Cu single crystal indicating the formation of less corrugated film. Furthermore, the cluster size effects on adsorption dynamics in the cases of Cu/silica and Au/silica are compared. Au clusters show unique cluster size effects due to the defect sites. Cu clusters reveal only a weak cluster size effect. Thus, the molecular beam scattering technique allow us to map the active sites of the catalysts.

Adsorption kinetics and dynamics of CO and CO_2 on EBL fabricated silica-supported Cu/CuO_x clusters was investigated. Nonactivated and molecular adsorption of CO was detected. Adsorption probability depends on Cu cluster size, in consistence with the CZM. Adsorption dynamics was affected by the oxidation state of Cu clusters. Metallic clusters are more reactive for CO adsorption than oxidic clusters. In addition, cluster size effects are only evident for metallic clusters. The uniqueness of EBL samples together with molecular beam scattering allows us to identify the active sites on the catalyst. We experimentally prove that CO_2 adsorbs solely along the rim of CuO clusters; whereas, CO occupies both the rim and terrace sites.

The surface science studies conducted on IF-MoS_2 and INT-WS_2 and silica-supported Mo clusters helped us to nanofabricate reactive HDS nanocatalysts, such as Ni/Co coated INT-WS_2. This result is promising for the development of novel HDS nanocatalysts with high activity and selectivity. Several parameters, such as the active metal particle size, amount of loading, and support, etc. can be adjusted to synthesize an ideal HDS nanocatalyst.

The surface science studies conducted on silica-supported PVD Cu clusters and EBL Cu/CuO_x clusters allowed us to identify the Cu cluster size effects and effect of oxidation state (if any) on adsorption dynamics. This finally resulted in a meaningful strategy to identify the active sites of a catalyst. Because the rims along CuO nanoclusters were identified as active sites in the case of EBL Cu/CuO_x clusters, the catalyst can be optimized to increase the rim length of nanoclusters in order to have high coverages of reactants, which eventually can lead to better product formation rates.

Overall, the results obtained from the surface chemistry investigations of hydrodesulfurization and methanol synthesis model catalysts can be used for the development of highly active and selective catalysts that can pave the way for green chemistry.

REFERENCES

1. Anastas, P. T.; Warne, J. C., *Green Chemistry: Theory and Practice*. Oxford University Press: New York, 2000.
2. Grunes, J.; Zhu, A.; Somorjai, G. A., *Chem. Commun.* **2003,** (18), 2257-2260.
3. Somorjai, G. A.; McCrea, K., *Appl. Catal., A* **2001,** *222* (1-2), 3-18.
4. Gao, F.; Goodman, D. W., *Annu. Rev. Phys. Chem* **2012,** *63* (1), 265-286.
5. Ertl, G.; Prigge, D.; Schloegl, R.; Weiss, M., *J. Catal.* **1983,** *79* (2), 359-377.
6. Ertl, G., *Angew. Chem., Int. Ed.* **2008,** *47* (19), 3524-3535.
7. Haruta, M.; Yamada, N.; Kobayashi, T.; Iijima, S., *J. Catal.* **1989,** *115* (2), 301-309.
8. Xu, X.; Vesecky, S. M.; Goodman, D. W., *Science (Washington, D. C., U. S.)* **1992,** *258* (5083), 788-790.
9. Campbell, C. T., *Science (Washington, DC, U. S.)* **2004,** *306* (5694), 234-235.
10. Chen, M. S.; Goodman, D. W., *Science (Washington, DC, U. S.)* **2004,** *306* (5694), 252-255.
11. Ertl, G.; Knözinger, H.; Schüth, F.; Weitkamp, J., (Eds) *Handbook of Heterogeneous Catalysis* Wiley-VCH: Weinheim, Germany, 1997; Vol. 1.
12. Narayanan, R.; El-Sayed, M. A., *Nano Lett.* **2004,** *4* (7), 1343-1348.
13. Toshima, N.; Yonezawa, T., *New J. Chem.* **1998,** *22* (11), 1179-1201.
14. Tao, A. R.; Habas, S.; Yang, P. D., *Small* **2008,** *4* (3), 310-325.
15. Liz-Marzan, L. M., *Langmuir* **2006,** *22* (1), 32-41.
16. Liu, C.; Burghaus, U.; Besenbacher, F.; Wang, Z. L., *ACS Nano* **2010,** *4* (10), 5517-5526.
17. Kalidindi, S. B.; Jagirdar, B. R., *ChemSusChem* **2012,** *5* (1), 65-75.

18. Bartholomew, C. H.; Farrauto, R. J., *Fundamentals of Industrial Catalytic Processes*. 2 ed.; Wiley-AIChE: New York, 2005.

19. Somorjai, G. A.; Li, Y. M., *Introduction to Surface Chemistry and Catalysis*. 2 ed.; Wiley & Sons: New York, 2010.

20. Ertl, G., *Reactions at Solid Surfaces*. Wiley & Sons: 2009.

21. Henry, C. R., *Surf. Sci. Rep.* **1998,** *31* (7-8), 235-325.

22. Goodman, D. W., *Chem. Rev.* **1995,** *95* (3), 523-536.

23. Campbell, C. T., *Surf. Sci. Rep.* **1997,** *27* (1-3), 1-111.

24. Blakely, D. W.; Kozak, E. I.; Sexton, B. A.; Somorjai, G. A., *J. Vac. Sci. Technol.* **1976,** *13* (5), 1091-1096.

25. Campbell, C. T., Studies of Model Catalysts with Well-Defined Surfaces Combining Ultrahigh Vacuum Surface Characterization with Medium- and High-Pressure Kinetics. In *Adv. Catal.*, D.D. Eley, H. P.; Paul, B. W., Eds. Academic Press: 1989; Vol. Volume 36, pp 1-54.

26. Baumer, M.; Freund, H. J., *Prog. Surf. Sci.* **1999,** *61* (7-8), 127-198.

27. Freund, H. J., *Chem. Eur. J.* **2010,** *16* (31), 9384-9397.

28. Askgaard, T. S.; Norskov, J. K.; Ovesen, C. V.; Stoltze, P., *J. Catal.* **1995,** *156* (2), 229-242.

29. Kelley, R. D.; Goodman, D. W., *Surf. Sci. Lett.* **1982,** *123* (2-3), L743-L749.

30. Vannice, M. A., *Cat. Rev. Sci. Eng.* **1976,** *14* (2), 153-191.

31. Goodman, D. W., *J. Phys. Chem.* **1996,** *100* (31), 13090-13102.

32. Goodman, D. W., *Appl. Surf. Sci.* **1984,** *19* (1-4), 1-13.

33. Goodman, D. W., *Surf. Sci.* **1982,** *123* (1), L679-L685.

34. Rainer, D. R.; Vesecky, S. M.; Koranne, M.; Oh, W. S.; Goodman, D. W., *J. Catal.* **1997,** *167* (1), 234-241.

35. Chen, M. S.; Santra, A. K.; Goodman, D. W., *Phys. Rev. B* **2004,** *69* (15), 155404.

36. Wu, M. C.; Goodman, D. W., *J. Phys. Chem.* **1994,** *98* (39), 9874-9881.

37. Wu, M. C.; Corneille, J. S.; Estrada, C. A.; He, J. W.; Goodman, D. W., *Chem. Phys. Lett.* **1991,** *182* (5), 472-478.

38. Xu, C.; Lai, X.; Zajac, G. W.; Goodman, D. W., *Phys. Rev. B* **1997,** *56* (20), 13464-13482.

39. Komarneni, M.; Shan, J.; Burghaus, U., *J. Phys. Chem. C* **2011,** *115* (33), 16590-16597.

40. Kadossov, E.; Cabrini, S.; Burghaus, U., *J. Mol. Catal. A Chem.* **2010,** *321* (1-2), 101-109.

41. Lai, X.; St Clair, T. P.; Valden, M.; Goodman, D. W., *Prog. Surf. Sci.* **1998,** *59* (1-4), 25-52.

42. Heiz, U.; Vanolli, F.; Trento, L.; Schneider, W. D., *Rev. Sci. Instrum.* **1997,** *68* (5), 1986-1994.

43. Bromann, K.; Felix, C.; Brune, H.; Harbich, W.; Monot, R.; Buttet, J.; Kern, K., *Science* **1996,** *274* (5289), 956-958.

44. Kleyn, A. W., *Chem. Soc. rev* **2003,** *32* (2), 87-95.

45. Avoyan, A.; Rupprechter, G.; Eppler, A. S.; Somorjai, G. A., *Top. Catal.* **2000,** *10* (1/2), 107-113.

46. Jacobs, P. W.; Ribeiro, F. H.; Somorjai, G. A.; Wind, S. J., *Catal. Lett.* **1996,** *37* (3,4), 131-136.

47. Schildenberger, M.; Bonetti, Y.; Aeschlimann, M.; Scandella, L.; Gobrecht, J.; Prins, R., *Catal. Lett.* **1998,** *56* (1), 1-6.

48. Komarneni, M.; Shan, J.; Chakradhar, A.; Kadossov, E.; Cabrini, S.; Burghaus, U., *J. Phys. Chem. C* **2012,** *116* (9), 5792-5801.

49. Haruta, M., *Catal. Today* **1997,** *36* (1), 153-166.

50. Hashmi, A. S. K.; Hutchings, G. J., *Angew. Chem., Int. Ed.* **2006,** *45* (47), 7896-7936.

51. Valden, M.; Pak, S.; Lai, X.; Goodman, D. W., *Catal. Lett.* **1998,** *56* (1), 7-10.

52. Iizuka, Y.; Fujiki, H.; Yamauchi, N.; Chijiiwa, T.; Arai, S.; Tsubota, S.; Haruta, M., *Catal. Today* **1997,** *36* (1), 115-123.

53. Lai, X. F.; Goodman, D. W., *J. Mol. Catal. A Chem.* **2000,** *162* (1-2), 33-50.

54. Valden, M.; Lai, X.; Goodman, D. W., *Science* **1998,** *281* (5383), 1647-1650.

55. Chen, M. S.; Goodman, D. W., *Science* **2004,** *306* (5694), 252-255.

56. Chen; Cai, Y.; Yan, Z.; Goodman, D. W., *J. Am. Chem. Soc.* **2006,** *128* (19), 6341-6346.

57. Komarneni, M.; Sand, A.; Burghaus, U., *Catal. Lett.* **2009,** *129* (1-2), 66-70.

58. Komarneni, M.; Sand, A.; Nevin, P.; Zak, A.; Burghaus, U., *Chem. Phys. Lett.* **2009,** *479* (1-3), 109-112.

59. Tsverin, Y.; Popovitz-Biro, R.; Feldman, Y.; Tenne, R.; Komarneni, M. R.; Yu, Z.; Chakradhar, A.; Sand, A.; Burghaus, U., *Mater. Res. Bull.* **2012,** *47* (7), 1653-1660.

60. Komarneni, M. R.; Yu, Z.; Burghaus, U.; Tsverin, Y.; Zak, A.; Feldman, Y.; Tenne, R., *submitted to Isr. J. Chem* **2012**.

61. Komarneni, M.; Kadossov, E.; Justin, J.; Lu, M.; Burghaus, U., *Surf. Sci.* **2010,** *604* (13-14), 1221-1229.

62. Chinchen, G. C.; Denny, P. J.; Jennings, J. R.; Spencer, M. S.; Waugh, K. C., *Appl. Catal.* **1988,** *36* (1-2), 1-65.

63. Chinchen, G. C.; Waugh, K. C.; Whan, D. A., *Appl. Catal.* **1986,** *25* (1-2), 101-107.

64. Chinchen, G. C.; Hay, C. M.; Vandervell, H. D.; Waugh, K. C., *J. Catal.* **1987,** *103* (1), 79-86.

65. Fleisch, T. H.; Mieville, R. L., *J. Catal.* **1984,** *90* (1), 165-172.

66. Clausen, B. S.; Steffensen, G.; Fabius, B.; Villadsen, J.; Feidenhansl, R.; Topsoe, H., *J. Catal.* **1991,** *132* (2), 524-535.

67. Klier, K., *Adv. Catal.* **1982,** *31*, 243-313.

68. Chinchen, G. C.; Denny, P. J.; Parker, D. G.; Spencer, M. S.; Whan, D. A., *Appl. Catal.* **1987,** *30* (2), 333-338.

69. Muhler, M.; Nielsen, L. P.; Tornqvist, E.; Clausen, B. S.; Topsoe, H., *Catal. Lett.* **1992,** *14* (3-4), 241-249.

70. Rasmussen, P. B.; Holmblad, P. M.; Askgaard, T.; Ovesen, C. V.; Stoltze, P.; Norskov, J. K.; Chorkendorff, I., *Catal. Lett.* **1994,** *26* (3-4), 373-381.

71. Millar, G. J.; Rochester, C. H.; Waugh, K. C., *Catal. Lett.* **1992,** *14* (3-4), 289-295.

72. Shan, J.; Komarneni, M.; Burghaus, U., *Chem. Phys. Lett.* **2011,** *517* (1-3), 59-61.

73. Chakradhar, A.; Shan, J.; Komarneni, M.; Lu, M.; Burghaus, U., *Chem. Phys. Lett. in press*.

74. Komarneni, M.; Sand, A.; Goering, J.; Burghaus, U.; Lu, M.; Monica Veca, L.; Sun, Y.-P., *Chem. Phys. Lett.* **2009,** *476* (4-6), 227-231.

75. Auger, P., *J. Phys. Radium* **1925,** *6*, 205-208.

76. Siegbahn, K., *Nova Acta Regiae Soc. Sci. Upsaliensis* **1967,** *20* (Ser. IV).

77. Ramsay, W., *Proc. Roy. Soc. Lond. A* **1905,** *76* (508), 111-114.

78. Tswett, M., *Ber. Dtsch. Botan. Ges* **1906,** *24*, 316-326.

79. Tswett, M., *Ber. Dtsch. Botan. Ges* **1906,** *24*, 384-392.

80. JAMES, A. T.; MARTIN, A. J. P., *Biochem. J.* **1952,** *50*, 679-690.

81. Rapoport, L.; Bilik, Y.; Feldman, Y.; Homyonfer, M.; Cohen, S. R.; Tenne, R., *Nature (London)* **1997,** *387* (6635), 791-793.

82. Chhowalla, M.; Amaratunga, G. A. J., *Nature (London)* **2000,** *407* (6801), 164-167.

83. Dong, K.; Ma, X.; Zhang, H.; Lin, G., *J. Nat. Gas Chem.* **2006,** *15* (1), 28-37.

84. Li, X.; Ma, D.; Chen, L.; Bao, X., *Catal. Lett.* **2007,** *116* (1-2), 63-69.

85. Song, X. C.; Zheng, Y. F.; Zhao, Y.; Yin, H. Y., *Mater. Lett.* **2006,** *60* (19), 2346-2348.

86. Goering, J.; Burghaus, U.; Arey, B. W.; Eidelman, O.; Zak, A.; Tenne, R., *Catal. Lett.* **2008,** *125* (3-4), 236-242.

87. Dhas, N. A.; Suslick, K. S., *J. Am. Chem. Soc.* **2005,** *127* (8), 2368-2369.

88. Chen, J.; Li, S.-L.; Xu, Q.; Tanaka, K., *Chem. Commun.* **2002,** (16), 1722-1723.

89. Friend, C. M.; Chen, D. A., *Polyhedron* **1997,** *16* (18), 3165-3175.

90. Topsøe, H.; Clausen, B. S.; Massoth, F. E., *Hydrotreating Catalysis, Science and Technology*. Springer-Verlag: Berlin, 1996; Vol. 11.

91. Prins, R.; De Beer, V. H. J.; Somorjai, G. A., *Catal. Rev. - Sci. Eng.* **1989,** *31* (1-2), 1-41.

92. Lauritsen, J. V.; Nyberg, M.; Norskov, J. K.; Clausen, B. S.; Topsoe, H.; Laegsgaard, E.; Besenbacher, F., *J. Catal.* **2004,** *224* (1), 94-106.

93. Kibsgaard, J.; Lauritsen, J. V.; Lgsgaard, E.; Clausen, B. S.; Topsoe, H.; Besenbacher, F., *J. Am. Chem. Soc.* **2006,** *128* (42), 13950-13958.

94. Zak, A.; Feldman, Y.; Alperovich, V.; Rosentsveig, R.; Tenne, R., *J. Am. Chem. Soc.* **2000,** *122* (45), 11108-11116.

95. Rosentsveig, R.; Margolin, A.; Gorodnev, A.; Popovitz-Biro, R.; Feldman, Y.; Rapoport, L.; Novema, Y.; Naveh, G.; Tenne, R., *J. Mater. Chem.* **2009,** *19* (25), 4368-4374.

96. Bar Sadan, M.; Houben, L.; Enyashin, A. N.; Seifert, G.; Tenne, R., *Proc. Natl. Acad. Sci. U. S. A.* **2008,** *105* (41), 15643-15648.

97. Frey, G. L.; Elani, S.; Homyonfer, M.; Feldman, Y.; Tenne, R., *Phys. Rev. B Condens. Matter Mater. Phys.* **1998,** *57* (11), 6666-6671.

98. Parilla, P. A.; Dillon, A. C.; Jones, K. M.; Riker, G.; Schulz, D. L.; Ginley, D. S.; Heben, M. J., *Nature* **1999,** *397* (6715), 114-114.

99. Funk, S.; Burghaus, U.; White, B.; O'Brien, S.; Turro, N. J., *J. Phys. Chem. C* **2007,** *111* (22), 8043-8049.

100. Funk, S.; Nurkic, T.; Burghaus, U., *Appl. Surf. Sci.* **2007,** *253* (11), 4860-4865.

101. Funk, S.; Goering, J.; Burghaus, U., *Appl. Surf. Sci.* **2008,** *254* (16), 5271-5275.

102. Zhou, B.; Hermans, S.; Somorjai, G. A., (Eds.), *Nanotechnology in Catalysis, Springer Series: Nanostructure Science and Technology* Springer: 2004.

103. Heiz, U.; Landman, U., (Eds.), *Nanocatalysis, Springer Series: NanoScience and Technology* 2007.

104. Zak, A.; Sallacan-Ecker, L.; Margolin, A.; Genut, M.; Tenne, R., *Nano* **2009,** *4* (2), 91-98.

105. Scheffer, L.; Rosentzveig, R.; Margolin, A.; Popovitz-Biro, R.; Seifert, G.; Cohen, S. R.; Tenne, R., *Phys. Chem. Chem. Phys.* **2002,** *4* (11), 2095-2098.

106. Komarneni, M.; Sand, A.; Goering, J.; Burghaus, U., *Chem. Phys. Lett.* **2009,** *473* (1-3), 131-134.

107. Burghaus, U., *Gas-carbon nanotube interactions: a review of ultra-high vacuum surface science studies on CNTs, Chapter one in Carbon nanotubes – Research Trends* Nova Science: New York, 2009.

108. Kondratyuk, P.; Wang, Y.; Johnson, J. K.; Yates, J. T., Jr., *J. Phys. Chem. B* **2005,** *109* (44), 20999-21005.

109. Wang, J.; Hokkanen, B.; Burghaus, U., *Surf. Sci.* **2005,** *577* (2-3), 158-166.

110. Kondratyuk, P.; Yates, J. T., *Chem. Phys. Lett.* **2005,** *410* (4-6), 324-329.

111. Hokkanen, B.; Funk, S.; Burghaus, U.; Ghicov, A.; Schmuki, P., *Surf. Sci.* **2007,** *601* (19), 4620-4628.

112. Grange, P., *Catal. Rev. - Sci. Eng.* **1980,** *21* (1), 135-181.

113. Tanaka, K.; Okuhara, T., *Catal. Rev. - Sci. Eng.* **1977,** *15* (2), 249-92.

114. Startsev, A. N., *Catal. Rev. - Sci. Eng.* **1995,** *37* (3), 353-423.

115. Chianelli, R. R.; Daage, M.; Ledoux, M. J., Fundamental Studies of Transition-Metal Sulfide Catalytic Materials. In *Advances in Catalysis*, D.D. Eley, H. P.; Werner, O. H., Eds. Academic Press: 1994; Vol. Volume 40, pp 177-232.

116. Lauritsen, J. V.; Nyberg, M.; Vang, R. T.; Bollinger, M. V.; Clausen, B. S.; Topsoe, H.; Jacobsen, K. W.; Laegsgaard, E.; Norskov, J. K.; Besenbacher, F., *Nanotechnology* **2003,** *14* (3), 385-389.

117. Rodriguez, J. A.; Goodman, D. W., *Surf. Sci. Rep.* **1991,** *14* (1-2), 1-107.

118. Toulhoat, H.; Raybaud, P.; Kasztelan, S.; Kresse, G.; Hafner, J., *Catal. Today* **1999,** *50* (3-4), 629-636.

119. Aegerter, P. A.; Quigley, W. W. C.; Simpson, G. J.; Ziegler, D. D.; Logan, J. W.; McCrea, K. R.; Glazier, S.; Bussell, M. E., *J. Catal.* **1996,** *164* (1), 109-121.

120. St. Clair, T. P.; Oyama, S. T.; Cox, D. F., *Surf. Sci.* **2002,** *511* (1–3), 294-302.

121. Helveg, S.; Lauritsen, J. V.; Laegsgaard, E.; Stensgaard, I.; Norskov, J. K.; Clausen, B. S.; Topsoe, H.; Besenbacher, F., *Phys. Rev. Lett.* **2000,** *84* (5), 951-954.

122. Lauritsen, J. V.; Bollinger, M. V.; Laegsgaard, E.; Jacobsen, K. W.; Norskov, J. K.; Clausen, B. S.; Topsoe, H.; Besenbacher, F., *J. Catal.* **2004,** *221* (2), 510-522.

123. Rodriguez, J. A.; Dvorak, J.; Jirsak, T.; Hrbek, J., *Surf. Sci.* **2001,** *490* (3), 315-326.

124. Potapenko, D. V.; Horn, J. M.; Beuhler, R. J.; Song, Z.; White, M. G., *Surf. Sci.* **2005,** *574* (2-3), 244-258.

125. Salmeron, M.; Somorjai, G. A.; Wold, A.; Chianelli, R.; Liang, K. S., *Chem. Phys. Lett.* **1982,** *90* (2), 105-107.

126. Kushmerick, J. G.; Weiss, P. S., *J. Phys. Chem. B* **1998,** *102* (50), 10094-10097.

127. Peterson, S. L.; Schulz, K. H., *Langmuir* **1996,** *12* (4), 941-945.

128. Wiegenstein, C. G.; Schulz, K. H., *J. Phys. Chem. B* **1999,** *103* (33), 6913-6918.

129. Altibelli, A.; Joachim, C.; Sautet, P., *Surf. Sci.* **1996,** *367* (2), 209-220.

130. Park, K. T.; Richards-Babb, M.; Freund, M. S.; Weiss, J.; Klier, K., *J. Phys. Chem.* **1996,** *100* (25), 10739-10745.

131. Perrot, E.; Humbert, A.; Piednoir, A.; Chapon, C.; Henry, C. R., *Surf. Sci.* **2000,** *445* (2-3), 407-419.

132. Cheng, L.; Bocarsly, A. B.; Bernasek, S. L.; Ramanarayanan, T. A., *Surf. Sci.* **1997,** *374* (1-3), 357-372.

133. Parker, B.; Gellman, A. J., *Surf. Sci.* **1993,** *292* (3), 223-234.

134. Liu, G.; Rodriguez, J. A.; Dvorak, J.; Hrbek, J.; Jirsak, T., *Surf. Sci.* **2002,** *505* (0), 295-307.

135. Mattila, S.; Leiro, J. A.; Heinonen, M.; Laiho, T., *Surf. Sci.* **2006,** *600* (24), 5168-5175.

136. Rodriguez, J. A.; Jirsak, T.; Perez, M.; Chaturvedi, S.; Kuhn, M.; Gonzalez, L.; Maiti, A., *J. Am. Chem. Soc.* **2000,** *122* (49), 12362-12370.

137. Dvorak, J.; Jirsak, T.; Rodriguez, J. A., *Surf. Sci.* **2001,** *479* (1-3), 155-168.

138. Liu, P.; Rodriguez, J. A.; Muckerman, J. T., *J. Phys. Chem. B* **2004,** *108* (40), 15662-15670.

139. Liu, P.; Rodriguez, J. A.; Asakura, T.; Gomes, J.; Nakamura, K., *J. Phys. Chem. B* **2005,** *109* (10), 4575-4583.

140. Speight, J. G., *The Chemistry and Technology of Petroleum*. 3 ed.; Marcel Dekker Inc: New York, 1991.

141. Camacho-Bragado, G. A.; Elechiguerra, J. L.; Olivas, A.; Fuentes, S.; Galvan, D.; Yacaman, M. J., *J. Catal.* **2005,** *234* (1), 182-190.

142. Nielsen, J. H.; Bech, L.; Nielsen, K.; Tison, Y.; Jorgensen, K. P.; Bonde, J. L.; Horch, S.; Jaramillo, T. F.; Chorkendorff, I., *Surf. Sci.* **2009,** *603* (9), 1182-1189.

143. Zaera, F.; Kollin, E. B.; Gland, J. L., *Surf. Sci.* **1987,** *184* (1-2), 75-89.

144. Gellman, A. J.; Farias, M. H.; Salmeron, M.; Somorjai, G. A., *Surf. Sci.* **1984,** *136* (1), 217-228.

145. Gellman, A. J.; Neiman, D.; Somorjai, G. A., *J. Catal.* **1987,** *107* (1), 92-102.

146. Jaramillo, T. F.; Jorgensen, K. P.; Bonde, J.; Nielsen, J. H.; Horch, S.; Chorkendorff, I., *Science (Washington, DC, U. S.)* **2007,** *317* (5834), 100-102.

147. Spirko, J. A.; Neiman, M. L.; Oelker, A. M.; Klier, K., *Surf. Sci.* **2003,** *542* (3), 192-204.

148. Spirko, J. A.; Neiman, M. L.; Oelker, A. M.; Klier, K., *Surf. Sci.* **2004,** *572* (2–3), 191-205.

149. Raybaud, P.; Hafner, J.; Kresse, G.; Toulhoat, H., *Surf. Sci.* **1998,** *407* (1-3), 237-250.

150. Fuhr, J. D.; Sofo, J. O.; Saul, A., *Surf. Sci.* **2002,** *506* (1-2), 161-171.

151. Rodriguez, J. A., *Surf. Sci.* **1992,** *278* (3), 326-338.

152. Ren, J.; Huo, C.-F.; Wen, X.-D.; Cao, Z.; Wang, J.; Li, Y.-W.; Jiao, H., *J. Phys. Chem. B* **2006,** *110* (45), 22563-22569.

153. Kadossov, E.; Justin, J.; Lu, M.; Rosenmann, D.; Ocola, L. E.; Cabrini, S.; Burghaus, U., *Chem. Phys. Lett.* **2009,** *483* (4-6), 250-253.

154. Wang, J.; Burghaus, U., *J. Chem. Phys.* **2005,** *123* (18), 184716-184727.

155. Davis, L. E., *Handbook of Auger Electron Spectroscopy* Physical Electronics: 1996.

156. http://webbook.nist.gov/chemistry/.

157. Ling, L.-X.; Zhang, R.-G.; Wang, B.-J.; Xie, K.-C., *J. Mol. Struct. THEOCHEM* **2009,** *905* (1-3), 8-12.

158. Blondeau-Patissier, V.; Domenichini, B.; Steinbrunn, A.; Bourgeois, S., *Appl. Surf. Sci.* **2001,** *175-176*, 674-677.

159. Kadossov, E.; Funk, S.; Burghaus, U., *Catal. Lett.* **2008,** *120* (3-4), 179-183.

160. Rumpf, F.; Poppa, H.; Boudart, M., *Langmuir* **1988,** *4* (3), 722-728.

161. Gillet, E.; Channakhone, S.; Matolin, V.; Gillet, M., *Surf. Sci.* **1985,** *152-153* (1), 603-614.

162. Fulmer, J. P.; Zaera, F.; Tysoe, W. T., *J. Phys. Chem.* **1988,** *92* (14), 4147-4150.

163. Weinberg, W. H.; Sun, Y. K., *Science* **1991,** *253* (5019), 542-545.

164. Ding, J.; Burghaus, U.; Weinberg, W. H., *Surf. Sci.* **2000,** *446* (1-2), 46-54.

165. Arumainayagam, C. R.; Madix, R. J., *Prog. Surf. Sci.* **1991,** *38* (1), 1-102.

166. Chianelli, R. R., *Catal. Rev. - Sci. Eng.* **1984,** *26* (3-4), 361-393.

167. Pecoraro, T. A.; Chianelli, R. R., *J. Catal.* **1981,** *67* (2), 430-445.

168. Norskov, J. K.; Clausen, B. S.; Topsoe, H., *Catal. Lett.* **1992,** *13* (1-2), 1-8.

169. Kibsgaard, J.; Tuxen, A.; Knudsen, K. G.; Brorson, M.; Topsoe, H.; Laegsgaard, E.; Lauritsen, J. V.; Besenbacher, F., *J. Catal.* **2010,** *272* (2), 195-203.

170. Tenne, R.; Margulis, L.; Genut, M.; Hodes, G., *Nature* **1992,** *360* (6403), 444-446.

171. Tenne, R., *Nat. Nanotechnol.* **2006,** *1* (2), 103-111.

172. Cheng, F. Y.; Chen, J.; Gou, X. L., *Adv. Mater.* **2006,** *18* (19), 2561-2564.

173. Zak, A.; Sallacan-Ecker, L.; Efrati, R.; Drangai, L.; Fleischer, N.; Tenne, R., *Sensors and Transducers. in press.*

174. Wang, H. M.; Iglesia, E., *J. Catal.* **2010,** *273* (2), 245-256.

175. Tuxen, A.; Kibsgaard, J.; Gobel, H.; Laegsgaard, E.; Topsoe, H.; Lauritsen, J. V.; Besenbacher, F., *ACS Nano* **2010,** *4* (8), 4677-4682.

176. Schuffenhauer, C.; Wildermuth, G.; Felsche, J.; Tenne, R., *Phys. Chem. Chem. Phys.* **2004,** *6* (15), 3991-4002.

177. Yamada, M., *Catal. Surv. Jpn.* **1999,** *3* (1), 3-15.

178. Sajkowski, D. J.; Lee, J. Y.; Schwank, J.; Tian, Y.; Goodwin, J. G., *J. Catal.* **1986,** *97* (2), 549-560.

179. Leliveld, R. G.; van Dillen, A. J.; Geus, J. W.; Koningsberger, D. C., *J. Catal.* **1998,** *175* (1), 108-116.

180. Kasztelan, S., *Langmuir* **1990,** *6* (3), 590-595.

181. Prada Silvy, R.; Grange, P.; Delmon, B., In *Catalysts in Petroleum Refining 1989 (Eds: D. L. Trimm, S. Akashah, M. Absi-Halabi, A. BIshara*, Elsivier: Amsterdam, 1989; pp 233-260.

182. Delmon, B., *Bull. Soc. Chim. Belges.* **1979,** *88*, 979-987

183. Byskov, L. S.; Norskov, J. K.; Clausen, B. S.; Topsoe, H., *J. Catal.* **1999,** *187* (1), 109-122.

184. Moses, P. G.; Hinnemann, B.; Topsoe, H.; Norskov, J. K., *J. Catal.* **2009,** *268* (2), 201-208.

185. Zhu, X.; Huo, P.; Zhang, Y.-p.; Cheng, D.-g.; Liu, C.-j., *Appl. Catal., B* **2008,** *81* (1–2), 132-140.

186. Goering, J.; Burghaus, U., *Chem. Phys. Lett.* **2007,** *447* (1-3), 121-126.

187. De la Rosa, M. P.; Texier, S.; Berhault, G.; Camacho, A.; Yacaman, M. J.; Mehta, A.; Fuentes, S.; Montoya, J. A.; Murrieta, F.; Chianelli, R. R., *J. Catal.* **2004,** *225* (2), 288-299.

188. Kadossov, E.; Komarneni, M.; Justin, J.; Burghaus, U., *Prepr. Symp. - Am. Chem. Soc., Div. Fuel Chem.* **2010,** *55* (2), 42-43.

189. Galvan, D. H.; Amarillas, A. P.; Jose-Yacaman, M., *Catal. Lett.* **2009,** *132* (3-4), 323-328.

190. Bollinger, M. V.; Jacobsen, K. W.; Nørskov, J. K., *Phys. Rev. B* **2003,** *67* (8), 085410.

191. http://www.topsoe.com/.

192. http://lowerfriction.com/.

193. Tenne, R., *Colloids Surf., A* **2002,** *208* (1), 83-92.

194. Tenne, R.; Homyonfer, M.; Feldman, Y., *Chem. Mater.* **1998,** *10* (11), 3225-3238.

195. http://www.apnano.com/.

196. Shahar, C.; Levi, R.; Cohen, S. R.; Tenne, R., *J. Phys. Chem. Lett.* **2010,** *1* (2), 540-543.

197. Graham, A. H.; Lindsay, R. W.; Read, H. J., *J. Electrochem. Soc.* **1965,** *112* (4), 401-413.

198. Deepak, F. L.; Popovitz-Biro, R.; Feldman, Y.; Cohen, H.; Enyashin, A.; Seifert, G.; Tenne, R., *Chem-Asian J* **2008,** *3* (8-9), 1568-1574.

199. Burghaus, U.; Zak, A.; Rosentsveig, R., *Isr. J. Chem.* **2010,** *50* (4), 449-452.

200. Gunter, P. L. J.; Niemantsverdriet, J. W.; Ribeiro, F. H.; Somorjai, G. A., *Catal. Rev.: Sci. Eng* **1997,** *39* (1-2), 77-168.

201. Ertl, G.; Freund, H.-J., *Phys. Today* **1999,** *52* (1), 32-38.

202. McClure, S. M.; Goodman, D. W., *Chem. Phys. Lett.* **2009,** *469* (1-3), 1-13.

203. Diez-Pascual, A. M.; Naffakh, M.; Marco, C.; Ellis, G., *Composites Part A* **2012,** *43* (4), 603-612.

204. Li, S. Y.; Rodriguez, J. A.; Hrbek, J.; Huang, H. H.; Xu, G. Q., *Surf. Sci.* **1996,** *366* (1), 29-42.

205. Thomas, J. M.; Thomas, W. J., *Principles and practice of heterogeneous catalysis*. VCH Verlagsgesellschaft mbH, Weinheim, Germany and VCH Publishers Inc., New York, U.S.A.: 1996.

206. Lee, I.; Albiter, M. A.; Zhang, Q.; Ge, J.; Yin, Y.; Zaera, F., *Phys. Chem. Chem. Phys.* **2011,** *13* (7), 2449-2456.

207. Choudhary, T. V.; Goodman, D. W., *Top. Catal.* **2002,** *21* (1-3), 25-34.

208. Kadossov, E.; Burghaus, U., *Catal. Lett.* **2010,** *134* (3-4), 228-232.

209. Bowker, M.; Houghton, H.; Waugh, K. C., *J. Chem. Soc., Faraday Trans. 1* **1981,** *77* (12), 3023-3036, 1 plate.

210. Hansen, J. B., . In *Handbook of Heterogeneous Catalysis G. Ertl, H. Knözinger, J. Weitkamp, Eds., vol. 4,* , Wiley-VCH New York 1997; Vol. 4, pp 1856–1876

211. Wang, J.; Funk, S.; Burghaus, U., *Catal. Lett.* **2005,** *103* (3-4), 219-223.

212. Wang, J.; Funk, S.; Burghaus, U., *J. Chem. Phys.* **2005,** *123* (20), 204710-204717.

213. Xu, X.; Goodman, D. W., *Appl. Phys. Lett.* **1992,** *61* (15), 1799-1801.

214. Pierce, D. E.; Burns, R. P.; Gabriel, K. A., *Thin Solid Films* **1991,** *206* (1–2), 340-344.

215. Xu, X.; He, J.-W.; Goodman, D. W., *Surf. Sci.* **1993,** *284* (1-2), 103-108.

216. Xu, X.; Goodman, D. W., *J. Phys. Chem.* **1993,** *97* (3), 683-689.

217. Dumas, P.; Tobin, R. G.; Richards, P. L., *Surf. Sci.* **1986,** *171* (3), 579-99.

218. Dutta, A.; Goswami, J.; Shivashankar, S. A., *Bull. Mater. Sci.* **1995,** *18* (7), 901-910.

219. van den Oetelaar, L. C. A.; Partridge, A.; Toussaint, S. L. G.; Flipse, C. F. J.; Brongersma, H. H., *J. Phys. Chem. B* **1998,** *102* (47), 9541-9549.

220. Zhou, J. B.; Lu, H. C.; Gustafsson, T.; Garfunkel, E., *Surf. Sci.* **1993,** *293* (3), L887-L892.

221. Espinos, J. P.; Morales, J.; Barranco, A.; Caballero, A.; Holgado, J. P.; Gonzalez-Elipe, A. R., *J. Phys. Chem. B* **2002,** *106* (27), 6921-6929.

222. Childs, K. D.; Carlson, B. A.; Vanier, L. A.; Moulder, J. F.; Paul, D. F.; Stickle, W. F.; Watson, D. G.; Hedberg, C. L., Ed. , *Handbook of Auger Electron Spectroscopy*. 3 ed.; Physical Electronics Eden Prairie, MN 1995.

223. Moulder, J. F.; Stickle, W. F.; Sobol, P. E., *Handbook of X-Ray Photoelectron Spectroscopy*. Perkin-Elmer, Physical Electronics Division U.S.A, 1980.

224. Wang, J.; Burghaus, U., *J. Chem. Phys.* **2005,** *122* (4), 44705-44715.

225. Funk, S.; Hokkanen, B.; Burghaus, U.; Bozzolo, G.; Garcés, J. E., *Surf. Sci.* **2006,** *600* (9), 1870-1876.

226. Briggs, D., Ed.;, *Handbook of X-Ray and Ultraviolet Photoelectron Spectroscopy*. Heyden & Son 1977.

227. Poulston, S.; Parlett, P. M.; Stone, P.; Bowker, M., *Surf. Interface Anal.* **1996,** *24* (12), 811-820.

228. Nakamura, J.; Rodriguez, J. A.; Campbell, C. T., *J. Phys. Condens. Matter* **1989,** *1* (Suppl. B), SB149-SB160.

229. King, D. A.; Wells, M. G., *Surf. Sci.* **1972,** *29* (2), 454-482.

230. Henry, C. R., *Surf. Sci. Rep.* **1998,** *31* (7–8), 231-325.

231. Bowker, M.; Stone, P.; Bennett, R.; Perkins, N., *Surf. Sci.* **2002,** *497* (1-3), 155-165.

232. Henry, C. R.; Chapon, C.; Duriez, C., *J. Chem. Phys.* **1991,** *95* (1), 700-705.

233. Goering, J.; Kadossov, E.; Burghaus, U.; Yu, Z. Q.; Thevuthasan, S.; Saraf, L. V., *Catal. Lett.* **2007,** *116* (1-2), 9-14.

234. Kneitz, S.; Gemeinhardt, J.; Steinruck, H. P., *Surf. Sci.* **1999,** *440* (3), 307-320.

235. Burghaus, U.; Ding, J.; Weinberg, W. H., *Surf. Sci.* **1997,** *384* (1-3), L869-L874.

236. Bowker, M.; Bowker, L. J.; Bennett, R. A.; Stone, P.; Ramirez-Cuesta, A., *J. Mol. Catal. A Chem.* **2000,** *163* (1-2), 221-232.

237. Libuda, J.; Freund, H. J., *Surf. Sci. Rep.* **2005,** *57* (7-8), 157-298.

238. Libuda, J., *Surf. Sci.* **2005,** *587* (1-2), 55-68.

239. Burghaus, U., *Catal. Today* **2009,** *148* (3-4), 212-220.

240. Taylor, H. S., *Proc. R. Soc. London, Ser. A* **1925,** *108*, 105-111.

241. Zambelli, T.; Wintterlin, J.; Trost, J.; Ertl, G., *Science (Washington, D. C., U. S.)* **1996,** *273* (5282), 1688-1690.

242. Norskov, J. K.; Bligaard, T.; Hvolbaek, B.; Abild-Pedersen, F.; Chorkendorff, I.; Christensen, C. H., *Chem. Soc. Rev.* **2008,** *37* (10), 2163-2171.

243. Kim, T. S.; Stiehl, J. D.; Reeves, C. T.; Meyer, R. J.; Mullins, C. B., *J. Am. Chem. Soc.* **2003,** *125* (8), 2018-2019.

244. Stiehl, J. D.; Kim, T. S.; McClure, S. M.; Mullins, C. B., *J. Am. Chem. Soc.* **2004,** *126* (6), 1606-1607.

245. Stiehl, J. D.; Kim, T. S.; Reeves, C. T.; Meyer, R. J.; Mullins, C. B., *J. Phys. Chem. B* **2004,** *108* (23), 7917-7926.

246. Lee, S.; Fan, C.; Wu, T.; Anderson, S. L., *J. Am. Chem. Soc.* **2004,** *126* (18), 5682-5683.

247. Sueyoshi, T.; Sasaki, T.; Iwasawa, Y., *Surf. Sci.* **1995,** *343* (1/2), 1-16.

248. Lemire, C.; Meyer, R.; Shaikhutdinov, S.; Freund, H.-J., *Angew. Chem., Int. Ed.* **2004,** *43* (1), 118-121.

249. Vittadini, A.; Selloni, A., *J. Chem. Phys.* **2002,** *117* (1), 353-361.

250. Yim, W.-L.; Nowitzki, T.; Necke, M.; Schnars, H.; Nickut, P.; Biener, J.; Biener, M. M.; Zielasek, V.; Al-Shamery, K.; Kluener, T.; Baeumer, M., *J. Phys. Chem. C* **2007,** *111* (1), 445-451.

251. Pacchioni, G.; Ferrari, A. M.; Bagus, P. S., *Surf. Sci.* **1996,** *350* (1-3), 159-175.

252. Luo, K.; Kim, D. Y.; Goodman, D. W., *J. Mol. Catal. A Chem.* **2001,** *167* (1-2), 191-198.

253. Wallace, W. T.; Min, B. K.; Goodman, D. W., *J. Mol. Catal. A Chem.* **2005,** *228* (1-2), 3-10.

254. Min, B. K.; Wallace, W. T.; Santra, A. K.; Goodman, D. W., *J. Phys. Chem. B* **2004,** *108* (42), 16339-16343.

255. Cechal, J.; Polcak, J.; Kolibal, M.; Babor, P.; Sikola, T., *Appl. Surf. Sci.* **2010,** *256* (11), 3636-3641.

256. Zhou, J. B.; Gustafsson, T.; Garfunkel, E., *Surf. Sci.* **1997,** *372* (1-3), 21-27.

257. Kneitz, S.; Gemeinhardt, J.; Koschel, H.; Held, G.; Steinrück, H. P., *Surf. Sci.* **1999,** *433–435* (0), 27-31.

258. Schimpf, S.; Lucas, M.; Mohr, C.; Rodemerck, U.; Bruckner, A.; Radnik, J.; Hofmeister, H.; Claus, P., *Catal. Today* **2002,** *72* (1-2), 63-78.

259. Ribeiro, F. H.; Somorjai, G. A., *Recl. Trav. Chim. Pays-Bas* **1994,** *113* (10), 419-422.

260. Wong, K.; Johansson, S.; Kasemo, B., *Faraday Discuss.* **1997,** *105* (Catalysis and Surface Science at High Resolution), 237-246.

261. Johanek, V.; Laurin, M.; Grant, A. W.; Kasemo, B.; Henry, C. R.; Libuda, J., *Science (Washington, DC, U. S.)* **2004,** *304* (5677), 1639-1644.

262. Kobayashi, H.; Takezawa, N.; Minochi, C., *J. Catal.* **1981,** *69* (2), 487-494.

263. Ossipoff, N. J.; Cant, N. W., *J. Catal.* **1994,** *148* (1), 125-133.

264. Kadossov, E.; Burghaus, U., *Surf. Interface Anal.* **2008,** *40* (5), 893-898.

265. Kadossov, E.; Goering, J.; Burghaus, U., *Surf. Sci.* **2008,** *602* (3), 811-818.

266. Sadykov, V. A.; Tikhov, S. F.; Bulgakov, N. N.; Gerasev, A. P., *Catal. Today* **2009,** *144* (3-4), 324-333.

267. Newsome, D. S., *Catal. Rev. - Sci. Eng.* **1980,** *21* (2), 275-318.

268. Hara, M.; Kondo, T.; Komoda, M.; Ikeda, S.; Shinohara, K.; Tanaka, A.; Kondo, J. N.; Domen, K., *Chem. Commun.* **1998,** (3), 357-358.

269. Musa, A. O.; Akomolafe, T.; Carter, M. J., *Sol. Energy Mater. Sol. Cells* **1998,** *51* (3-4), 305-316.

270. Bednorz, J. G.; Mueller, K. A., *Z. Phys. B Condens. Matter* **1986,** *64* (2), 189-193.

271. Chan, G. H.; Zhao, J.; Hicks, E. M.; Schatz, G. C.; Van Duyne, R. P., *Nano Lett.* **2007,** *7* (7), 1947-1952.

272. White, B.; Yin, M.; Hall, A.; Le, D.; Stolbov, S.; Rahman, T.; Turro, N.; O'Brien, S., *Nano Lett.* **2006,** *6* (9), 2095-2098.

273. Premkumar, T.; Geckeler, K. E., *J. Phys. Chem. Solids* **2006,** *67* (7), 1451-1456.

274. Cox, P. A., *Transition Metal Oxides − an Introduction to Their Electronic Structure and Properties*. Clarendon Press: Oxford, 1995.

275. Cox, D. F.; Schulz, K. H., *Surf. Sci.* **1991,** *249* (1-3), 138-148.

276. Wang, J.; Burghaus, U., *Chem. Phys. Lett.* **2005,** *403* (1-3), 42-46.

277. Wang, J.; Johnson, E.; Burghaus, U., *Chem. Phys. Lett.* **2005,** *410* (1-3), 131-135.

278. Golunski, S., *Platinum Met. Rev.* **2007,** *51* (3), 162.

279. Panzner, G.; Egert, B.; Schmidt, H. P., *Surf. Sci.* **1985,** *151* (2–3), 400-408.

280. Moretti, G.; De Rossi, S.; Ferraris, G., *Appl. Surf. Sci.* **1990,** *45* (4), 341-349.

281. Barreca, D.; Gasparotto, A.; Tondello, E., *Surf. Sci. Spectra* **2008,** *14*, 41-51.

282. Wu, C.-K.; Yin, M.; O'Brien, S.; Koberstein, J. T., *Chem. Mater.* **2006,** *18* (25), 6054-6058.

283. Fu, S. S.; Somorjai, G. A., *Surf. Sci.* **1992,** *262* (1-2), 68-76.

284. Wachs, I. E.; Madix, R. J., *J. Catal.* **1978,** *53* (2), 208-227.

285. Kessler, J.; Thieme, F., *Surf. Sci.* **1977,** *67* (2), 405-415.

286. Linsebigler, A.; Lu, G.; Yates, J. T., Jr., *J. Chem. Phys.* **1995,** *103* (21), 9438-9443.

287. Henderson, M. A., *Surf. Sci.* **1998,** *400* (1-3), 203-219.

288. Lemire, C.; Meyer, R.; Henrich, V. E.; Shaikhutdinov, S.; Freund, H. J., *Surf. Sci.* **2004,** *572* (1), 103-114.

289. Kunat, M.; Boas, C.; Becker, T.; Burghaus, U.; Woll, C., *Surf. Sci.* **2001,** *474* (1-3), 114-128.

290. Kunat, M.; Burghaus, U., *Surf. Sci.* **2003,** *544* (2-3), 170-182.

291. Bowker, M., *Surf. Rev. Lett.* **1994,** *1* (4), 549-551.

292. Zheng, X. G.; Suzuki, M.; Xu, C. N., *Mater. Res. Bull.* **1998,** *33* (4), 605-610.

293. Woodward, R. B.; Hoffmann, R., *Angew. Chem., Int. Ed.* **1969,** *8* (11), 781-853.

294. Frost, J. C., *Nature* **1988,** *334* (6183), 577-580.

295. Olah, G. A.; Goeppert, A.; Surya Prakash, G. K., *Beyond Oil and Gas: The Methanol Economy*. 1 ed.; Wiley-VCH 2006.

296. Kao, C.-L.; Carlsson, A.; Madix, R. J., *Surf. Sci.* **2002,** *497* (1–3), 356-372.

297. Funk, S.; Hokkanen, B.; Wang, J.; Burghaus, U.; Bozzolo, G.; Garces, J. E., *Surf. Sci.* **2006,** *600* (3), 583-590.

298. D'Evelyn, M. P.; Hamza, A. V.; Gdowski, G. E.; Madix, R. J., *Surf. Sci.* **1986,** *167* (2–3), 451-473.

299. Vattuone, L.; Savio, L.; Rocca, M., *Surf. Sci. Rep.* **2008,** *63* (3), 101-168.

300. Costantini, G.; de Mongeot, F. B.; Rusponi, S.; Boragno, C.; Valbusa, U.; Vattuone, L.; Burghaus, U.; Savio, L.; Rocca, M., *J. Chem. Phys.* **2000,** *112* (15), 6840-6843.

301. Burghaus, U., *Trends. Phys. Chem* **2006,** *11*, 1-19.

302. Funk, S.; Burghaus, U., *Phys. Chem. Chem. Phys.* **2006,** *8* (41), 4805-4813.

303. Hansen, W.; Bertolo, M.; Jacobi, K., *Surf. Sci.* **1991,** *253* (1–3), 1-12.

304. Camplin, J. P.; Clowes, S. K.; Cook, J. C.; McCash, E. M., *Surf. Rev. Lett.* **1997,** *4* (6), 1365-1370.

305. Hadenfeldt, S.; Benndorf, C.; Stricker, A.; Towe, M., *Surf. Sci.* **1996,** *352*, 295-299.

306. Wang, G.-C.; Jiang, L.; Morikawa, Y.; Nakamura, J.; Cai, Z.-S.; Pan, Y.-M.; Zhao, X.-Z., *Surf. Sci.* **2004,** *570* (3), 205-217.

307. Kadossov, E.; Burghaus, U., *J. Phys. Chem. C* **2008,** *112* (19), 7390-7400.

308. Freund, H. J.; Roberts, M. W., *Surf. Sci. Rep.* **1996,** *25* (8), 225-273.

309. Burghaus, U., Elsevier: New and future deveopment in catalysis: Activation of carbon dioxide, 2012.

310. Bönicke, I.; Kirstein, W.; Spinzig, S.; Thieme, F., *Surf. Sci.* **1994,** *313* (3), 231-238.

311. Shan, J.; Chakradhar, A.; Komarneni, M.; Burghaus, U., *submitted to J. Phys. Chem. C* **2012**.

312. Saito, R.; Dresselhaus, G.; Dresselhaus, M. S., *Physical properties of carbon nanotubes*. Imperial College Press: 1998.

313. Rotkin, S. V.; Subramoney, S., (Eds.), *Applied Physics of Carbon Nanotubes*. Springer: New York, 2005.

314. Loiseau, A.; Launois, P.; Petit, P.; Roche, S.; Salvetat, J. P., (Eds.), *Understanding Carbon Nanotubes*. Springer: New York, 2006; Vol. 677.

315. Reich, S.; Thomsen, C.; Maultzsch, J., *Carbon Nanotubes: Basic Concepts and Physical Properties*. Wiley-VCH: Darmstadt.

316. Funk, S.; Nurkic, T.; Hokkanen, B.; Burghaus, U., *Appl. Surf. Sci.* **2007,** *253* (17), 7108-7114.

317. Komarneni, M.; Sand, A.; Lu, M.; Burghaus, U., *Chem. Phys. Lett.* **2009,** *470* (4-6), 300-303.

318. http://www.jcrystal.com/.

319. O'Connell, M. J.; Bachilo, S. M.; Huffman, C. B.; Moore, V. C.; Strano, M. S.; Haroz, E. H.; Rialon, K. L.; Boul, P. J.; Noon, W. H.; Kittrell, C.; Ma, J.; Hauge, R. H.; Weisman, R. B.; Smalley, R. E., *Science (Washington, DC, U. S.)* **2002,** *297* (5581), 593-596.

320. Bachilo, S. M.; Balzano, L.; Herrera, J. E.; Pompeo, F.; Resasco, D. E.; Weisman, R. B., *J. Am. Chem. Soc.* **2003,** *125* (37), 11186-11187.

321. Tan, P. H.; Hasan, T.; Bonaccorso, F.; Scardaci, V.; Rozhin, A. G.; Milne, W. I.; Ferrari, A. C., *Phys. E (Amsterdam, Neth.)* **2008,** *40* (7), 2352-2359.

322. White, B.; Banerjee, S.; O'Brien, S.; Turro, N. J.; Herman, I. P., *J. Phys. Chem. C* **2007,** *111* (37), 13684-13690.

323. Tan, P. H.; Rozhin, A. G.; Hasan, T.; Hu, P.; Scardaci, V.; Milne, W. I.; Ferrari, A. C., *Phys. Rev. Lett.* **2007,** *99* (13), 137402.

324. O'Connell, M. J.; Bachilo, S. M.; Huffman, C. B.; Moore, V. C.; Strano, M. S.; Haroz, E. H.; Rialon, K. L.; Boul, P. J.; Noon, W. H.; Kittrell, C.; Ma, J.; Hauge, R. H.; Weisman, R. B.; Smalley, R. E., *Science* **2002,** *297* (5581), 593-596.

325. Dukovic, G.; White, B. E.; Zhou, Z.; Wang, F.; Jockusch, S.; Steigerwald, M. L.; Heinz, T. F.; Friesner, R. A.; Turro, N. J.; Brus, L. E., *J. Am. Chem. Soc.* **2004,** *126* (46), 15269-15276.

326. Wetterer, S. M.; Lavrich, D. J.; Cummings, T.; Bernasek, S. L.; Scoles, G., *J. Phys. Chem. B* **1998,** *102* (46), 9266-9275.

327. Dicks, A. L., *J. Power Sources* **2006,** *156* (2), 128-141.

328. Kuznetsova, A.; Yates, J. T.; Liu, J.; Smalley, R. E., *J. Chem. Phys.* **2000,** *112* (21), 9590-9598.

329. Ulbricht, H.; Zacharia, R.; Cindir, N.; Hertel, T., *Carbon* **2006,** *44* (14), 2931-2942.

330. Burghaus, U.; Bye, D.; Cosert, K.; Goering, J.; Guerard, A.; Kadossov, E.; Lee, E.; Nadoyama, Y.; Richter, N.; Schaefer, E.; Smith, J.; Ulness, D.; Wymore, B., *Chem. Phys. Lett.* **2007,** *442* (4-6), 344-347.

331. Goering, J.; Kadossov, E.; Burghaus, U., *J. Phys. Chem. C* **2008,** *112* (27), 10114-10124.

332. Niyogi, S.; Hamon, M. A.; Hu, H.; Zhao, B.; Bhowmik, P.; Sen, R.; Itkis, M. E.; Haddon, R. C., *Acc. Chem. Res.* **2002,** *35* (12), 1105-1113.

333. Bergin, S. D.; Nicolosi, V.; Streich, P. V.; Giordani, S.; Sun, Z.; Windle, A. H.; Ryan, P.; Niraj, N. P. P.; Wang, Z.-T. T.; Carpenter, L.; Blau, W. J.; Boland, J. J.; Hamilton, J. P.; Coleman, J. N., *Adv. Mater. (Weinheim, Ger.)* **2008,** *20* (10), 1876-1881.

334. Bolina, A. S.; Wolff, A. J.; Brown, W. A., *J. Chem. Phys.* **2005,** *122* (4), 44713-44725.

335. Tournus, F.; Latil, S.; Heggie, M. I.; Charlier, J. C., *Phys. Rev. B* **2005,** *72* (7), 075431.

336. Strano, M. S.; Dyke, C. A.; Usrey, M. L.; Barone, P. W.; Allen, M. J.; Shan, H.; Kittrell, C.; Hauge, R. H.; Tour, J. M.; Smalley, R. E., *Science (Washington, DC, U. S.)* **2003,** *301* (5639), 1519-1522.

337. Wang, W.; Fernando, K. A. S.; Lin, Y.; Meziani, M. J.; Veca, L. M.; Cao, L.; Zhang, P.; Kimani, M. M.; Sun, Y.-P., *J. Am. Chem. Soc.* **2008,** *130* (4), 1415-1419.

338. Bahome, M. C.; Jewell, L. L.; Hildebrandt, D.; Glasser, D.; Coville, N. J., *Appl. Catal., A* **2005,** *287* (1), 60-67.

339. Alexiadis, A.; Kassinos, S., *Chem. Rev. (Washington, DC, U. S.)* **2008,** *108* (12), 5014-5034.

340. Tournus, F.; Charlier, J. C., *Phys. Rev. B* **2005,** *71* (16), 165421.

341. Alldredge, E. S.; Bădescu, Ş. C.; Bajwa, N.; Perkins, F. K.; Snow, E. S.; Reinecke, T. L.; Passmore, J. L.; Chang, Y. L., *Phys. Rev. B* **2008,** *78* (16), 161403.

342. Sumanasekera, G. U.; Adu, C. K. W.; Fang, S.; Eklund, P. C., *Phys. Rev. Lett.* **2000,** *85* (5), 1096-1099.

343. da Silva, L. B.; Fagan, S. B.; Mota, R., *Nano Lett.* **2003,** *4* (1), 65-67.

344. Chen, Z.; Thiel, W.; Hirsch, A., *ChemPhysChem* **2003,** *4* (1), 93-97.

345. Zacharia, R.; Ulbricht, H.; Hertel, T., *Phys. Rev. B* **2004,** *69* (15), 155406.

346. Gauden, P. A.; Terzyk, A. P.; Rychlicki, G.; Kowalczyk, P.; Lota, K.; Raymundo-Pinero, E.; Frackowiak, E.; Beguin, F., *Chem. Phys. Lett.* **2006,** *421* (4-6), 409-414.

347. Fan, J.; Yudasaka, M.; Kasuya, Y.; Kasuya, D.; Iijima, S., *Chem. Phys. Lett.* **2004,** *397* (1-3), 5-10.

348. Zhao, J.; Buldum, A.; Han, J.; Lu, J. P., *Nanotechnology* **2002,** *13* (2), 195-200.